

OBSERVATIONAL SIGNATURES OF CONVECTION IN SOLAR TYPE STARS

by

Devon Hamilton

A Thesis submitted in conformity with the requirements
for the Degree of Doctor of Philosophy.
Graduate Department of Astronomy and Astrophysics.
in the University of Toronto.

© Copyright by Devon Hamilton 2001



National Library
of Canada

Acquisitions and
Bibliographic Services

395 Wellington Street
Ottawa ON K1A 0N4
Canada

Bibliothèque nationale
du Canada

Acquisitions et
services bibliographiques

395, rue Wellington
Ottawa ON K1A 0N4
Canada

Your file *Voire référence*

Our file *Notre référence*

The author has granted a non-exclusive licence allowing the National Library of Canada to reproduce, loan, distribute or sell copies of this thesis in microform, paper or electronic formats.

The author retains ownership of the copyright in this thesis. Neither the thesis nor substantial extracts from it may be printed or otherwise reproduced without the author's permission.

L'auteur a accordé une licence non exclusive permettant à la Bibliothèque nationale du Canada de reproduire, prêter, distribuer ou vendre des copies de cette thèse sous la forme de microfiche/film, de reproduction sur papier ou sur format électronique.

L'auteur conserve la propriété du droit d'auteur qui protège cette thèse. Ni la thèse ni des extraits substantiels de celle-ci ne doivent être imprimés ou autrement reproduits sans son autorisation.

0-612-58914-5

Canada

Observational Signatures of Convection in Solar Type Stars

Doctor of Philosophy, 2001
Devon Hamilton
Graduate Department of Astronomy and Astrophysics
University of Toronto

Abstract

In this thesis, a new technique for studying convection is developed using relative line-shifts. The technique is tested using the sun's visible flux spectrum and the most current Fe I line positions available, and can be applied at significantly lower spectral resolutions and signal-to-noise ratios than has been done previously. These line-shifts show a clear dependence on both line strength and wavelength. Similar observations in the solar intensity spectrum demonstrate that the effects of limb darkening on the line-shifts are relatively minor. Because the solar intensity spectrum has been observed well into the infrared, it has been used to study the line-shift techniques over the broadest possible spectral region. The Fe I line-core shift distributions show clear evidence of a dependence on line strength at all wavelengths, and sensitivities to wavelength are found at shorter wavelengths. Line-shifts for 1323 CO lines between 2.2 and 5.5 μm are also determined. Clear evidence of a dependence on line strength is found at all wavelengths, and interesting line-shift behavior is found when the excitation energy and quantum numbers of the CO transitions are examined. A similar study of CO and OH line-shifts is done using a sunspot umbral spectrum, and the convective motions are found to be greatly suppressed. Line-shifts are also examined in the infrared spectrum of six cool giant stars. The vigorous nature of convection seems to decline with T_{eff} , which is consistent with expectations.

Acknowledgements

To properly express my gratitude to all the different people who have influenced this thesis is truly a daunting task.

I owe a tremendous debt to my supervisor, John Lester, who supported and guided my research over the past five years. His suggestions and insight lead to some of the more interesting and useful portions of this thesis; thanks John! The initial impetus for this thesis came from both John Lester and from Slavek Rucinski, who suggested a particular review article that sparked the author's curiosity. Slavek has also proven to be a valuable critic of much of this work, and his insight is appreciated.

Without the great assistance of Jean-Pierre Maillard, and of course the night assistants at CFHT, it would not have been possible to complete this thesis. J.-P. provided both technical assistance with the FTS and scientific advice, which was very helpful. Discussion with Allan Irwin, Dainis Dravins and Dag Gullberg also influenced the direction and content of this thesis, which is greatly appreciated. And of course, a debt of gratitude is owed to the referees for the CFHT time allocation requests and the journal paper PASP 111:1132, much of which was incorporated into Chapter 2. The suggestions and comments of the referees were most valuable. Large portions of Chapter 2 originally appeared in the Publications of the Astronomical Society of the Pacific (Hamilton and Lester, 1999, PASP, 111, 1132). Copyright 2000, Astronomical Society of the Pacific; reproduced with permission of the Editors.

I am grateful to Chuck Shepherd for both his friendship and his useful suggestions. Chuck often proved himself to be a strong sounding board off of him ideas could be bounced.

A special note of thanks has to be extended to Mike Allen, who provided a great deal of assistance the formatting and writing of this thesis, and for being an easy mark in the various hockey pools we have had over the years.

Perhaps the greatest debt of gratitude I owe is to my family, whose love, patience and support have carried throughout the last 5 years. To my parents Glen and Rae, who have given me their love and support throughout this long process, a heartfelt thank you. To my children, Megan and Patrick, whose curiosity has often been an inspiration to me, I dedicate this thesis with all of my love. Last, but definitely not least, the greatest debt I owe is to my wife, Erin. Her love, support, patience, humor and understanding have sustained me throughout this process, and I am eternally grateful for that (goodness knows, I certainly did not deserve it!).

Contents

0.1	Abstract	i
0.2	Acknowledgements	ii
1	An Introduction to Photospheric Convection	1
1.1	Background	1
1.2	Atmospheric Convection	2
1.3	The Mixing Length Theory	5
1.4	Current Approaches	6
1.4.1	Turbulent Convection Theories	6
1.4.2	Numerical Simulations	8
1.5	Convection and Spectral Line Asymmetries	10
1.6	Diagnostic Candidates	13
2	A Technique for the Study of Stellar Convection:	
	The Visible Solar Flux Spectrum	17
2.1	Introduction	17
2.2	Methodology	18
2.2.1	Solar Flux Spectrum	18
2.2.2	The Determination of Line Positions	18
2.2.3	Errors	22
2.3	Analysis	22
2.3.1	Line-shifts	22
2.3.2	Spectral Resolution Effects	30
2.4	Conclusions	37

3	Fe I in the Central Intensity Spectrum of the Sun	42
3.1	Introduction	42
3.2	Methodology	43
3.2.1	Spectral Sources	43
3.2.2	Wavelength Errors	45
3.3	Line Selection	46
3.3.1	Fe I	46
3.3.2	Ti I	46
3.4	Analysis	47
3.4.1	Flux-Intensity Comparison	47
3.4.2	Fe I	47
3.4.3	Ti I	59
3.4.4	Summary	61
3.5	Intensity Spectra	62
3.5.1	Wavelength Dependence	62
3.5.2	Line-Depth Dependence	64
3.5.3	Excitation Energy Dependence	67
3.5.4	Line Formation Depth	69
3.6	Conclusions	75
4	CO in The Central Intensity Spectrum of the Sun	77
4.1	Introduction	77
4.2	Methodology	78
4.2.1	Solar Intensity Spectral Atlases	78
4.2.2	Line Selection	78
4.2.3	Errors	79
4.3	Analysis	80
4.3.1	CN	80
4.3.2	CO $\Delta v = 1$	81
4.3.3	CO $\Delta v = 2$	90
4.4	Discussion	90
4.5	Conclusions	96

5	Line Shifts in a Sunspot Umbral Spectrum	98
5.1	Introduction	98
5.2	Methodology	99
5.2.1	The Sunspot Spectral Atlases	99
5.2.2	Line Selection	100
5.2.3	Errors	102
5.3	Analysis	102
5.3.1	CO $\Delta v = 1$	102
5.3.2	CO $\Delta v = 2$	103
5.3.3	CO $\Delta v = 3$	110
5.3.4	OH	111
5.3.5	TiO	116
5.4	Discussion	116
6	Line Shifts in the Spectra of K Giants and Supergiants	121
6.1	Introduction	121
6.1.1	The G - K Giants and Supergiants	122
6.2	Line-Shifts in Arcturus	123
6.2.1	Line Selection	124
6.2.2	Fe I	125
6.2.3	OH	134
6.2.4	CN	135
6.2.5	CO	136
6.3	The CFHT Stars	140
6.4	Discussion	146
7	Summary and Future Work	153
7.1	Observing Convection in the Sun	153
7.1.1	Solar Flux: Fe I	154
7.1.2	Solar Central Intensity Observations	155
7.1.3	Molecular Line-shifts as Diagnostics	156
7.1.4	Umbral Line-shifts	157
7.2	Observing Convection in Solar-Type Stars	157

7.3	Future Projects	159
7.3.1	Exploring Convection in Stellar Parameter Space	159
7.3.2	Fe I Line-shifts at High χ_I	160
7.3.3	CO Formation Altitudes	160

List of Tables

2.1	Fe I Visible Flux Bin Characteristics	41
6.1	Properties of Observed Stars	141
6.2	CFHT Observations	143
6.3	CO $\Delta v=2$ Distribution Properties	144

List of Figures

1.1	Two example bisectors.	11
1.2	Tracing the bisector using line-core positions	12
2.1	Method schematic	20
2.2	Fe I line-shifts vs. χ_l	24
2.3	Fe I line-shifts vs χ_l binned by λ and line strength	25
2.4	Fe I line-shift vs. line depth	28
2.5	Fe I line-shifts vs. wavelength	29
2.6	Fe I median bisectors	31
2.7	Resolution effects on Fe I line-shift distributions	33
2.8	Slope of Fe I line depth/line-shift distributions vs. R	35
2.9	Resolution effects on Fe I wavelength dependence	36
2.10	Comparison to other methods	38
3.1	Fe I line-shift dependence on λ : Flux and Intensity	50
3.2	FeI line-shift vs. line depth: Flux vs. Intensity	52
3.3	FeI line-shifts vs. χ_l	55
3.4	Fe I median bisectors: Flux vs. Intensity	57
3.5	Fe I median bisectors by line depth bins: Flux vs. Intensity	58
3.6	Fe I median bisectors by λ bin: Flux vs. Intensity	59
3.7	Ti I line-shifts vs. λ	60
3.8	Ti I line-shifts vs. λ	61
3.9	Fe I line-shifts vs λ : 400 nm to 2 μm	63
3.10	Fe I line-shift vs. line depth: 400 nm to 2 μm	65
3.11	Fe I line shifts in the ATMOS IR sample	68

3.12	Physical height of simulated lines vs. λ	71
3.13	Velocity vs. physical height: strength and λ	73
4.1	CO $\Delta v = 1$ line-shifts vs. quantum number	82
4.2	CO $\Delta v = 1$ line-shifts vs. line depths	84
4.3	The changing slope of the line depth distributions for the $\Delta v = 1$ bands	86
4.4	CO $\Delta v = 1$ line-shifts vs. wavenumber	87
4.5	CO $\Delta v = 1$ line-shifts vs. χ_l	88
4.6	Close view of the line depth dependence near 25% of the continuum	89
4.7	CO $\Delta v = 2$ line-shifts vs. line depth	91
4.8	CO $\Delta v = 2$ line-shifts vs. wavenumber	91
4.9	Granulation and contrast inversion schematic	94
5.1	CO $\Delta v = 2$ umbral line-shifts vs. quantum number	104
5.2	CO $\Delta v = 2$ umbral line-shifts vs. line depth	105
5.3	CO $\Delta v = 2$ umbral line-shifts vs. wavenumber	107
5.4	CO 3 – 1 R branch line-shifts vs. wavenumber and χ_l	108
5.5	CO $\Delta v = 2$ line-shifts vs. χ_l	109
5.6	CO $\Delta v = 2$ median line bisectors	110
5.7	OH $\Delta v = 1$ line-shifts vs. line depth	112
5.8	OH $\Delta v = 1$ line-shifts vs quantum number	113
5.9	OH $\Delta v = 2$ line-shifts vs. line depth	114
5.10	OH $\Delta v = 2$ line-shifts vs. wavenumber	115
5.11	OH $\Delta v = 2$ line-shifts vs quantum number	115
5.12	TiO γ bands line-shifts vs line depth	117
5.13	TiO γ bands line-shifts vs. quantum number	117
6.1	Arcturus: Fe I line-shifts vs. wavenumber	126
6.2	Arcturus: Fe I line-shifts vs. wavenumber by filter band	127
6.3	Arcturus: Fe I line-shifts vs. line depth	130
6.4	Solar: NIR Fe I line-shifts vs. line depth, $\lambda/\Delta\lambda = 10^5$	131
6.5	Arcturus: Fe I line-shifts vs. χ_l	132
6.6	Arcturus: OH $\Delta v = 1$ line-shifts vs. line depth	134

6.7	Arcturus: CO $\Delta v = 1$ line-shifts vs. line depth	137
6.8	Arcturus: CO $\Delta v = 2$ line-shifts vs. line depth	138
6.9	Arcturus: CO $\Delta v = 3$ line-shifts vs. χ_l and quantum number	139
6.10	Line-shifts vs. line depth for the CFHT observations	145
6.11	The bottom of the CO line at $4222.9542 \text{ cm}^{-1}$ of four of the CFHT stars.	149

Chapter 1

An Introduction to Photospheric Convection

1.1 Background

The term '*granule*' was first used to describe the mottled appearance of the Sun's surface in 1864 by the Reverend William Dawes, although the most realistic observations of granulation in the 19th century were probably those conducted by Father Secchi (published in his book *Le Soleil* in 1875). Secchi's sketches of bright, slightly irregular grains surrounded by narrower, interconnected darker regions, bear a remarkable similarity to modern images of the solar surface (Bray et al. 1984). An association between granulation and convection was not made until 1930, when Unsöld proposed that the observed granulation was the result of convective currents in the hydrogen ionization zone. In 1933, Siedentopf theorized that the granules were the result of ascending bubbles of hotter gas rising through cooler, descending material. Siedentopf's ideas were based on Prandtl's work on a '*mixing length*' theory, where turbulent eddies would transfer energy over some parameterized distance (Bray et al. 1984).

It was only in 1957 that the connection between solar granulation and convection was firmly established (Leighton 1957). In 1958, Böhm-Vitense produced what has become the standard description of stellar convection, the **Mixing Length Theory (MLT)**, a phenomenological treatment with a 'tunable' free parameter to describe the length scale of the eddies (Böhm-Vitense 1958). Over 40 years later, the MLT is still the basis for most modern approaches to stellar convection (Bray et al. 1984; Spruit 1997). However, this treatment is an inadequate approximation of astrophysical

reality.

Many aspects of stellar atmospheric models have shown remarkable improvements in recent years; especially in areas such as magneto-hydrodynamics and opacity. Unfortunately, convection treatments based upon the MLT have lagged far behind. However, the prospects for improving our understanding of stellar convection are increasing. Improvements in computational speed and numerical simulations have been challenging the traditional view of convection in stellar atmospheres, and new analytical approaches to convection are in development (see §1.4).

With these potential enhancements in stellar atmospheric modeling, there is a pressing need to develop observational diagnostics to test these improvements. This thesis is an examination of one of these observational diagnostics, and its possible utility in studying convection in solar-type stars.

This first chapter introduces the role convection plays in solar-type stars, and how it is treated in atmospheric modeling; summarizing some of the current techniques for treating convection and provides some of the background regarding the diagnostic in question. Chapter Two summarizes the application and testing of the technique using the *Solar Visible Flux Spectrum* (Kurucz et al. 1984). The third chapter extends the technique over greater wavelengths using central intensity spectral atlases of the Sun. The fourth chapter continues applying the technique to the central intensity spectrum of the Sun using molecular spectral lines and emphasizes the goal of exploring the possibility of applying the technique to cooler stars. The fifth chapter then uses the diagnostics to study convection in sunspot spectra. Chapter Six describes the application of the technique to other stars over a range of T_{eff} and $\log g$. The final chapter provides a summary and outline of future applications.

1.2 Atmospheric Convection

The onset of convection occurs when radiation is no longer the most efficient means of transporting energy through a star. In the case of the Sun, and other solar-type stars, this is usually associated with the increase in opacity due to the hydrogen ionization/recombination layer.

To begin, assume that at a given layer in the star the gas is in hydrostatic equilibrium, and there is a volume element that is small compared to the scale of the star. If this volume element suffers some perturbation, it will either undergo convection and rise (or sink), or the perturbation will be damped and the element will return to its original location (for thorough discussions of this

scenario see Bray et al. 1984, Cox and Giuli 1968 or Mihalas 1978).

The stability of the volume element is expressed using the Schwarzschild criterion (following Mihalas 1978):

$$(\Delta\rho)_E = (d\rho/dr)_A \Delta r < (\Delta\rho)_R = (d\rho/dr)_R \Delta r \quad (1.1)$$

where $(\Delta\rho)_E$ is the decrease in density due to expansion. The volume element is considered to be adiabatic (subscript A), and the surrounding gas is radiative (subscript R). The terms $(d\rho/dr)_A$ and $(d\rho/dr)_R$ are the adiabatic and radiative density gradients. If we assume that both the gas in the element and in the surroundings can be described as ideal, then the equation of state within the element is:

$$\ln p = \gamma \ln \rho + constant \quad (1.2)$$

and the equation of state in the radiative gas is given by:

$$\ln p = \ln \rho + \ln T + constant \quad (1.3)$$

If these two equations of state are substituted back into (1.1) and the pressure gradients are taken as being equal then the Schwarzschild criterion is:

$$[(\gamma - 1)/\gamma](-d \ln p/dr)_R < (-d \ln T/dr)_R \quad (1.4)$$

where γ is the ratio of the specific heats c_p/c_v . The criterion is usually given as:

$$\nabla_R > \nabla_A \quad (1.5)$$

where:

$$\nabla_R \equiv (d \ln T/d \ln p)_R \quad (1.6)$$

$$\nabla_A \equiv (d \ln T/d \ln p)_A \quad (1.7)$$

$$\equiv (\gamma - 1)/\gamma \quad (1.8)$$

This relation assumes that the volume element remains in pressure balance with the radiative surroundings and that the atmosphere is an ideal gas. However, it is possible to generalize the relation so that $\nabla_A = (\Gamma - 1)/\Gamma$, where Γ is the ratio of specific heats for a non-ideal gas (Mihalas 1978; Cox & Giuli 1968). This form of the definition can be used to take into account radiation pressure and ionization, both of which can change ∇_A substantially. These effects combine with the increase in opacity that results from recombination (which steepen the radiative gradient, ∇_R)

and give rise to a convective instability deep within the hydrogen ionization zone, a situation first recognized by Unsöld. (For a more complete discussion of the Schwarzschild criterion and the stability of compressible fluid in a gravitational field see Bray et al. (1984) p. 108).

When the local temperature gradient becomes superadiabatic, convection ensues. How convection is physically described in the extreme environments that are stellar atmospheres is problematic. Deep within the star, $\nabla = \nabla_A$, and is easily dealt with. It is in the outer convection zone, where $\nabla_R > \nabla > \nabla_A$, that the difficulties in describing convection arise. In general, two approximations are made when attempting to solve the hydrodynamic equations that describe the behavior of the gas: the *Boussinesq* and *anelastic* approximations.

Under the Boussinesq approximation the vertical size of the system is considered to be substantially less than the scale height. The extreme density stratification in a stellar photosphere is neglected. This results in the background density variations being negligible and the convective motions are then determined using the temperature and velocity fields, with any change in the pressure being solved for after the motion has been found (Bray et al. 1984). The variations in the density and pressure are only considered in so far as they relate directly to the vertical buoyancy of the material. The most relevant astrophysical example of a Boussinesq-like process outside of the laboratory is the Mixing Length Theory (see §1.3). A Boussinesq fluid becomes turbulent at relatively low Rayleigh numbers ($Ra \leq 10^4$) when the Prandtl number (Pr) is low. For the Sun, $Pr \approx 10^{-9}$ and $Ra \approx 2 \times 10^{11}$, which is clearly well within the turbulent regime. In turbulent convection the distribution of kinetic energy over eddy sizes (wavenumber k) is given by the Komolgorov spectrum:

$$E(k) \propto k^{-5/3} \tag{1.9}$$

Those eddies with the largest scales have the largest energies and the largest velocities, and the energy cascades down to smaller scales by kinetic interactions, until the energy eventually dissipates via diffusion.

The anelastic approximation also simplifies the initial hydrodynamic equations, but still retains non-local and nonlinear characteristics, which are usually lost in Boussinesq-like treatments. Under this approximation, the weak coupling between the convective velocities and acoustic waves are neglected. The hydrodynamic equations can be expanded about an initial static state, with the fluctuations from the initial state contained in the expansion terms. If the fluctuating terms are small, the equations can then be linearized and solved. However, those nonlinear terms involving velocity are retained, since the velocity fluctuations are not small (Gough 1969). This scenario is

applicable if the convective velocities are substantially less than the sound speed and the density, pressure and temperature variations are small over a few scale heights (Bray et al. 1984; Stein & Nordlund 1998).

1.3 The Mixing Length Theory

The Mixing Length can trace its origins to Prandtl's application of kinetic theory to turbulent fluids in the early years of the 20th century (Bray et al. 1984). In this scenario the eddies interact by intermittent collisions: transferring energy and operating over some mean free path. This assumes the eddies are interacting only at discrete points and, in the case of turbulent motion, the mean free path has to be set as a free parameter. This path length is followed by some characteristic eddy, at the end of which the energy of the eddy is dissipated or transferred to another eddy. For a given stellar radius, the convective packages are all considered to have the same average physical characteristics: size, temperatures, and velocity (Bray et al. 1984).

This formalism considers convection to be a turbulent phenomenon, driven by heating at the base of the convection zone. The MLT produces a mean convective heat flux, essentially treating all the turbulent eddies as having uniform sizes and characteristics throughout the entire convection zone. However, non-local effects and variations in opacity are neglected, and the amount of energy dissipated to other eddies due to interactions and the amount lost radiatively is at best an estimation. The MLT does not provide any information regarding the atmospheric dynamics, nor does it provide very much information on variations about the mean values for temperature, density and pressure. Convective overshooting or penetration, the degree of mixing and the interaction between acoustic waves and convective motions remain un-addressed (Zahn 1999).

The key parameter (and the source of much contention) in MLT is the mixing length itself, Λ . This parameter is the average path length followed by the convective eddies, and is usually set to be some multiple of the pressure scale height,

$$\Lambda = \alpha H_p \tag{1.10}$$

$$H_p = P/\rho g \tag{1.11}$$

The parameter α is a free parameter, usually set using the Sun so as to match the atmospheric model flux with the observed flux and yield the correct solar radius. The value of α used depends upon the atmospheric model used, and often varies depending upon the type of star being studied.

Typical values for α are between 1 and 2, however in some cases values as low as 0.5 or as high as 3 are used.

One of the more serious potential consequences for the value of α is the implications its value has for calculating evolutionary models. Chaboyer (1995) demonstrated that the largest source of uncertainty in estimating the ages of globular clusters lay in the value of α utilized: changing α between 1 and 3 leads to changing globular cluster age estimates by between 14 and 19%, depending upon the evolutionary models used. This translates to age differences between models of up to 2 *billion* years.

An additional problem with the MLT, and with all local models of convection, is the description of the overshoot region where

$$\nabla - \nabla_A < 0 \quad (1.12)$$

In the stratified stable region overlying the convection zone, the convecting material is still in motion even though it is no longer being driven. The convective material dissipates its energy in this layer via diffusion, which is a non-local process (Canuto & Dubovikov 1998).

The MLT enjoys wide use across the astronomical community even though it is a simplistic description of convection. This is largely because of the intractability of the hydrodynamic equations in the extreme environment that is a stellar atmosphere: variations in density by a factor of 10^6 , changes in temperature by 10^4 K and in Ra by 10^{12} (Bray et al. 1984; Spruit 1997). The MLT is an easily implemented formalism that provides a good 0th order approximation of the gross effects of convection.

However, there are a number of astrophysical problems that require a refinement in how convection is addressed: understanding stellar structure, stellar activity, the generation of magnetic fields, element depletion, the interplay between convection and rotation, stellar evolution and chemical mixing are some of the most prominent (Zahn 1999). Improvements in instrumentation, opacities and in other stellar physical theories have reached the point where convection is one of the chief obstacles to understanding many stellar astrophysical problems.

1.4 Current Approaches

1.4.1 Turbulent Convection Theories

The local nature of MLT is considered to be one of its greatest drawbacks. Any attempt to formulate a replacement for MLT has to be non-local, and has to be more physically consistent with reality.

Numerous attempts have been made in recent years to formulate an analytical turbulent model for stellar convection (Canuto 1997; Canuto & Mazzitelli 1992; Canuto 1992; Canuto 1993; Canuto & Mazzitelli 1991; Canuto & Dubovikov 1998; Xiong et al. 1997; Grossman 1996). These new treatments attempt to provide a more complete picture of the nature of convection. Instead of treating convection as a uniform average eddy, they address the full Komolgorov spectrum of eddy sizes and energies with a hierarchy of larger eddies feeding energy to smaller ones.

These models use a collection of hydrodynamic moment equations that are solved by ensemble averages of the fields involved in convection (temperature, pressure and velocity). The moment equations are derived from the compressible Navier-Stokes equations, and the ensembles that are averaged are either realizations of solutions to the Navier-Stokes equations, averages over similar initial states for the Navier-Stokes equations or are obtained by averaging over different convective cells with a range of temperatures and velocities (see Kupka (1999) for a summary). The first moment equations require the determination of higher moments (second and third). Unfortunately, the solution to the second and third moment equations require even higher moments – the hierarchy of moment equations is infinite. These infinite series of moment equations are dealt with by making some sort of assumptions for closure – which usually involves invoking a type of mixing length-like free parameter, often related to the physical depth, or a technique known as the Reynolds-Stress Model, which has difficulty handling radiative losses and convective overshoot. The alternative to these closure assumptions is the use of a non-local set of dynamic equations for the higher moments (Canuto & Dubovikov 1998).

These treatments, while still using the Boussinesq approximation, are more physically correct than the MLT. The use of this approximation is justified by the consideration that the actual region where convection becomes inefficient and the relation $\nabla = \nabla_A$ does not hold is a relatively thin layer, close to the surface and includes the overshoot layer (Canuto & Dubovikov 1998).

A number of implementations of these newer convection treatments have been tested – most notably the Complete Model (CM) (Canuto & Mazzitelli 1992; Canuto 1993) and its successor, a newer turbulent convection model (CD) (Canuto & Dubovikov 1998). Usually these treatments are tested versus the MLT or numerical simulations and observed solar and stellar characteristics (Kupka 1999; Kupka 1999a; Canuto et al. 1996). The CM model has outperformed or matched MLT in several tests: the CM predicts more accurate solar p-mode eigenfrequencies (Paternò et al. 1993; Basu & Antia 1994); the CM matches the performance of MLT in modeling outer envelopes of Red Giants and Supergiants (Stothers & Chin 1995); pre-Main Sequence evolutionary tracks for

low mass stars (D'Antona & Mazzitelli 1994); globular cluster isochrones (Mazzitelli et al. 1995; D'Antona et al. 1992); stellar colors, Balmer line profiles and atmospheres (Kupka 1996; Smalley & Kupka 1997; Gardiner et al. 1999). A summary of these tests and results can be found in Mazzitelli (1999).

1.4.2 Numerical Simulations

The recent remarkable progress in computing resources and computational efficiency has led to the development of physically realistic numerical simulations, which have provided a new perspective on the physical conditions of convection. The input physics include the full three dimensional hydrodynamic equations, with realistic equations of state, opacities and radiative transport within the anelastic approximation (Stein & Nordlund 1998; Stein & Nordlund 1989; Spruit 1997). One of the key differences between the numerical simulations and the analytical Boussinesq approximations is the manner in which the density stratification is addressed. Within the Boussinesq approximation it is ignored, whereas in the anelastic approach the density variation is taken into account.

There are two types of simulations that are done: *Direct Numerical Simulations* (DNS) and *Large Eddy Simulations* (LES). Unfortunately, there are serious drawbacks to the use of three dimensional numerical simulations of solar and stellar convection. The simulation of the entire convection zone places prohibitive demands upon computer memory and speed; usually only a shallow upper portion of the convection zone can be simulated over the relevant time-scales. It is estimated that the fully resolved numerical solution to the Navier-Stokes Equations could be simulated in three dimensions using a grid of 10^{20} to 10^{30} points (Kupka 1999). Direct Numerical Simulations (DNS) have been applied to convection, but only at intermediate Rayleigh numbers and using idealized physics. DNS cannot be used for the more typical Rayleigh numbers found in stellar convection zones, the computing costs are too high. The alternative is to resolve only the largest time-dependent scales in the simulations (LES), and model the unresolved smaller scales and their impact on the larger scales. These smaller scales are modeled using a sub-grid scale model (Kupka 1999).

Stellar convection is usually simulated within a LES context, simulating a thin slab of the photosphere. The large range of both length scales and time scales of the whole convection zone cannot be accommodated in simulations such as these. The thermal relaxation time for the convection zone is $\sim 10^5$ years, whereas the dynamic time scale is on the order of minutes. Similarly the length scales required are tremendous; from the whole convection zone (30% of the solar radius) to

the narrow regions of the upper photosphere. The size of the simulations are severely constrained; as a result only the upper layers of the convection zone can be simulated at the required spatial and temporal resolution. The typical simulation uses a box with periodic vertical boundaries and a horizontal surface area equivalent in size to several granules. Typical sizes are 6000 km by 6000 km in area and 2500 km in depth, while the average granule has a diameter of ≈ 1000 km. The spatial resolution of the simulation is selected so as to mimic the observed spatial resolution of solar observations. Lower boundary conditions can be set so as to conserve the mass flux by varying the pressure in time, and the effectiveness of the lower boundary conditions can be checked by comparison with simulations that penetrate deeper into the convection zone (Stein & Nordlund 1998). One of the drawbacks to the use of LES is the assumption that the unresolved sub-grid scales are entirely dissipative. Canuto (2000) has demonstrated that the unresolved scales are still large enough to contain both diffusive and advective terms, in addition to dissipative effects. These terms give rise to advective velocities not accounted for in previous LES simulations. Canuto has also demonstrated even when the models are restricted to dissipation processes for the sub-grid scales, the current LES models lack an internal consistency check.

These numerical simulations have met with a tremendous degree of success in reproducing the appearance and behavior of surface granulation. Simulations have succeeded in reproducing the apparent solar granulation patterns (Stein & Nordlund 1989; Nordlund & Stein 1996; Stein & Nordlund 1998) and even exhibit '*exploding granules*' (Nordlund 1985; Rast 1995). The simulations also predict that in certain wavelength regions the edges of the granules will be brighter than the centers due to compression heating (Stein & Nordlund 1998). This contrast inversion has been observed in the centers of strong CO lines in the infrared (Uitenbroek 2000; Solanki et al. 1996). The numerical simulations also produce line profile asymmetries that are associated with the convective motions and their penetration into the photosphere (Dravins 1990; Spruit 1997). Numerical simulations predict a depth for the convection zone that closely matches the depth measured using helioseismology (Rosenthal et al. 1999).

The picture of convection that emerges from the numerical simulations is completely at odds with that of turbulent convection. The motions are driven not from heating at the bottom of the convection zone, but by radiative cooling in a thin surface layer (Stein & Nordlund 1998). The up-welling material in the center of the granules is neutrally buoyant, rising to replace material that has cooled and has started to settle in downdrafts located at the intergranular lanes. These downdrafts intersect, and become turbulent below the solar (or stellar) surface, and it is here where

the work is done that drives the motions. The density scale height at the surface is small, so the flow at the top of the granules is forced into horizontal motion over a relatively shallow depth before the flow is overturned into a downdraft. This small scale of variation is inconsistent with the local analytical models, which predict large changes in both velocity and temperature over this region, especially when the cell sizes are an order of magnitude larger than these scales (Nordlund & Stein 1996). The LES also show that at a given optical depth the solar surface is heavily corrugated in physical depth (and vice versa), reflecting rapid changes in opacity and temperature (H^- has a temperature sensitivity of T^{10}) (Stein & Nordlund 1998).

These results cast serious doubt on whether solar/stellar convection should even be considered as a turbulent phenomenon, despite the high Reynolds number in stellar convection zones (Nordlund et al. 1997). This interpretation is based upon a comparison between the power spectra of granulation images and those from theoretical turbulent cascade models. The power that is observed is attributed to turbulence at the edges of granules and the overall laminar behavior of the up-welling material is attributed to the effect of the density stratification on the upflows (Nordlund et al. 1997). Laboratory experiments of convection at high Rayleigh number (although still substantially less than that in the solar environment) reveal a geometry that may be consistent with this new view of atmospheric convection (Spruit 1997).

1.5 Convection and Spectral Line Asymmetries

To constrain and test these competing models, it is necessary to develop diagnostics of convection. Studies of the solar intensity spectrum have shown that line profile asymmetries are informative signatures that are also applicable to the flux spectrum of the sun and other stars (Dravins et al. 1981). The line profile contains two key kinds of information: surface radial velocity and the variation of the line source function with depth. If we avoid scattering lines, the source function reflects the local thermal characteristics of the plasma.

At each point on the stellar surface, granules (hotter rising material) will contribute a larger flux than the intergranular regions, and this flux will be blue-shifted slightly due to the up-welling velocity. Similarly, the intergranular contribution will be red-shifted, cooler, and fainter because of its smaller area and lower temperature. For an absorption line at a wavelength λ_0 , the contributions to the line profile come from different physical depths, and the amount of radiation at different points on the profile reflects the physical conditions at those depths. These contributions differ both

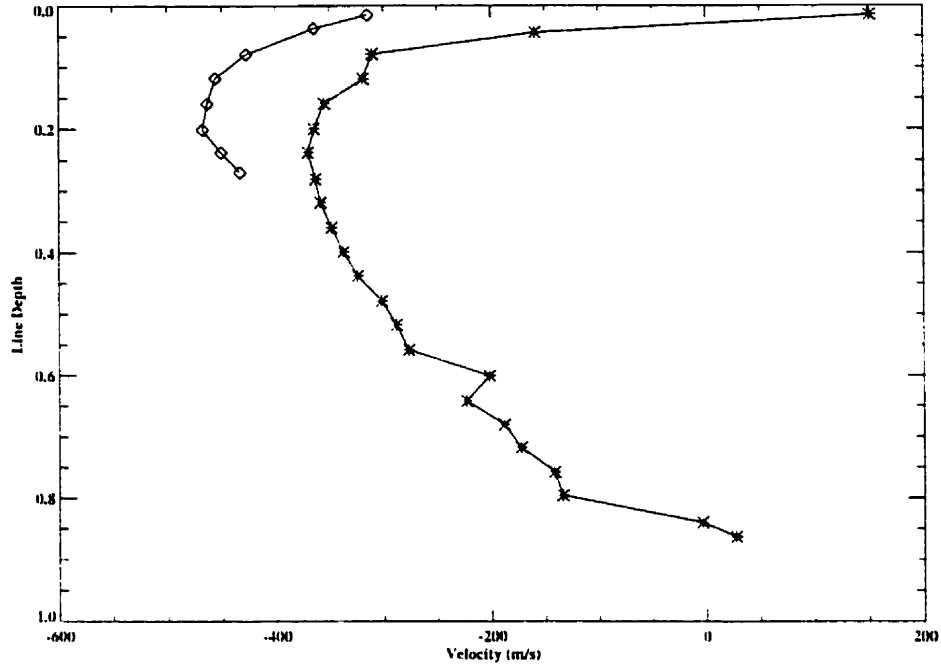


Figure 1.1: Two sample bisectors. The strongest lines have bisectors that resemble a ‘C’, while weaker lines tend to have bisectors that more closely resemble the top portion of a ‘C’.

on the vertical scale through the atmosphere – reflecting changes in both velocity and temperature, and on the horizontal scale – reflecting the spatial effects of the granulation. The net effect of these contributions, integrated over the surface of the star, is the total asymmetry of the flux line profile.

Line asymmetries have been quantified primarily using bisectors, the locus of points midway between the two sides of the rectified line profile at equal levels of intensity. In solar-type stars, the bisectors for stronger lines have full ‘C’ shapes, while weaker lines have shapes that are just the top part of the ‘C’ (see Figure 1.1). A ‘convection boundary’ exists in the HR diagram (Gray & Nagel 1989), beyond which hotter stars (non-convective) have backwards ‘C’-shaped bisectors. The slope and extent of the bisector curve is a direct measure of how vigorous the convection is over the range of the photosphere where that line is formed. Various ways of comparing line bisectors have been developed, such as averaged bisectors (Dravins et al. 1981; Gray & Nagel 1989), and bisector slope parameters (Neckel & Labs 1990).

Dravins (1987a) found that reasonable bisector measurements can be made for observations with spectral resolving powers $R \equiv \lambda/\Delta\lambda \geq 100,000$. However, even at this very high resolution, the bisector shape will be affected by the instrumental response until R reaches 200,000. This

sensitivity to resolution makes it challenging to define accurately the changing slopes of the bisector at $R < 100,000$ for a solar-type dwarf star. Stars that are hotter and more luminous than the sun are less demanding of spectral resolution because of their broader lines.

A second signature of surface convection is the core line-shift, usually defined as the change in the position of the line minimum or the bottom portion of the line with respect to its predicted laboratory position (Nadeau 1988; Dravins et al. 1981; Dravins 1987a; Allende Prieto & García López 1998). In the past, these positions have been found by fitting polynomials to a wavelength ‘window’ around the line minimum (Allende Prieto & García López 1998) or by choosing a point on the bisector close to the line minimum (Dravins et al. 1981; Dravins et al. 1986; Dravins 1987a).

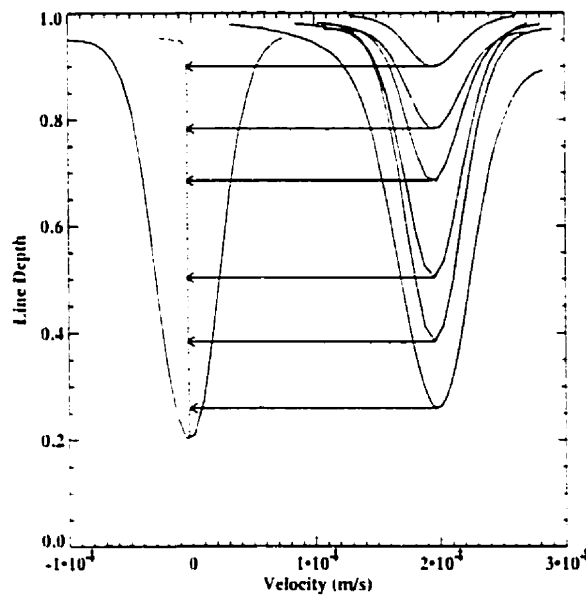


Figure 1.2: The relationship between the bisector of a line profile and the line-core positions of a set of lines of different depths. The ensemble of line-core positions maps the shape of the bisector.

This proves to be much easier to measure than the bisector because it is a feature of the line core rather than a differential property of the profile. As a result, it is possible to measure relative line-shifts with less than ultra-high spectral resolution, which greatly expands their utility.

The central characteristic to appreciate is that the line core is the bottom of a line bisector. Because the cores of lines of different depths sample different atmospheric levels, an ensemble of lines of different strengths should recover the convective information contained in high resolution line bisectors, with much less observational effort, as shown in Figure 1.2. We are not attempting to determine the ‘true’ velocity of the whole line or of the star, but to use the positions of the cores

of many lines to recover the line bisector.

The use of a large number of absorption lines allows for the development of a more complete statistical picture of the convective dynamics. Using large numbers of lines at different strengths allows us to generate the same information as averaged line bisectors, but at lower resolving powers and signal-to-noise ratios. The relative temperature contrast between the granules and lanes changes with wavelength, as does the continuous opacity. How the changes in contrast and opacity affect the appearance of convection can be examined by using a large sample of lines of different strengths and wavelengths. The use of these distributions can also be used to investigate how limb darkening may possibly affect the observability of convection.

1.6 Diagnostic Candidates

There are a number of key ingredients required in selecting potential diagnostic candidate species for line core shifts and line bisectors (for a review of some of these characteristics, see Dravins et al. 1981):

- accurate laboratory rest wavelengths
- line source function dominated by local thermal characteristics
- wide wavelength coverage
- few isotopic blends
- large number of lines
- large range in excitation energy (χ_l)
- large range in line depth
- well established transition properties ($\log gf$, χ_l)
- minimal hyperfine splitting
- low thermal broadening

Obviously, the first two properties are the most fundamental. However, it is important to try and use absorption line profiles that are as clean as possible. Blending, whether it is a result of

hyperfine splitting, isotopes or just blending with other atomic or molecular species, distorts the line profile and makes determination of the true line-shift problematic.

Species that have wide wavelength ranges, large variations in line strength and wide coverage in χ_l permit a more comprehensive study of how the line-shifts depend upon these parameters. Using a species (or several species) over large spans of wavelength permits a study of the varying effects that temperature contrast and changing continuous opacity may have. Lines of varying strength and χ_l probe different layers of the atmosphere, providing insight into the average velocity structure of the atmosphere.

For solar-type stars, the best atomic candidate is Fe I (Dravins et al. 1981). Fe I is the most prevalent species in the solar spectrum, with lines of varying degrees of strength spanning wavelengths from the ultraviolet to the infrared. These lines also exhibit a very large range in χ_l . Because of its high mass, the Fe I lines have low thermal broadening, and the Fe I spectrum is dominated by a single isotope, ^{56}Fe . The Fe I laboratory line positions have been reestablished to an unprecedented level of absolute accuracy (Nave et al. 1994). The new rest positions have been established with an absolute positional accuracy of $\leq 0.02 \text{ cm}^{-1}$ in the visible (Nave et al. 1994; Nave 1999).

For stars cooler than the Sun, or for the infrared portion of the solar spectrum, additional candidate species would be useful because the Fe I lines weaken considerably, and the positional accuracy of the lines decrease when expressed as Doppler velocities ($\sigma(v) = \Delta\nu/\nu$). Given these criteria, the most obvious candidate species should be molecular. There are four molecular species of varying utility available in the solar spectrum that meet most of the above criteria: CO, CN, OH and TiO.

From an astrophysical perspective, the properties of CO are probably the most well established of all the diatomic molecules. There are three prominent bands of CO in the infrared spectrum of the Sun: the fundamental ($\Delta v = 1$, between 4.2 and 6 μm) and the first overtone sequences ($\Delta v = 2$, between 2.2 and 2.5 μm) are present in both the normal solar spectrum and the solar umbral spectrum, and the second overtone sequence ($\Delta v = 3$, between 1.5 and 1.8 μm) is found in a sunspot umbral spectrum. The calculated line positions and other properties for CO are established to an incredible accuracy (see §4.2), the $^{12}\text{C}^{16}\text{O}$ isotope is dominant and there are thousands of potential lines of varying degrees of strength and excitation energy. CO is also very useful for examining cooler stars and the solar umbral spectrum since both the first and second overtone bands increase in prominence as effective temperature decreases.

There are two major drawbacks in using CO as a diagnostic: (1) the telluric absorption in both the fundamental and first overtone bands, (2) the difficulty in establishing where in the solar photosphere a CO line is formed. Here, the first problem is dealt with by using a combination of ground based and space based observations. The second difficulty is more problematic.

CO is a very temperature sensitive molecule formed throughout the solar photosphere. Weak CO lines are formed fairly deep in the atmosphere, while the strongest lines are formed near the temperature minimum. Observations of CO lines in solar limb spectra indicate temperatures in the upper photosphere that are inconsistent with the temperature minimum derived from atomic lines such as the Ca II H and K lines (Ayres et al. 1986). One proposed explanation is that there is a temperature bifurcation in this region of the atmosphere; a cool '*COmosphere*' that is the source of the CO lines, and hotter, mechanically heated regions which produce the atomic lines (Ayres et al. 1986). Typical one-dimensional atmospheric models cannot account for both types of feature, and any derived altitudes of formation for these features are highly model dependent (Uitenbroek 2000). The location of the CO line formation could be further complicated if, as Uitenbroek has concluded, the CO concentration is not given by its instantaneous Saha equilibrium value; which would lower the height of line formation. The time-scale for CO formation may be comparable to the convection time-scale at low densities, thus material rising upwards may not have had sufficient time to form CO. This leads to a reduction in the actual heights of CO line formation when compared to those predicted when instantaneous chemical equilibrium is used (Uitenbroek 2000). To understand properly the formation of the CO lines in the solar atmosphere requires multidimensional hydrodynamic modeling that includes CO cooling effects (Uitenbroek 2000). However, the CO lines can still provide information on the average convective velocities, but not the exact corresponding vertical positions. The relative distribution of line-shifts for CO may provide insight into the relative vigor of convection and the possible effects of excitation energy and wavelength.

CN is a potential complementary diagnostic for the CO bands. In the solar spectrum the CN lines are weak, but they do extend into the red and near infrared portions of the spectrum, a region unsampled by other molecular lines. Both TiO and OH have powerful potential as diagnostics for both the solar umbral spectrum and for cooler stars. The most prominent set of OH lines, the Meinel system, have well established rest positions (Abrams et al. 1994), and cover a wide range of wavelengths (the $\Delta v = 1$ bands between 2.6 and 4 μm and the $\Delta v = 2$ bands between 1.4 and 1.7 μm). The OH bands have a wide range in line strengths when observed in both the solar umbral

spectrum (see §5.3) and in the spectra of K giants such as Arcturus (see §6.2). The TiO γ bands are especially prominent in the red portion of the visible sunspot spectrum. Recent laboratory positions (Ram et al. 1996; Ram et al. 1999) enhance the utility of TiO as a convection indicator in very cool stars, despite the high density of lines and degree of blending in the red spectra of cooler stars.

Chapter 2

A Technique for the Study of Stellar Convection: The Visible Solar Flux Spectrum

2.1 Introduction

Previous studies of the Sun and several solar-type stars (Dravins et al. 1981; Dravins et al. 1986; Dravins 1987b; Nordlund & Dravins 1990) have used both line bisectors and line-shifts of Fe I and Fe II lines to probe convection. These studies found some similarity in the dependence of the two indicators on line strength, wavelength, and excitation energy, although there were also discrepancies (Nadeau 1988; Allende Prieto & García López 1998). As discussed in Chapter 1, bisectors require not only high resolving powers, they also require high signal-to-noise in order to properly define their slope in the core.

The core of the line is also the portion of the line profile most sensitive to noise, which is a serious complication in determining line shifts. The signal in a line profile is always lowest in the core, enhancing the impact of all sources of noise. In addition, because the core has the shallowest slope of the profile, the velocity shift produces the smallest signal there, making it vulnerable to photometric errors. Therefore, it is necessary to use points farther up the line profile that have larger slopes (see Figure 2.1 and §2.2). However, if the points used to define the core position come from too high up the sides of the line profile, where the line is most sensitive to velocity shifts, then there is the danger of deriving some measure of the line's velocity integrated over a large vertical span of the atmosphere. The challenge is to find a technique that achieves both isolation of the core and is responsive to small velocity shifts.

A further complication in using line-shifts is the specification of the velocity zero point in the

rest frame of the star. Stellar radial velocities are typically determined by using as much of the spectrum as possible, and the current state of the art can detect velocity *variations* of $\leq 10 \text{ ms}^{-1}$ (Butler et al. 1996). However, these radial velocities are entangled with the surface velocity fields and are *not* absolute in nature. The Sun is the only star with both a precise and an accurate absolute radial velocity, based on orbital dynamics. However, the Sun can be used as a fiducial point for stellar observations to achieve precise relative line-shift *distributions* of different lines, even though the absolute stellar radial velocity is unknown.

By concentrating on the behavior of the *distributions* of the relative stellar line-shifts, the absolute radial velocity zero point becomes irrelevant. To achieve this, the Sun's *flux* spectrum must be used, although this introduces effects due to limb-darkening and rotational broadening.

2.2 Methodology

2.2.1 Solar Flux Spectrum

This study is based on the *Solar Flux Atlas*¹ (Kurucz et al. 1984), which was observed with the Fourier Transform Spectrometer (FTS) at the McMath Solar Telescope at KPNO. The Atlas covers the spectrum from 296 to 1300 nm with a resolving power that varies from 348,000 to 522,000 and with S/N ranging from 2900 to 9000. The wavelength calibration is based on the O₂ line at 688.38335 nm, and the conversion to air wavelengths was done using the formula of Edlén (1966). Scans without the O₂ line were calibrated using clean solar lines from the scan overlap regions. The maximum velocity error for the ultraviolet spectral regions in the Atlas, farthest from the calibrating O₂ line, was estimated by Kurucz et al. as 100 ms^{-1} . Due to the linear nature of FTS observations, this error estimate also applies as an upper limit to the other scans extending through the remainder of the Atlas. Allende Prieto & García López (1998) also used the same Atlas and found that its wavelength calibration in the visible was consistent with the stated uncertainty. The effect of the solar cycle on the wavelength stability of the Sun is relatively small, with an upper limit to the variation of line asymmetries of 5 ms^{-1} over one cycle (Wallace et al. 1988).

2.2.2 The Determination of Line Positions

The goal here is to determine the positions of the cores of individual spectral lines, not the bulk velocity of the star. Therefore, different techniques must be used than those that are appropriate

¹NSO/Kitt Peak FTS data used here were produced by NSF/NOAO.

for, say, searches for extrasolar planets. Also, one of the primary purposes of this study is to use the solar spectrum to develop methods that can be applied to the study of other stars. Therefore, the technique used to find core line-shifts must be as independent of the instrument as possible and designed to minimize its sensitivity to differences in resolutions and rotation.

The most obvious measure of line position, the line minimum, is not suitable because it is excessively sensitive to noise. Noise also affects fitting a parabola or a higher order polynomial to the lowest three or five points in the line profile, and this method is also very sensitive to spectral resolution (see §2.3.2). While fitting polynomials to the region around the line minimum has proven to be effective at high resolution (Allende Prieto & García López 1998), lower resolutions do not provide enough points along the bottom portions of the line profile to provide an accurate fit, even if the fitting window is expanded.

Line bisectors offer an alternative way to define line positions in general, and core positions in particular. Traditionally, the shapes and amplitudes of bisectors, determined with $R \geq 100,000$ and high signal-to-noise, have been used to probe convection. However, line bisectors can be determined at much lower resolutions. Although the shape and curvature of the bisectors are extremely fragile, being very sensitive to noise, it is possible to use these low resolution bisectors to determine the shift of different levels within the line, and this method can be applied at various resolutions. Past studies (Dravins et al. 1981; Dravins et al. 1986) used a point on the bisector of the profile that is 7% above the line minimum. Unfortunately this approach requires interpolations and the use of high resolving powers (see §2.3.2).

We tested many different methods of determining the line core position, and the most satisfactory method is illustrated in Figure 2.1. To begin, the core of the line profile was fit with a cubic spline interpolation. Next, the two lowest non-minima points were used to identify two levels in the profile, and the bisector at each level was determined using the original point on one side of the profile and the interpolated point at the same level on the opposite side. The position of the line is defined to be the average of the two bisector positions. For high spectral resolutions, the two points are very close to the bottom of the line, and are not greatly sensitive to the slope of the bisector. At lower resolutions, the slope of the bisector does come into consideration (see §2.3.2). The two lowest non-minima points are used (instead of the second and third lowest points), because, on occasion, some line profiles have two minima. The use of any one of these points was found to corrupt the line position substantially. Using the observed line minimum itself was found to introduce an anomalous hook to the bottom of the bisector (relative to its nearest observed

neighboring points in intensity) due to the discrete sampling across the profile. At high resolutions these points are very close to the bottom of the line, and are sensitive to noise. However, the data source used here is of sufficient S/N (2900 to 9000) that these noise effects are minimal. At lower resolutions, the points sample higher up the sides of the line profile, where the slope of the profile is steeper, and thus are less sensitive to noise.

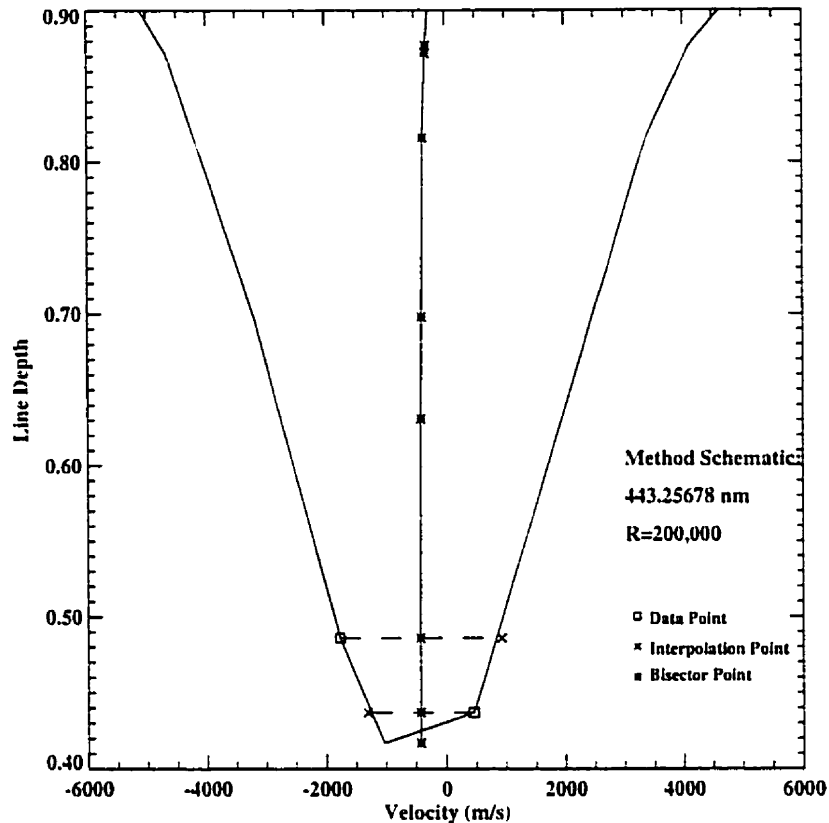


Figure 2.1: The core of a line profile illustrating the method used to determine the observed line-core position. The lowest non-minimum point from each side of the line profile is used to identify a particular level. The interpolated point from the opposite side of the profile, found from a cubic spline, is used to determine the line bisector for that level. The average of the two bisectors defines the line position.

With the observed line center determined, the line-shift of the core is found by comparison with the laboratory wavelength. In the visible, *all* the Fe I lines have stated absolute positional uncertainties of $\leq 0.02 \text{ cm}^{-1}$ (Nave 1999), or better than 300 ms^{-1} at 500 nm. A large majority (79%) of the lines used here have laboratory uncertainties $\leq 0.005 \text{ cm}^{-1}$, or better than 75 ms^{-1} at 500 nm. Starting with this line set, apparent blends were identified by visual inspection of the solar spectrum and rejected from further use. Additional lines that were suspected as potential blends (based on the line profile or an anomalous line-shift) were compared to the solar line identifications

from existing atlases and tables (Moore et al. 1966; Swensson et al. 1970; Livingston & Wallace 1991; Wallace et al. 1998; Wallace et al. 1993). The remaining suspect lines were checked versus a synthetic solar flux spectrum generated by the Kurucz Atlas 9 suite of programs (Kurucz & Avrett 1982). The final set had 122 lines in common with the more stringently defined set of Rutten and van der Zalm (1984). Line-shifts were then calculated using:

$$v = c(\lambda_{\odot} - \lambda_{lab})/\lambda_{lab} - 636 \text{ ms}^{-1} \quad (2.1)$$

where λ_{\odot} is the solar line position, λ_{lab} is the laboratory position and 636 ms^{-1} is the gravitational red-shift of the Sun ².

In previous work (Dravins et al. 1981; Gray & Toner 1985; Dravins et al. 1986) mean line bisectors were computed for different classes of lines. The shapes of these bisectors give information on the overall behavior of the line profiles in each line class, which provides a way of determining functional dependencies, analogous to the use of line-shifts. To be consistent with previous studies, we determined mean line bisectors by averaging all the points from a set of bisectors that fell within a particular line-depth bin. The size of the bins can be set based upon the resolving power. When a small set of bisectors was examined, it was found that the mean bisector could be extremely sensitive to any outliers of the set. To compensate for this, we also investigated median-bisectors. Instead of averaging all the points from the set of bisectors that fell within a given line-depth bin, the median of these points was found. The median bisectors tend to follow the mean bisectors in shape, but without any aberrant jumps or ‘noise’ from the unusual members, and the median bisector comes much closer to resembling the ‘typical’ bisector for that sample. This eliminates the need for the use of smoothing over the mean bisector. These median bisectors for different sets of lines can be used to test the efficacy of the line-shift method (see §2.3).

To test empirically the dependence of the line core position on spectral resolution, the Solar Flux Atlas was rebinned to a variety of lower resolutions using the IDL routine REBIN, which uses neighborhood averaging for compression. Once the Atlas was rebinned to a lower resolution, the analysis was repeated. A second empirical test was how noise affected the method. Noise was added to the Atlas by generating a set of random numbers for the Atlas fluxes with an average of zero and a standard deviation set to the S/N level desired, and the analysis was repeated.

²An additional correction of 3 ms^{-1} for Earth-based observations can also be applied (Lindgren et al. 1999), however this results in a small uniform shift to all the line-shifts and can be neglected

2.2.3 Errors

The original observations of the solar spectrum have a stated precision of $\leq 100 \text{ ms}^{-1}$ (Kurucz et al. 1984) for any particular point on the FTS scans. The absolute positions of the Fe I lines have uncertainty estimates that depend on the signal-to-noise ratio of the features, on calibration errors and on possible pressure shifts (Nave et al. 1994). The combination of these sources of uncertainty (from both Kurucz et al. 1984 and Nave et al. 1994) give a formal estimate of the observational error. It was found that 79% of the sample had **upper limit** error estimates of $\leq 125 \text{ ms}^{-1}$, and only 5% had estimates of $\geq 300 \text{ ms}^{-1}$. The mean upper limit on the uncertainty was 135 ms^{-1} with a standard deviation of 61 ms^{-1} and a median of 113 ms^{-1} . These errors are estimates only of the upper limits for individual points. The true errors appear to be smaller than the formal errors, as judged from the smooth curves shown in Figures 2.4(a) and 2.4(b).

Repeating the analysis with the Solar Flux Atlas rebinned to lower resolution showed that the main effect was to increase the scatter of the line core positions. For example, using the $R = 75,000$ data set gave a mean shift in line position of only 60 ms^{-1} . Only 50% of the line positions were shifted by $\geq 50 \text{ ms}^{-1}$, and only 18% were changed by $\geq 100 \text{ ms}^{-1}$. There were, however, systematic changes in the line positions, which are discussed more completely in §2.3.2.

2.3 Analysis

2.3.1 Line-shifts

A total of 298 Fe I lines, spanning 430–700 nm in the solar flux spectrum, were selected for study based on the criteria outlined earlier. Previous studies of line-shifts (Dravins et al. 1981; Dravins et al. 1986) have found strong dependencies on line strength and on wavelength region, and a weaker dependence upon excitation potential. This wavelength range also coincides with that used by Dravins et al. (1981).

The study by Dravins et al. (1981) used 311 Fe I lines, selected from the best laboratory line list then available. Crosswhite (1975), and central intensity spectra from the Solar Atlas of Pierce and Breckinridge (1973). Since this time, the advent of both digital technologies and the use of Fourier Transform Spectrometers have greatly improved the available Solar atlases, in both signal-to-noise and in wavelength calibration. As was mentioned previously, the laboratory line positions of Nave et al. (1994) have very small absolute uncertainties in the visible.

Here we employ an ensemble approach, using as large a sample of lines as possible to make

the information more reliable, to determine dependencies of the core line-shifts on line strength, wavelength, and excitation potential spanning the widest possible range of values. This approach reveals unusual features and gives a better visualization of the dependencies on the different parameters. It also avoids individual features, which can be aberrant and have very low information content.

To analyze properly the dependence on a given parameter, the lines have been binned in line depth, in wavelength and in excitation energy. By isolating each parameter as much as possible, real trends in the distributions of the line-shifts can be seen without being masked by confusion between the parameters.

Empirical Dependence on Excitation Potential

Plotting line-shift as a function of the excitation energy of the lower level (Figure 2.2), we see that lines with larger excitation energies tend to have more negative line-shifts. This is consistent with an earlier study of Fe I in the visible (Dravins et al. 1981). However, this apparent dependence neglects the influence of line strength. When we bin by line strength *and* by wavelength, the line-shifts do *not* have a strong dependence upon excitation potential (Figure 2.3).

Obviously, for a particular strength bin over a particular wavelength region, the excitation potential can be very 'clumpy' and does not cover a wide range of values. Also, many of these subsets are small in number, and thus may not be truly indicative of any trends. However, several of the subsets do span a wide range in excitation potential, and these show little or no dependence of the line-shifts upon potential. The apparent dependence observed in Figure 2.2 seems to result from the uneven distribution of line depth with respect to the excitation potential. Figures 2.3(a)-(d) show that the shallower lines tend to have higher excitation potentials, so the dependence seen in Figure 2.2 is actually reflecting the sensitivity to line depth (see the following section). Therefore, we conclude the dependence on excitation potential is negligible, and we concentrate on wavelength and line strength dependencies. While this does not completely exclude a dependence on excitation potentials, a proper investigation of this will require larger subsets and perhaps a greater range in potential (*i.e.* across species).

Empirical Dependence on Line-depth

Line-shifts show a strong dependence on the strength of the line, as expressed by the line depth (Figure 2.4). The deepest lines have the smallest shifts and the shallowest lines the greatest.

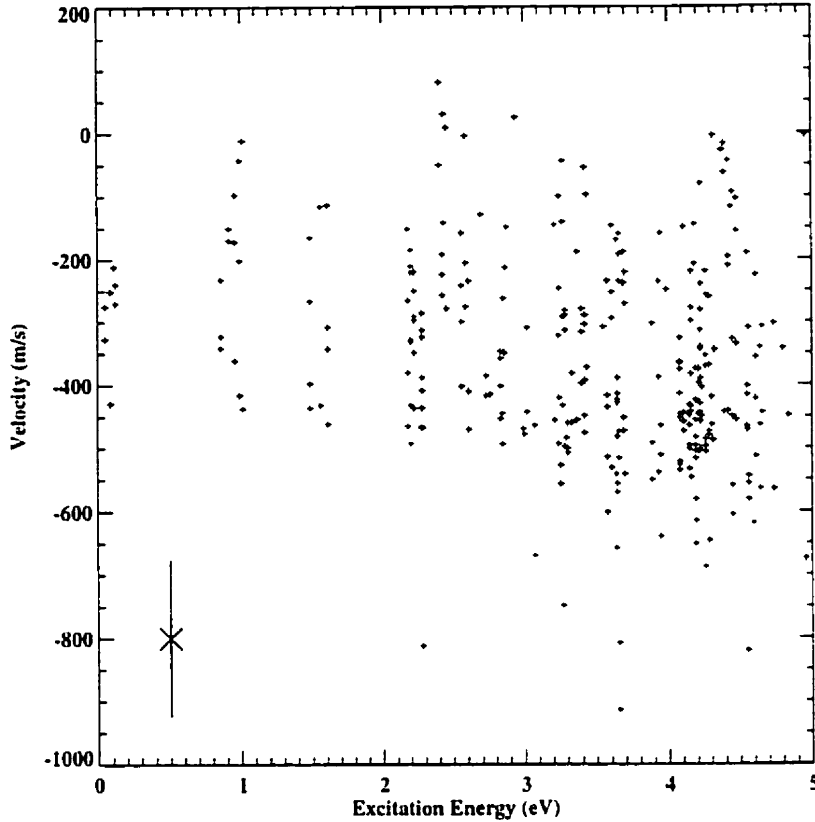


Figure 2.2: The distribution of convective line-core shifts as a function of the lower excitation energy. Although there is large velocity scatter, transitions with larger lower excitation energies appear to have slightly more negative line-shifts. However, the dependencies on other parameters have not been taken into account. For 79% of the sample, the errors are estimated to be $\leq 125 \text{ ms}^{-1}$, as shown by the error bars.

although the shallower lines also have the largest scatter. Note that the shapes shown in Figure 2.4(a) are essentially the traditional 'C' bisector shapes for strong lines, rotated counterclockwise by 90° . This is shown in part (b) of the figure, in which the distribution for the lines in the 500–600 nm region is over-plotted with the median bisector for this same set of lines. This median bisector covers all the lines in the wavelength bin, both weak and strong. Because this bisector is a composite, the 'top' portion of the bisector reflects contributions from both weak and strong lines, whereas the 'bottom portion' reflects only the strongest lines. The error bars in Figure 2.4(b) represent the standard deviation for each bin in the median bisector. The bins of the bisector near the pseudo-continuum contain errors from several sources. Both weak and strong lines contribute to these bins, and these two sets of lines behave differently (see Figure 2.6 and the following sections). Second, the wings of lines have shallow slopes, which makes them more vulnerable to photometric errors. Third, strong lines have extended wings, which makes them sensitive to distant blends.

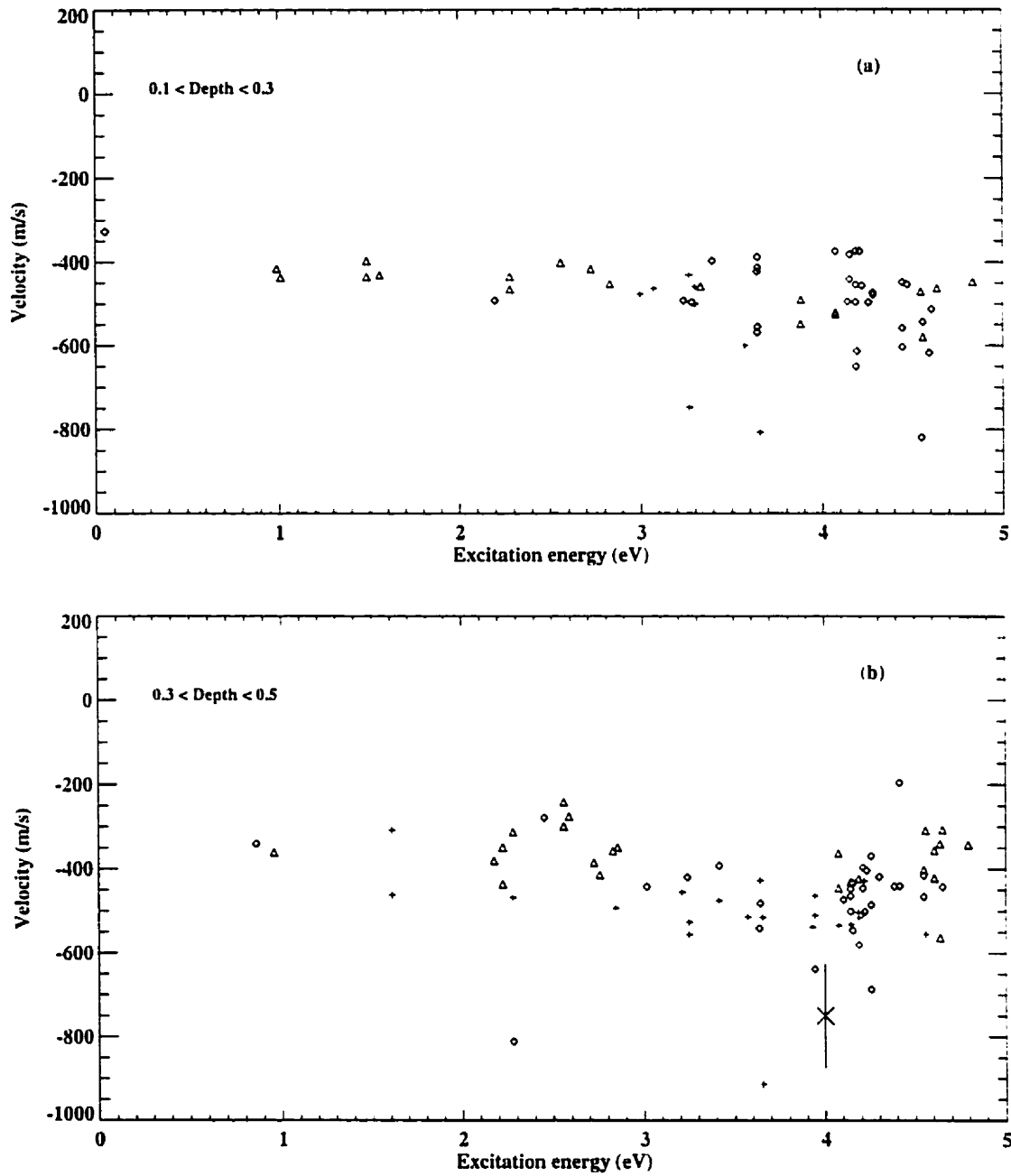
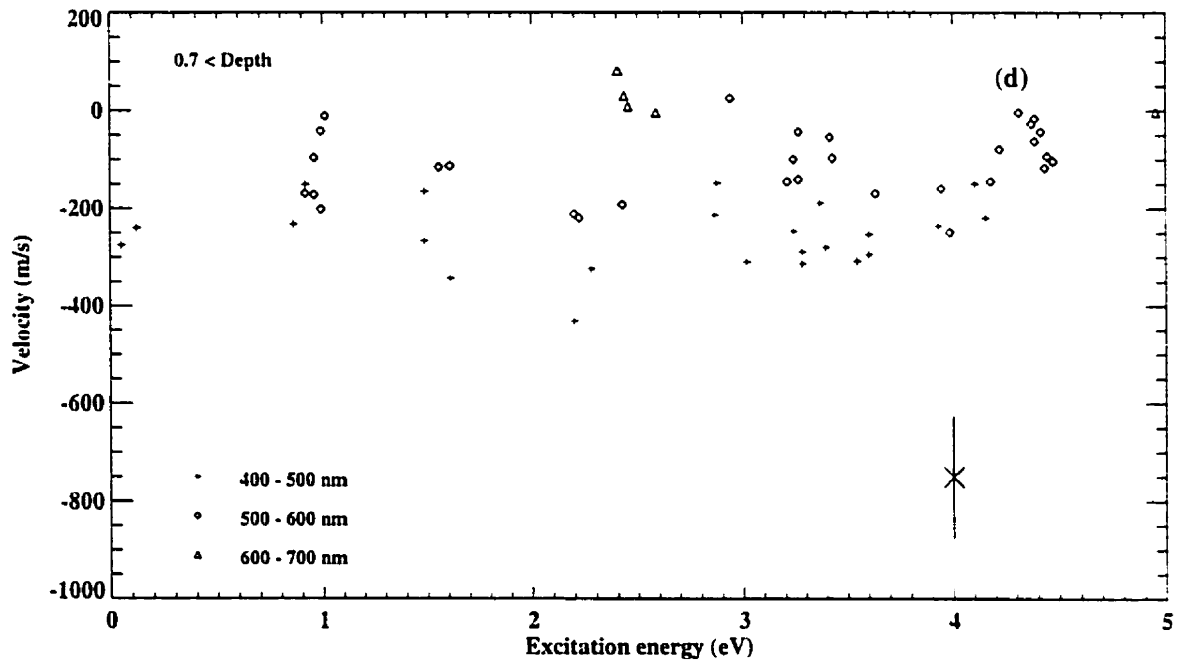
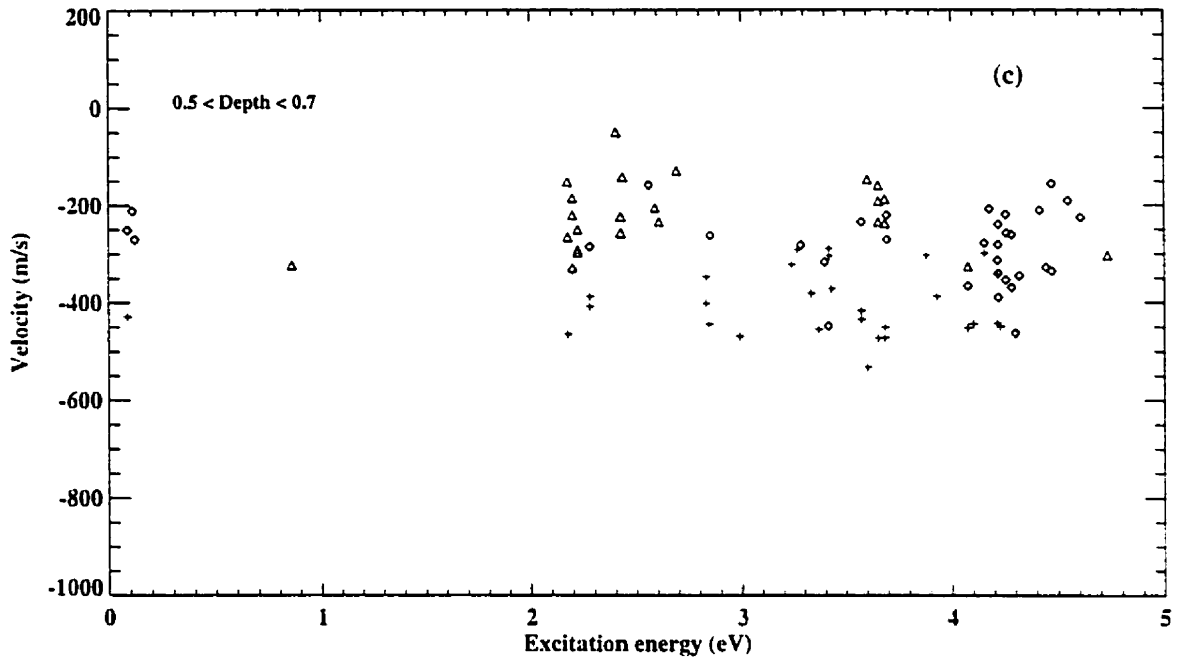


Figure 2.3: The distribution of convective line-shifts as a function of the lower excitation energy binned by line depth and wavelength region. Parts (a)-(d) demonstrate that when the dependence on wavelength and line depth are separated, much of the apparent dependence of the line-shifts on excitation energy is removed. There appears to be a large scatter in velocity for any depth/wavelength bin at a particular energy value. All of the different subsets which extend over most of the energy range are easily fit with a line of zero slope.



These effects combine to give the very large standard deviations to the bisectors for these bins. This explains why the median bisector deviates from the distribution near the weaker lines. In this respect, the use of line core positions produces a cleaner representation of the convective motions at the deepest atmospheric levels.

This depth dependence results from the deeper lines forming higher in the photosphere, where convective velocities are decelerated ballistically and where the temperature difference, and hence the contrast, between the granules and intergranular lanes is smaller. The contributions from the granules and intergranule regions are more balanced in the line core. The recovery of the bisector 'C' shape, shown in Figure 2.4, achieves one of the major goals of this chapter: the method developed here using core line-shifts contains the information present in the traditional line bisectors.

To separate the dependence on line depths from the dependence on wavelength, we have grouped the lines into several wavelength bins. We still see a strong dependence of the line-shifts on line depth that is consistent with the total ensemble of lines. However, we also find that in each wavelength bin, the depth/velocity distribution is offset, with the redder lines having smaller line-shifts for a particular line depth, although the distributions all have similar shapes. Much of the scatter for a particular line depth in the overall distribution is due to this 'overlap' of the different wavelengths. The shallower lines tend to have less of an offset from their counterparts at different wavelengths than the deeper lines. Polynomial fits were applied to the data bins, and it was found that the parabolic fits were optimal. Fitting parabolas to the different sets of data, we find that the blue distribution has a 'flatter' shape than the red. The difference in shape between the red and blue subsets may reflect the effects of limb darkening on the observed line shifts. However, the difference is not great, and it would be premature to draw any conclusions at this point. A comparison with the central intensity observations and a study involving a longer wavelength baseline may resolve this issue.

Empirical Dependence on Wavelength

Previous studies of the dependence of convective line-shifts on wavelength have reached conflicting conclusions. Dravins et al. (1981) found that there is a dependence upon wavelength for bins of a particular depth. However, later studies (Nadeau 1988; Allende Prieto & García López 1998) contradict this finding.

This conflict is resolved by recognizing that there is a significant dependence on line depth that must be isolated; lines of shorter wavelengths also tend to be deeper than longer wavelength lines.

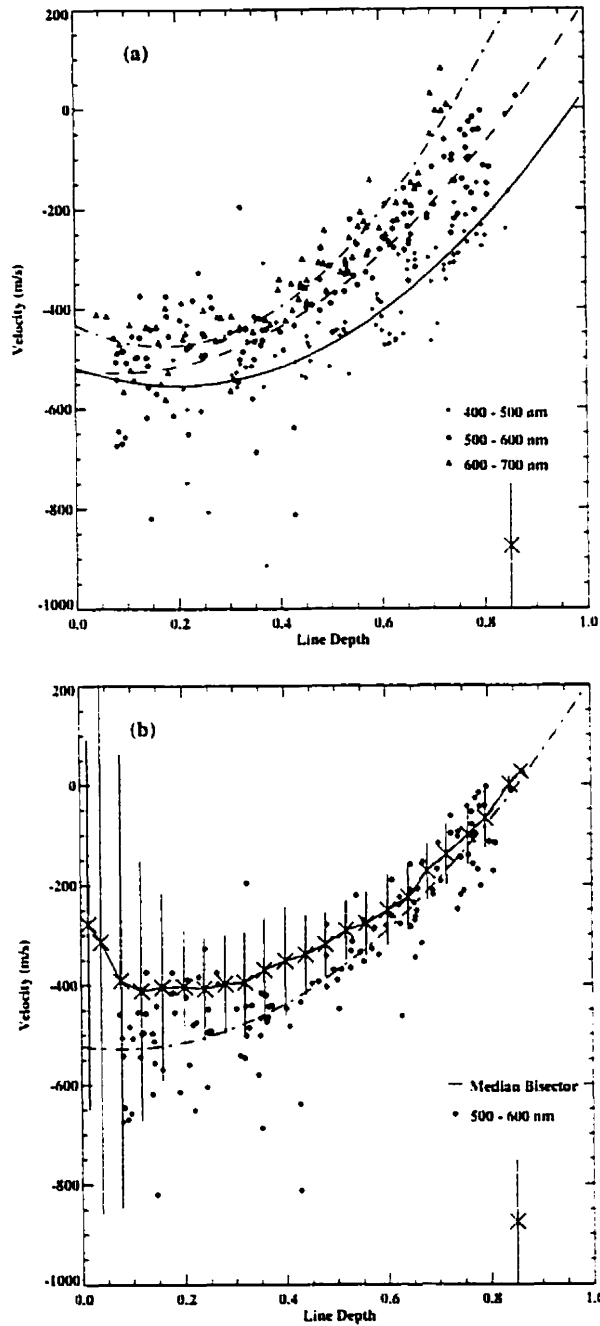


Figure 2.4: Convective line-shift velocities as a function of line depth binned by wavelength. The degree of the dependence of the line-shifts on line depth is clearly seen. The wavelength dependence can also be seen in this distribution, and most of the scatter at a particular depth is due to the overlapping wavelength distributions. Part (b) replots the wavelength bin from 500–600 nm, together with a traditional median line bisector derived from the same lines, rotated counterclockwise by 90° , to illustrate that the core line-shifts provide essentially the same information as the bisectors. The standard deviation for each bin of the median bisector has been plotted. (see text)

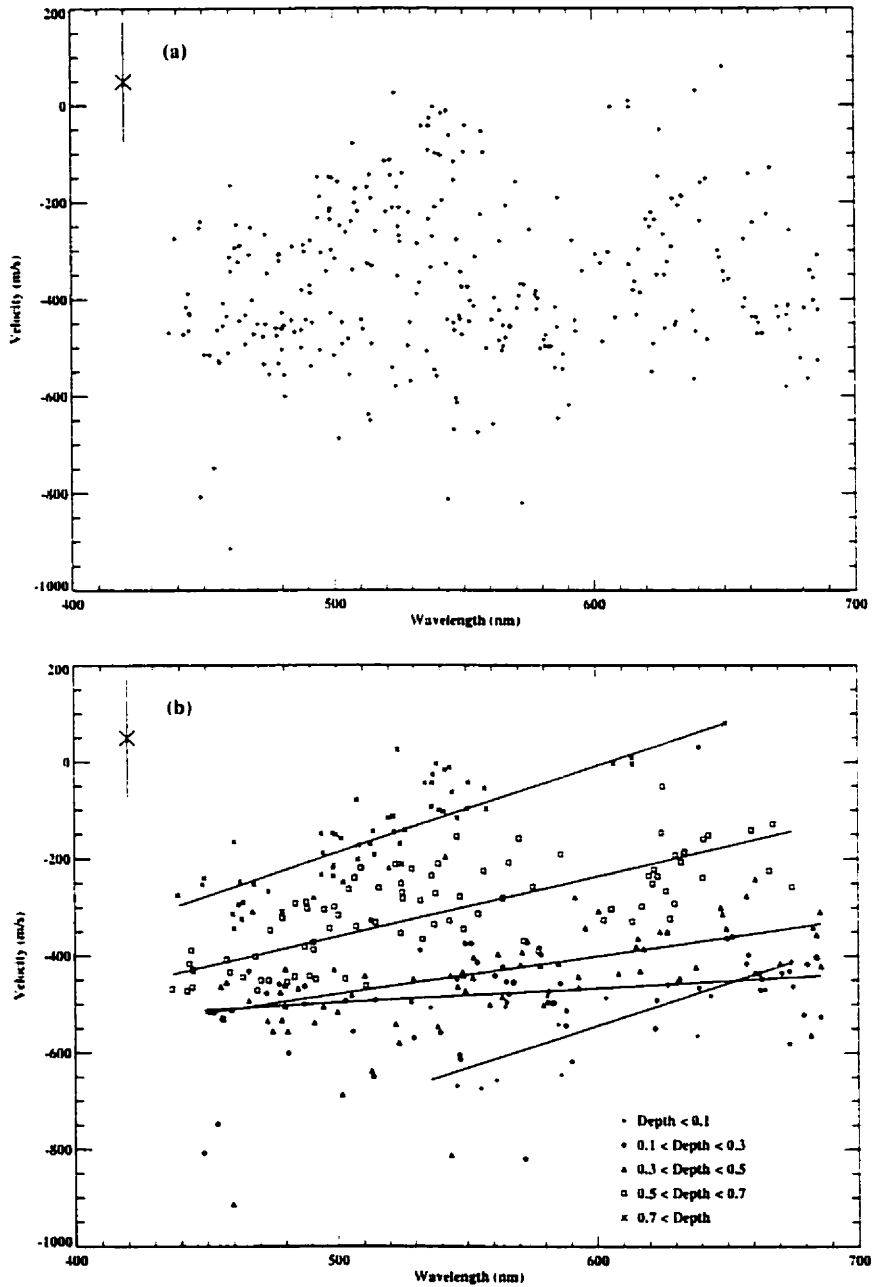


Figure 2.5: Line-shifts as a function of wavelength. Part (a) shows all lines without distinguishing line depths. Part (b) has identified the lines by depth. The core line-shifts for each depth group have been given a robust linear fit. The deeper the line, the steeper the dependence of the line-shifts upon wavelength. Only the shallowest line group deviates from this, but this bin is the smallest sample by a factor of four, has the smallest wavelength span and has the lines that are the most susceptible to undetected blends.

If the interplay between the depth and the wavelength dependencies is ignored, the distribution of line-shift appears to be uncorrelated with wavelength (Figure 2.5(a)). In fact, the bluer lines *are* blue-shifted more, but this is countered by the bluer lines also being deeper, and deeper lines tend to have smaller shifts, as described above. To separate the two dependencies, we consider lines over specific depth ranges. The robust linear fit to each depth bin in Figure 2.5(b) shows clearly that the line-shift of deeper lines is a steep function of wavelength. Shallower lines show much less of a dependence on wavelength, but this is clouded by the absence of the shallowest lines below 500 nm and by the small sample size, smaller than the others by a factor of four. Table 2.1 outlines the characteristics for each bin in depth and wavelength.

Bisectors

Median and mean bisectors were calculated for all the Fe I lines in the sample using the groupings shown in Table 2.1. The bisectors behave consistently with the line-shifts. The median bisectors for the different depth bins all have very similar shapes and offsets similar to those observed previously (Dravins et al. 1981). Figure 2.6 displays the median bisectors for the different depth bins. The error bars are the standard deviation for each depth bin of the bisector for medium strength lines. The size of the standard deviations for these bins increases as the pseudo-continuum is approached. This reflects the error sources discussed earlier in §2.2.3. Similar results are seen when the wavelength sensitivities are considered.

2.3.2 Spectral Resolution Effects

As was mentioned earlier, Dravins (1987a) has shown that using lower resolving powers seriously distorts the line bisector shapes, decreasing their usefulness substantially. Because there are fewer observed points across a line, much of the information present in the shape of the bisector is eliminated, especially in the middle section of the profile.

In contrast, line-shifts are much less sensitive to the effects of resolution. As Figure 2.7 demonstrates, even when the observations have been degraded to a resolving power of 52,000, the trend of velocity with line depth is still unmistakable, albeit the distribution is flattened. This flattening occurs because the points used to define the position of the line core from the bisector come from higher up the sides of the profile when lower resolutions are used. Thus, the line-shift follows the original shape of the bisector. Deeper lines have a larger blue-shift at lower resolutions because they are sampling the bottom part of the bisector shape, while shallower lines behave in the opposite

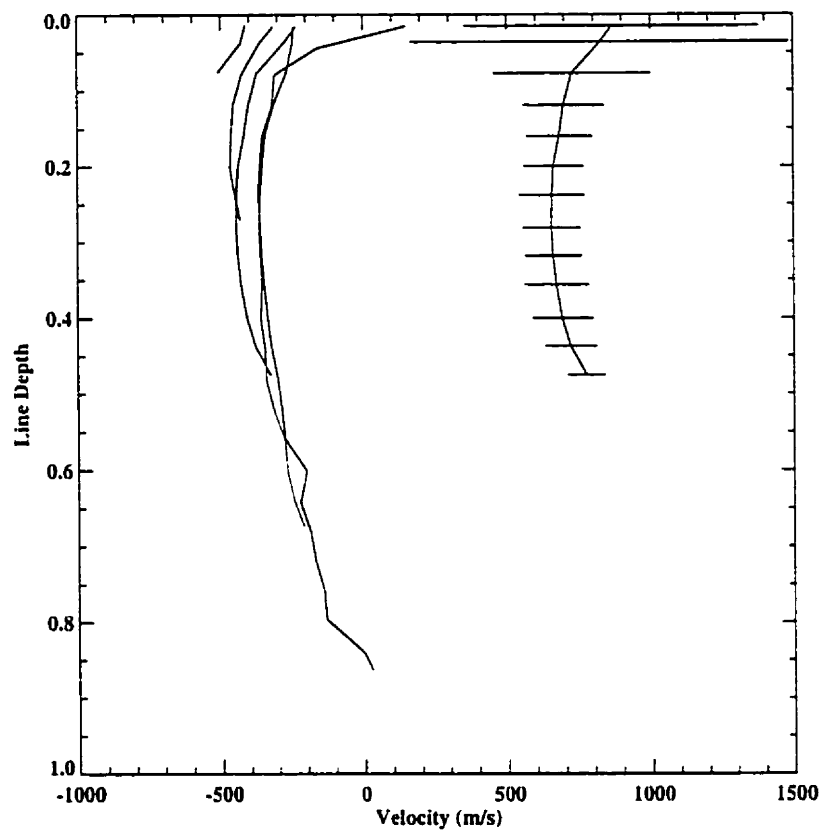


Figure 2.6: Median bisectors for each line depth group are displayed. The shapes of the bisectors are consistent with those of Dravins et al. (1981). Note that the median bisectors for the weaker lines are at larger blueshifts at a given depth than their stronger counterparts. This reflects the uneven distribution of line strengths over the wavelength regions. The error bars measure the standard deviation for each bin of the medium strength bisector ($0.5 \geq \text{Depth} \geq 0.3$) and have been plotted to one side for clarity. The larger σ for the top bins of the bisector are due to variations in the wings of the lines used.

sense because they sample the upper part of the bisector.

At the lower resolutions the presence of noise (at levels of S/N of 100 and 200) leaves the deeper lines largely unaffected. The *average* behavior of the shallower lines is also largely unaffected, although the scatter is much larger than for the low-noise samples. When noise was added to the original atlas data, the shape of the distribution remained unchanged, however as Figure 2.7(d) demonstrates, the scatter within each bin increases substantially. This reflects the sensitivity of the very bottom of the line core to noise (see §2.2.2). The lower resolution data sets display smaller degrees of scatter when the signal to noise is lowered. At lower resolutions, the line position is determined by using points slightly higher up on the line profile, which is less sensitive to noise.

The curves in Figure 2.7 for the different resolution samples all have very similar shapes, differing only by a translation. This can be seen by plotting the slopes, obtained from a least squares linear fit done for each line depth distribution, against their corresponding resolving powers (Figure 2.8). Examining Figure 2.8, we reach two important conclusions. First, the information content in the line-shifts converges to the full information present well before the highest spectral resolution is reached: the slope of the distribution at $R = 200,000$ is almost the same as the slope at the full resolving power of $> 500,000$. Second, there is a simple, nearly linear relationship between the slopes at lower resolving power and the slope at $R = 200,000$. This result, together with the first one, shows that there is a reliable way to correct lower resolution observations to be equivalent to the highest resolution.

Spectral resolution also affects the dependence of line-shift on wavelength, for each of the line depth bins, in nearly the same way as for the velocity/line depth dependence shown earlier in Figure 2.7. Figure 2.9 shows that the least squares linear fit to the individual depth bins flattens at shorter wavelengths in comparison to the original data set. The effect of reducing the resolving power is to ‘fill in’ the lines. With fewer points across a line, there is less likelihood of sampling the actual bottom of the profile. This is particularly true for deeper lines because of the steeper sides of the profile. However, a wavelength dependence is still present that is similar to the original distribution. As expected, the major exception occurs for the shallowest lines. However, this is the smallest subset, with much greater scatter than any of the other subsets.

Previous methods used to define line core positions have been largely resolution specific. Allende Prieto and García López (1998) used a 55 mÅ ‘window’ around the bottom of each line and then fit the points in the window with a fourth order polynomial. At the original resolving power of 500,000, there is no significant difference between the core line-shifts determined by the two-point

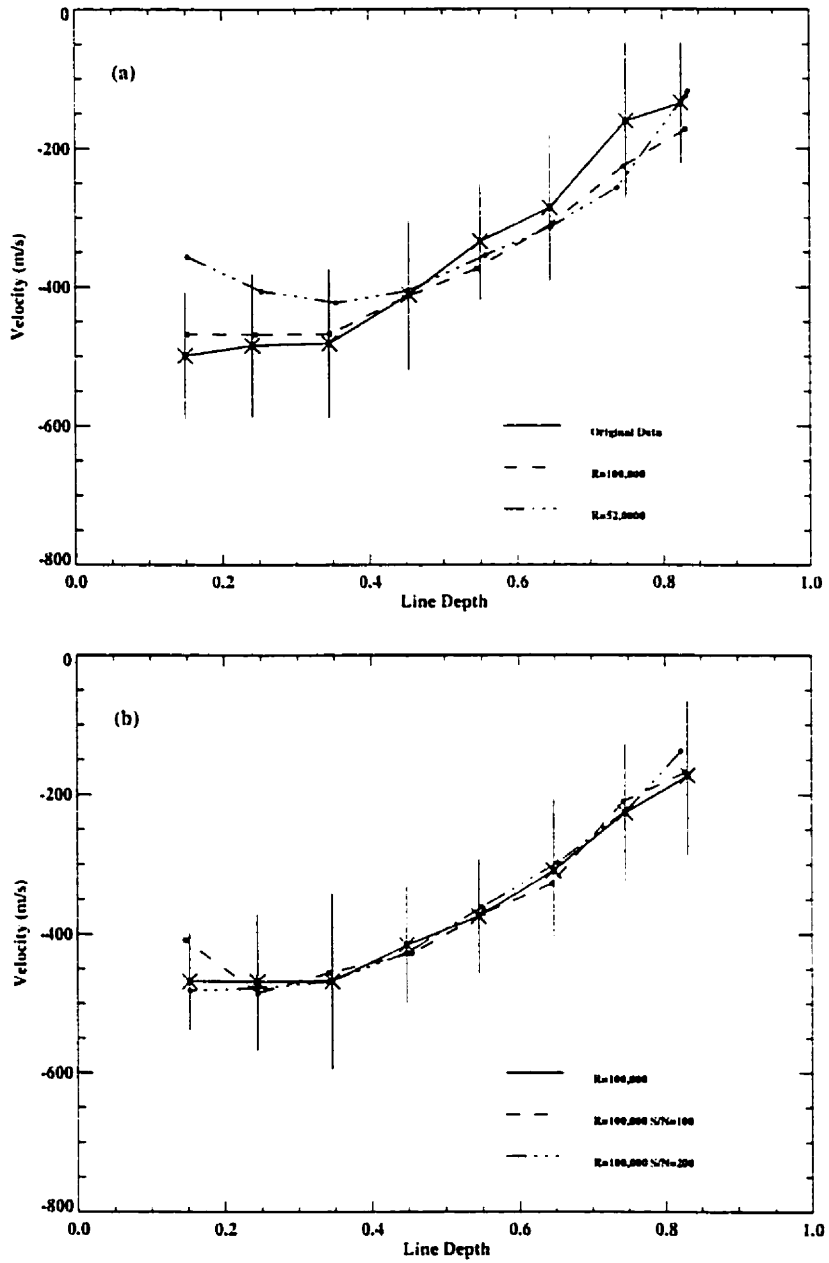
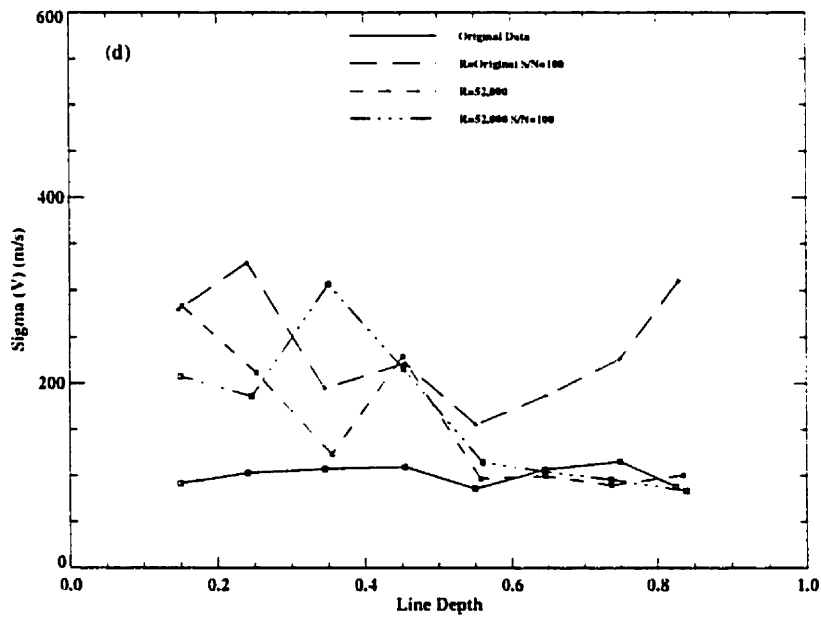
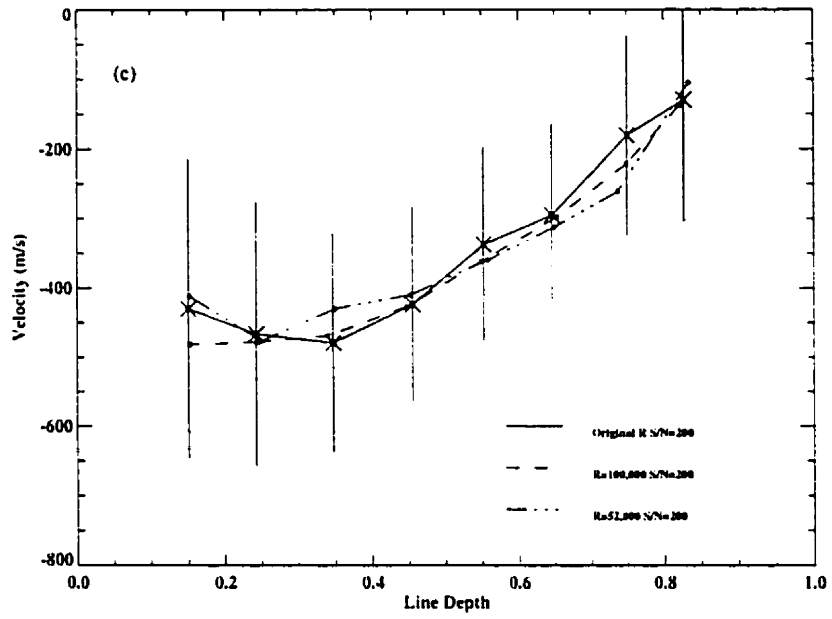


Figure 2.7: In parts (a)-(c) the lines have been grouped by depth. Error bars represent the scatter of each bin for the data represented by the solid line. The source atlas was then rebinned to lower resolutions, and, for two cases, noise has been added (see text). The distribution of velocities flattens as lower resolutions are used, however, the distribution still has a measurable slope even at $R = 52,000$. Part (d) shows how noise can drastically affect the scatter in the line-shifts for shallower lines. The addition of noise to the high resolution data clearly shows the sensitivity of the line minima to noise for all line depths.



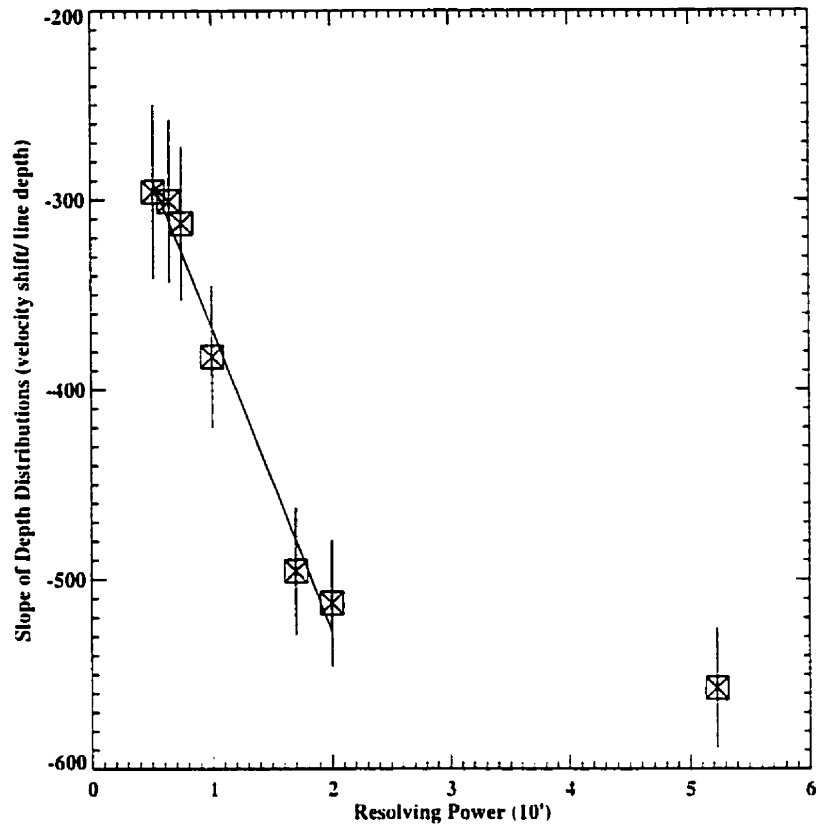


Figure 2.8: The dependence of the slope of the line depth distributions on resolving power (see text). The slope does not change significantly beyond $R = 200000$, showing that there is no gain in going to still higher resolving powers. Below $R = 200000$, there is a nearly linear change of slope with spectral resolution, enabling a simple correction of lower resolution to the highest resolution. The solid line is a linear fit to the 6 lower resolving powers.

method used here and that of Allende Prieto (Figure 2.10(a)). However, as lower resolutions are used, the 'window' method quickly becomes ineffective.

For the $R = 100,000$ data set, the window technique of Allende Prieto could be used only if the window were expanded to 75 m\AA , and then it would only encompass 3-4 data points. When we degraded the resolution to $R = 75,000$, the two-point method had the smallest scatter and was the method that came closest to reproducing the original distribution. As Figure 2.10 shows clearly, when the polynomial fitting techniques are used, the scatter almost completely overwhelms any possible shape to the depth dependence for the line-shifts.

Dravins et al. (1981) defined the line position as the point on the bisector 7% above the line minimum. Again, this is a technique that is resolution specific. While the two-point bisector method and the Dravins et al. method compare very favorably at higher resolutions, the technique of Dravins et al. displays a larger scatter when lower resolutions are used, even though the distribution

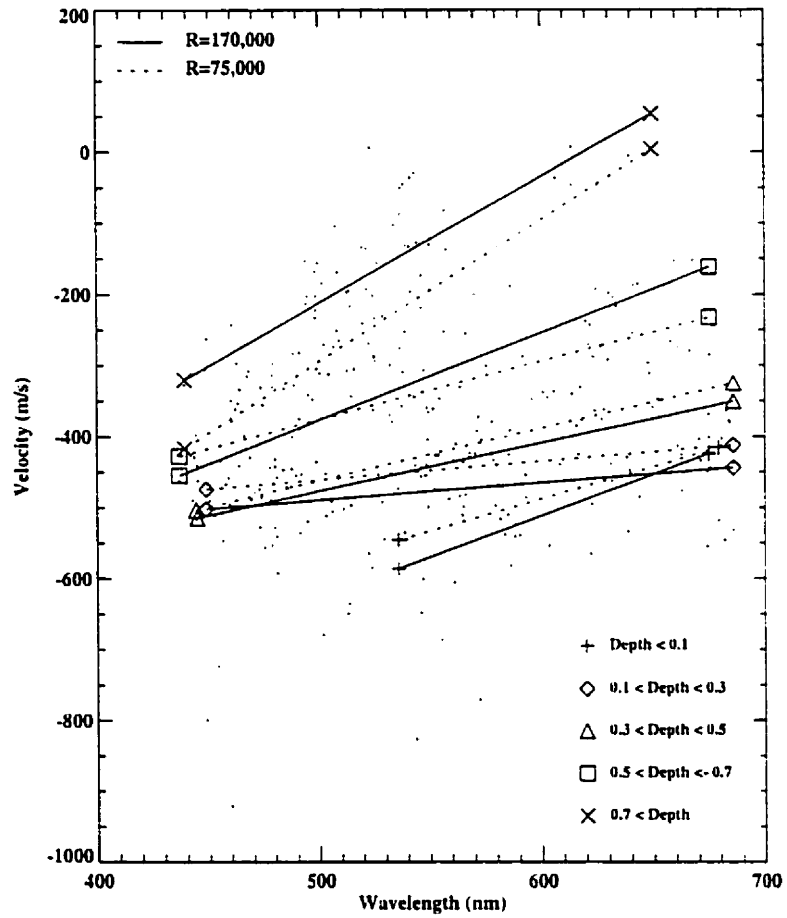


Figure 2.9: Lower resolutions flatten out the dependence of the core line-shifts upon wavelength. When the $R = 170,000$ fits are compared to those at $R = 75,000$, the whole distribution seems to be compressed and flattened. The strongest features are no longer as distinct from the shallower classes of lines. However the wavelength dependence is still noticeable.

shapes are very similar. The Dravins et al. technique proves ineffective at lower resolutions for the same reason as that of Allende Prieto and García López: a paucity of points close to the line minimum to meet the constraints of their technique.

A third alternative (Irwin 1998) involves fitting a cubic spline to the bottom portion of the line. This method works very well at high resolving powers, but at lower resolutions has a slightly higher scatter than the two-point method. Again, the scatter comes from there being too few points near the bottom of the line for the interpolation. This method is also more sensitive to noise effects on the line minimum, which can greatly skew the spline interpolation.

2.4 Conclusions

Line-shifts, derived using accurate laboratory positions (Nave et al. 1994) have been shown to be an effective technique to study convective motions in the Sun's atmosphere at moderate to high resolving powers. A set of lines with a wide range of line depths samples a wide range of levels in the stellar atmosphere, just as the bisector of a line profile does. At a given depth in the line profile, the asymmetry of the bisector reflects the velocity characteristics of the particular level in the stellar atmosphere where that part of the line forms. In the same way, the position of the cores of a set of lines spanning the full range of line depths will sample the vertical velocity structure of the stellar atmosphere.

Unlike line bisectors, it is not necessary to use ultra-high resolving power and signal-to-noise ratio. We have shown that it is possible to gather information on the velocity distributions for solar lines at resolving powers as low as 52,000. The technique that has been developed is portable and relatively insensitive to noise.

The convective line-shifts show a clear dependence upon both line depth and wavelength, which is consistent with the work of Dravins et al. (1981, 1986). However, it is essential to isolate the particular parameters under consideration. In the case of Fe I, the distribution of line depths is not uniform over the wavelength range. The bluer lines tended to be deeper and the dependence of the line shifts on the two parameters canceled out.

The dependence of the line-shifts upon the lower excitation potential is somewhat questionable. This may be due to the small range in excitation potential for a particular line depth bin. A greater range in excitation potential, perhaps over different species, may be required to decide this question. This will require highly accurate laboratory wavelengths for other species. The best

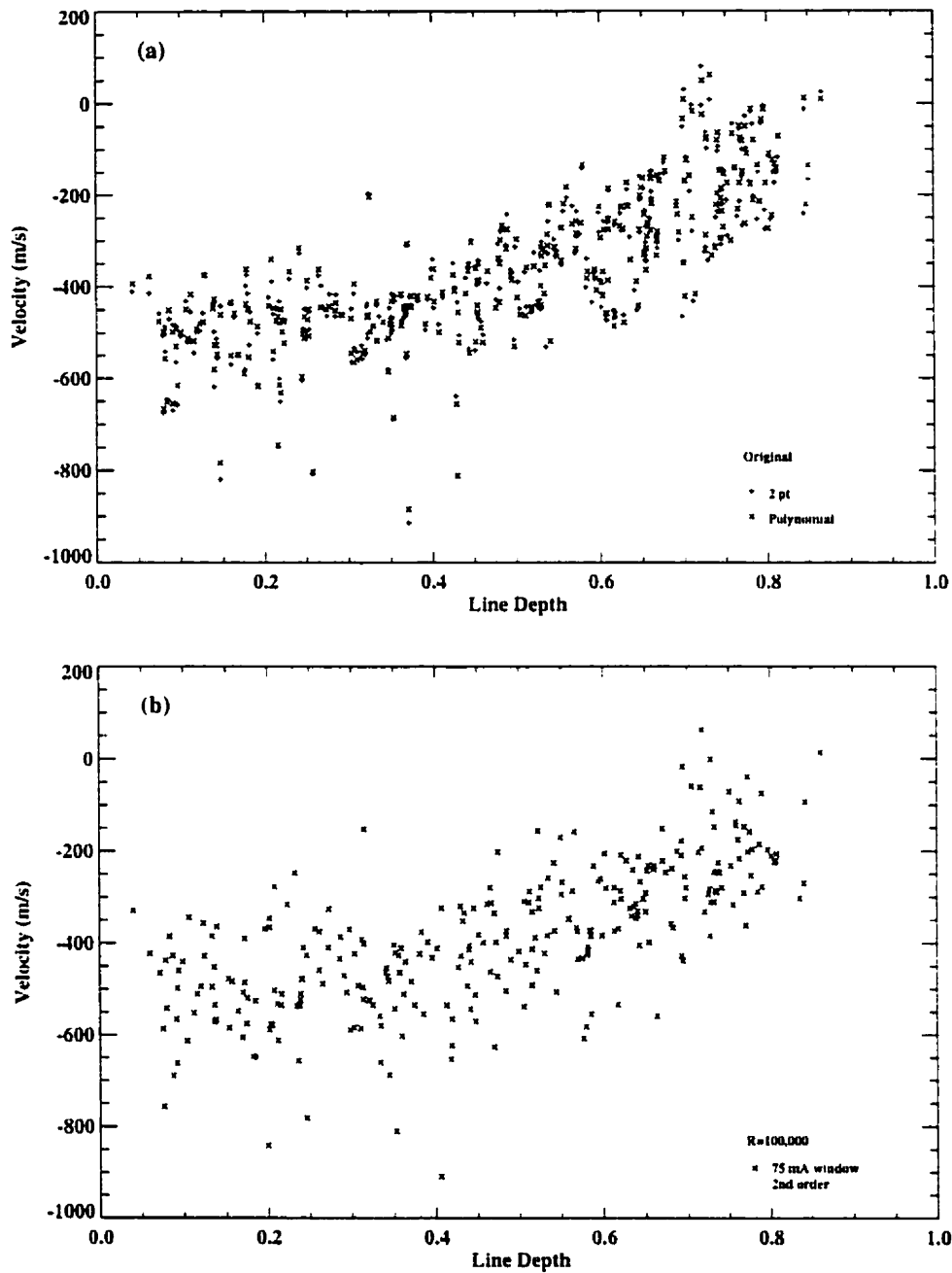
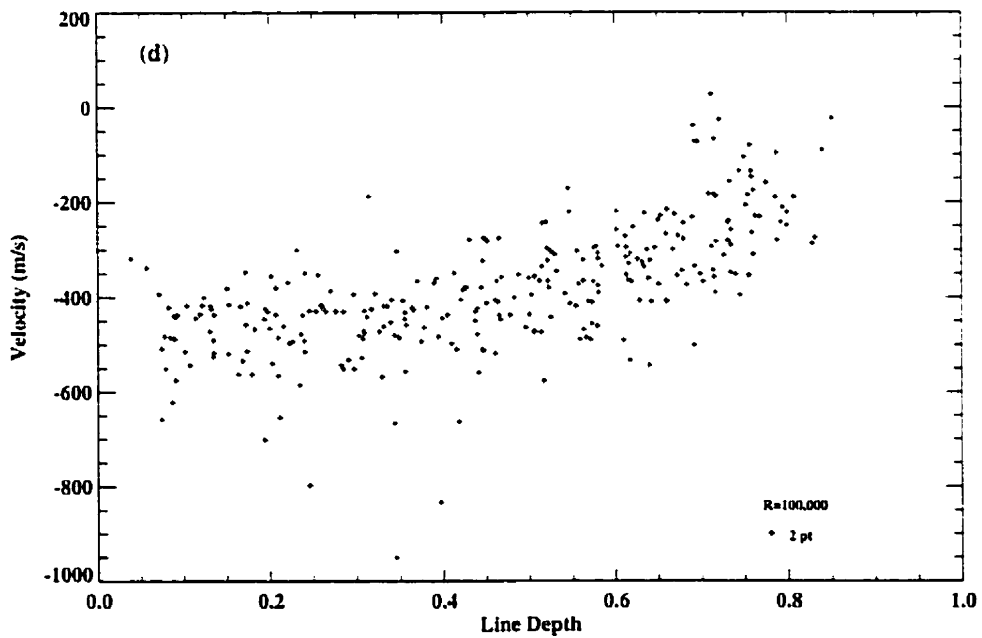
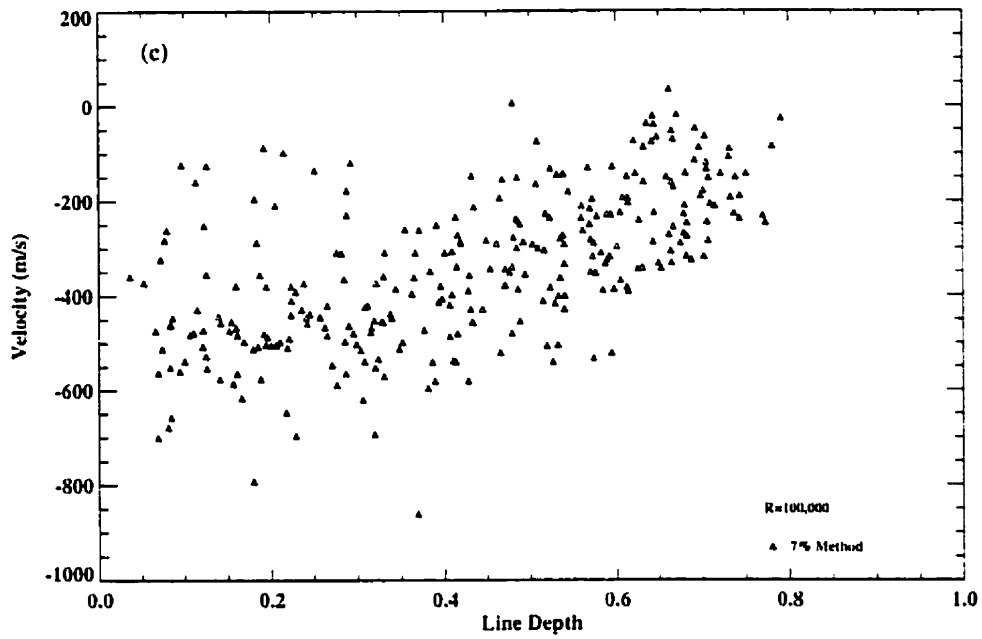


Figure 2.10: At the original resolution there is no greatly discernible difference in the velocities found using the two point bisector technique and the more traditional techniques of fitting a fourth order polynomial to the bottom of the line features, or using the technique employed by Dravins et al. (1981) (part a). However, as lower resolutions are used, the other techniques display more scatter than the two point bisector technique. This can be seen when the techniques are compared at the relatively high resolving power of 100,000 (parts(b)-(d)). At lower resolutions, the two point bisector method still provides information consistent with ultra-high resolution results (part(d)), while the other fitting methods have much greater scatter. At lower resolutions, the fitting window for the polynomial technique has to be increased in size and the order of the polynomials have to be decreased to compensate for the smaller number of points within the window.



candidate species would be Fe II because it has a similar atomic structure and is found over the same wavelength region.

Chapter 3 is an examination of the intensity spectrum of the Sun in the visible and infrared using Fe I lines. The use of a larger wavelength baseline will allow for a more comprehensive study of these trends and how they correlate with observable parameters. The use of the Solar Flux Spectra provides a useful fiducial sample for studying the relative convective velocity distributions in other stars. By comparing the Solar velocity distribution with those of other stars, the scaling behavior of the line-shifts with both gravity and temperature can be examined.

Previously (Dravins 1987b), the bisector shapes found for other solar-type stars (most notably Procyon, α Cen and β Hydri) have been markedly different from their solar counterparts. Dravins (1987b, 1990) attributes these differences to scaling effects in $\log g$ and T_{eff} . The vertical velocity structure in these types of stars is reflected in the shape of their line profile bisectors. It will be an interesting test to see if the velocity structures are also reflected in the stellar distributions of line-shifts.

Table 2.1: Fe I Visible Flux Bin Characteristics

Depth	λ Range (nm)	$\langle V. \text{ (ms}^{-1}\text{)} \rangle$	σ_v	$\langle \lambda \rangle$	σ_λ	$\langle \text{Depth} \rangle$	σ_D	N
$D \leq 0.1$	$400 \leq \lambda \leq 700$	-531.3	90.7	598.8	48.1	0.08	0.015	15
$0.1 < D \leq 0.3$	$400 \leq \lambda \leq 700$	-491.2	97.2	577.1	67.0	0.20	0.053	60
$0.3 < D \leq 0.5$	$400 \leq \lambda \leq 700$	-447.1	113.2	559.7	72.4	0.40	0.061	76
$0.5 < D \leq 0.7$	$400 \leq \lambda \leq 700$	-306.5	100.6	541.6	66.2	0.60	0.055	87
$0.7 < D$	$400 \leq \lambda \leq 700$	-156.3	110.9	515.1	46.0	0.76	0.039	60
$0 \leq D \leq 1$	$\lambda < 500$	-403.4	138.8	473.0	17.8	0.56	0.183	83
$0 \leq D \leq 1$	$500 \leq \lambda < 600$	-352.2	182.3	544.8	26.0	0.46	0.24	137
$0 \leq D \leq 1$	$600 \leq \lambda$	-329.9	147.7	644.5	25.2	0.41	0.20	78
$D \leq 0.1$	$500 \leq \lambda < 600$	-571.4	88.7	564.7	17.4	0.09	0.009	9
$D \leq 0.1$	$600 \leq \lambda$	-471.2	56.8	649.9	27.5	0.08	0.02	6
$0.1 < D \leq 0.3$	$\lambda < 500$	-561.2	143.5	471.8	14.7	0.24	0.036	8
$0.1 < D \leq 0.3$	$500 \leq \lambda < 600$	-490.3	99.0	555.2	26.2	0.19	0.051	33
$0.1 < D \leq 0.3$	$600 \leq \lambda$	-463.2	50.2	659.2	21.1	0.20	0.056	19
$0.3 < D \leq 0.5$	$\lambda < 500$	-509.4	105	473.5	15.2	0.39	0.061	22
$0.3 < D \leq 0.5$	$500 \leq \lambda < 600$	-463.5	115.1	552.9	27.2	0.38	0.059	30
$0.3 < D \leq 0.5$	$600 \leq \lambda$	-369.6	67.3	647.3	27.8	0.42	0.059	24
$0.5 < D \leq 0.7$	$\lambda < 500$	-402.1	65.9	472.1	19.3	0.61	0.055	29
$0.5 < D \leq 0.7$	$500 \leq \lambda < 600$	-284.2	74.0	536.7	24.1	0.60	0.057	34
$0.5 < D \leq 0.7$	$600 \leq \lambda$	-222.7	71.2	632.7	18.7	0.60	0.056	24
$0.7 < D$	$\lambda < 500$	-255.3	68.2	474.1	19.9	0.77	0.040	24
$0.7 < D$	$500 \leq \lambda < 600$	-108.6	70.4	529.3	16.2	0.77	0.038	31
$0.7 < D$	$600 \leq \lambda$	22.6	35.5	624.6	18.7	0.72	0.012	5

The data have been binned by wavelength or by line depth, or by both. The average line-shift velocity, wavelength, depth and their standard deviations are given for each subset and range. The trends mentioned in the text can clearly be seen here. The line-shift is dependent on both line depth and wavelength.

Chapter 3

Fe I in the Central Intensity Spectrum of the Sun

3.1 Introduction

Chapter 2 demonstrated a technique for determining the convection-induced shifts of line cores at a variety of resolutions and signal-to-noise ratios, and demonstrated their consistency with line bisectors. As seen in Chapter 2, and elsewhere (Dravins et al. 1981; Dravins et al. 1986; Nadeau 1988), the line-core shifts for Fe I show sensitivities to both line strength and wavelength. There is some evidence that there is also a dependence upon lower excitation energy (Dravins et al. 1981; Dravins et al. 1986), however, as seen in Chapter 2, that dependence on χ_l may be questionable. Larger samples, in both number of lines and wavelength range could resolve this issue.

A larger wavelength baseline also allows an examination of how the varying continuous opacity affects the line-core shifts, as well as a more complete examination of how the change in temperature contrast between the granules and lanes affects the observed distribution of velocities. At longer wavelengths, the granules contribute relatively less flux than at visible wavelengths. This change in the contrast should be apparent in the shapes of the line-shift distributions for the different wavelength regimes.

Both flux and central intensity atlases are available for the Sun's visible spectrum, but only central intensity atlases are available for the infrared. Comparisons between distributions of line-core shifts from both flux and intensity sources yield a greater understanding of how limb darkening and moderate rotation affect the observed convective line-core shifts in flux spectra, which is important for determining the effectiveness of this diagnostic for other stars.

Here, the study is extended into the infrared by using central intensity solar atlases. This allows

for wavelength coverage from 400 nm to 5.5 μm . We are in a position to compare the Fe I line-core shifts in the visible flux and in the central intensity observations, and examine them for the effects of limb darkening. The influence of the Solar H⁻ opacity minimum near 1.6 microns is also a subject of study.

Coupling the observed velocities with approximate physical heights of formation for simulated lines cores permits an approximate determination of the Sun's atmospheric velocity gradient and the consequences of changes in both opacity and the temperature contrast at different wavelengths. The change in contrast with wavelength should be reflected in the velocities for lines formed at the same height but at different wavelengths. The changing continuous opacity determines which levels of the atmosphere are sampled by lines, and is important in understanding how the velocity distributions change with wavelength.

3.2 Methodology

3.2.1 Spectral Sources

In Chapter 2, we assessed the Solar Flux Atlas (Kurucz et al. 1984). Here we extend our investigation to the central intensity spectrum from 400 nm to 5.5 μm . Fortunately, there are four solar intensity atlases, all of which were recorded using Fourier Transform Spectrometers (FTS) at very high resolving powers and signal-to-noise ratios, which provide for continuous wavelength coverage from 400 nm to beyond 5 μm .

Visible

The Wallace et al. (1998)¹ atlas, which was recorded at Kitt Peak using the FTS on the McMath-Pierce Solar Telescope, covers from 3750 to 7405 Å at resolving powers between 337,500 and 700,000. This atlas is a composite of three different FTS scans, put on a common wavenumber scale using the 6 cm⁻¹ overlap between each scan. The atlas data points are interpolated to a two-point resolution of 0.020 cm⁻¹, and are set to a pseudo-continuum established by a series of polynomials fit to spectral high points. The telluric spectrum has also been removed (Wallace et al. 1998). Since our study involves comparisons over a wide range of wavelengths, all the atlases are set to a common wavenumber scale using this atlas as the fiducial wavenumber scale. The atlas identifies both atomic and molecular lines using a range of sources.

¹NSO/Kitt Peak FTS data used here were produced by NSF/NOAO.

Near Infrared

The atlas of Wallace *et al.* (1993)¹, also recorded with the McMath-Pierce Solar Telescope and FTS, was used for the spectrum extending from 7350 to 11230 Å at resolving powers between 590,000 and 900,000, corresponding to a resolution of 0.0073 cm⁻¹ per point. The spectra were obtained at disk center at a time when it was free of sunspots. To average out surface structure, the image, which covered an angular region ≈ 40 arc-sec in diameter, was intentionally defocused. Telluric atmospheric lines were removed using high air mass observations extrapolated to the air mass of the scans. Line identifications for major features, both molecular and atomic, are also provided (Wallace *et al.* 1993).

Ground-Based Infrared

The ground-based infrared atlas (Livingston & Wallace 1991)¹ is a center-disk intensity atlas covering 1.1 to 5.4 μm, and was also obtained at the McMath Solar Telescope and FTS. The solar region observed was sunspot free and surface variations were averaged out by using a 1 meter out of focus image (spanning ≈ 40 arc-sec). The observed spectrum was corrected for telluric atmospheric absorption by a point-by-point extrapolation to zero air mass using spectra at effective air masses of 1.8 and 5.2 (Livingston & Wallace 1991). The resolution was ≈ 0.018 cm⁻¹, with resolving powers between 100,000 and 460,000. Line identifications of major features, both molecular and atomic, are also provided.

Space-Based Infrared

The partial opacity of the Earth's atmosphere is the main obstacle to using infrared spectra, especially for wavelengths longer than approximately 2 μm. Space-based infrared observations allow for complete wavelength coverage over the wavelength range which includes such useful molecular spectra as CO and OH. Ground-based spectra over this wavelength range are patchy and incomplete in coverage, and the removal of the telluric spectrum greatly affects the resulting signal-to-noise, while some telluric features completely obscure portions of the spectrum. This is especially the case when molecules which are present both in the solar spectrum and the telluric spectrum are being studied. Space-based observations permit a much more complete study, free of these complications.

The ATMOS² (Atmospheric Trace Molecule Spectroscopy) Solar Atlas provides coverage from

²Jet Propulsion Laboratory, California Institute of Technology, under contract to NASA

625 to 4800 cm^{-1} . The ATMOS instrument is an FTS that flew aboard the Space Shuttle in 1985 and in 1994 (Abrams et al. 1996). The instrument has an unapodized spectral resolution of 0.0105 cm^{-1} , and consists of five different bandpasses: 625-1500, 1100-2000, 1580-3400, 3100-4800, and 625-2450 cm^{-1} . The data for each one of these bandpasses are available from the Jet Propulsion Laboratory³. Each bandpass consists of averages of disk-centered spectra (Abrams et al. 1996). The area of integration is large, corresponding to a circle with a radius of 0.28 R_J (4 arc-minutes) for $\lambda < 4.97 \mu\text{m}$. This integration area, while not including the limb, is substantially larger than those used for the other sources. The signal-to-noise ratio of the resulting atlas is 300:1 at the smallest wavenumbers, degrading to 50:1 at the largest wavenumbers (the 3100-4800 cm^{-1} bandpass). The wavenumber regions of the three bandpasses used in this study (1580-3400, 3100-4800 and 625-2450 cm^{-1}) all overlap with the KPNO Infrared Atlas (Livingston & Wallace 1991).

Although the ATMOS data have a wavenumber calibration (Abrams et al. 1996), we found it to be less accurate than our study required. Because the ATMOS data were taken primarily to remove the effects of the solar spectrum from Earth's atmospheric spectrum, slight distortions of the wavenumber calibration may have resulted (Abrams, private communication). Therefore, the three bandpasses used here were all calibrated against the KPNO IR Atlas (Livingston & Wallace 1991) and against one another, using both line positions and also cross correlation radial velocity techniques. The resulting corrections were small: a zero point shift of 0.010 cm^{-1} and a Doppler correction of 960 ms^{-1} for the 625-2450 cm^{-1} bandpass and a 0.005 cm^{-1} zero point shift combined with a Doppler correction of 1765 ms^{-1} for the 1580-3400 cm^{-1} bandpass. The 3100-4800 cm^{-1} bandpass simply required a Doppler shift of 1250 ms^{-1} .

3.2.2 Wavelength Errors

One of the distinct advantages that the FTS enjoys over grating spectrographs is the wavenumber calibration. For a particular scan, the positional accuracy of every data point within that scan is tied to the stability of the metrology laser, and the resulting linear calibration means that any error will affect all the points in the scan by the same amount. While none of the atlases used here provide an estimation of their positional uncertainty, three of the four atlases were obtained with the same FTS at McMath. The flux atlas used in Chapter 2 was also obtained with this instrument at a similar resolving power, and in that case the positional uncertainty is provided (Kurucz et al. 1984). For any point within an individual scan, it is estimated that the upper limit to its positional

³<http://remus.jpl.nasa.gov:80/atmos/atmos.html>

uncertainty relative to any other point in the same scan, or in the adjacent scans of the same atlas is 100 ms^{-1} (Kurucz et al. 1984). Here we adopt a similar upper limit to the positional uncertainty. The wavenumber calibrations between the different atlases in this study have been checked using radial velocity cross correlation techniques and by matching clean solar lines present in overlapping wavenumber regions.

3.3 Line Selection

3.3.1 Fe I

The criteria used for selecting candidate Fe I lines are the same as those outlined in Chapter 2. All apparent line blends were removed from the sample. The lines selected were also compared to the solar line identifications from existing atlases and tables (Moore et al. 1966; Swensson et al. 1970; Livingston & Wallace 1991; Wallace et al. 1993; Wallace et al. 1998), and the remaining suspect lines were checked against synthetic spectra computed with the Atlas 9 suite of programs (Kurucz & Avrett 1982).

All the lines in the visible and infrared have positions known to better than 0.02 cm^{-1} , which corresponds to 300 ms^{-1} at 500 nm and 3000 ms^{-1} at $5 \mu\text{m}$, and the *majority* of the lines have positions known to better than 0.005 cm^{-1} , or 75 and 750 ms^{-1} at 500 nm and $5 \mu\text{m}$, respectively.

While the positional uncertainty increases with wavelength, the majority of the lines used in this study are less than $2 \mu\text{m}$. Thus, the uncertainties for the line positions are very small. To maintain a uniform accuracy, only those lines with experimental positional uncertainties of less than 0.005 cm^{-1} were used beyond $2 \mu\text{m}$. Thus, at $5 \mu\text{m}$, the upper limit of the positional uncertainties is 750 ms^{-1} . These estimates are then combined with the wavenumber scale calibration uncertainties to provide overall position uncertainties. Most of the lines, especially those in the visible region, have positional uncertainties well below these limits.

3.3.2 Ti I

Ti I has not been used previously in studies of convective line-core shift, but it may be a useful supplement to Fe I. The best available laboratory line-position list is that of Forsberg (1991), which contains 3300 lines between 1900 and $55,000 \text{ \AA}$. These measurements were obtained using the FTS at the National Solar Observatory at Kitt Peak and a water-cooled cathode discharge experiment. Unfortunately, the resolution of the observations is not high enough for all isotopic shifts to be

identified, and there is no estimate of the positional accuracy for the individual lines, but both the observed and calculated positions for the Ti I lines are provided. Even though the linelist contains positions in the near infrared and infrared, only those in the visible are used here because of the uncertainty in the potential errors in the line positions. Any velocity uncertainty in the line position increases with decreasing wavenumber.

To estimate a lower limit to the uncertainty in the line positions, average $O - C$ values for the lines in this sample were examined. For the 111 Ti I lines used here, the average $O - C$ value is 0.004 cm^{-1} with a standard deviation of 0.004 cm^{-1} . For the entire set of Ti I lines, 90% have $O - C$ values less than 0.008 cm^{-1} , which corresponds to 120 ms^{-1} at 500 nm . We will take this value to define the lower limit for the positional uncertainty for the Ti I lines.

3.4 Analysis

3.4.1 Flux-Intensity Comparison

For comparison with Chapter 2, the different distributions of line-core shifts have been binned by common parameters: wavelength, line depth and (if warranted) lower excitation energy (χ_l). Median bisectors were also determined for comparison with those from the flux data set in Chapter 2. The differences reveal the effects of both limb darkening and rotation on the convective signatures.

3.4.2 Fe I

Wavelength Dependence

Previous work on the solar flux spectrum (Dravins et al. 1981; Dravins 1990) found a wavelength dependence for the line-core velocity distributions. Figure 3.1(a) displays the line-shifts for all 436 Fe I lines in the KPNO sample, binned into 5 line depth classes. All five bins clearly show a dependence upon wavelength, with the dependence being largest for the strongest lines. A least-squares linear fit has been done to each bin, and the slopes of these distribution fits decrease with line depth, except for the weakest bin (line depth $\leq 10\%$ of continuum), which shows the largest scatter and is the smallest sample in both size and in wavelength coverage, thus the value of the slope for the weakest bin is unreliable.

The set of 436 lines in the visible intensity spectrum overlaps substantially with the set used in Chapter 2. Of the 298 Fe I observed in the flux spectrum, 263 were also candidate lines in the

intensity spectrum. The overlap is not 100% since some features were rejected due to saturation effects, and some others were rejected due to distortions in their line profiles. The central intensity sample is larger than the flux sample for three reasons: (1) the flux spectrum has a smaller range of wavelength coverage; (2) rotational broadening can lead to a greater amount of blending (especially in the wings); (3) off axis contributions from the limb increases weak line blending, which eliminates many of the lines from the flux sample. The Fe I sample in Chapter 2 was selected so as to facilitate comparisons with the earlier work of Dravins et al. (1981), and the wavelength ranges were selected accordingly.

When the intensity and flux distributions are compared (Figure 3.1(b)), there are some marked differences. The three strongest bins from the flux spectrum all have steeper slopes than the corresponding intensity bins. This difference can be partly explained by a combination of limb darkening and the "limb effect". The "limb effect" (or center-to-limb effect) is noticed when a spectral line is observed at different position angles ($\cos\theta$) on the disk of the Sun. As the limb is approached the shape of the line bisector changes, becoming distorted from the disk center's 'C' shape (Dravins 1982). The extent of the distortion varies depending on the line and species, and is most pronounced near the limb (beyond $\cos\theta \approx 0.85$). Generally this change is attributed to both a change in the layer of the atmosphere that is observed, and the fact that the velocity that is observed is the projection of the granular velocity along the line of sight. Close to the limb, much of the granular velocity information will be almost perpendicular to the line of sight. Balthasar (1985) also argues that the contrast between the bright granules and the dark lanes change. Depending upon the height in the atmosphere, the respective geometric cross sections of the granules and lanes shift because of projection effects. Horizontal mass motions begin to make contributions to the line of sight velocity component and alter the profile. This becomes especially significant at higher altitudes where the contrast inversion occurs, because the downward vertical component becomes dominant in the central profile, however, the limb profile is still significantly affected by the horizontal granular motions. Pierce (1991) has argued that the extra observed redshift in the line profiles is a result of scattering by atoms in a anisotropic velocity field. However Balthasar (1984) has shown that the degree of the limb effect is very sensitive to the altitudes where the line profile cores are formed. However, the effects of the limb effect on the line profiles from the flux spectrum should be very small because the changes to the line profile only become significant near the limb, and the degree of distortion varies widely even between lines from the same species with similar properties.

In the flux spectrum, lines in the blue are dominated by radiation from the hotter, deeper regions visible at the center of the disk. Lines in the red portion of the spectrum have a much greater relative contribution from the solar limb, which is higher, cooler and viewed at steeper angles, enhancing the limb effect. These higher layers have slowed ballistically, and only a fraction of this radial motion contributes to the line of sight. For the observer, most of the vertical radial motion appears to be horizontal, and does not contribute to the Doppler Shift. In contrast, the central intensity has a single line of sight perpendicular to the solar surface. This penetrates to the hottest visible depths and receives the full effect of the mostly radial convective motion. The effect is more pronounced for the strongest lines than the weaker lines because, at the limb the strong lines do not sample very deeply into the photosphere where convective motions are larger. The limb component of the strongest lines are forming very high up in the atmosphere, where the velocities are drastically reduced. Again, the bin for the weakest lines does not quite follow this trend, but this may be a result of an uneven distribution of weak features over wavelength and the small size of the sample involved.

It is apparent that limb darkening and the center-to-limb limb effect affect the steepness of the slope, but it does not change the nature of the overall *distribution* of the line-shifts. In fact, working in the flux spectrum actually enhances the observability of the convective signature because the limb darkening increases the contrast between the red and blue wavelengths.

Line Strength Dependence

Line-core shifts show a very strong dependence on the strength of the line (Figure 3.2). The deepest lines have the smallest shifts, and the shallowest lines have the greatest shifts. These differences are a direct result of where the lines form in the solar atmosphere. The weakest lines form at the largest visible depths, where the upwelling velocities are highest and the temperature contrast between the rising and sinking plasma is greatest, giving the rising elements the greatest weight. The stronger lines form at higher physical locations, where the convective velocities are smaller because the material has been decelerated ballistically, and the temperature difference, and hence luminosity contrast, between the granules and intergranular lanes is smaller. An additional contributing factor is the change in the relative areas of the granules and lanes with altitude. Deeper in the atmosphere, the region of upwelling material is significantly larger than at higher altitudes, where much of the vertical motion has been transferred into horizontal motion because of the conservation of mass and the change in the density stratification of the atmosphere. The strongest lines form at atmospheric

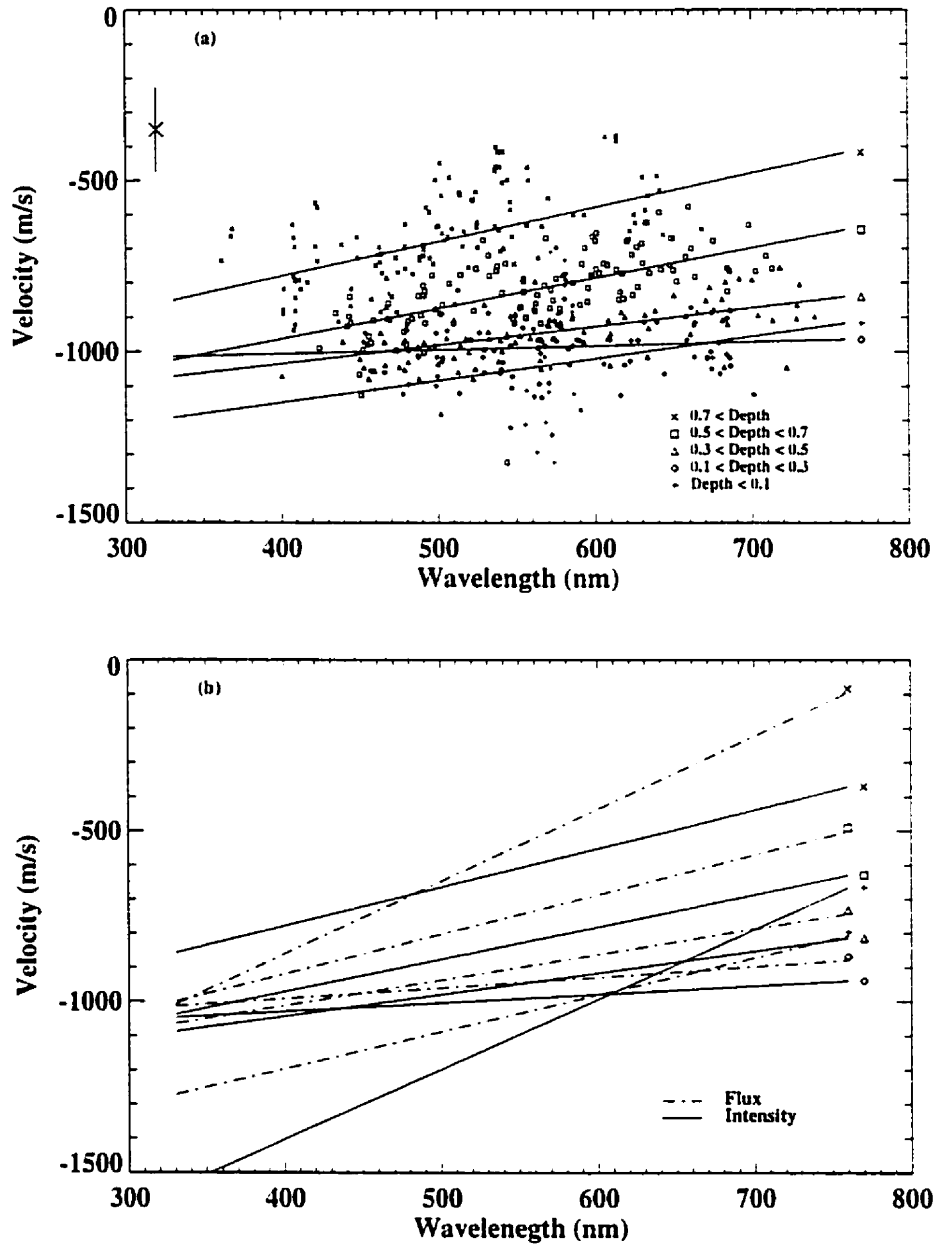


Figure 3.1: The dependence of the different Fe I strength bins on wavelength for the visible central intensity sample (a). There are 436 Fe I lines divided into five line depth bins, and the slope of the fits to each of the bins decreases with line strength (except for the weakest). Those lines common to both the flux and central intensity atlases are shown in (b). The distribution for strong lines from the flux sample is steeper than its counterpart from the intensity sample (see §3.4.1). The error bars are the typical upper limit error estimate for an individual point.

layers where most of the vertical motion is now horizontal, as the material overturns and enters into the downdrafts.

To separate the wavelength dependence from the line strength dependence, the 436 Fe I lines have been binned by wavelength in Figure 3.2. The wavelength dependence seen in Figure 3.1 is also apparent here. To see the trends more clearly, each of the three wavelength bins has been fit with a parabola. All three bins demonstrate similar line-shift behavior with line depth. However, for each of these bins the depth/velocity distribution is clearly offset, and have slightly different slopes. This reflects the wavelength dependence and also accounts for much of the scatter present at any given line depth. The distribution of blue lines appears to be flatter than the red distribution.

Similar results were found in the study of the flux data set in Chapter 2. The 263 Fe I lines in common between the two data sets can be compared to assess the effects of limb darkening upon the distributions. In Figure 3.2(b)-(d) the overlap between the flux and intensity data sets has been compared for the three wavelength bins. The least squares parabolic fits to each bin are shown, as well as the differences for each Fe I line and a least squares linear fit to these differences.

The major result of Figures 3.2(b)-(d) is that the flux and intensity distributions are very similar. The intensity-flux differences do show positive slopes with increasing line depth, but the slopes are small. The positive slopes mean that the intensity distributions are steeper than the flux distributions, which is no surprise because the flux contains shallow-angle contributions (the limb effect) to the line profiles, which introduces information about regions higher in the atmosphere where the temperature and velocity contrasts are smaller, and the motions along the line of sight are smaller, including possible horizontal motion contributions.

The largest difference between the intensity and flux distributions occurs for the blue lines. This is not immediately clear from the parabolic fits, but a least-square linear fit to the differences is steepest for the blue lines.

At first sight, this is counter to expectations. Because of the temperature variation, the blue portion of the flux spectrum is dominated by light from the center of the disk. This acts to minimize the differences between the flux and intensity data sets. However, there are other competing factors. One factor is that the distribution of velocity with the line-core depth is flatter in the blue than in the red. This is apparent in Figure 3.2(a) and it was also found for the flux data set in Chapter 2. Therefore, any steepening of this distribution is more apparent than for the already steeper distribution found for the redder lines.

Second, the contrast between granular and intergranular lanes is also more pronounced in the

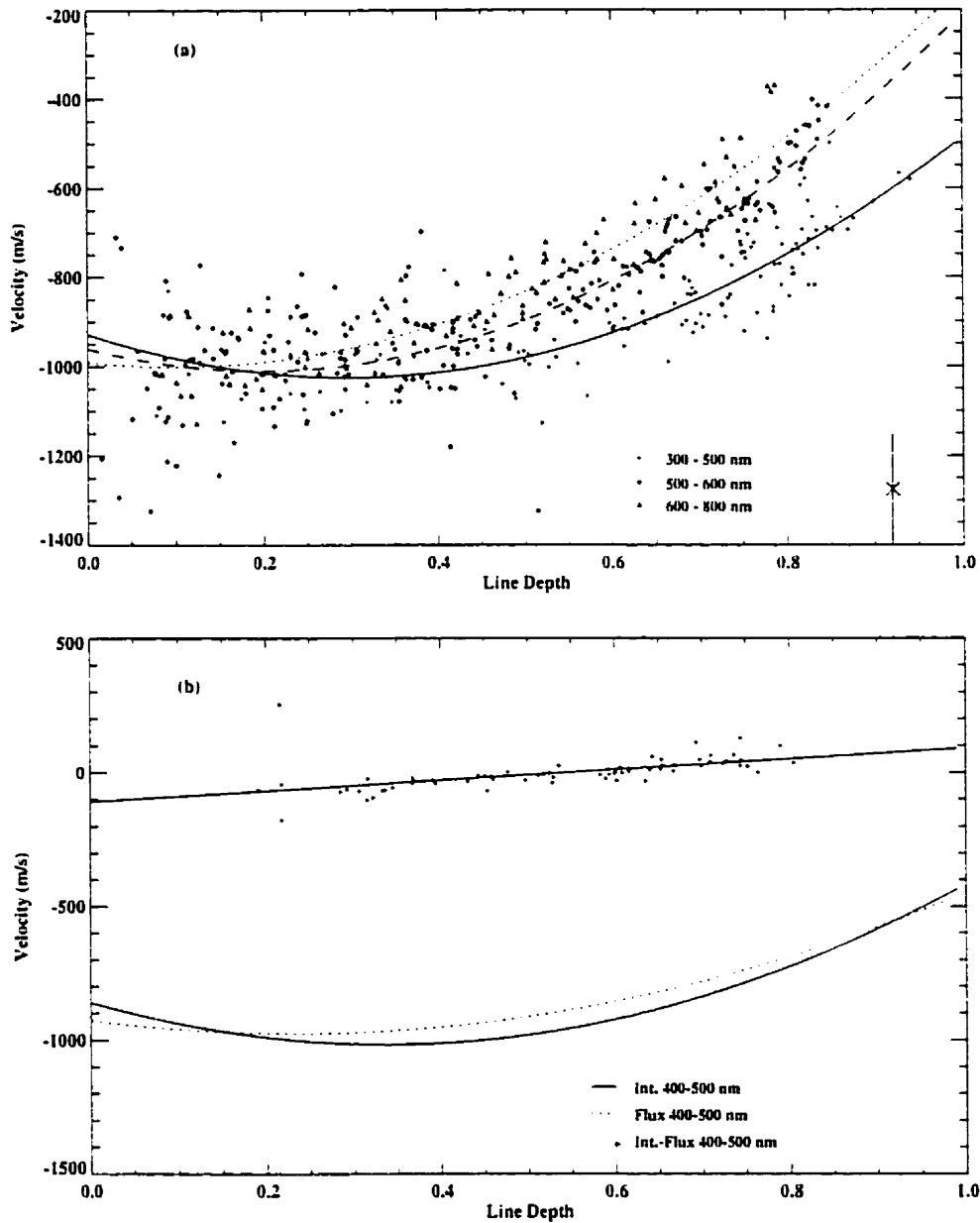
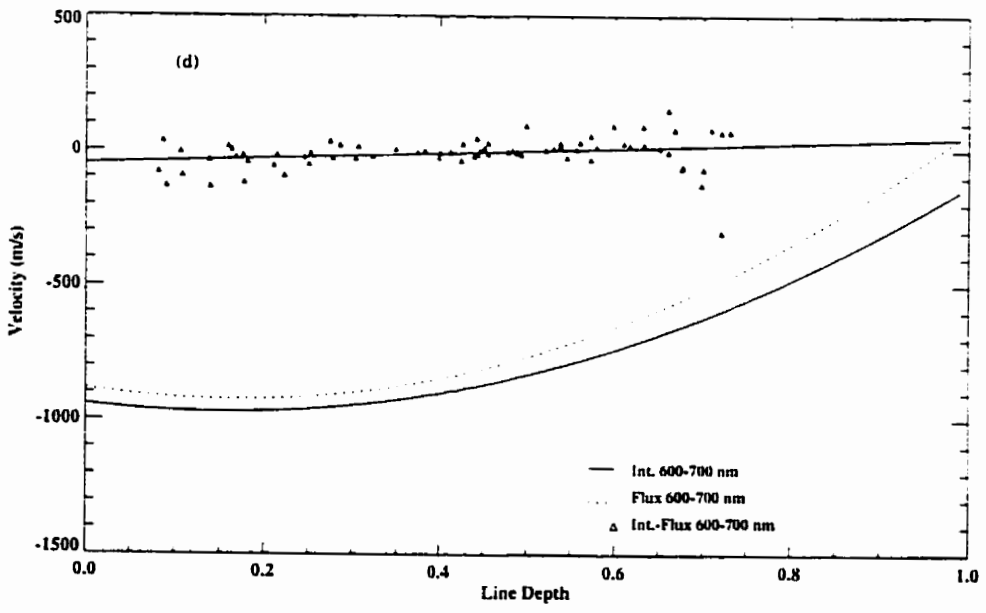
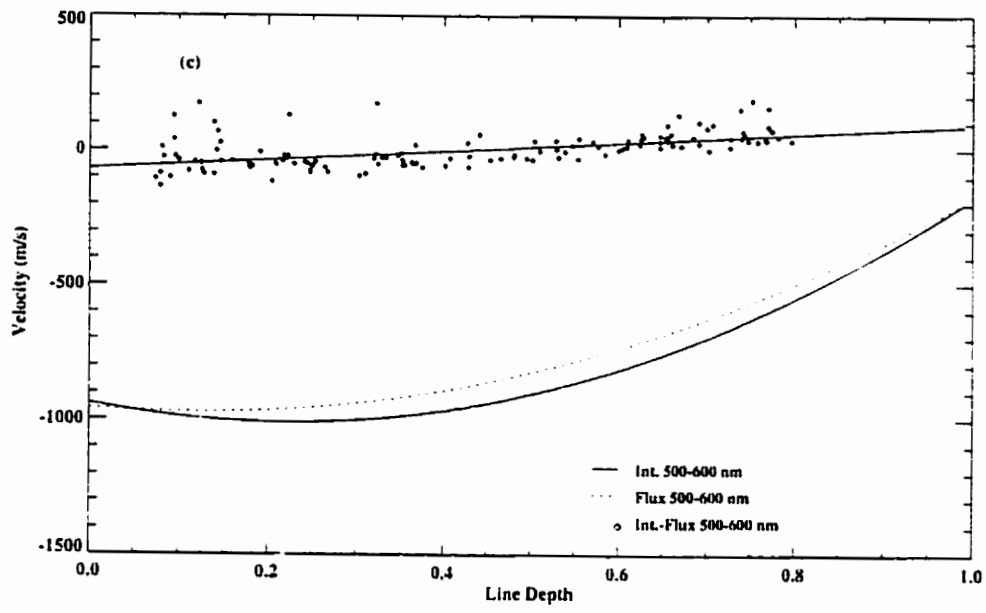


Figure 3.2: The sensitivity of the line-core shifts to line strength is shown in (a). All the line-core shifts from the visible intensity sample have been placed into three wavelength bins. There is a clear progression in wavelength across the distributions, with the bluest being flattest. Comparisons between the lines that are common between the central intensity and flux samples (b)-(d) for each of these wavelength bins illustrate the possible effects of limb-darkening. Parabolas are fit to the distributions for both samples, and are plotted in each frame for comparison. The differences between the central intensity velocities and the flux velocities are plotted, together with a linear least-squares fit



blue than in the red. For the central intensity observations, the radial line of sight allows for deeper penetration into the atmosphere than is possible for the flux observations. This means that the Doppler shift in line-core position for blue lines are more pronounced for the central intensity data than for the flux. This is especially the case when contrasting the weak lines with the stronger lines. The decrease in velocity toward the surface should be ballistic, and as such a slight increase in the physical depth of the atmosphere that is being sampled by weak lines will encounter a greater velocity change than a similar increase for stronger lines higher in the atmosphere.

Therefore, the slight change in the behavior of the distributions with wavelength shown in Figure 3.2 is understandable, but the key result is that the intensity and flux line-core distributions are remarkably similar. The central intensity observations span a relatively small area, with a diameter of 40 arc-seconds, which corresponds to approximately 500 to 800 granules. The strong similarity in the shape and scatter for the intensity and flux distributions shows that there are no significant statistical variations between the two samples, even though one is much larger in size. There is no evidence that the central intensity observations are statistically unstable.

Excitation Energy

In Chapter 2, we briefly discussed the possibility of a line-core shift dependence upon lower excitation energy (χ_l). Previous studies (Dravins et al. 1986; Nadeau 1988) have indicated the existence of this dependence; however, our results in Chapter 2 were inconclusive. In particular, we binned the line shifts in both wavelength and line depth to eliminate any confusion from these factors, and the resulting distributions showed no clear indication of a residual dependence upon the χ_l . A possible reason for this was the small number of points combined with the limited χ_l coverage within these bins. We concluded that if there were an energy dependence, it was smaller and secondary to the wavelength and line depth dependencies. A larger sample of lines, and/or a greater range in energies is required to test for this dependence.

With this current study, we have a sample 1.46 times larger than in Chapter 2. In Figure 3.3 the lines are divided into the same bins as in Chapter 2, and least-squares linear fits have been applied. For all the linear fits shown in Figure 3.3, only one fit has a slope that is more than 2σ from zero - implying that there is little or no dependence for the line shifts over these energies. Of the twelve fits, five of them have slopes which are within one σ of zero. Even though the sample sizes are larger, the distribution of the features over the range of energies is not very smooth, and the fits are highly uncertain.

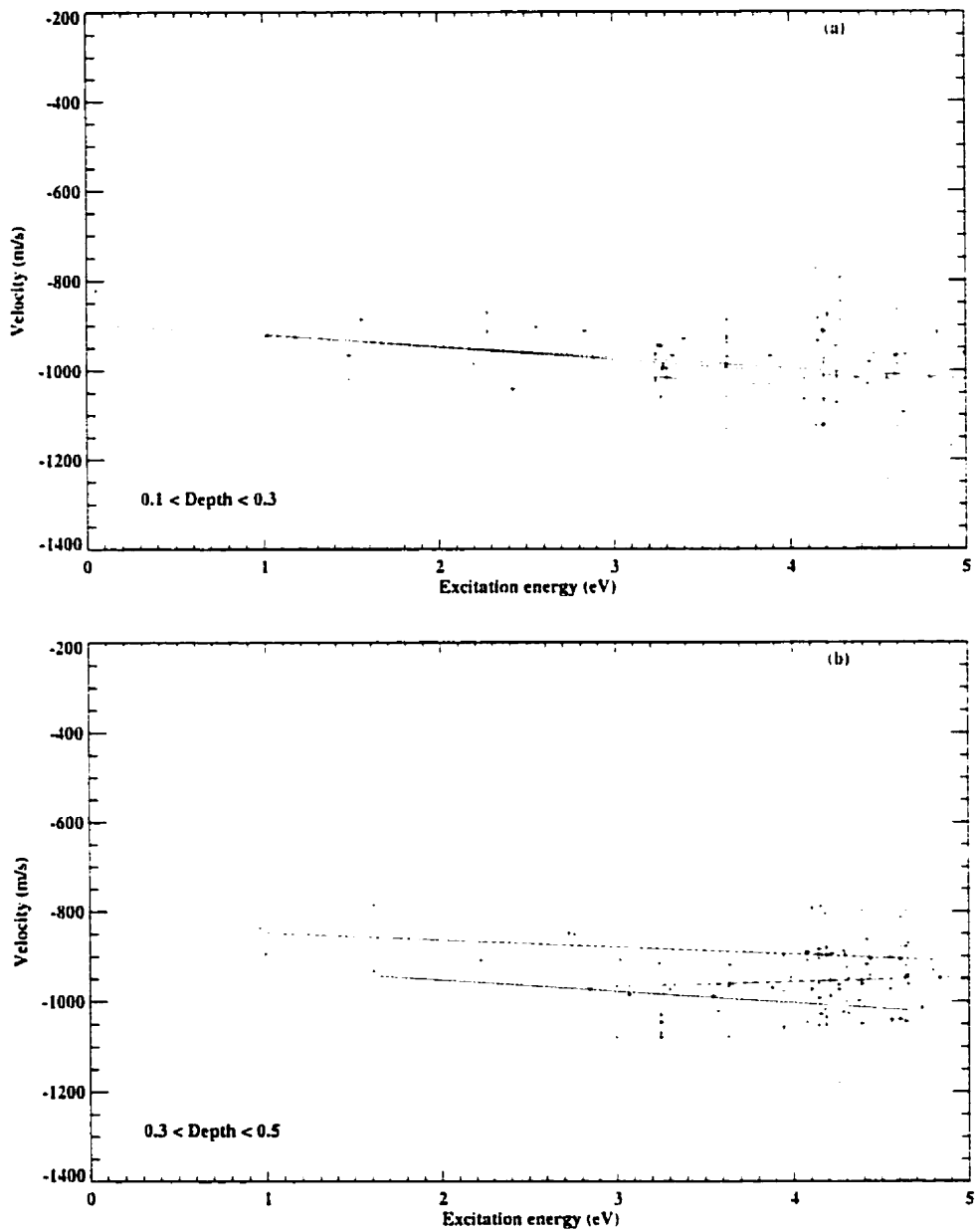
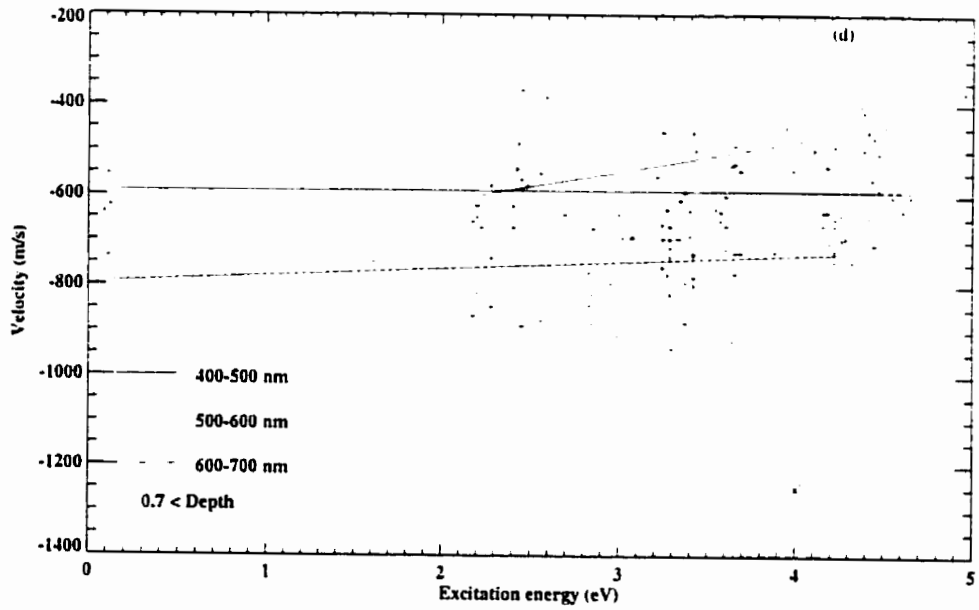
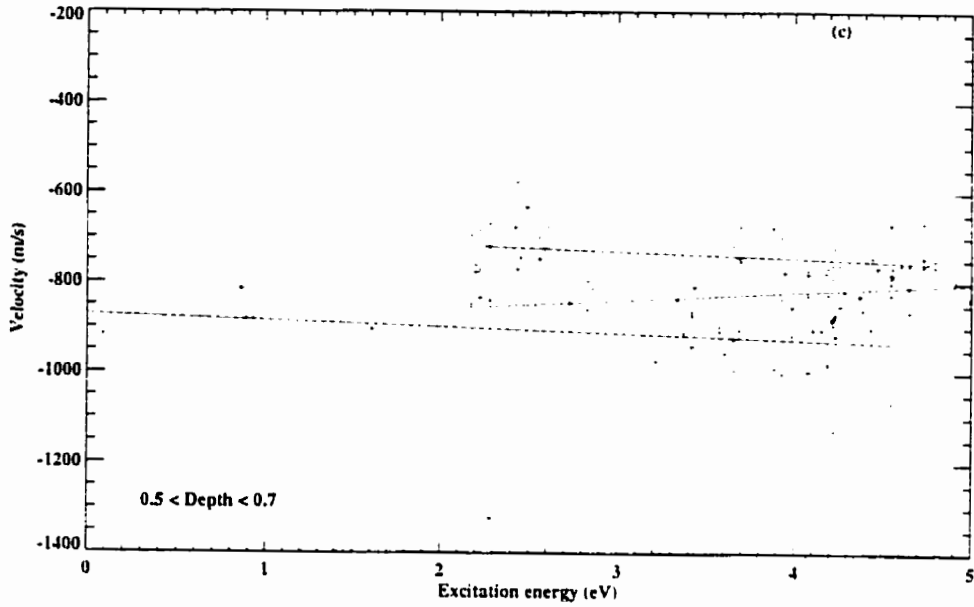


Figure 3.3: No clear line-core shift dependence upon χ_I was found for the Fe I flux sample in Chapter 2. Here the central intensity sample has been binned in both wavelength and line strength, and then a linear least squares fit is applied. While there may be a slight dependence for some of the bins, none of the linear fits has a non-zero slope with 3σ certainty. Of the 12 fits shown, five have slopes within one σ of zero.



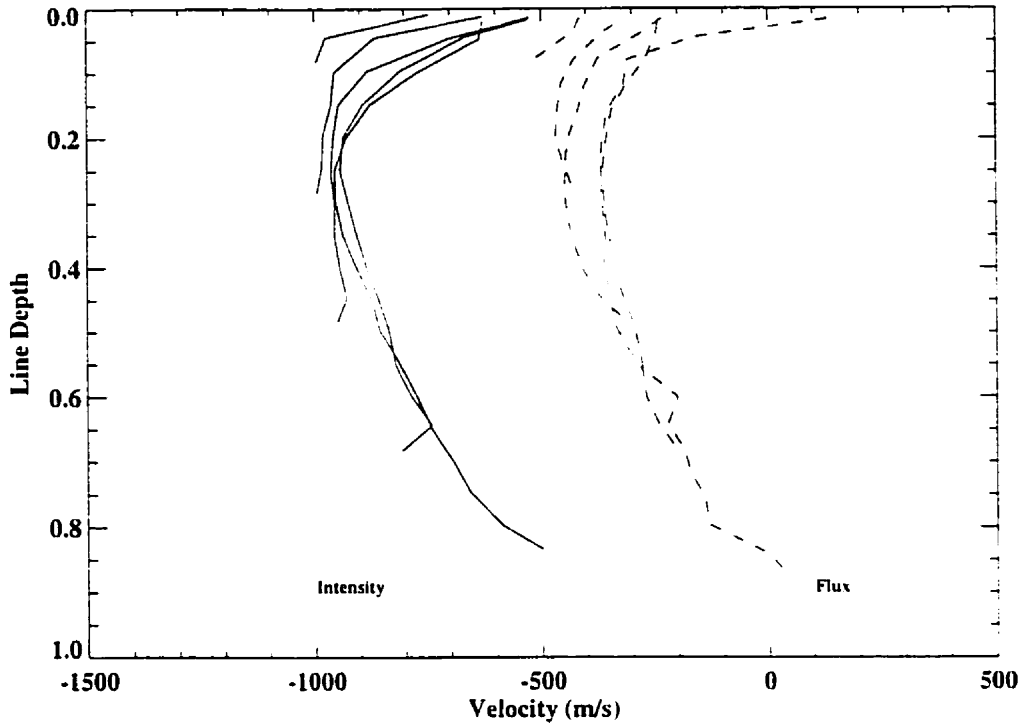


Figure 3.4: The median bisectors for the line strength bins from both the intensity and flux samples are shown. Superficially they appear very similar, however there are subtle differences in shape that reflect the effects of limb-darkening and rotation. The two sets have been offset in velocity for clarity.

Median Bisectors

Median bisectors (see Chapter 2 for details on how the median bisector is determined) for the central intensity data set show interesting differences when compared with those taken from the flux data set in Chapter 2. Figure 3.4 displays the median bisectors for each depth bin from both data sets.

Although the sets of bisectors are superficially similar, closer inspection reveals that the central intensity bisectors have a larger span in velocity, and the top curve in the 'C' shape of the bisector occurs closer to the continuum level. The weaker lines in the flux set have a more complete bottom portion of the classical 'C' shape for bisectors (Figure 3.5(a)-(d)).

The differences between the data sets are far more substantial when the median bisectors for the different wavelength bins are compared (Figure 3.6). While the trend with increasing wavelength is the same, it is far more pronounced with the intensity data. The median bisectors for the intensity wavelength bins show much greater spans in velocity and are much more distinct from one another than their flux counterparts.

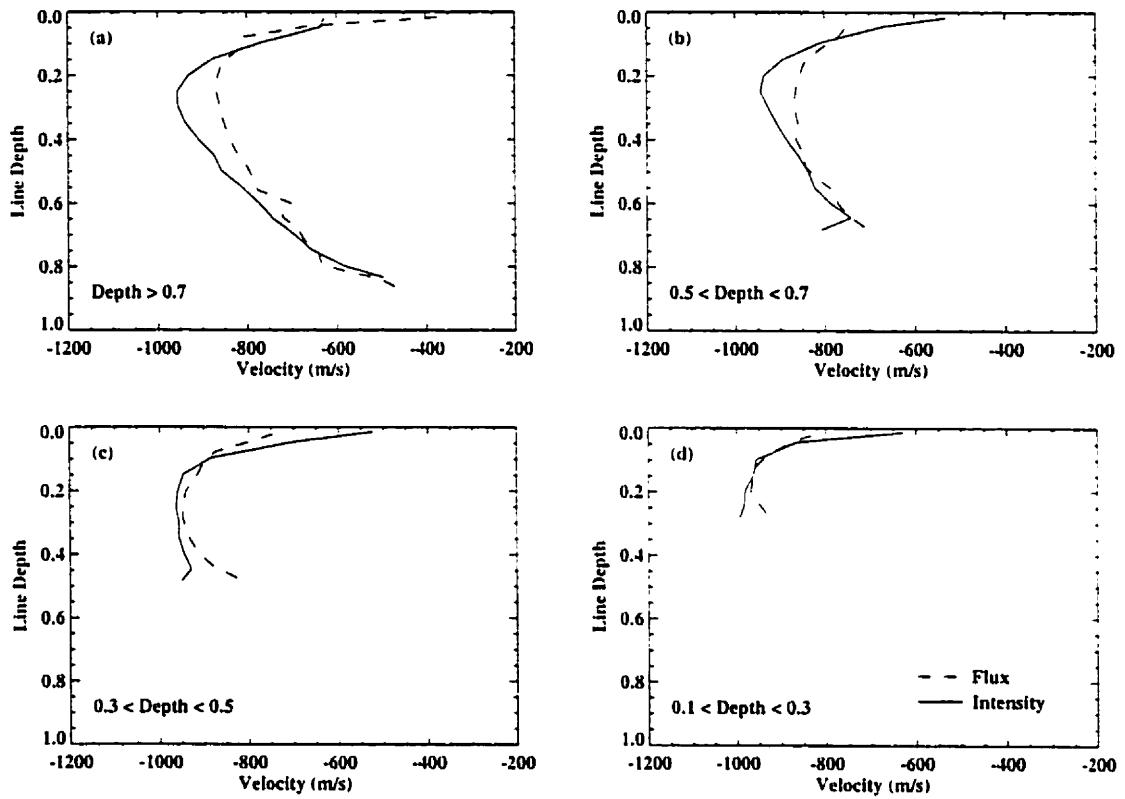


Figure 3.5: The median bisectors for the strongest depth bins from both the intensity and flux samples are superimposed (a)-(d). The central intensity median bisectors appear to have the larger spans in velocity, and the bend in the 'C' shape arises closer to the continuum.

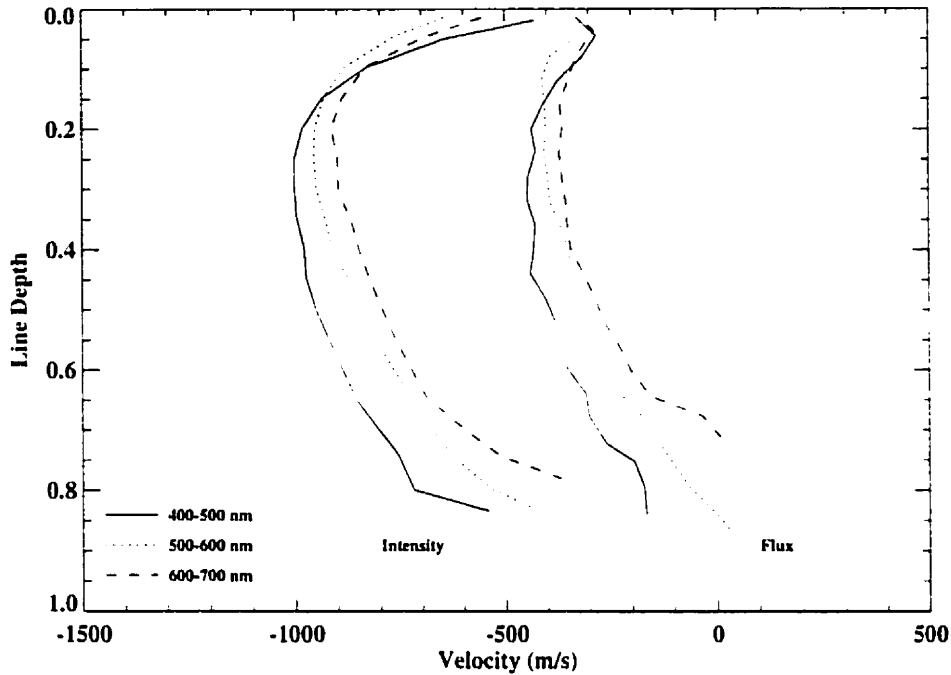


Figure 3.6: The median bisectors for each wavelength bin for the two samples. The intensity bisectors seem to more closely resemble the classical 'C' shape. Note how in both sets of bisectors, the bluest bin has substantially less of a curve than the other two. The two sets of bisectors have been offset in velocity for clarity.

The intensity bisectors more closely resemble the classic 'C' shape. This comes as no surprise since both rotation and off-axis radiation contributions to the line profile should flatten the bisector and smooth it out. It is also apparent that the bottom half of the flux median bisectors are more consistent with their intensity counterparts than the top halves of the flux median bisectors. All of this is consistent with and supports our interpretation of the differences between the central intensity and flux line-shift distributions. If Figure 3.5(a) or (b) is rotated 90°, the difference between the intensity and flux median bisectors mimics the differences between the flux and intensity line-core shift distributions in Figure 3.2. However, the differences between the flux and intensity median bisectors are greater than the differences between the flux and intensity line-shift distributions. The line-shifts appear to be a more robust diagnostic of convection than the bisectors.

3.4.3 Ti I

Ti I lines are found throughout the visible spectrum with a wide array of strengths. From the available line list (Forsberg 1991) 111 candidate lines were selected. Unfortunately, the lines are subject to isotopic shifts and the accuracy of the original linelist is not known. The Ti I lines are

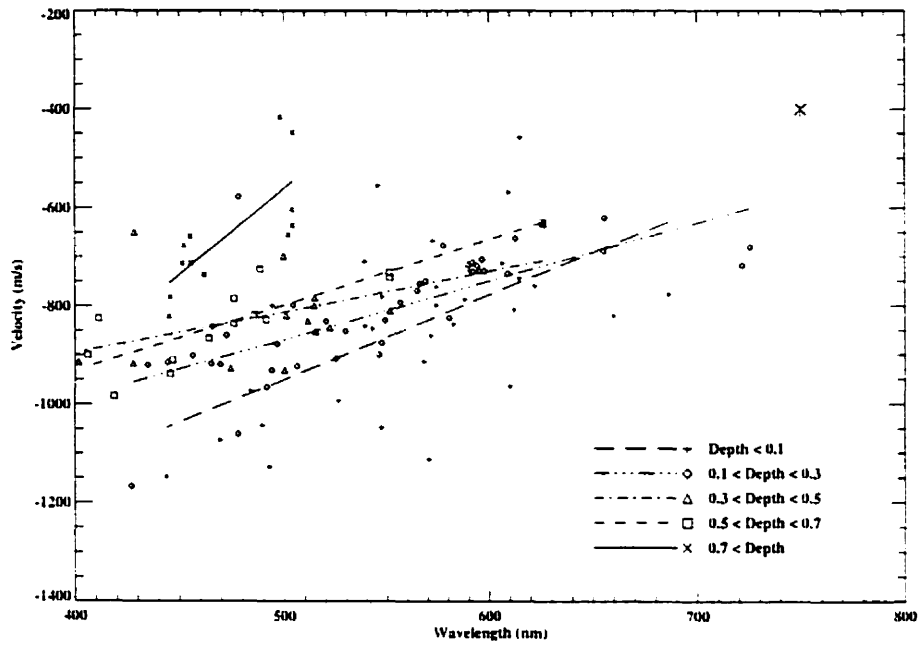


Figure 3.7: Ti I line-core shifts are binned by line depth and fit using linear least squares. The behavior appears similar to that of Fe I (Figure 3.1), however, the slopes of the fits are steeper. Note that the scatter within each bin is much larger and the wavelength coverage for the stronger lines is substantially less than is seen for the Fe I distributions.

included here as a complement to Fe I, and are acknowledged to be less accurate. As was done with the Fe I, the Ti I lines have been examined in terms of their dependence upon wavelength and line depth.

Wavelength

The Ti I lines have been binned by strength to isolate the wavelength dependence. As Figure 3.7 shows, there is a fairly clear dependence upon wavelength for the different line depth bins. The Ti I lines seem to show similar behavior to the Fe I lines. However, the Ti I lines show much greater scatter, especially for the weak lines, and the strong lines do not have wide coverage over the wavelength range. Unlike the Fe I sample, the slopes of these distributions do not appear to be decreasing with decreasing line strength.

Line Depth

As was found with the Fe I sample, there is a clear dependence upon line depth. Figure 3.8 displays all 111 Ti I lines binned by wavelength. Surprisingly, the different bins are quite distinct from one

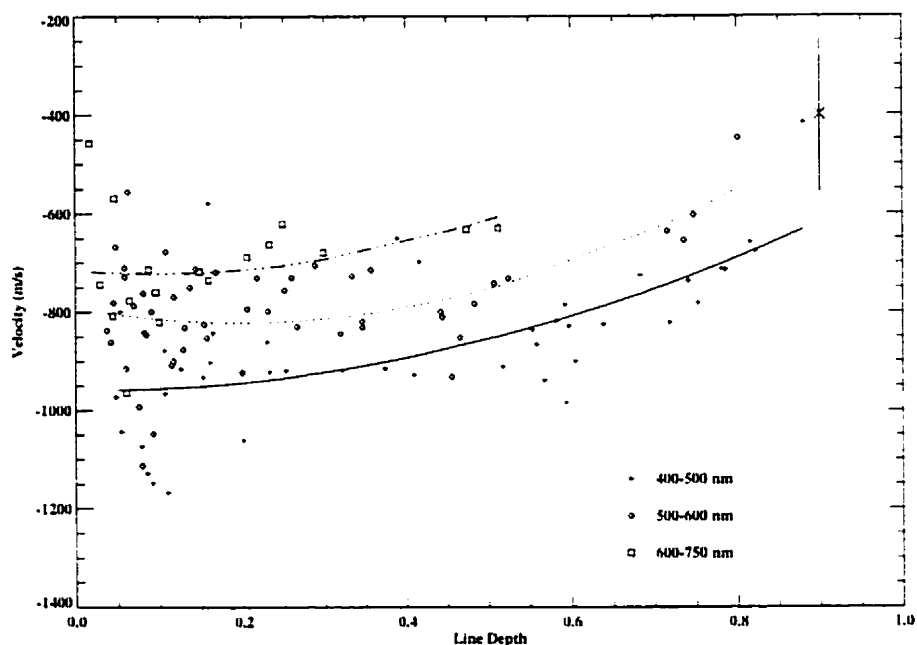


Figure 3.8: The Ti I line-core shifts are binned by wavelength. The behavior seen here is quite similar to that of the Fe I distributions. However the scatter within each wavelength bin is substantially larger. As is seen with the Fe I sample, the fit to the blue bin is flatter.

another, and do not overlap nearly to the same extent as their Fe I counterparts. The parabolic fits in Figure 3.8 are applied to bins in which the internal scatter is fairly large and the coverage in line depth is not complete. The longest wavelength bin has very few lines stronger than 50% of continuum.

The slopes of the three line depth/velocity distributions are all substantially shallower than their Fe I counterparts. Given the poorly defined limits upon the accuracy of the line positions and the possible effect of isotopic broadening and shifts, the differences between this sample and that of Fe I may not be very significant.

3.4.4 Summary

The line-shift distributions derived from intensity spectra in this chapter are very similar to the distributions derived from flux spectra in Chapter 2. We find that the dependence on wavelength is actually smaller for the intensity data because of the reduced contrast. The dependence on line depth is almost identical for the two data sets, and any dependence on excitation energy is marginal for both intensity and flux. The intensity median bisectors have a slightly larger amplitude and sensitivity to wavelength, however, the differences are not large, and do not greatly affect the

bottom portions of the line bisectors. We conclude that the effects of limb darkening, the limb effect and modest rotation do not significantly degrade the use of line-core shifts derived from flux spectra as convection diagnostics.

3.5 Intensity Spectra

A second goal of this chapter is to use the additional intensity spectral atlases described in §3.2.1 to follow the behavior of the line shifts from the visible into the infrared.

We found that the KPNO Near Infrared atlas contains 262 Fe I lines meeting our selection criteria. From the ground-based infrared atlas, an additional 293 Fe I lines were selected for study. Unfortunately, in the infrared there are few lines stronger than 50% of the continuum. In addition, the positional uncertainties increase substantially. To constrain our errors, we have limited our sample in the infrared and near-infrared to only those lines with positional uncertainties (Nave et al. 1994) less than 0.005 cm^{-1} . An additional complication is the presence of telluric absorption. While the weaker telluric lines have been removed (Livingston & Wallace 1991), the act of removal degrades the signal-to-noise ratio, and there are large regions where the absorption was so severe that the spectrum could not be salvaged.

The space-based infrared atlas does not suffer from telluric absorption, but the positional uncertainty of the Fe I lines increases with wavelength. We selected 122 lines of Fe I for use here.

3.5.1 Wavelength Dependence

Continuing from the visible sample, there is a clear dependence of the line-core shifts upon wavelength through the near-IR and into the infrared, as shown in Figure 3.9(a)-(c). The collections of intensity line-shifts have been set to a common velocity scale and the individual strength bins for each of these sets has been fit linearly. In general, the line strength bins in the visible exhibit a stronger dependence upon wavelength than their counterparts in the near infrared and infrared. The wavelength/velocity distributions for the stronger lines (those with depths greater than 0.3 of the continuum) have shallower slopes in the near infrared than their counterparts in the visible, and lines stronger than 50% of continuum are scarce in the infrared. While the velocities for the weak and medium strength lines do not have as steep a dependence as the stronger lines, they still display both a sensitivity to wavelength and a decrease of that sensitivity at longer wavelengths. The decrease in this sensitivity for the weaker lines is less dramatic than that seen for the medium

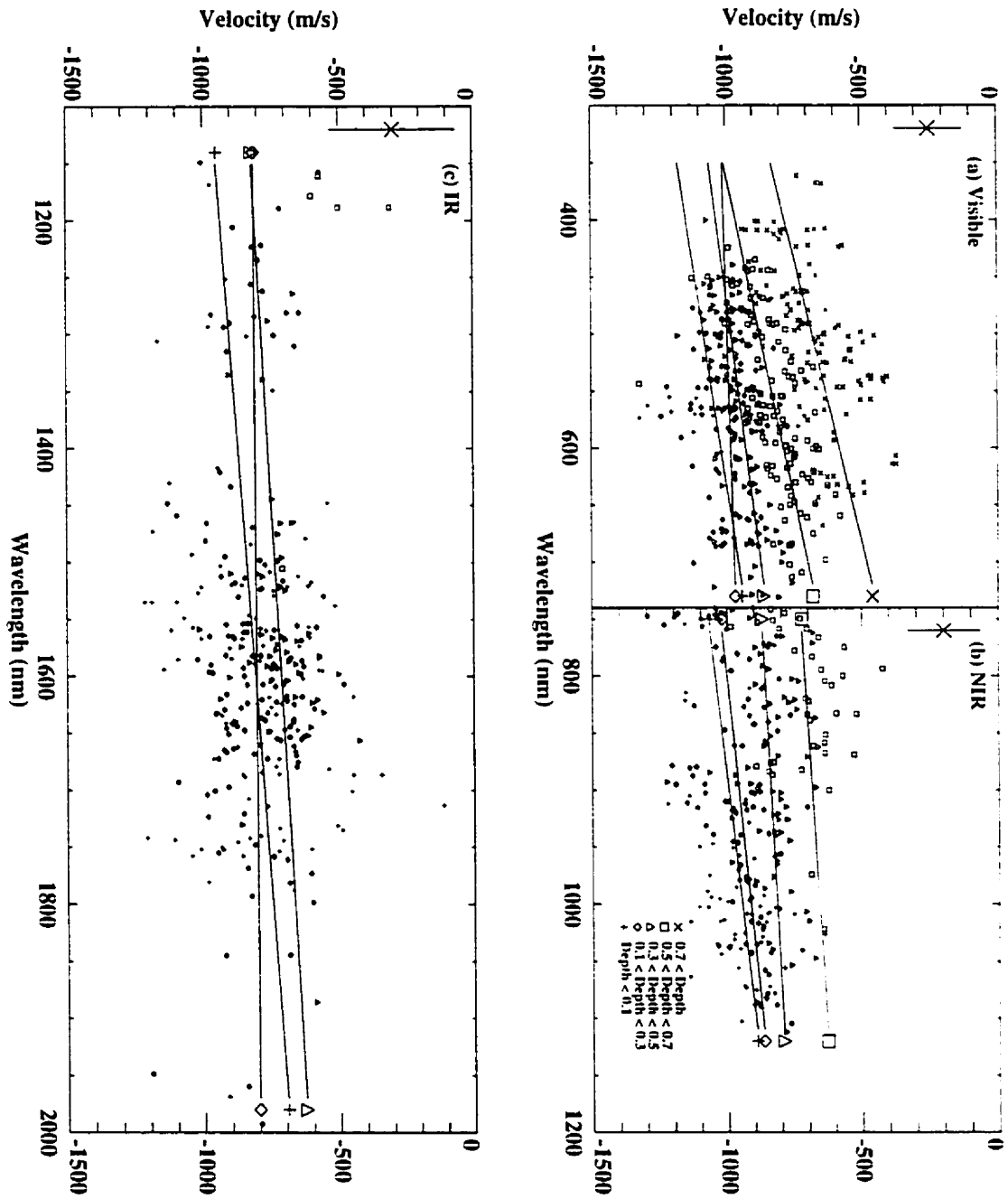


Figure 3.9: The line depth/velocity shift distributions for Fe I in the visible (a), the NIR (b) and the ground-based IR (c). The samples are binned by line depth and then linear least squares fits are applied. There is a clear dependence upon wavelength for each one of the bins in the visible and NIR, however for the NIR bins the slopes are shallower than for the similar bins in the visible sample. The fits to the IR bins (c) are much shallower, and exhibit far greater scatter than their visible and NIR counterparts.

and strong lines. These weaker line classes exhibit scatter that is substantially higher in the infrared than in the visible. The different strength classes in 3.9(c) do not appear nearly as distinct from one another as they did at shorter wavelengths in 3.9(a) and 3.9(b). This increase in scatter can be attributed to the increase in positional uncertainties at these longer wavelengths (recall that $\sigma \approx \Delta\nu/\nu$), which is four times larger at 2 μm than at 500 nm.

The wavelength sensitivity can be combined with that of line depth, as shown in Figure 3.10(a)-(c) where the lines in the visible (a), NIR (b) and ground-based IR (c) samples have been binned by wavelength and displayed against line depth. Each wavelength bin has been fit using a least-squares parabola. For both the visible and NIR samples, the individual bins are relatively distinct, with the parabolic fits offset from each other and decreasing in line-shift monotonically with increasing wavelength. However, the differences between these fits are smaller in the NIR than in the visible, which is consistent with the decrease in wavelength sensitivity shown in Figure 3.9.

In the ground-based IR, Figure 3.9(c) shows that there may still be a small dependence upon wavelength for the line-core shifts, and this is reflected in Figure 3.10(c). All four wavelength bins have been fit using parabolas. If only the weakest lines are considered, there is a progression from the blue to the red, consistent with what was observed with the other samples. The reddest bin (1700-2000 nm) is an exception to this, although it has the smallest number of lines and the greatest uncertainties in line positions. In addition, the longest wavelength bin has no lines deeper than 45% of continuum. As in the near-infrared sample, the parabolic fits to the distributions for the different wavelength bins become flatter at longer wavelengths.

3.5.2 Line-Depth Dependence

In the near infrared (NIR), the overall shape of the distribution of line-core shifts with line depth is very similar to the visible distribution (Figure 3.10(a)-(b)). The visible sample has a slightly steeper velocity/depth distribution than the near infrared sample; however, the visible sample contains many more strong lines than the NIR sample. The uneven distribution in line strengths between the two samples probably accounts for much of this difference.

When the near infrared lines are binned by wavelength, the different parabolic fits display the same behavior as seen in the visible, with the longer wavelength bins having smaller blueshifts. In the visible the depth/velocity distributions are steeper for the longer wavelengths, whereas the opposite was found in the near infrared: the longer the wavelength the shallower the depth/velocity distribution. Although this may result from the uneven distribution of line strengths (there are

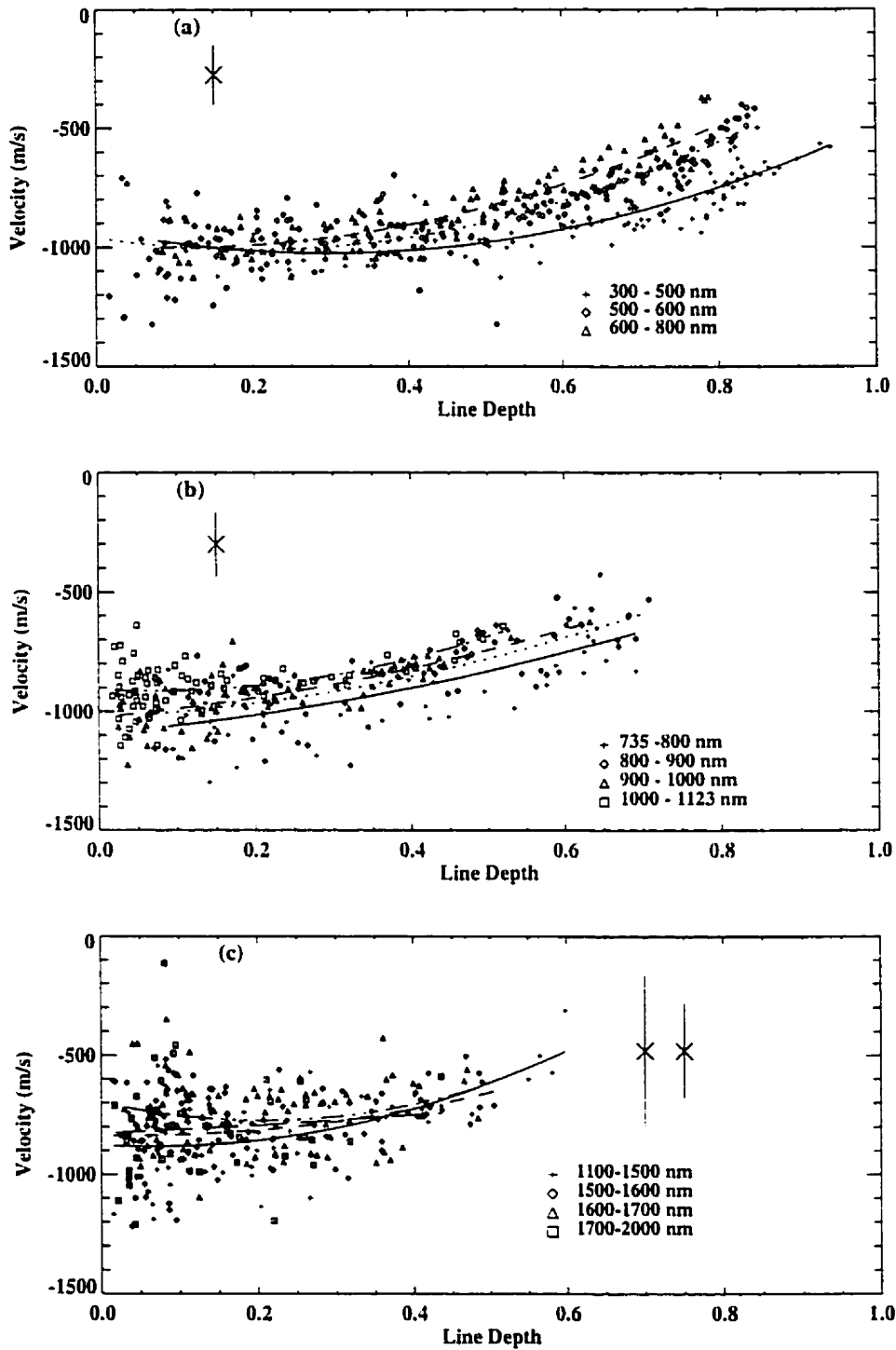


Figure 3.10: The velocity/line depth distributions for all three ground based samples of Fe I lines: visible (a), NIR (b) and IR (c) samples. For the NIR (b) the lines have been placed into four different wavenumber bins. As was found in the visible, at a particular depth there is a monotonic progression in velocity with wavelength. For the IR sample (c) there is still a dependence of line-core shifts upon depth, however the scatter is much larger than in the near infrared or visible. The error bars in (c) display the positional uncertainty for the line-shifts for lines at 1100 nm and 2000 nm.

fewer strong lines at longer wavelengths) the trend holds for the medium and weak lines. The NIR distributions overlap more than the distributions in the visible and the fits in the NIR have very similar slopes for both the weak and medium strength lines. This behavior is found for the visible samples even when the strongest lines (those with depth ≥ 0.7) are ignored in the fitting process.

Two mechanisms are responsible for the change of the slope with increasing wavelength. One is a contrast effect. The light at shorter wavelengths is dominated by the higher temperatures of the upwelling granules; while at longer wavelengths the contrast between the lanes and granules is less, increasing the relative contribution from the lanes, which flattens the distribution. The second effect is the variation of the continuous opacity, which has a broad maximum near $0.85 \mu\text{m}$, decreases to a minimum at $1.6 \mu\text{m}$ before increasing again at longer wavelengths. Near the opacity maximum the observer is seeing higher in the atmosphere where the opacity gradient with depth is less than in the visible and at longer wavelengths where the observer sees deeper (see §3.5.4 and Figure 3.12). This means that in the NIR, the observer is actually seeing deeper into the photosphere at longer wavelengths, which is the opposite of what occurs in the visible. Not only are the velocities different at these depths, but the relative areas of the granules and lanes change with physical depth. These changes in area also change the relative contributions from the granules and lanes. At shallower depths, the relative area occupied by the up-welling material is smaller than at higher altitudes - the simulations of Stein and Nordlund (1998) demonstrate that conservation of mass requires that the up-welling material overturn rapidly into largely horizontal motion near the upper boundary of the simulation box. This results in rapid changes in the relative areas covered by the granules and lanes. This explains why the shapes of the distributions in the two data sets display opposite trends.

As seen for both the visible and NIR samples, the ground-based IR has a clear dependence of the line-core shift upon line depth. The line-depth dependence is apparent in Figure 3.10(c), even though the scatter is much higher than in the previous samples. The points in Figure 3.10(c) have been binned by their wavelengths, and the majority of the lines lie between 1500 and 1800 nm. If the binning is done in equal wavelength spans, the number of lines in the reddest and bluest bins will be very small. To obtain the most meaningful statistics, the bins have been selected to be of comparable size, without averaging over too large a wavelength span.

3.5.3 Excitation Energy Dependence

Previously, (§3.4.2 and Chapter 2) the dependence of the line shifts upon excitation energy in the visible was determined to be weak at best, and questionable when other parameters are taken into account. This is also found to be true for the line-shifts in the NIR and ground-based IR samples, almost all of which have $\chi_l < 6.5$ eV. However, the 2 to 5 μm region contains lines with excitation energies ≥ 6.5 eV, and these lines show a different behavior. Figure 3.11 shows the distribution of line-core shifts with line depth (a) and excitation energy (b) for the 122 Fe I candidate lines between 2 and 5 microns, 30% of which have $\chi_l \geq 6.5$ eV.

As explained earlier, the positional uncertainties for the Fe I lines increase with wavelength. Thus, for wavelengths longer than 2 μm , the distributions of line-shifts display much larger scatter and prove to be more difficult to analyze. This is illustrated by the pairs of error bars displayed in Figure 3.11(a)-(b), representing the growth in the positional uncertainties for individual points at longer wavelengths.

Figure 3.11(a) shows the line-core shifts as a function of line depth for three energy bins of the space-based IR atlas. In the lowest energy bin, the depth/velocity distribution is similar to the KPNO infrared and NIR atlases. Most of the lines are weak, but there is still a shallow dependence upon line depth. The middle energy bin (6 to 6.8 eV) also shows some depth dependence, but its behavior is quite different from the lower energy bin. All of these lines are relatively weak, so the depth dependencies may be questionable, especially considering the positional uncertainties and the large scatter. The third bin ($\chi_l \geq 6.8$ eV) is too small to fit meaningfully.

In Figure 3.11(b) the line-shifts are examined as a function of χ_l . For those lines with $\chi_l < 6$ eV, the distribution and behavior is similar to what was found for the other spectral regions: little or no dependence. However, at higher energies, the behavior of the line-shifts changes dramatically. At the highest energies (≥ 6.8 eV), the line-core positions differ from the typical values by approximately $+1000 \text{ ms}^{-1}$. For slightly lower χ_l , between 6 and 6.8 eV, the line-core shift distribution appears to “dip” and then rise back up to very high positive values for the line shifts over a very small range of energy. Previous studies (Dravins et al. 1981; Dravins et al. 1986) indicate that the sizes of the line-shifts increase for those lines with higher χ_l , and lines of a given strength are more likely to have a larger blueshift if they have a larger χ_l . The lines with χ_l between ≈ 6 and 6.5 eV are consistent with this. However, those lines with even higher energies behave in the opposite manner. The most extreme line-shifts belong to those lines with $\chi_l \geq 6.8$ eV: they are relatively

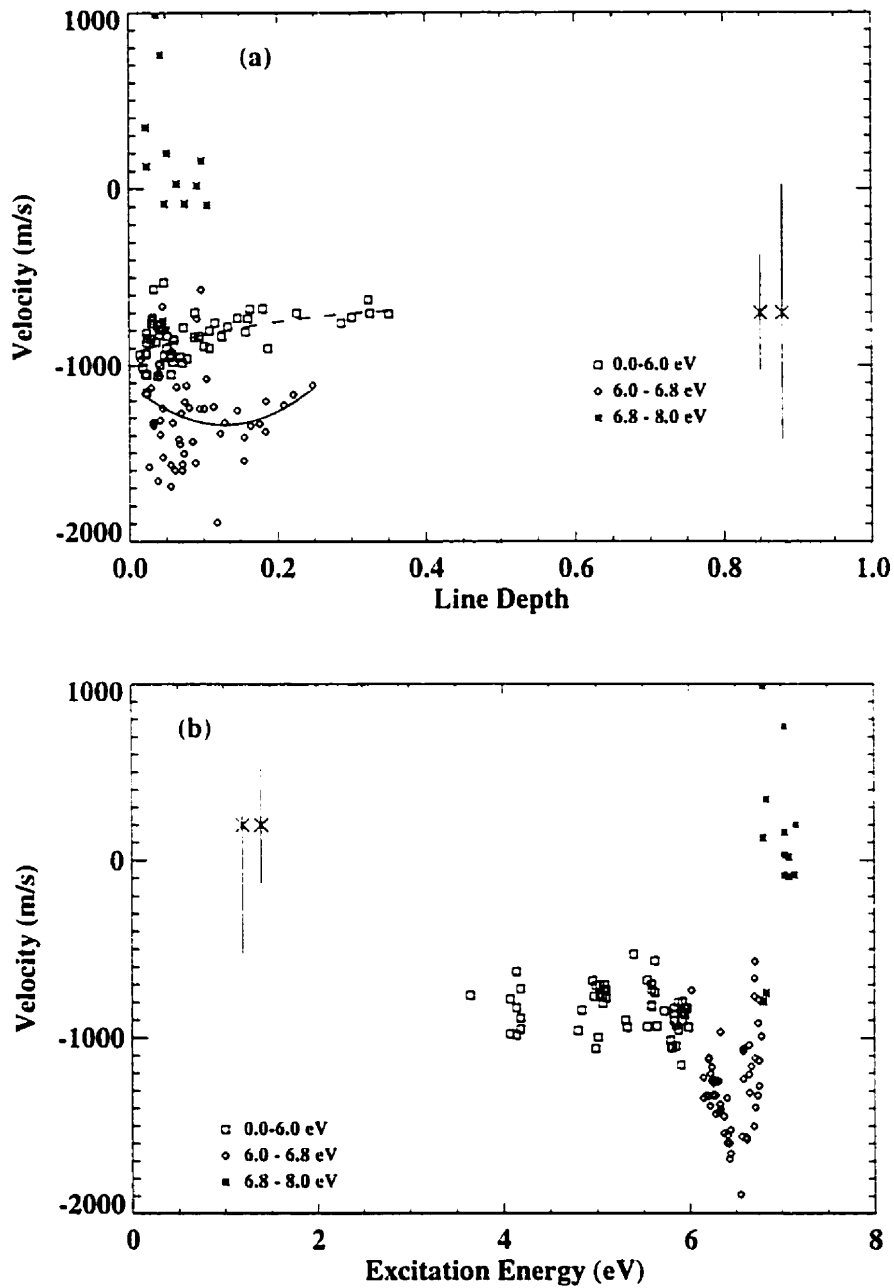


Figure 3.11: The distribution of Fe I line-core shifts with line depth (a) and χ_I (b) for the ATMOS sample. The data set can be divided into three populations, although this is not explained by either wavelength or line depth sensitivities. For the longest wavelengths, the positional uncertainty this far into the infrared almost overwhelms the line depth dependence (a). This is further complicated by the unusual behavior exhibited by the lines with $\chi_I \geq 6$ eV (b). Some of the more extreme behavior may be spurious. Note that almost all of the Fe I lines for the other spectral regions have χ_I less than 6.5 eV. The error bars demonstrate the change in the positional uncertainty for individual line-shifts. Recall that $\sigma \propto \lambda$.

weak, found near $4 \mu\text{m}$ and many have similar multiplet numbers (of the 11 extreme line-shifts, 4 are from multiplet number 2781 and 2 are from multiplet number 2782). If the line-shift velocity is plotted as a function of multiplet number, the distribution is strikingly similar to that in Figure 3.11(b).

It is worth noting at this point, that the typical uncertainties in the line positions are quite large here, between 330 and 730 ms^{-1} depending upon the wavenumber. The majority of the lines with $v_l \geq 6.5$ are found at smaller wavenumbers, so the uncertainty in their positions is quite significant.

The reason for this behavior with v_l is not immediately clear. These energies are much closer to the ionization energy, and may be subject to pressure effects (Nave, personal communication). In addition to this, undetected blends may also be a factor due to the paucity of accurate line lists over this spectral region. However, all suspected blends have been removed, and the region is not especially rich in lines. While some of the behavior observed may be real, some of it may also be spurious. The possibility of problems with the transition characteristics and line positions at these high energies is a potential avenue for investigation.

3.5.4 Line Formation Depth

The primary goal of this thesis is to investigate the utility of line-core shifts as diagnostics for observing convection in solar-type stars. To do this, a close examination of the line-shift distributions for the Sun is required. These distributions can be combined with atmospheric models to determine the approximate velocity structure of the Solar atmosphere. Ideally, the observed line-shifts would be combined with three dimensional hydrodynamic models to determine the altitude of the line-core formation over the surface of the Sun, simulating both the central intensity and flux observations. Unfortunately, this is not yet computationally feasible. The best available hydrodynamical models can only address areas much smaller than the $40'$ aperture of the central intensity observations. Multidimensional atmospheric models for solar-type stars are not yet feasible, and if the observations of other stars are to be compared with those from the Sun, the same type of model should be used for consistency (even though that model may in principle be less physically correct.) Due to computational limitations, the stellar models are largely limited to one-dimensional simulations - which are widely used and are currently the standard in the astronomical community.

Here, the Atlas 9 suite of programs (Kurucz & Avrett 1982) and a solar model atmosphere are used to compute more than 240 test lines between 400 and 2500 nm , spanning line depths ranging from 10% to 95% of continuum. This has been done using both a solar flux model and a central

intensity model. The *approximate* physical height of each line core is defined to be where $\tau_\nu = 2/3$, referenced to the location of Rosseland $\tau = 2/3$. The strengths and positions of the lines are varied by changing the input $\log gf$ and wavelengths. These theoretical lines are then binned in depth and wavelength using the same criteria as the observed Fe I lines. Obviously, these altitudes of formation are only approximate when compared to the much more realistic spatial resolution obtainable with multidimensional models. However, they do provide an **average** altitude of formation for the line cores, which provides some insight into the velocity structure of the Sun and facilitates any comparisons that may be made to the flux observations of other stars. The solar flux model used includes limb-darkening affects in the determination of the height of line formation.

Changing the wavelength changes the continuous opacity, which then changes the atmospheric layers probed by the spectral lines. Figure 3.12 displays the physical heights corresponding to each of the line-strength classes as a function of wavelength for the central intensity lines. The error bars for these bins represent the physical height ranges sampled by the simulated lines making up the bins. The weakest lines clearly show the minimum of the continuous opacity at 1650 nm. The lines in the medium-strength bin (30-50% of continuum) are not as sensitive to the continuous opacity as the weaker lines. While weak lines sample very similar physical heights over all wavelengths, for the medium and stronger lines there is a *clear* shift to greater physical heights in the atmosphere at longer wavelengths. For example, a line with a strength 60% of continuum at 1000 nm samples the same physical region as a much stronger line at 500 nm. This explains the change in the slopes of the line-depth distributions in Figures 3.2 and 3.10(a)-(c). These changes in physical height are much smaller for the weaker lines, which explains why the wavelength dependence is seen to decrease with wavelength in the IR. The paucity of strong Fe I lines in the IR means we are not sampling the higher physical levels of the atmosphere.

The average velocity for each line strength class and wavelength bin have been determined (50 in all) for all three Fe I central intensity samples and for the flux line-shift bins in Chapter 2. In Figure 3.13(a), these average velocities are matched with the corresponding simulated physical heights, where the error bars correspond to the standard deviation of the velocities for each bin. Those points without error bars correspond to bins with only a single velocity – and are obviously highly questionable from a statistical viewpoint, but they are also consistent with all of the other data. The different wavelength regions from the central intensity data are represented by different symbols, while all the flux data (430-680 nm) are represented by a common symbol. Three different linear fits have been applied: (1) to the entire set of central intensity points, (2) to the flux data

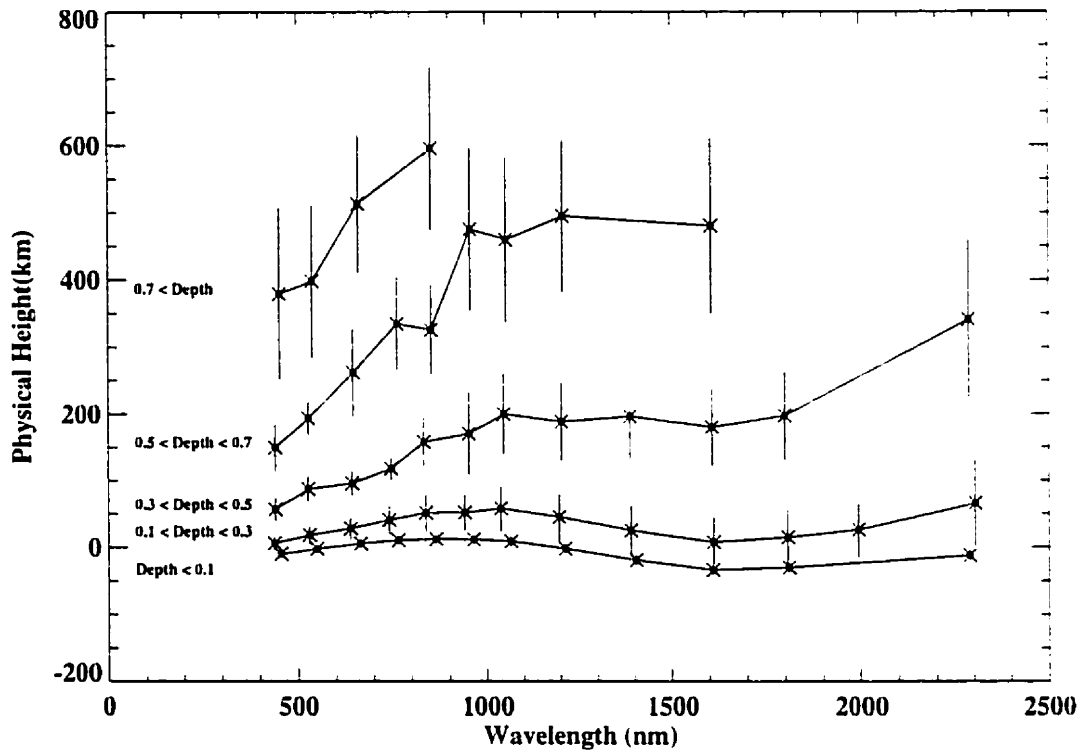


Figure 3.12: The physical formation height of the simulated Fe I lines binned by strength and wavelength, displayed as a function of wavelength. The error bars are the physical depth range sampled by each bin. Note the “kink” in the weak lines near 1650 nm - corresponding to the minimum in continuous opacity for the sun. Also note that the strong lines do not sample well outside of the visible.

points (430-680 nm) and (3) to the corresponding central intensity points (430-680 nm).

The convective velocity shifts show clear changes with physical height, however there seems to be a strong difference for the IR lines when they are compared to the NIR and visible lines. Most of the IR bins have smaller convective shifts than their bluer counterparts formed at the same height. This can be explained as a *contrast effect* between lanes and granules. At a given physical layer, the geometry between the granules and lanes should be the same at different wavelengths, but the contributions of photons to the flux from the lanes and granules will be different. At shorter wavelengths, the upwelling granule will contribute far more of the light than the lanes will, but at longer wavelengths this contrast will decrease. The lanes contribute redshifted photons, and at longer wavelengths the lanes provide a higher percentage of the photons to the net line profile, which results in a smaller net shift to the line minimum.

When the fit for the flux data is compared to the fits for the central intensity measurements, two trends are apparent: (1) the flux distribution is steeper than either central intensity distribution, with the lines that form at higher altitudes having smaller blueshifts than their central intensity counterparts and (2) the weak lines in the central intensity data have a larger scatter. The fit to the flux distribution would be expected to be steeper than the fit to the intensity measurements, which includes all the wavelengths in the study. This introduces the contrast effect that results in many of the weak lines having smaller blueshifts (as discussed above). However, if the intensity fit is restricted to the same wavelength span used for the flux fit, the fit to the flux data is still slightly steeper [(intensity slope)/(flux slope) \approx 0.88, within $\approx 2\sigma$ of 1]. This small difference is a result of a combination of limb darkening and the distribution of the stronger lines in the two different samples. The approximate altitude of height formation for the flux lines includes the off-angle contributions to the line profiles from steeper viewing angles and higher altitudes (but the same optical depth). While this changes the altitude of the lines somewhat, the effect is relatively small. In general, for theoretical lines of similar wavelength and strength, those computed using the flux model had a slightly higher average height of formation than their central intensity counterparts. However, because of the size of the line strength and wavelength bins, the region of the heights of formation for these bins overlap substantially. The heights of formation for all the line classes in the flux model were within 1.5 sigma of their central intensity counterparts.

The central intensity observations contain a relatively larger number of strong lines in the blue portion of the spectrum than the flux observations. Recall that for a given line strength in the visible, lines at shorter wavelengths have larger blueshifts. Since the central intensity sample has a

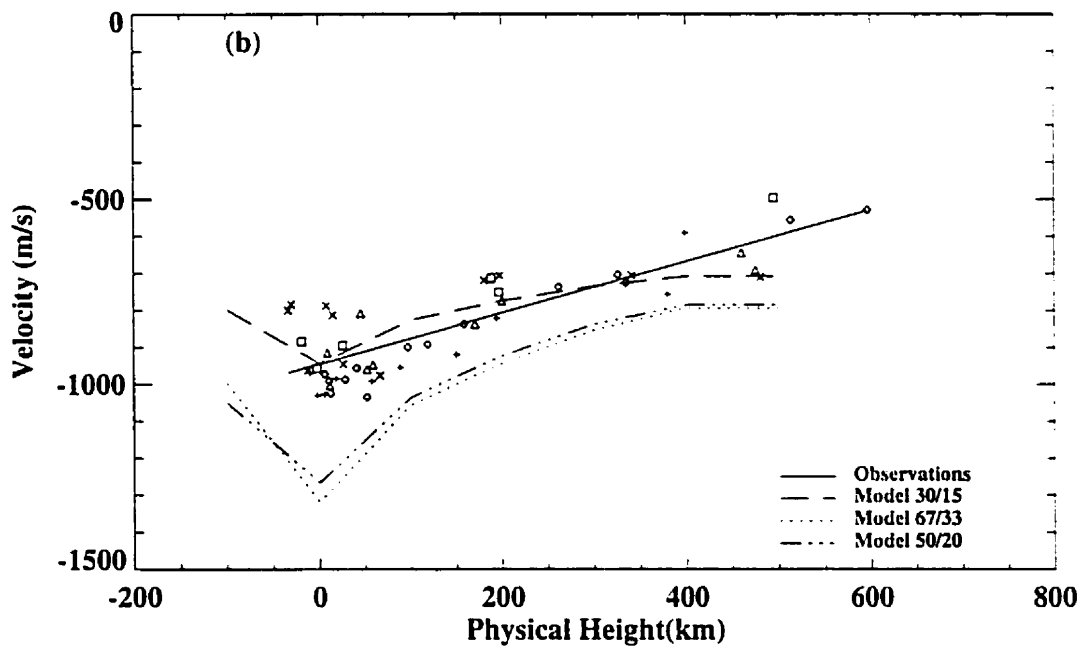
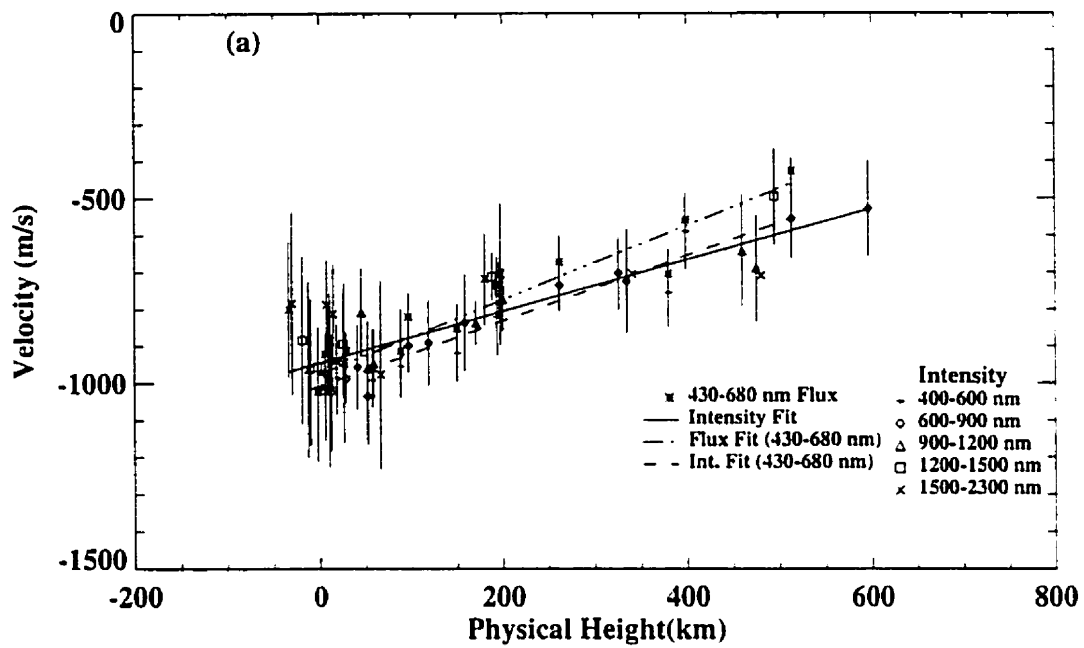


Figure 3.13: The convective velocity for each bin in wavelength and strength as a function of modeled physical formation height (a). The visible flux bins have a steeper slope than their intensity counterparts, which reflects both the effects of different distributions of line strengths with wavelength and the effect of limb darkening (see §3.5.4). The error bars are the standard deviation for the observed velocities in each bin. In (b) the observed velocities are compared to velocities taken from 3-dimensional hydrodynamic simulations that have been modeled using three different filling factors (see §3.5.4).

larger fraction of strong lines at shorter wavelengths than the flux observations do (14% vs. 10%), the average velocity for the stronger intensity bins are shifted a little further to the blue. As was pointed out in §3.4, the flux data actually exhibit a greater sensitivity to wavelength than the central intensity data because limb darkening affects the relative shifts for lines in the blue versus those in the red. We found that the red lines for a particular strength have a smaller shift in the flux data than in the central intensity data, and this effect was most pronounced for the stronger lines. This effect also steepens the distribution of velocities with altitude for the flux data, combining with the uneven distribution of strong lines with wavelength.

These approximate heights and their accompanying velocities can be loosely compared with the output of three dimensional numerical simulations. Stein and Nordlund (1998) have pointed out that for any particular optical depth, the surface of the Sun is actually corrugated in physical height; for optical depth of unity in the continuum the rms variations in physical altitude are ≈ 30 kilometers. However, while the heights of formation for these test lines have been determined using a one-dimensional hydrostatic model, a comparison with the predictions of a more complete three dimensional simulations should prove to be illuminating. The test lines for the central intensity velocities and the linear fit to the data are re-displayed in Figure 3.13(b) (the error bars have been suppressed for clarity). Also displayed in Figure 3.13(b) are three other sets of velocities derived from average up and down flow velocities in a snapshot from the simulations of Stein and Nordlund (Stein, private communication). These velocities have been modeled in three ways. Model 30/15 weights the average vertical velocities using the weighting scheme of Dravins (1990) where the upwelling and downdraft filling factors are 30% and 15% of the surface area respectively. Model 67/33 weights the velocities as 67% and 33%, consistent with the results of the simulations (Stein & Nordlund 1998), and Model 50/20 is a hybrid of the two, with filling factors of 50% and 20% respectively. All the sets of velocities include the gravitational redshift of 636 ms^{-1} . However, the true zero point for the solar velocities is not firmly established, since all of the source atlases had to be calibrated against each other.

An additional uncertainty in the comparison is the choice of origin for the physical height scales. Our one-dimensional model sets the zero point of the physical height where Rosseland $\tau = 2/3$, whereas the Stein and Nordlund simulation defines the zero point where $\langle \tau \rangle = 1$. The actual altitude difference between these two values is much smaller than the scale of the photosphere, since τ increases rapidly with depth. Our primary interest, however, is not whether the zero points of the different data sets match, but the agreement of the overall slopes. All three models have very

similar slopes to the linear fit to the observed velocities, especially for the medium strength lines, between 100 and 500 kilometers. If the filling factors for the granules are increased, the slope of the simulated velocities increase substantially. Using filling factors of 80% and 20% for the granules and lanes gives a slope ≈ 3 times larger than the observed slope. Figure 3.13(b) indicates that the three dimensional simulations of solar convection are consistent with our observed velocities. A more thorough analysis would involve reproducing these test lines using a three dimensional hydrodynamic solar atmosphere model.

3.6 Conclusions

Central intensity solar atlases have been used to study convective line-core shifts from 400 nm to beyond 5.5 μm . The behaviors found here are consistent with the results from Chapter 2 for the line-core shifts derived from the solar flux. In this study the Fe I lines in the visible and NIR spectral regions demonstrate clear dependencies upon both line strength and wavelength. In the IR, there is a clear sensitivity to line depth, but the wavelength dependence is substantially smaller. There may be an additional small sensitivity to χ_l , but this is seen only between 2 and 5 μm , and only for high values of χ_l . The χ_l dependence of the line-shifts in the visible is very slight and uncertain.

The differences between the flux and intensity distributions for the Fe I lines demonstrate some subtle limb darkening and rotational effects, but these differences are not substantial. The velocity/wavelength distributions for strong lines are actually steeper in the flux spectrum than in the central intensity spectrum, making convection easier to observe in the flux. This is a result of the uneven distribution of strong lines over the wavelength region combined with the off-axis contributions from the Solar limb. This has implications for the observability of the convection in the visible spectra of other solar-type stars.

The behavior of the Fe I distributions changes with the wavelength regime. At longer wavelengths, the wavelength sensitivity of the line-shifts decreases. This can largely be attributed to a decrease in the brightness contrast between the granular and intergranular lanes. However, there is a continuous opacity effect as well, since the slopes of the velocity/line depth distributions for the different wavelength bins change on either side of the peak in H^- opacity. While the decrease in wavelength sensitivity coincides with the overall decrease in solar continuous opacity, it is difficult to determine whether there is a relationship because the Fe I lines beyond the opacity minimum

have very significant positional uncertainties that may have obscured any sensitivity of line-core shifts with wavelength.

One-dimensional atmospheric central intensity model line simulations are used to establish the approximate physical height for where the line-cores form, and are consistent with our interpretation that the change in the wavelength dependence results from the decrease in contrast between the lanes and the granules combined with the change in the continuous opacity. Stronger lines rapidly change the atmospheric levels they sample as the wavelengths become larger. This explains why the slopes of the fits in Figure 3.2(a) increase at longer wavelengths. While the weaker lines still approximately sample the same physical layer, the stronger lines sample layers at substantially higher altitudes. The weaker lines continue to sample the same physical level, with any variations in this layer largely a result of the change in the continuous opacity. In the infrared the dependence disappears because there are not enough strong lines. At the same time, the weaker lines in the infrared exhibit a smaller blueshift than their red counterparts because of the change in the contrast between the granules and the intergranular lanes.

In many ways, the medium strength Fe I lines represent the best tools for probing convection. They are present at almost all wavelengths, are present in sufficient numbers for reliable statistics, are not greatly sensitive to noise and can sample a large range of physical depths depending on which wavelength regimes are used.

At longer wavelengths (beyond $4 \mu\text{m}$) there may be an additional sensitivity to χ_I above 6 eV. How much of this behavior is real remains an open question because of possible inaccuracies in the laboratory line positions. However, there could be some type of change in the line-core shift behavior for those transitions with χ_I greater than 6 eV.

Chapter 4

CO in The Central Intensity Spectrum of the Sun

4.1 Introduction

The infrared spectrum of the Sun provides a useful means of probing the convective structure of the solar atmosphere. There are both atomic and molecular species present that have well defined laboratory positions and sample a wide range of energy levels. An additional bonus is the comparatively low density of lines, which decreases the potential effects of line blending. The continuous opacity reaches a minimum in the near infrared (the H^- minimum at $1.65 \mu\text{m}$) and then begins to increase at longer wavelengths. This change in the continuous opacity influences which layers of the atmosphere are sampled by the lines. To extend this technique to cooler stars, the infrared is the natural wavelength region to use because the visible spectra of cooler stars become overcrowded with lines as the molecular bands become more prominent at lower effective temperatures. Comparisons between these cooler stars and the Sun would then best be done using infrared lines.

The use of alternative species allows for a comparison to the Fe I results from Chapters 2 and 3. Previously, the dependence of the Fe I line-shifts upon wavelength was found to diminish substantially in the infrared and the dependence upon line depth becomes more uncertain; other species that are more prominent in the infrared allow a more thorough investigation.

Recent spectroscopic imaging (Uitenbroek 2000) of solar CO lines near $4.6 \mu\text{m}$ shows that strong CO lines have an inverted granular contrast, with the lanes appearing brighter than the granules. These observations are consistent with numerical simulations (Stein & Nordlund 1989; Stein & Nordlund 1998; Uitenbroek 2000), which show that when the uprising material in a granule en-

counters the steep density gradient of the overlying stable layer, the upflowing material expands in order to conserve mass. This rapid expansion cools the upwelling material and when the material coalesces over the lanes to begin sinking, the descending gas heats up due to compression. Multidimensional radiative transfer modeling of CO line formation indicates that the strong CO lines are formed near this inversion layer (Uitenbroek 2000). The reverse of contrast between the granules and lanes may influence the overall distribution of line core velocity displacements with line strength.

4.2 Methodology

4.2.1 Solar Intensity Spectral Atlases

The Solar Intensity Atlases used in this chapter are the same ones used in Chapter 3: the KPNO NIR atlas (Wallace et al. 1993), the KPNO IR atlas (Livingston & Wallace 1991) and the ATMOS IR atlas (Abrams et al. 1996). Details of all these atlases are found in §3.2.1. All three atlases are the results of defocused central intensity FTS scans of the Sun.

4.2.2 Line Selection

CN

The CN line positions in the infrared and near infrared have been taken from unpublished work by Rao and Davis (Davis, private communication). Details of the experiment and apparatus are unavailable. While the data are used here, they have been used with strong reservations and are intended solely as a supplement to the other, more stringently defined CO list.

CO

The infrared transitions for CO are probably the best known for all the diatomic molecules. The line positions used here are taken from the *ab initio* calculations of Goorvitch (1994). Goorvitch also provides the energies and quantum numbers for each line. The different isotopes of CO are also included in the Goorvitch data set, however this study is restricted to the dominant isotope, $^{12}\text{C}^{16}\text{O}$. Blending with the other isotopes does complicate the line selection process, and all those $^{12}\text{C}^{16}\text{O}$ lines close to lines of the other major isotopes in the Goorvitch line list were eliminated from the sample. As with the other species of lines in this study, apparent and suspected blends

were removed based upon visual inspection of the lines and comparison with the various atlas line identifications (see §2.2, §3.3).

It has also been shown that the CO fundamental ($\Delta v = 1$) lines are relatively immune to non-LTE effects, and their strengths are a fairly accurate reflection of the atmospheric temperature structure (Uitenbroek 2000b). However, the actual physical height of formation for these lines is not stable, but fluctuates with opacity. The temperature and density derived from the strength of a CO line do not directly correspond to one particular physical location in the solar atmosphere, but rather a range of heights that reflect both the spatial and temporal variations inherent in a real dynamic atmosphere (Uitenbroek 2000).

4.2.3 Errors

CN

As mentioned above, the laboratory line positions for CN are unpublished results from Rao and Davis (Davis, private communication). In the determination of the Dunham coefficients, a standard deviation of 0.0068 cm^{-1} is cited (Davis, private communication). If we use this as the potential error in the accuracy of the line position, combined with the calibration uncertainty of the atlas (see §3.2.2), we obtain positional uncertainties equivalent to velocities between 250 and 183 ms^{-1} in the NIR, and 335 ms^{-1} in the infrared (IR). However, at best this must serve as a lower limit on the potential uncertainty, because the standard deviation for the line positions derived from the determination of the Dunham constants was for a much larger set of lines (26722).

CO

The absolute positions of the CO fundamental and first overtone ($\Delta v = 1$ and 2) sequences are the results of *ab initio* calculations. However, many of the lines (383) have been observed using heterodyne laser calibrations at NIST¹. The agreement between the calculations and the observed line positions for these 383 lines are all less than 15 ms^{-1} , with an average absolute difference of only 0.26 ms^{-1} . The estimated uncertainties in the lines positions for the NIST observations are all less than 3.4 ms^{-1} , with an average uncertainty of 0.60 ms^{-1} . In the solar spectral atlases, all the CO features for a particular band are found in the same scan, and the uncertainty in the overall calibration is estimated at an upper limit of 100 ms^{-1} (see §3.2.2). Therefore, the combined

¹physics.nist.gov/PhysRefData/wavenum/html/spect.html

uncertainty estimate for any of these lines is 102 ms^{-1} .

4.3 Analysis

As was done in Chapters 2 and 3, the different distributions of line core shifts have been binned by common parameters: wavelength, line depth and (if warranted) lower excitation energy (χ_l). The transitions used here are the rotation-vibration bands. The vibrational and rotational state of a molecule are denoted by their respective quantum number; v and J ; both of which are integers. Changes in the vibrational state of the molecule are represented as Δv , and the changes in the rotational state of the molecule are represented as ΔJ . The possible vibration transitions for a particular Δv give rise to bands composed of transitions in rotation number. For example, there may be a particular line that results from a transition in the $\Delta v = 1 \ 5 - 4$ band with a value of $J = 100$. The vibration bands can be subdivided into branches, depending on whether the rotation quantum number is increasing or decreasing: $\Delta J = -1$ rotational transitions are the P Branch, $\Delta J = 0$ are the Q Branch and $\Delta J = 1$ are the R Branch. Thus a particular molecular rotation-vibration absorption line is specified by the change in the vibration quantum number (Δv), the upper and lower vibration quantum numbers (the band), the change in the rotation quantum number (ΔJ , or the branch) and the final rotation quantum number (J). Further specifications that can be made regarding these transitions relate to the nuclear spin directions and parity; however these distinctions are not necessary in this study.

4.3.1 CN

The Near Infrared

The 179 CN lines found in the near infrared cover a very small range in line core depth: the strongest line has a depth of only 15% that of continuum. However, because several different bands are present within this wavelength span, the behavior of the line core shifts between these groups may prove illuminating.

A total of four sequences were recorded: $\Delta v = 0$ through 3, although the last two sets were very poorly sampled. The first band (0-0) had 57 candidate lines, the second set of bands (2-1, 3-2, 4-3) had 111 candidate lines. The two sequences were very similar in strength, however they occupy very different wavelength regions, and their average line core shifts are different: -550 ms^{-1} versus -786 ms^{-1} . Both samples exhibit large scatter for individual lines, and there are no discernible

internal trends within the samples.

Infrared

There are only 59 CN candidate lines in the KPNO IR atlas. All of these lines are weak, with only one feature having a line core depth of greater than 10%. However, it is possible to compare the average line core shift with the CN lines found in the NIR atlas. Here two sequences are sampled, the $\Delta v = -1$ and 0. When the infrared KPNO atlas is calibrated to a common wavelength scale with the NIR atlas, it was found that the $\Delta v = -1$ sample had an average line core shift of -443 ms^{-1} (54 features), whereas the $\Delta v = 0$ sample (4 features) had an average line core shift of -584 ms^{-1} , consistent with those found in the NIR sample of -550 ms^{-1} .

4.3.2 CO $\Delta v = 1$

There are 757 CO lines from the $\Delta v = 1$ sequence that meet the selection criteria for inclusion in this study. All the lines included here are $^{12}\text{C}^{16}\text{O}$ lines, with potential isotopic blends removed. Goorvitch (1994) gives wavenumbers, energies, quantum numbers and other parameters.

Initial inspection of the results reveals interesting behavior with respect to both band, branch and quantum number (J). Figure 4.1(a) shows the line core shifts plotted versus their quantum number. Very clear arches are apparent in the data. Each branch of a band was fit using a fifth order polynomial (two examples are shown in Figure 4.1, the R Branch from the $1 - 0$ and $9 - 8$ bands).

These arches in quantum number/velocity space decrease in amplitude as higher bands are sampled. The $9 - 8$ R band has an amplitude much smaller than the $1 - 0$ R band, which is not a surprise since it spans a much smaller range of line depths. These fits are quite good, as Figure 4.1(b) demonstrates (the standard deviation of the differences between the data and the fits are 30 and 25 ms^{-1} , respectively). In the remaining figures, all the data points shown are the original measured line-shifts, however all the curves shown will be those resulting from a fifth order polynomial fit to the individual bands in J -velocity parameter space. This has been done to better represent any trends in the observations.

Line Depth

Figure 4.2 displays the dependence of the line-shifts upon the depth of the line cores. As with the Fe I samples in Chapter 3, there is a strong dependence upon line depth. However, for CO the slope

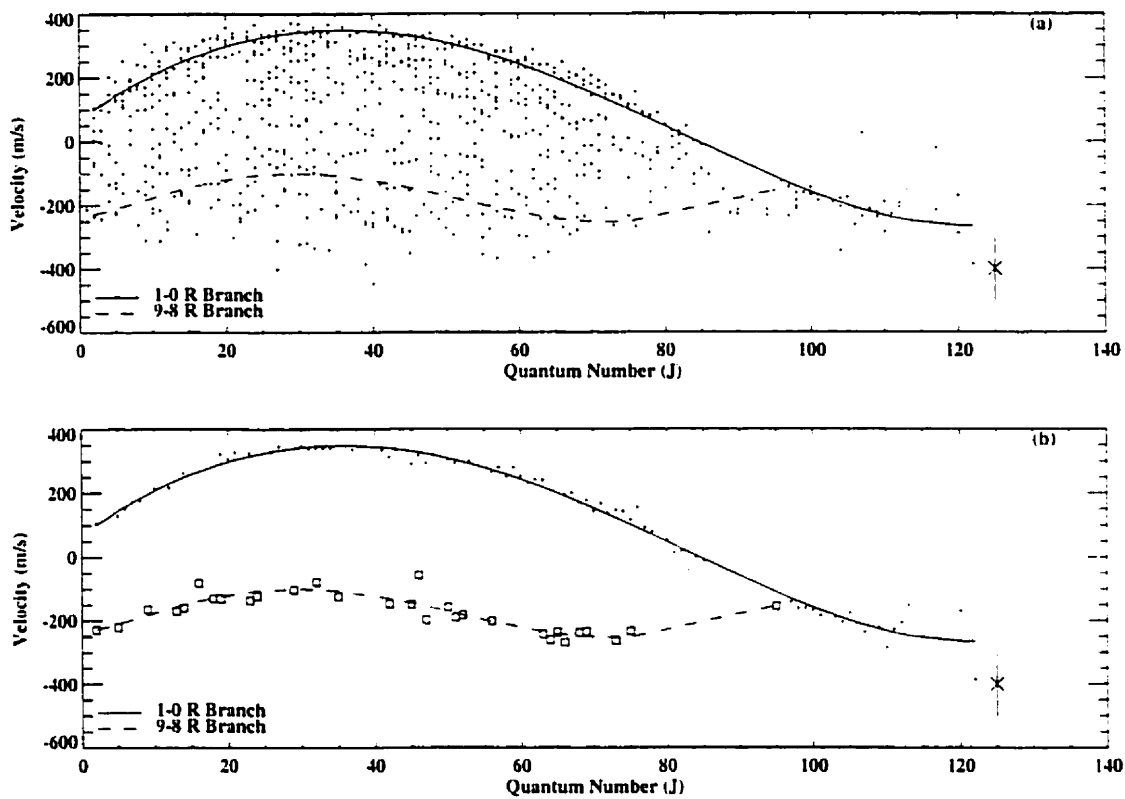


Figure 4.1: The 'arching' behavior of the line core shifts of CO $\Delta v = 1$ with quantum number (J) and band. In part (a) all 757 points are shown along with polynomial fits for the R branches of the 1 – 0 and 9 – 8 bands. Part (b) displays just those bands for clarity. There can be a degeneracy in velocity shift between quantum numbers for a given band. The 'peak' of these 'arches' is at $J \approx 35$.

of the distribution is much steeper and the distribution is much narrower than the distributions for the Fe I line-shifts (Chapter 3). The scatter that is seen in this distribution is largely a result of the overlapping of the 2 branches from the bands. The curves in Figure 4.2 are the 1 – 0 and 9 – 8 R branch bands shown in Figure 4.1. All the bands for both branches show this “doubling back” behavior, similar to the arches in Figure 4.1. The cusp for this doubling back appears at or near the lines which have $J \approx 35$, which coincides with the peaks in the arches seen in Figure 4.1. For a given band and line depth there may be two different line core shifts. However, the different bands have very divergent characteristics. This “doubling back” is most prominent for the lower bands, and decreases as band number increases, much as the amplitude in the “arches” in Figure 4.1 decreased. For the 1 – 0 band (and the other lower bands), those lines with the lower J values have the bluer convective shifts, whereas the higher J values have redder velocities. The two sides of each of these “doubling back” bands have significantly different excitation energies and $\log gf$ values. Those lines with low J values also have lower χ_l and $\log gf$, although their wavelengths are generally further to the red than lines of comparable strength in the same band. To illustrate this, the J values for three different points on each of the sample curves have been labeled.

For the higher bands (for example, the 9 – 8 band) the velocity difference between the high and low quantum numbers of lines of comparable strength are less (again this reflects the smaller velocity amplitudes seen in Figure 4.1) and they exhibit the opposite trend from the low bands - the lower J values have the redder convective shift and the higher J lines have the bluer shift. The medium bands (5 – 4 for example) show little difference at all between lines of the same strength and different quantum numbers.

When the fits to the velocity as a function of quantum number (see Figure 4.1) are subtracted from the line-shifts, the sensitivity to line depth disappears. Both the sensitivity to J and line depth are the same characteristic, just displayed in a different fashion. The absorption coefficient for rotation-vibration transitions is closely related to the rotation quantum number of the relevant state via both the Boltzmann distribution (giving the relevant populations of the states) and the Einstein coefficient, which are also related to the oscillator strength ($\log gf$) of the transition. Thus:

$$\alpha_{\nu r} \propto |\mu_J|^2 (2J + 1) \exp(-J(J + 1)) \quad (4.1)$$

Where $|\mu_J|^2$ is the electric dipole matrix element, which also depends in part upon J (Lang 1980).

In Figure 4.3 example fits from Figure 4.1 are plotted in line depth/velocity parameter space. For the lower bands (1 – 0 to 6 – 5) the slopes of the distributions steepen as the band numbers

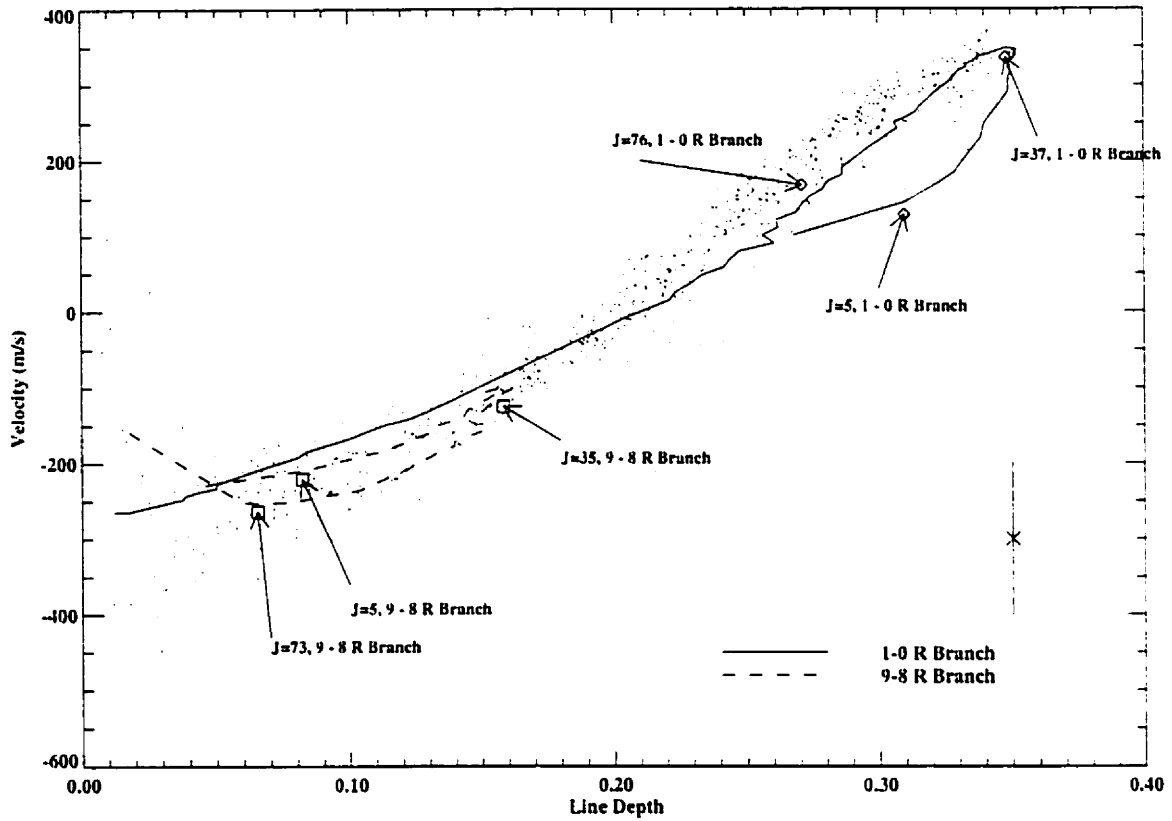


Figure 4.2: The line core depth dependence for the CO $\Delta v = 1$ sample. The slope is approximately twice as steep as seen for the Fe I visible sample (Chapter 3). The two example bands are shown to illustrate the degeneracy in velocity/depth. For each band, the slope of the distribution changes slightly. See section 4.3.2 for further details.

increase. For strong lines, the line-shifts for the 1 – 0 band are further to the blue than their counterparts from the 6 – 5 band. For the weaker lines, the 1 – 0 band line-shifts are further to the red than their counterparts from the 6 – 5 or 5 – 4 bands. This behavior is not clearly seen for the higher bands (7 – 6 and up), however these bands are entirely composed of weaker lines, at best, having only 1/2 the extent in line depth that the lower bands have. However, for the weak lines, the higher bands generally have line-shifts further to the blue than the lower band numbers. This is especially clear for the 1 – 0 and 2 – 1 bands, since both of these are large samples.

In both Figures 4.2 and 4.3, the progression and location of the line-shifts with J change. For the lower bands (i.e. 1 – 0), the lower (or bluer) portion of the "crook" corresponds to lower J values, with the point at the end being the minimal quantum number. The cusp of the distribution have $J \approx 35$, and the quantum numbers then increase as line strength decreases. For the higher bands (i.e. 8 – 7) the opposite holds. The minimum in J is found for the weakest line on the upper (or red) side of the "crook", the J value then increases with line strength until $J \approx 35$ which corresponds to the strongest line in the band. Then the J value continues to increase as line strength weakens over the blue portion of the distribution.

Wavenumber and Energy

When the $\Delta v = 1$ shifts are plotted with respect to either wavenumber (Figure 4.4) or λ_l (Figure 4.5), an "arch" structure for each band is seen. This "arch" is the same feature seen in Figure 4.1. The top-most points on the arches for each band are those lines with $J \approx 35$. When only a single band is considered the line-shifts from the two branches (R and P) exhibit very similar behavior, whether examined as functions of line depth or wavenumber. The largest J values for the two branches have very similar velocity shifts and line depths, even though their wavenumbers are separated from one another by almost 700 cm^{-1} (see Figure 4.4).

In this spectral region, the solar continuous opacity increases with decreasing wavenumber. Thus, if the CO lines were behaving in the same manner as the Fe I lines in Chapter 3, for a given line depth, those lines farther to the infrared should exhibit smaller blue-shifts. However, this is not observed. This implies that there is little dependence on wavenumber. In fact, for the 1 – 0 band (which is the band that demonstrated the greatest difference between low and high quantum numbers), those lines with low J values have larger blue-shifts and longer wavelengths than their high J counterparts of comparable strength in the same transition set. The differences between the low J and high J lines of the same strength cannot be attributed to the increase in the continuous

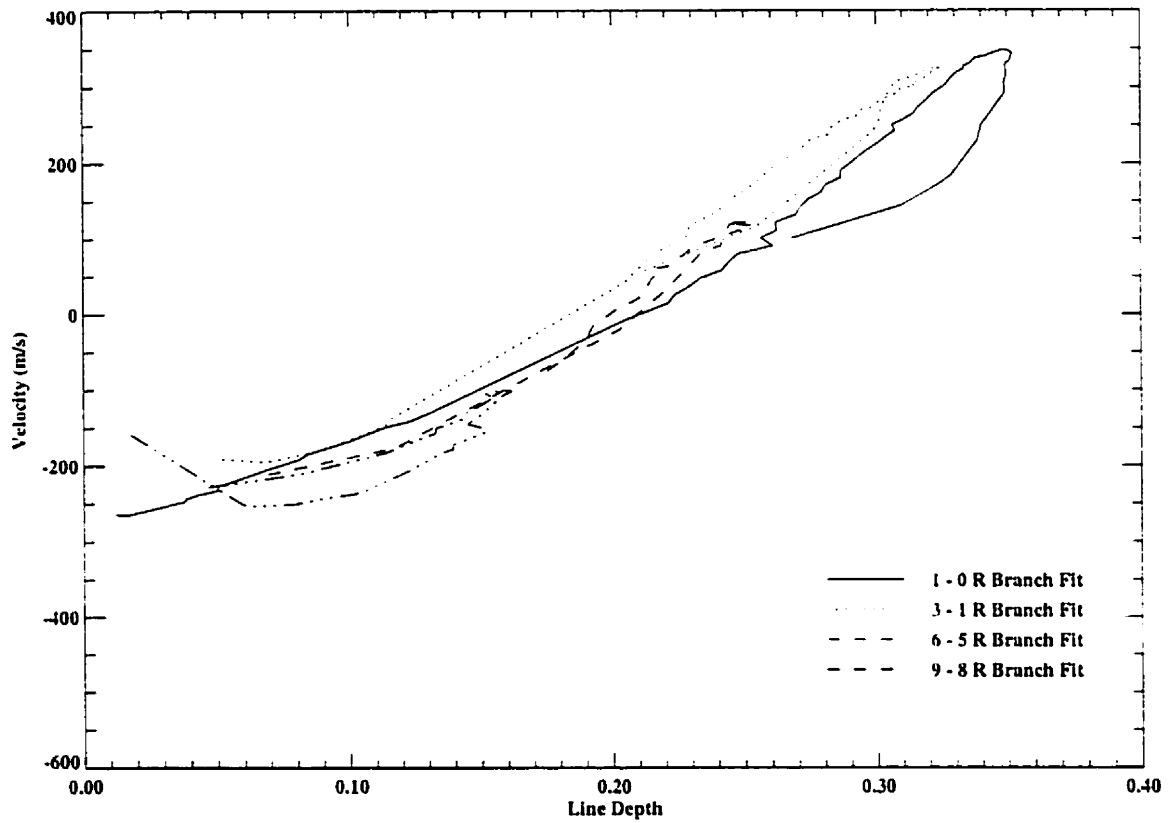


Figure 4.3: Sample polynomial fits (from Figure 4.1) for several bands illustrate the change in slope of the line depth/velocity distributions with band number.

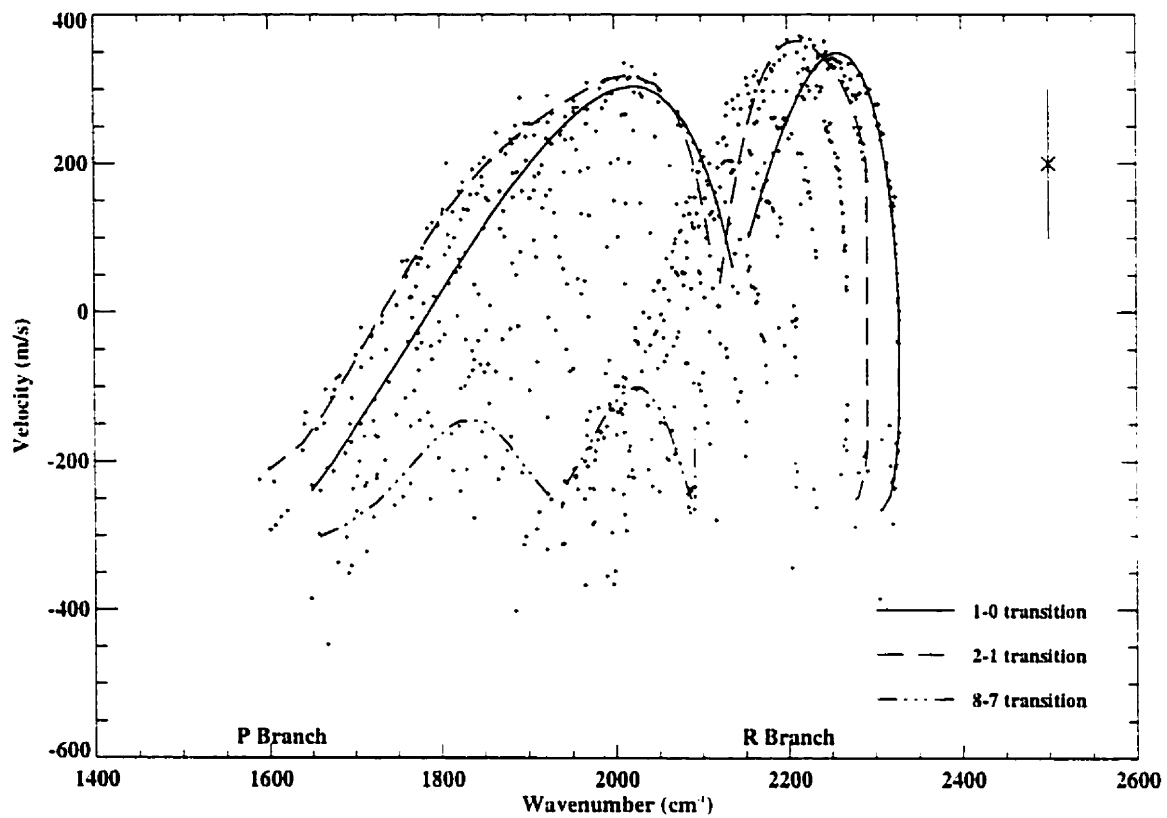


Figure 4.4: The line core shift distribution for CO $\Delta v = 1$ as a function of wavenumber. Again the degeneracy in velocity can be seen with the 'arch' shapes first seen in Figure 4.1. Three example bands for each branch are shown. The curves are all results of polynomial fits in $J/\text{velocity}$ parameter space. There is no clear evidence of a wavenumber dependence.

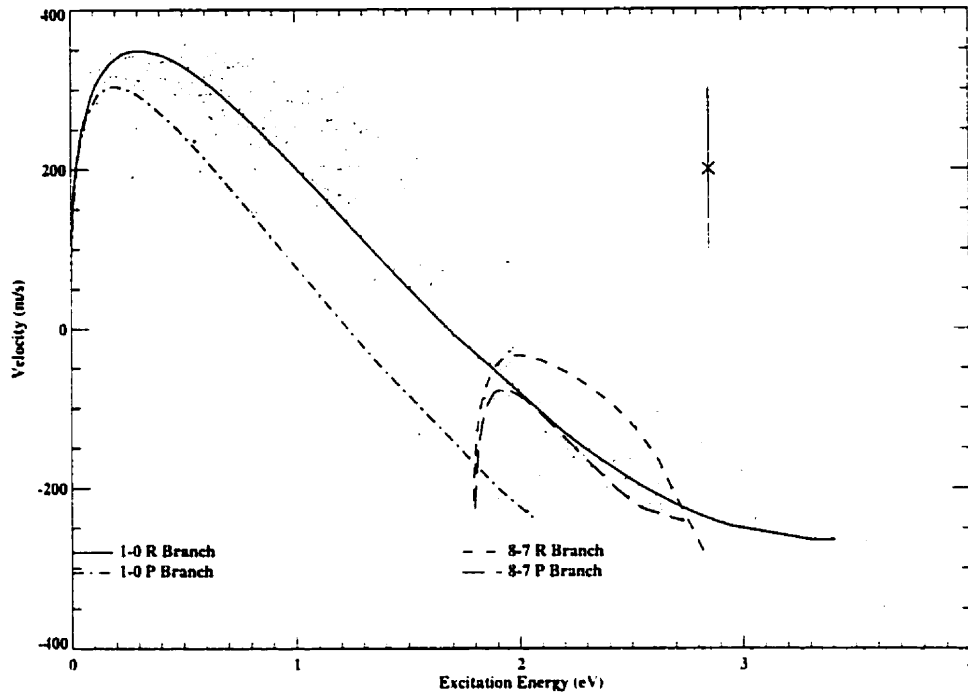


Figure 4.5: The distribution of line core shifts with lower excitation energy for CO $\Delta v = 1$. As was seen earlier, there is a clear 'arch' shape to the distributions for each band. The quantum number J increases with increasing excitation energy.

opacity. For the R branch bands the J values increase with wavenumber, while for the P branch bands, the J values decrease with increasing wavenumber.

When the same line-shift features are examined in light of their energies, similar behavior is seen. This is no surprise since the energy levels are directly tied to the rotational quantum numbers. Thus, any line-shift trends seen with ν_l are the same as those seen with J . The higher the lower excitation energy, the greater the quantum number J . The two branches (R and P) for the bands are offset from one another in energy, with the larger quantum numbers having the larger separation in energy (see Figure 4.5). These same features have very similar line core shifts, but energy differences of up to 0.7 eV. Another way to visualize this is that for a given energy, there are two possible line shifts, depending upon which branch is considered.

When the distributions for the 1 – 0 bands for the R and P branches are closely examined, it is found that at a particular line core depth there is a gap in J (for $J > 40$). For example, at the line depths close to 0.25, the points from the R branch have J values 11 or 12 larger than their P branch counterparts of similar strength. This is reasonable since the energy of the transitions are directly related to the quantum numbers for the features. If we consider a sample of lines from both

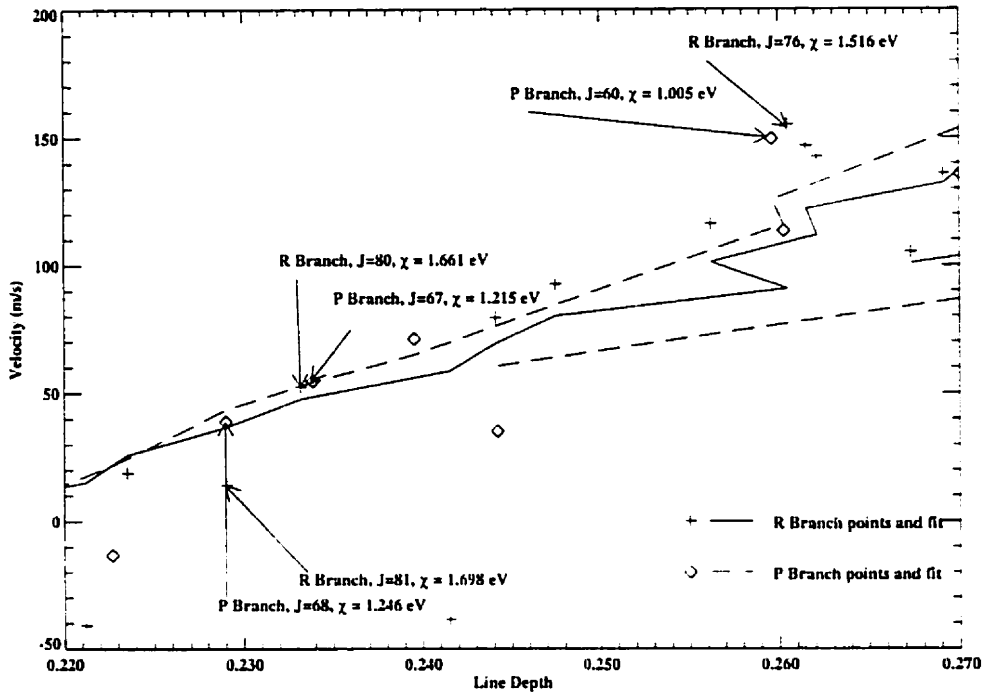


Figure 4.6: Line-shifts for the R and P branches of the 1 – 0 band with line depths near 25% of continuum. Example pairs are labeled by J and χ . The P branch lines have smaller J values and energies than their R branch counterparts.

transitions with similar J values (and thus energies) the line core depths of the R branch features will be stronger.

As was the case with the line depth distribution, when the fifth order polynomial fits in J/velocity parameter space are subtracted from the velocities, the arching behavior with the excitation energy and wavenumbers disappears. This same behavior is evident when the log gf values and expectation values for each of these transitions is examined. The differences between the high-J and low-J lines of comparable strength are reflected in differences in both wavenumber and χ . For two lines from the same band and of comparable strength, the differences in determined velocity must be reflecting slightly different conditions of formation. This can clearly be seen in Figure 4.6. A narrow slice in line depth near 25% of continuum has been taken for the R and P branches from the 1 – 0 band. Several different pairs of lines with very similar strengths and line-shifts have been labeled with both their quantum numbers and lower excitation energies. The lines from the P branch have energies about 0.4 eV and quantum numbers between 10 and 15 less than their R branch counterparts. The solid and dashed lines are the polynomial fits discussed in Figure 4.1.

4.3.3 CO $\Delta v = 2$

From the CO $\Delta v = 2$ sequence 566 candidate lines meet the selection criteria. The strongest lines reach a depth of only 15% that of continuum, and over 86% of the features have line depths of only 10% or less. The sample includes both the P and R branches, covering 3400 to 4400 cm^{-1} , including every band up to 12 – 10 and the maximum quantum number in the sample is $J=95$.

Unlike the $\Delta v = 1$ sequence, the $\Delta v = 2$ sample does not exhibit any obvious structure when the line shifts are examined versus energy or wavenumber. Even when the line shifts are examined in a similar fashion to the $\Delta v = 1$ sample, no structure is found.

This may be a result of the weakness of the lines in this sample. The lines are all fairly weak and the lines will be formed (for the most part) under fairly similar physical conditions, so the line-shifts will not be greatly different. An additional consideration is that the signal-to-noise ratio at this wavenumber is at its lowest for the atlas ($\approx 50:1$ at 4800 cm^{-1}). Weak lines such as these are much more susceptible to noise, as was shown in Chapter 2. This could contribute greatly to the scatter for an individual sequence of lines, and this increased noise may mask any subtle structure in the distribution.

Line Depth

Figure 4.7 demonstrates that there is some dependence of the line core shift upon line depth. The slope of this distribution is shallower than its counterpart for the $\Delta v = 1$ sample over the same line depth range ($m_{\Delta v=2}/m_{\Delta v=1} \approx 0.60$).

When the $\Delta v = 2$ sample is compared to the $\Delta v = 1$ sample as a function of wavenumber (Figure 4.8, where the two samples are superimposed on the same wavenumber scale), notice that the $\Delta v = 2$ sample resembles the weak line portion of the $\Delta v = 1$ sample, almost as if the stronger $\Delta v = 1$ lines have been “collapsed” down onto the weaker $\Delta v = 1$ lines. The two samples of lines have a small offset from one another in velocity, with the $\Delta v = 2$ lines having line-shifts $\approx 125 \text{ ms}^{-1}$ to the red of their $\Delta v = 1$ counterparts.

4.4 Discussion

The CO fundamental sample of lines has a slope nearly twice that of the Fe I sample in the visible (Chapters 2 and 3). However, the CO lines have a smaller range in line depth; the strongest CO lines have depths of $\approx 35\%$ that of continuum, whereas the strongest Fe I lines in Chapters 2 and

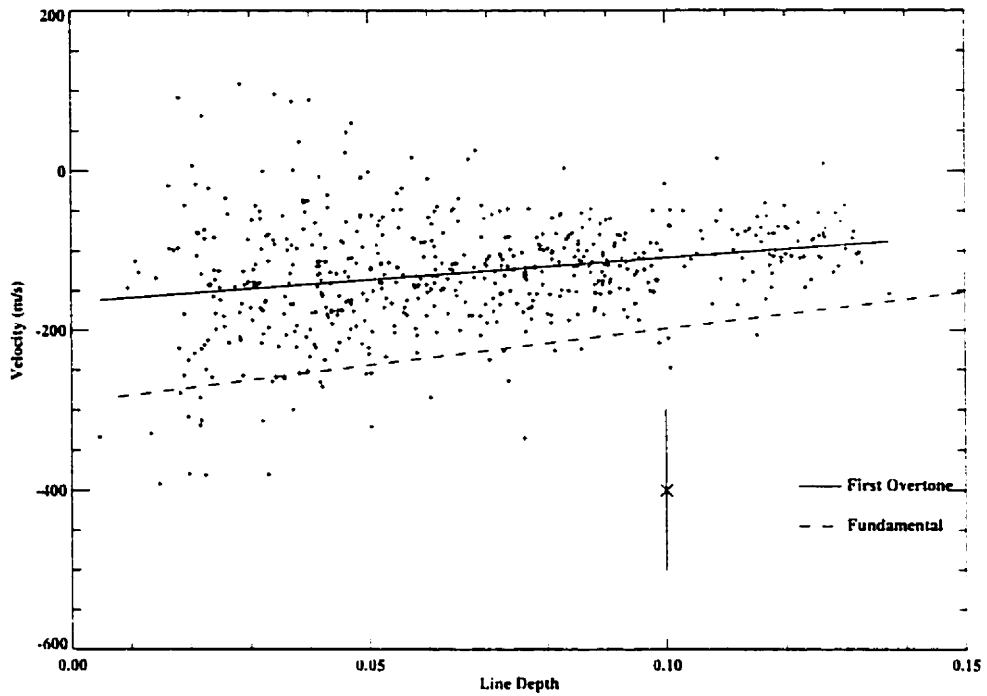


Figure 4.7: The CO $\Delta v = 2$ distribution of line-shifts with line depth. The slope for the $\Delta v = 2$ sample is slightly shallower than the slope for the $\Delta v = 1$ data set over the same range of line depth.

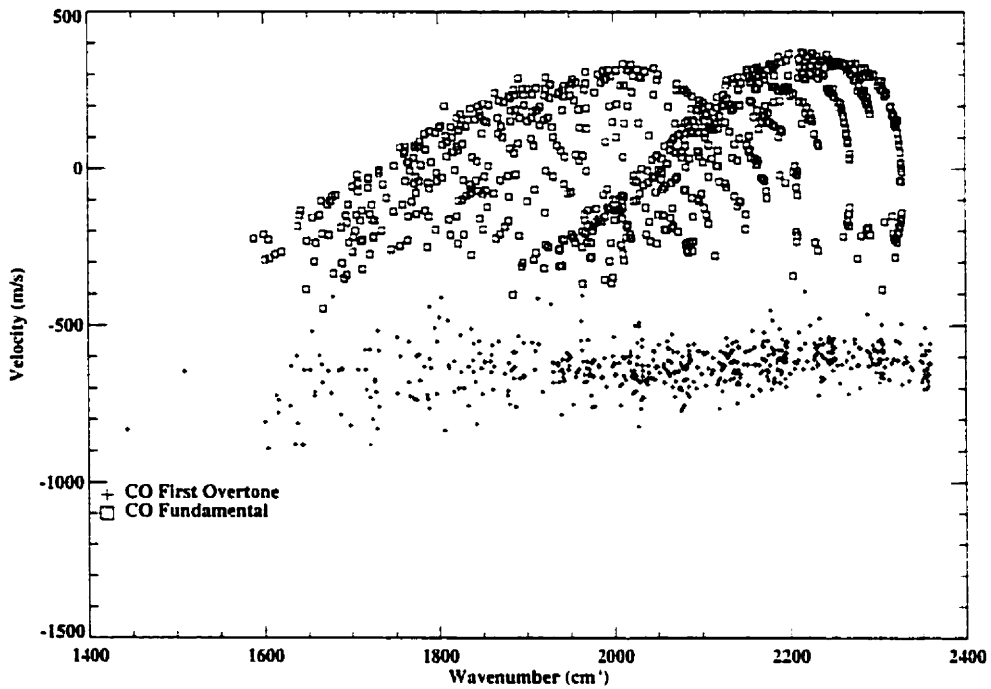


Figure 4.8: The line-shifts for the CO $\Delta v = 1$ and 2 samples as a function of wavenumber (with the $\Delta v = 2$ sample offset in both wavenumber and velocity for clarity). The $\Delta v = 2$ sample resembles a “collapsed” version of the $\Delta v = 1$ distribution.

3 had depths of $\approx 80\%$ of continuum. The superficial interpretation would be that the convection observed via the CO lines is more vigorous than that observed using the Fe I lines. As with Fe I, CO provides an excellent opportunity to probe the photosphere: the weakest lines of CO are formed deep in the photosphere, while the strongest lines are formed at high altitudes, close to the temperature minimum (Ayres & Brault 1990). However, the exact details of where the individual lines form, especially the strong ones, are much more complicated.

When strong CO lines are observed near the solar limb, the derived brightness temperature of these lines is estimated to be 3700 K, 700 K less than the value derived for T_{min} from the cores of the Ca II H and K lines (Noyes & Hall 1972). A possible explanation for these different temperatures is the existence of a cool "COmosphere" comprising about 90% of the Sun's photosphere at that altitude. These clouds of CO cool the photosphere radiatively, while the Ca II lines are produced in 'bright spots' where the gas has been mechanically heated and the local adiabatic cooling dominates over radiative cooling (Ayres 1981; Ayres et al. 1986; Ayres & Brault 1990; Ayres & Rabin 1996). An alternative proposal is that the cool CO cores are formed in 'cool spots' nested in a hot chromosphere. In either case, using a static one-dimensional atmospheric model to determine altitudes of formation for these lines is inadvisable since any such height would be very sensitive to the model used (Uitenbroek 2000), and would be averaging over a relatively large range of altitudes since the real atmosphere is dynamic and the optical depth is corrugated with respect to physical altitude (Uitenbroek 2000).

This corrugation of optical depth is a result of spatial differences in temperature, density and opacity. This changes the altitude at which these lines form, and a one dimensional static atmospheric model will be averaging all of these properties at the same physical height. As Stein & Nordlund (1998) have pointed out, not only is the surface of the Sun at a given physical altitude corrugated in optical depth, but it changes with time, and any average that is done at that altitude will by necessity be averaging over different optical depths, densities, temperatures and velocities and will have a temporal component (Uitenbroek 2000). This poses a serious problem for determining the altitude of formation for temperature sensitive lines such as CO.

With the granule/lane contrast inversion (Uitenbroek 2000) observed for some of the strong CO lines (notably 7 – 6 R68 and 3 – 2 R14), it may be possible to reinterpret the velocity/line depth distribution (Figure 4.2). This contrast inversion in the CO lines is actually predicted by numerical simulations (Stein & Nordlund 1989), and is consistent with the cooler T_{min} determined from the cool CO lines. When the upwelling granular material reaches the upper photosphere, almost all

of its vertical momentum has been transferred to horizontal expansion. This occurs because the rising material in the granule is running into the steep density gradient that is the stable layer that lies above the photosphere. Above the uprising material the pressure increases, due to higher temperatures and larger scale heights (Stein & Nordlund 1998). The center of the granule is warmer, and thus has a larger pressure scale height relative to the intergranular lanes. This high pressure region combines with dynamic pressure fluctuations that push mass into horizontal motions (Stein & Nordlund 1998). This excess pressure diverts the vertical motion to horizontal motion, and, if the pressure is not high enough to divert the material, then the local density increases until the pressure is high enough to push the mass out. Conservation of mass flux requires that the rising gas expand rapidly, which leads to a drop in the density and thus a deceleration of the upwelling material. The expansion allows the gas to cool substantially over the granule, and the gas decelerates rapidly when it reaches the lanes, compressing and heating up as it begins to descend (Solanki et al. 1996; Uitenbroek 2000). Figure 4.9 is a schematic diagram illustrating this motion. It is based upon a snapshot taken from a two dimensional simulation of solar granulation by Steffen (2000)². The contours of constant temperature extend to high altitudes in the upper atmosphere, which is consistent with the predicted compressive heating and the contrast inversion between the granules and lanes (Stein & Nordlund 1989).

The weaker lines are formed deeper within the atmosphere, below the stable layer. For those weak lines the upwelling granules are brighter and hotter than the lanes and contribute a more significant amount of flux to the line profile than the lanes. Similar behavior is seen when the Fe I lines are examined in both the visible and infrared wavelength regions for lines of all strengths (Chapters 2 and 3). As stronger CO lines are examined, the contrast between the lanes and granules will lessen as higher altitudes of the photosphere are sampled. The upwelling granular velocity is decelerating ballistically, and according to simulations (Uitenbroek 2000; Stein & Nordlund 1989; Stein & Nordlund 1998), spreading horizontally. Under this scenario, the vertical motion is being deflected into horizontal motion and the granular contribution to the line profile will be blue-shifted less than it would be if the motion were still largely vertical in nature. If this is the case, then there should be a point when the red-shifted lanes begin to dominate the flux contributions to the line profiles. For stronger lines, which sample higher in the photosphere, these downdraft velocities will be smaller, however the actual contribution by the downdrafts to the line profile will be greater since the inverted contrast between the lanes and the granules enhances the relative flux contribution

²www.aip.de/groups/sternphysik/stp/convect.html

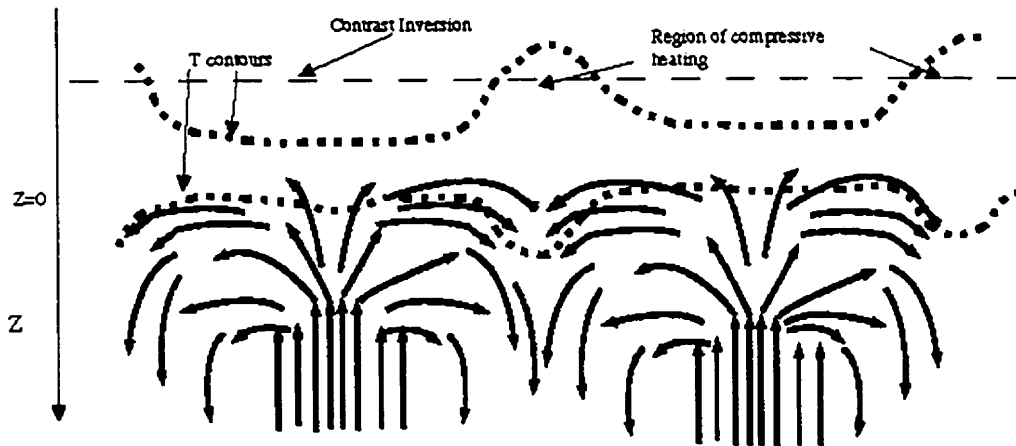


Figure 4.9: A schematic drawing of the horizontal deflection of uprising material (based on two dimensional simulations by Steffen (2000)). The contour lines are for constant temperatures. Note that higher in the atmosphere, the downdrafts are actually warmer than the regions over the granules due to compressive heating. Notice also the relative areal changes between the granules and lanes, which also contributes to the differences between weak and strong lines (see the text for details).

from the lanes. In addition to this, the uprising velocity should almost be completely converted into horizontal motions, thus the granular line profile should exhibit little or no Doppler shift. An additional consideration is that the relative geometries and areas of the lanes and granules will be different at greater physical altitudes, which will alter the relative flux contributions from the two components (see Figure 4.9). Multidimensional models show that at these altitudes the relative physical area where the material is rising is shrinking, while the relative area occupied by the downdrafts increases (Uitenbroek 2000). This change in the relative areas of the two components with altitude changes their contribution to the line profile substantially.

This contrast inversion for strong lines may also provide an explanation for the difference in behavior between the low-J (low χ_l) and high-J (high χ_l) lines. Previously (Dravins et al. 1981; Dravins et al. 1986; Chapter 3) there has been some indication that for a given line depth, lines with greater excitation energies exhibit larger shifts. These higher energy lines form slightly deeper in the atmosphere at higher temperatures. In the case of the strong CO lines, the lines with the smaller χ_l had the smaller line shifts. This could be due to the contrast inversion. For these strong lines the cooler lanes are brighter than the hotter granules. If the flux in a line profile is dominated by the contribution from the cooler lanes, which are red-shifted, those lines with higher excitation

energies should be forming at a slightly deeper average altitude. Thus the photons escaping from that altitude should reflect the downdraft velocity, which will be greater than at higher altitudes, where the contributions to the low χ_l lines arise.

As weaker lines are considered, the contrast inversion between the lanes and granules should disappear. The medium bands (such as the 5 – 4 R band) exhibit no strong difference between low and high quantum number lines of similar strength. The higher bands are composed of weaker lines (see Figure 4.2 and the 9 – 8 R band), these weaker lines are dominated by contributions from the granules. This explains the difference between the low and high energy lines in these bands. If, for a given strength, higher energy lines form at slightly higher temperatures in the granules and thus at slightly greater depths, the photons contributing to the line profiles will be blue-shifted more than those for the lower χ_l lines, which will form slightly higher in the atmosphere. Thus the behavior of the higher bands with J and χ_l is the opposite of what was seen for the lower bands, reflecting the effects of the contrast inversion. The medium bands do not show this degeneracy in velocity for a given depth because the contributions from the lanes and granules are more balanced. If, at a particular line depth, we consider a higher χ_l (or J) line, the contribution to the line profile from the lane will be at a slightly higher red-shift than for a similar line with a smaller χ_l ; however the contribution to the line profile from the granule will be at a slightly larger blue-shift and the two compensate for one another.

The $\Delta v = 2$ lines are formed closer to the opacity minimum at 1.6 μm than the fundamental bands are, and as such we are observing deeper into the atmosphere. Additionally, the granular contrast is much greater for the first overtone lines, and the upwelling granules would be making a greater contribution to the line profile. The combination of these two should imply that the velocities for the weak first overtone lines should exhibit a greater slope and larger blue-shifts than their fundamental counterparts. However, the formation of CO lines is complicated. As Uitenbroek (2000a; 2000b) has shown, understanding where the CO lines form requires full three dimensional hydrodynamic modeling. The actual relative contributions of flux from the granules and lanes to the CO $\Delta v = 2$ lines may not be entirely based upon the areal and temperature contrasts. If the timescales for CO formation are long enough, there may be a larger than expected number of weak lines forming in the downdrafts, enough to increase the relative weight of the lane contributions to the line profiles. The three dimensional hydrodynamical modeling technique employed by Uitenbroek (2000a; 2000b) may help explain the different behavior between the two different sets of bands.

4.5 Conclusions

The CO fundamental sequence between 4 and 5.5 μm provides an excellent probe into the solar atmosphere. The velocity/line depth distribution is very similar to that of the visible Fe I line-shifts, however it is much steeper. This steep slope is consistent with observing a net blue-shift for the weaker lines that is dominated by the granular contribution to the flux, while the strongest lines exhibit a red-shift dominated by contributions from the brighter intergranular lanes. This interpretation is consistent with the contrast inversion predicted by numerical simulations (Stein & Nordlund 1998) and observed in spectroscopic imaging of strong CO lines (Uitenbroek 2000).

No sensitivity to wavelength (or wavenumber) is found for this species, which is consistent with the behavior of the Fe I lines at infrared wavelengths (Chapter 3). There is some sensitivity to either energy or quantum number (or rather a combination of the two) which is shown by the 'arching' behavior when the velocity/J and velocity/ χ_l distributions are examined. The differences between the high J and low J transitions in a given band is obviously closely related to where in the atmosphere those particular lines are formed. However, the physical location of the CO line formation is an extremely complicated problem that is best investigated using multidimensional hydrodynamics.

The CO lines are all temperature sensitive, and the spatial temperature and opacity inhomogeneities of the atmosphere clearly influence which lines have profiles dominated by the granules and which have profiles dominated by the lanes. These differences between lines of the same strength but different energies may be closely related to how much of the radiation is contributed by the cooling granules versus the compressively heated lanes and the exact conditions under which these lines form. This could be further examined by observing a sample of such lines at high spatial resolution over both granules and lanes to determine the relationship between the line profile and the spatial distribution of its contributing flux.

The CO transitions do provide a window into the atmospheric dynamics of other solar-type stars. The CO lines are very temperature sensitive, and as T_{eff} drops, the strength of the lines increase and the higher transitions become available for study. The strongest CO lines are formed near the limits of where penetration by convection occurs, and the contrast inversion between the granules and lanes observed by Uitenbroeck (2000) on the Sun may also be present on other stars. The extent of the convective penetration into the more stable layers for other stars can be examined, and the possible scaling effects of differences in T_{eff} and $\log g$ should be apparent. The

variation in the continuous opacity in stars of different temperature may also introduce a stronger wavelength dependence, which could be observable via the large wavelength range that both the CO fundamental and first overtone sequences sample.

Chapter 5

Line Shifts in a Sunspot Umbral Spectrum

5.1 Introduction

A sunspot umbral spectrum provides an opportunity to examine how convective velocities in the solar atmosphere are affected by the presence of strong magnetic fields and a lower effective temperature. While a strong magnetic flux tube is expected to suppress the convective motions at the surface of the sunspot (Blanchflower et al. 1998), convection is required to transport the emergent energy flux underneath the sunspot. The umbral photosphere itself should be radiative, with few large vertical motions over significant sized areas (Weiss et al. 1990).

Previously, Beckers (1977) examined the profile and position of the Ti I line at 5713 Å for a number of different sunspot umbrae, and found no evidence for large scale vertical motions. However, some convective flux does penetrate to the surface via ‘umbral dots’ and ‘light bridges’ (Blanchflower et al. 1998 and sources therein). The umbral dots are found throughout the umbra, and occupy about 5% of the area of the umbra (Knobloch & Weiss 1984). These umbral dots have diameters ranging from 8 arc-seconds down to at least 0.28 arc-seconds, and the number density of the dots increases at smaller scales (Blanchflower et al. 1998). The umbral dots are responsible for the transport of about 15% of the energy radiated by the umbra, and may be a result of large-scale oscillatory convective overshooting, penetrating into the radiative layer of the umbral photosphere (Weiss et al. 1990). Estimations of the vertical velocities of the dots vary from $\approx 3\text{kms}^{-1}$ (Moore 1981; Kneer 1973), to an upper limit of only a few hundred ms^{-1} (Lites et al. 1991). Other small

scale motions include umbral turbulence, which may be associated with the oscillatory convection that terminates just beneath the umbral photosphere (Blanchflower et al. 1998). This turbulence has a rms velocity ceiling of $v_{rms} \approx 1.3 \pm 0.2 \text{ km s}^{-1}$ (Beckers 1976; Moore 1981). Strong and Faint Light Bridges (SLB and FLB) are also umbral core features that are associated with convection and granulation (Sobotka et al. 1994) and exhibit velocities comparable to those found in umbral dots. The umbral dots are often associated with penumbral grains and photospheric granulation (Sobotka 1997).

Perhaps the most prevalent motion associated with sunspots is the Evershed motion, which is a radial outflow of material through the penumbra that is almost entirely horizontal in nature. However, there is evidence for some vertical motion ($200 - 400 \text{ ms}^{-1}$) in the penumbral spectrum that may be a vertical component of the Evershed motion, or it may be a convective blueshift (Shine et al. 1993).

Infrared umbral spectra and molecular line positions may provide an opportunity to search for convective motions in sunspots. Convective line shifts in the atmospheres of cooler stars should be similar to those seen in an umbral spectrum, and molecular lines are relatively insensitive to Zeeman splitting. The difference in convective velocities between a cooled umbral patch of the Sun and that of a late K giant may shed some light on the influence of both $\log g$ and the suppression of convection by magnetic fields.

The solar umbral spectrum also provides the opportunity to assess the utility of other potential diagnostic molecular species. Candidate species such as the fundamental and first overtone OH lines are not present in the normal photospheric spectrum, and a high resolution and signal-to-noise solar atlas allows us to determine if these lines could be used for studies of convection in cooler stars.

5.2 Methodology

5.2.1 The Sunspot Spectral Atlases

There are two umbral spectral atlases under consideration here, both of which were taken using the FTS at KPNO (Wallace & Livingston 1992; Wallace et al. 1998). In both cases terrestrial telluric lines were subtracted. The digital spectral atlases include the observed umbral spectra, the telluric spectra and the final telluric-removed umbral spectra at ultra-high spectral resolution and high signal-to-noise.

Depending upon the wavelength region, and the molecular band under consideration, the spectrum of a sunspot can be given a spectral class. The infrared portion of the umbral spectrum studied here has been classified as between M2 and M5 (Wallace & Livingston 1992), however most spectral classifications of sunspots are usually between K0 and K5. In the case of the infrared umbral spectrum, the classification could be anywhere from late G to middle M, depending upon the molecular bands in question. Wallace and Livingston have based their spectral classification upon the strength of the CO 2 – 0 band head and the calibration of Kleinmann and Hall (1986) (Wallace & Livingston 1992).

The Infrared

The umbral atlas for the infrared spans the wavenumber range 1970 to 8640 cm^{-1} (Wallace & Livingston 1992). The spectra were obtained near disk center using the 1 m FTS at the McMath Telescope. The spot observed was a large, mature spot with a diameter of 29", several times the size of the FTS aperture of 7". An aperture this large should contain several unresolved umbral dots or light bridges that are associated with convection, and would span ~ 5 granules in the normal photosphere. The terrestrial telluric line spectrum was removed by combining two, one hour long integrations at airmasses of 1.5 and 2.3. The resolving power ranges from 100,000 at low wavenumbers to 450,000 for high wavenumbers.

The Visible Red and Near Infrared

The Red and Near Infrared umbral spectral atlas covers 8900 to 15050 cm^{-1} (Wallace et al. 1998). Two spectra at different airmasses were combined to remove the terrestrial telluric components. The resolving power for these observations varies between 460,000 and 770,000, and the exposure times were just under one hour in length (Wallace et al. 1998).

5.2.2 Line Selection

Previously, (Chapters 2 and 3, Dravins et al. 1981) the species of primary interest was Fe I. However, the low temperature of the umbral regions combined with the effects of Zeeman splitting render extensive use of Fe I ineffective. Molecular lines, specifically CO and OH do provide comprehensive coverage over the infrared and provide a compelling opportunity for comparison with the spectra of cooler stars.

CO

The CO line positions for the fundamental, first and second overtone sequences ($\Delta v = 1, 2$ and 3) were taken from Goorvitch (1994). Details on the accuracy of the line positions and the other properties for these transitions are discussed in Chapter 4.

OH

The OH laboratory line positions are primarily taken from the Meinel system. The positions used here are taken from Abrams et al. (1994), and were measured using an FTS and a hydrogen-ozone diffusion flame source. The derived molecular parameters had a standard deviation of 0.003 cm^{-1} . The error in the absolute line position strongly depends upon the strength of the line and the signal-to-noise. The accuracy of the OH line positions can be estimated using the observed minus calculated line positions ($O - C$) of Abrams et al. (1994). The $O - C$ values have an average of 267 ms^{-1} , with a standard deviation of 1182 ms^{-1} . The standard deviation is so large because, for a small number of lines under consideration, the observed $O - C$ residual is quite significant. Only seven of the 193 OH lines here have $O - C$ values greater than 500 ms^{-1} . When these seven $O - C$ values are discarded, the average $O - C$ falls to 102 ms^{-1} , with a standard deviation of only 92 ms^{-1} . These values provide a reasonable lower limit to the accuracy of the line positions and when combined with the accuracy of the wavenumber calibration, an overall average uncertainty of 286 ms^{-1} is found.

TiO

The Red-Near Infrared sunspot spectrum is particularly rich in TiO. The plethora of TiO lines leads to substantial line blending over this range of wavelengths. The best defined set of line positions are those for the γ bands (Ram et al. 1999). These positions are the result of FTS observations of a titanium hollow cathode lamp. Only the ^{48}TiO isotope was identified (Ram et al. 1999), and the majority (73%) of TiO lines are of this isotope; isotopic blending remains a concern, since these blends may be unresolved in the umbral spectra. There are both $O - C$ and precision estimates for each observed TiO line in the γ bands (Ram et al. 1999). The precision of the line positions ranges between 0.002 and 0.005 cm^{-1} , depending upon the signal-to-noise. If a minimum estimation of the line precision is based upon these estimates, then the TiO lines have an average lower limit of uncertainty of 93 ms^{-1} , with a standard deviation of 37 ms^{-1} for this sample. The maximum

lower limit would be 327 ms^{-1} , while 48% of the lines would have lower limits of less than 100 ms^{-1} . However, if the uncertainty estimate is based upon the given $O - C$ values, then the average minimum uncertainty for this sample would be 74 ms^{-1} with $\sigma=68 \text{ ms}^{-1}$, and 72% of the line positions would have minimum uncertainties $\leq 100 \text{ ms}^{-1}$. If this is combined with the estimated uncertainty for any one position on the scan, then the precision estimates give an average line position error of 137 ms^{-1} .

5.2.3 Errors

The two atlases used for this study have not been placed upon a common wavenumber scale because there is no overlap between the two. Any comparisons of the distributions of line core velocities will be restricted to the shapes of the distributions. Neither atlas contains an estimation of positional accuracy, however this same instrument has been used to observe the central intensity (Livingston & Wallace 1991; Wallace et al. 1993; Wallace et al. 1998) and flux spectra (Kurucz et al. 1984) of the Sun. As was done with the other FTS observations, the positional accuracy of scans taken with this instrument are estimated as 100 ms^{-1} for any particular point on a scan (Kurucz et al. 1984) (see §2.2.3, §3.2.2 and §4.2.3).

5.3 Analysis

As was done previously, the different distributions of line core shifts have been binned by common parameters: wavenumber, line depth, and for some cases lower excitation energy and transition number.

5.3.1 CO $\Delta v = 1$

The sequence of CO fundamental bands are found between 4.6 and $5 \mu\text{m}$. This set of bands has proven to be extremely interesting in the solar photosphere spectrum (see Chapter 4). One of the most useful characteristics of the observations used in Chapter 4 was the complete absence of any telluric interference for the $\Delta v = 1$ lines. Unfortunately, the ground based umbral spectrum does not possess this advantage. This spectral region is very rich in CO lines, however the signal to noise is relatively low and there are several swaths where the opacity of the terrestrial atmosphere has obscured the spectrum entirely. There are also SiO bands present near $4 \mu\text{m}$, which effectively removes most of the spectral region used in Chapter 4. As a result of all of these obscuration and

signal-to-noise problems, only 28 lines of the $\Delta v = 1$ bands are accessible. The combination of the crowded spectrum, the low temperature conditions and the poor signal to noise mean that only strong lines are available. The weakest line that satisfies our selection criteria has a depth of only 20% that of continuum, and only 10% of the lines have strengths less than 30% of the continuum.

In order to compare this small sample of lines with the earlier results, individual bands need to be isolated. Some of these bands (e.g. the 5 – 4 band) display similar behavior to what was found previously. However, all of these samples are very small in size, and this behavior is not clearly seen for all the bands represented here. In Chapter 4, 757 lines of more than 12 different bands for 2 branches were studied. In the photospheric intensity solar spectra, the 5 – 4 band had 78 members which could be used; in the umbral spectrum there are 5. These small sample sizes make it very difficult to conduct an analysis for dependence as was done in earlier chapters. No meaningful trends are discernible from this collection of line-shifts.

5.3.2 CO $\Delta v = 2$

The observed umbral spectrum can be used to estimate an “effective” spectral class and corresponding temperature for the spot even though the molecular line strengths can vary from point to point across the same spot (Wallace & Livingston 1992). The CO 2 – 0 band head was used to estimate a spectral classification of between M2V and M5V for the KPNO IR umbral atlas (Wallace & Livingston 1992). While this may not apply for all the regions of the spectrum, and most definitely cannot be applied to temperature estimations for other umbral atlases, it does provide some information on the physical conditions for the CO $\Delta v = 2$ line distributions. From the $\Delta v = 2$ set of lines near 2.2 μm , 194 candidate lines were selected. The lines are all $^{12}\text{C}^{16}\text{O}$, and are estimated to be relatively unblended. Suspected solar and telluric blends were removed from the sample using the same methods as in earlier chapters. The vast majority (82%) of the lines come from the R branch, up to and including lines from the 7 – 5 band.

Quantum Number J

As was seen in Chapter 4, the line core shifts show some interesting behavior with respect to quantum number (J). Figure 5.1(a) displays all the $\Delta v = 2$ line core shifts plotted versus their respective quantum numbers. For clarity Figure 5.1(b) displays all the line core shifts from just two bands, 2 – 0 and 6 – 4, which display the “arch” structure inherent in the data. The displayed fits have standard deviations of 43 and 22 ms^{-1} respectively. As was found for the $\Delta v = 1$ sample

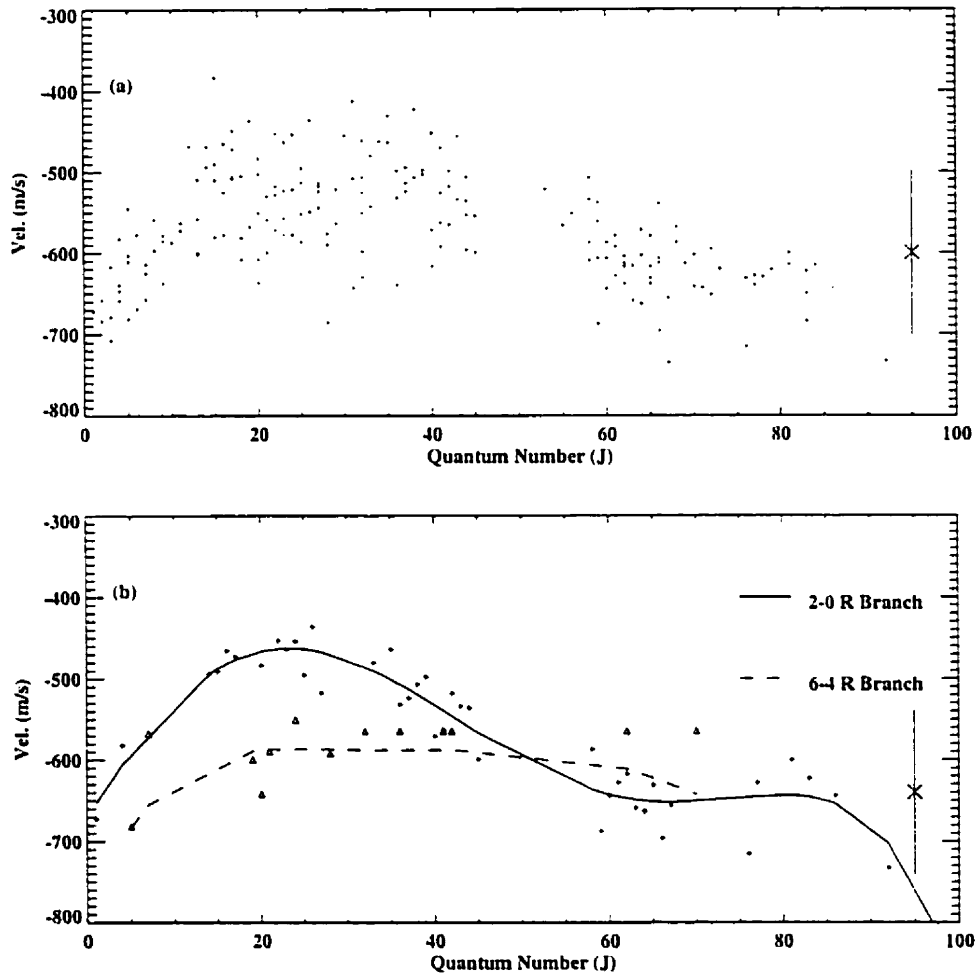


Figure 5.1: Line shift velocities versus quantum number (J) for the $\Delta v = 2$ CO sample. In part (b) fifth order polynomial fits to the 2 – 0 and 6 – 4 R bands are shown for clarity. Similar “arching” behavior was seen for the $\Delta v = 1$ sample in the photospheric intensity observations

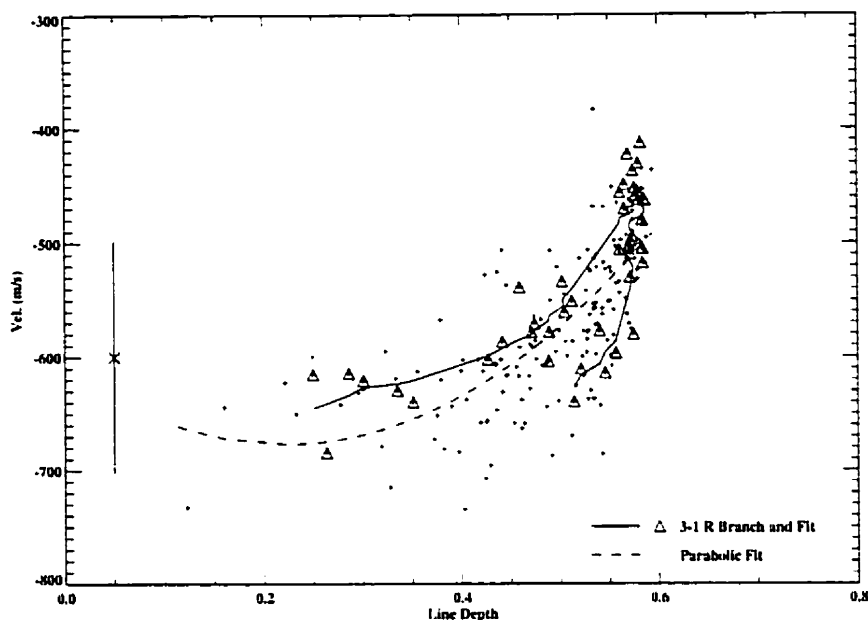


Figure 5.2: Line shift velocities versus line core depth for the $\Delta v = 2$ sample. The slope is approximately one half that seen for the $\Delta v = 1$ sample in the normal photosphere (Figure 4.2).

in the photosphere, arching behavior in the distributions for each band is seen. However, the velocity span for an individual band is smaller, and the dispersion is much greater. The arches in velocity/J space appear to peak at slightly lower J values than was found for the CO fundamental line distributions in Chapter 4. As in Chapter 4, the velocity distributions for the individual bands are fit with a fifth order polynomial in velocity/J parameter space. In all the remaining figures in this chapter, the curves shown will be from the velocities from these fits, although all data points shown are the original velocities.

Line Depth

In Figure 5.2 the $\Delta v = 2$ lines show some line-shift velocity dependence upon line depth, however, to a much smaller degree than was seen in the photospheric spectrum for the fundamental CO lines (see Figure 4.2). The slope is quite shallow, with a total velocity span of only approximately 300 ms^{-1} compared to more than 800 ms^{-1} for the photospheric $\Delta v = 1$ bands, which covered a smaller range in line depth (§4.3.2), and was observed at a similar resolution. It is also important to note that there does not seem to be any strong difference in the slopes for the different bands, as was seen in the photospheric solar spectrum for the fundamental CO bands. The first overtone bands examined in Chapter 4 were all comprised of weak lines, and the degeneracy seen in the

fundamental bands and in these line-shifts were not present. Over the sunspot, the temperature is cooler and the $\Delta v = 2$ lines may be forming higher in the atmosphere, under conditions more akin to those seen for the fundamental bands in Chapter 4. However, the weak first overtone lines in the solar photosphere are less likely to demonstrate the degeneracy because the lines are weak and sensitive to noise, there is less of a “dynamic range” in line depth for the degeneracy to become apparent.

There are very few weak lines present in the sample; only 13 lines have line depths less than 30% of continuum. As such it is actually difficult to judge how the line depth and the velocity shifts behave. The majority of the lines (58%) have strengths greater than 50% that of continuum, which is stronger than any of the CO lines seen in the photospheric solar spectrum.

Figure 5.2 clearly shows that there is a velocity dependence upon line depth for the strongest lines. The slope, however, does appear to flatten very quickly, unlike the behavior seen for the photospheric studies. For all the bands present in the $\Delta v = 2$ sample, only the 3 – 1 band in the P Branch shows the degeneracy in line depth for a given velocity. The polynomial fit to the velocity/ J distribution is plotted as well as the actual 3 – 1 velocities.

Previous studies of vertical motion of sunspot are inconsistent. Beckers (1977) concluded there were no vertical mass motions in umbrae spectra, and Lites et al. 1991 found that the vertical motions of Umbral Dots had velocities of only a few hundreds of meters per second. However, Sobotka et al. (1994) concluded that vertical convective motions were present in the strong light bridges present in some umbrae, giving rise to line asymmetries with line core displacements of several hundred meters per second. Both the Lites et al. (1991) and Sobotka et al. (1994) studies concentrated on small scale features within the umbra. The FTS aperture for these observations spans an angular diameter much larger than these features, and some of these features may be present, but unremarked upon.

Wavenumber and Energy

The line shift distribution displays an apparent dependence upon wavenumber (Figure 5.3). This apparent dependence is clearest when only the strongest lines are examined. However, it is important to note that the bands also have a non-uniform distribution with wavenumber. When only a single band (e.g. the 2 – 0 band) is considered the range in wavenumber sampled can be small.

The energy/velocity distributions are similar to those seen in Chapter 4, with the strongest lines in an individual band corresponding to those lines near the peaks of the “arches”. In Chap-

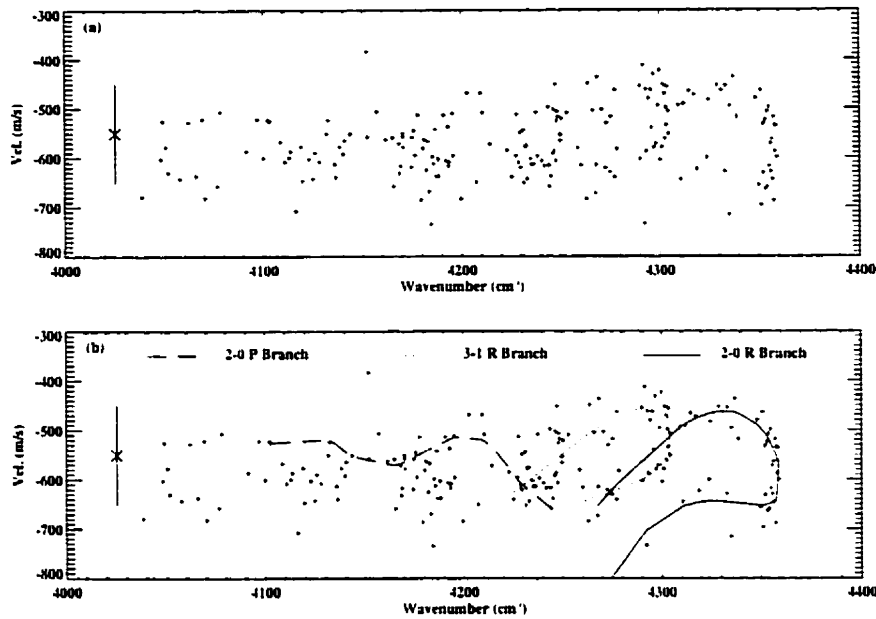


Figure 5.3: Line shift velocities versus wavenumber for the $\Delta v = 2$ CO sample. In (a) there is an apparent line-shift dependence on wavenumber, however, the different bands sample slightly different wavenumber regions (b), and the uneven distribution of line strengths may account for the apparent sensitivity to wavenumber.

ter 4, it was shown that there may be a degeneracy in the line core shift/lower excitation energies/wavenumber parameter space. In Figure 5.4, the line-shift/velocity distribution for the 3 – 1 R branch is shown with respect to both wavenumber (a) and lower excitation energy (b). Those lines with the smallest line core shifts correspond to the strongest lines also have the largest wavenumbers and are those with quantum numbers close to 20, the “peak” seen in Figure 5.4(b) and Figure 5.5. The behavior of the line-shifts with excitation energy matches the behavior with J , and is similar to the sensitivity of the line-shifts to wavenumber; apparently the dependencies upon wavenumber and lower excitation energy are almost the same. The variation in the distribution disappears when the effects of the other parameter is minimized by either considering only narrow bins in energy or wavenumber, or by applying a polynomial fit to the data in one parameter space and subtracting that fit from the data in the other parameter space. The “arching” with χ_l in Figure 5.5 is similar to what was seen for the CO fundamental bands in Figure 4.4. However the peaks of these distributions correspond to smaller values of J than was the case for the CO fundamental bands in the solar photospheric intensity spectrum.

The differences in velocity for two similar strength lines from the same branch are small, and if there is a trend as was found in Chapter 4, it is hard to distinguish because of the higher scatter in this sample. The distributions here are much shallower than those in Chapter 4, and the signal-

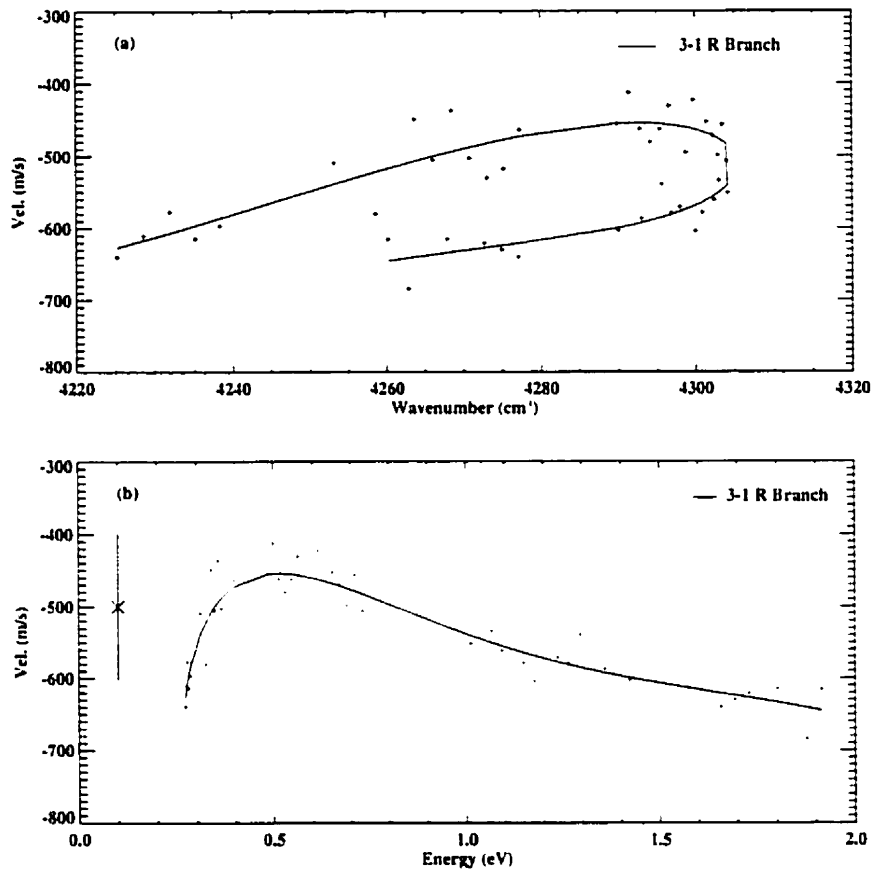


Figure 5.4: The CO 3 – 1 R branch: line velocity versus both wavenumber and χ_l . The maximum wavenumber corresponds to both the strongest lines and the peak in the velocity- χ_l plot. Those features with lower χ_l correspond to the lines that lie along the top half of the “arch” in (a), while those lines with higher χ_l (and J) are on the bottom half of the arch. Thus 2 lines from the same transition can have the same wavenumber, but slightly different velocity shifts ($\approx 100\text{ms}^{-1}$) and energies.

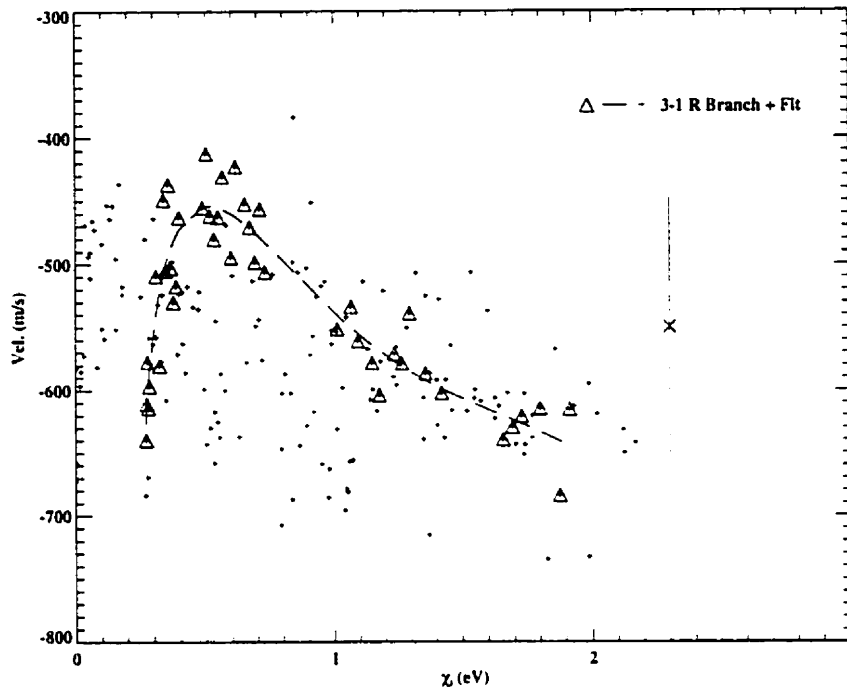


Figure 5.5: Lower excitation energy (χ_l) versus velocity shift for the $\Delta v = 2$ CO sample. Similar “arching” behavior was seen in Figure 4.4, with the peaks in the arches corresponding to the strongest lines. These peaks also correspond to those lines with $J \approx 20$.

to-noise is less. Unlike the case in Chapter 4, the umbral sample lacks a truly comprehensive large collection of lines from the same band that covers a range of line depths and energies, such as the $1 - 0$ band in the fundamental CO normal photosphere observations.

To examine the consistency of the observed line-shift distributions, median line bisectors have been determined for the 194 CO $\Delta v = 2$ lines. The bisectors have been binned in various combinations by strength, excitation energy and wavelength. Almost all of the different median bisectors (below depths of 10% of continuum) display a flattened version of the classical ‘C’ shape that is associated with convection. The spans of these bisectors are substantially less than that seen for the photospheric intensity bisectors examined in chapter 3, which is consistent with large-scale suppression of vertical motions by the sunspot. Figure 5.6(a)-(d) compares several different median bisectors. Part (a) shows the median bisectors for the three different line depth bins, which resemble the distribution of the line-shifts seen in Figure 5.2 rotated by 90 degrees. There very few weak lines in Figure 5.2, but the velocity span of the bisectors is comparable to the velocity span between the medium weak and strong lines in Figure 5.2.

Part (b) of Figure 5.6 compares the median bisectors for two different wavenumber regions and

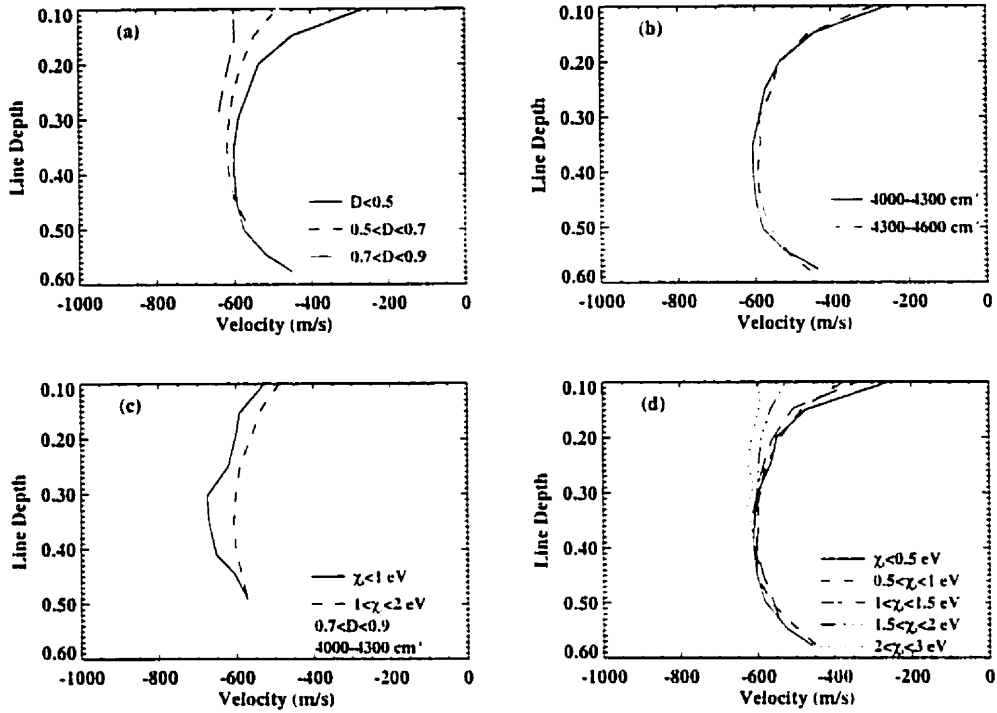


Figure 5.6: Median line bisectors for several different groups of CO $\Delta v = 2$ lines. (a) The median bisectors for the three different line depth bins, (b) the median bisectors for two different wavenumber bins. (c) the median bisectors for two different χ_l bins of the same line depth and wavenumber and (d) the median bisectors for several different χ_l bins.

are virtually indistinguishable from each other - which is consistent with there being little or no wavenumber dependence in the line-shifts. Part (c) compares the median bisectors for two different energy bins for lines of the same strength and wavenumber. Part (d) compares the median bisectors over χ_l , and while the bottom portions of the bisectors are all consistent, the top portions seem to deviate, the higher the energy the closer to the vertical the median bisector.

The general curves and shapes shown by the bisectors are consistent with the line-shift distributions, and are also consistent with the presence of small convective velocities in the umbra.

5.3.3 CO $\Delta v = 3$

The second overtone ($\Delta v = 3$) set of lines lies between 5600 and 6600 cm^{-1} , which unfortunately coincides with both strong telluric absorption and strong solar lines of other species. The telluric removal degrades the signal-to-noise in this region substantially - especially for wavenumbers between 5600 and 6000 cm^{-1} . The presence of both solar OH and H₂O bands increases the line density substantially. In total, 99 $\Delta v = 3$ lines meet the selection criteria. All of the lines are weak,

78% are weaker than 10% of the continuum, and the strongest line has a strength of only 15% that of continuum.

When the data set was initially examined for any trends, very little was apparent. All apparent dependence on wavenumber can be accounted for by the non-uniform distribution of line strengths with wavenumber. The stronger lines tend to be bluer, and the weaker lines tend to lie in the wavenumber region where the signal-to-noise is lowest. The weaker lines are more sensitive to signal-to-noise, and in general display larger scatter than lines of other strength (see Chapter 2). The “arch” or “crescent” behavior previously noted for the other sets of CO bands is not seen with this set. Neither is there any apparent dependence on line depth.

5.3.4 OH

$$\Delta v = 1$$

Between 2400 and 3900 cm^{-1} there are 50 lines from the OH fundamental bands that meet the selection criteria. All of these lines are P branch transitions, and all are moderately strong, with an average depth of 36% of continuum. As was done with the CO lines, the OH line shifts were binned by depth, wavenumber and quantum number.

Line Depth

The 50 lines in this sample span a depth range between 17 and 48% of continuum, and the majority of the lines are deeper than 30% the continuum intensity level. Figure 5.7 shows a clear depth dependence for the line shifts, even though there is substantial scatter. Each band samples a slightly different range of line depth, however there is some overlap between these bands. This is especially true for the 1 – 0 and 2 – 1 bands, both of which have the strongest lines in this sample. The slope of the linear fit in Figure 5.7 is less than one half that found for the CO fundamental sample in the photospheric solar spectrum over the same wavenumber region (see Figure 4.2). The data exhibits no sensitivity to wavenumber.

Quantum Number

A small dependence is seen when the OH line shifts are grouped by their bands and plotted versus quantum number (J) (Figure 5.8). The strongest lines tend to be members of either the 1 – 0 or 2 – 1 bands, however the 1 – 0 band samples higher quantum numbers (an average of $\langle J \rangle = 20$ for

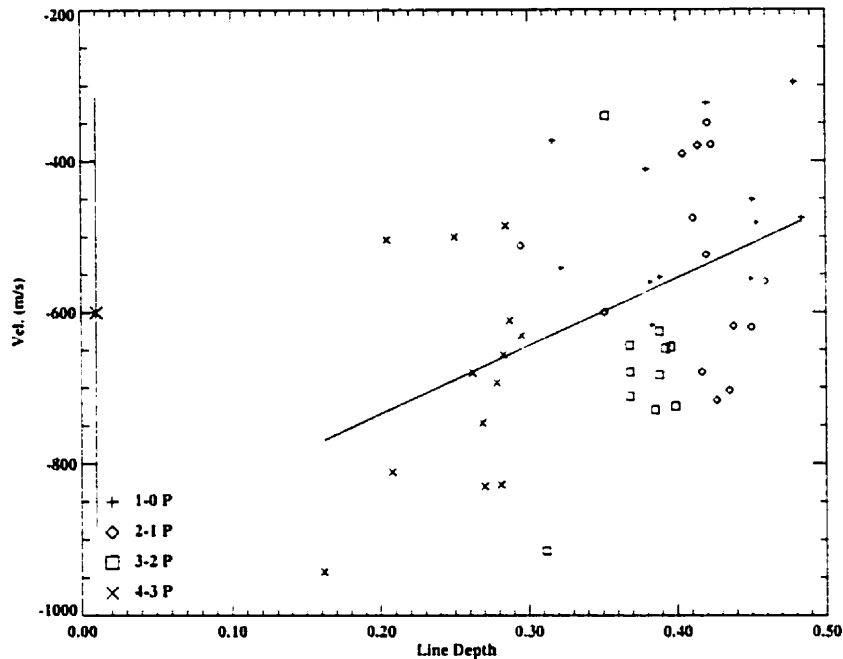


Figure 5.7: The different OH $\Delta v = 1$ P branch band velocities exhibit consistent behavior with line depth: a clear dependence upon line strength is present. The error bars reflect the upper limit estimation of positional uncertainty (see §5.2.3).

the 1 – 0 band versus $\langle J \rangle = 16$ for the 2 – 1 band) and have smaller blueshifts than the lines of similar strength from the 2 – 1 band. The differences between the two samples is not great, but similar behavior is found for all four bands. For a line of a given depth, the lower the quantum number, the greater the blueshift. However, this effect is not strong and is clearly secondary to the line depth sensitivity.

OH $\Delta v = 2$ P Branch

Line Depth

The majority of the 105 lines of the $\Delta v = 2$ P branch in this study are strong, with almost all the lines having depths greater than 30% of continuum. As was seen with the OH fundamental sample, there is a dependence upon line core depth. However, the slope, as Figure 5.9 shows, is approximately three times shallower than that for the $\Delta v = 1$ OH lines (see Figure 5.7). As with the fundamental OH lines, the different bands (2 – 0, 3 – 1, 4 – 2, 5 – 3) all occupy distinct ranges in line depth. Where the different bands overlap in line depth, no differences are discernible.

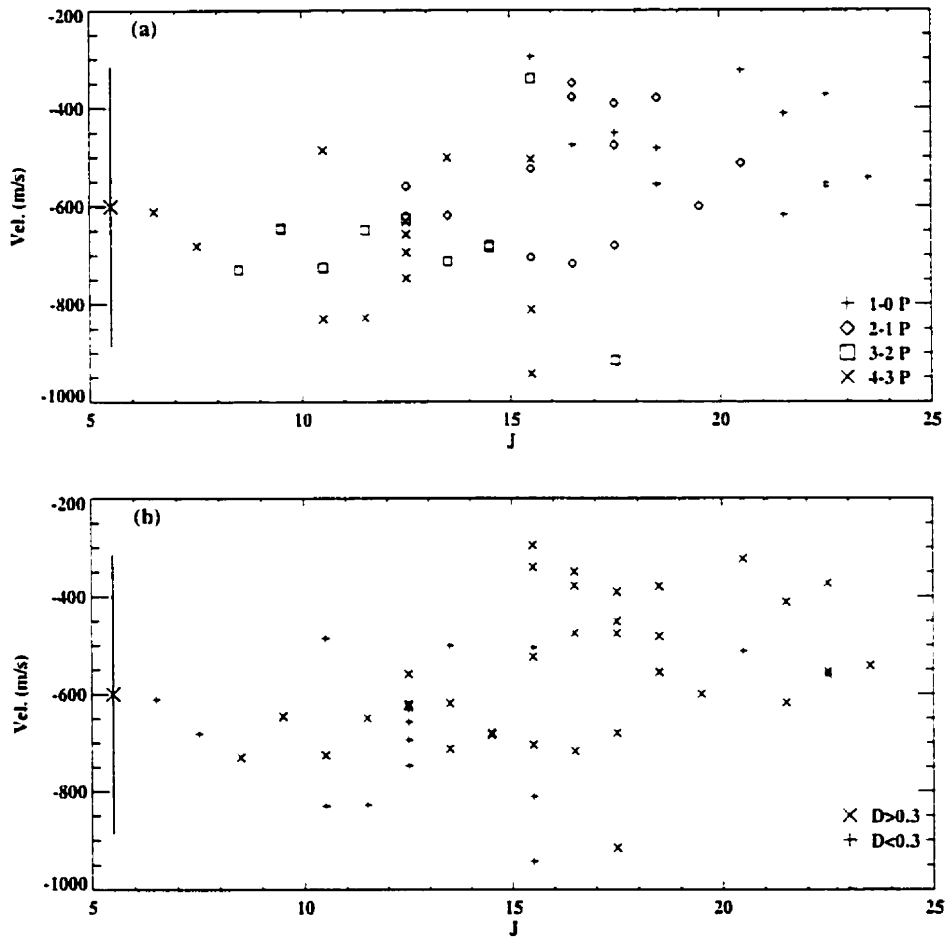


Figure 5.8: Velocity versus Quantum Number (J) by band (a) and line strength (b) for the $\Delta v = 1$ OH lines. There seems to be a small dependence of line shift upon J when the individual bands are examined, however this may be a result of the depth sensitivity. However, (b) shows that for all four bands at a given line strength, the lower the quantum number, the greater the blueshift.

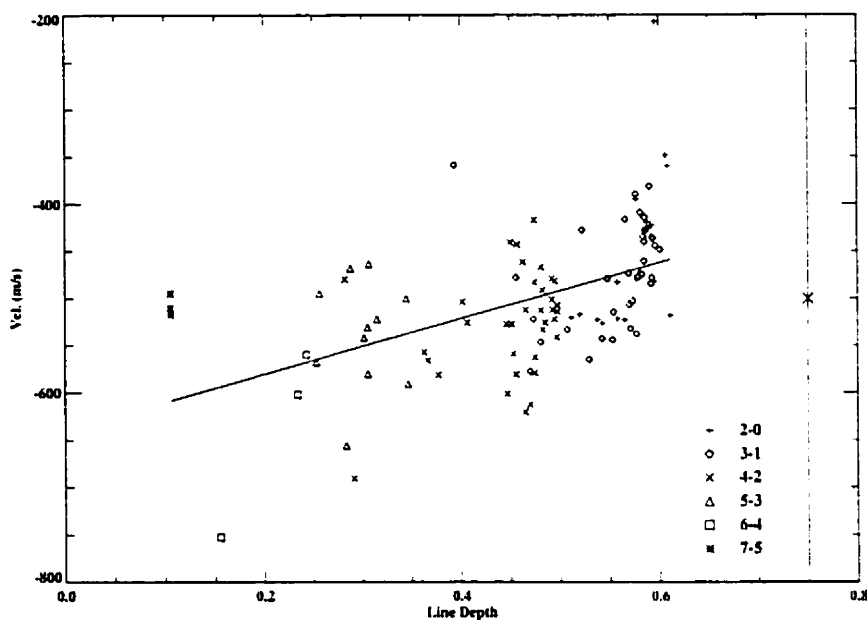


Figure 5.9: Line Depth versus velocity for the $\Delta v = 2$ OH sample. A clear dependence upon line depth is apparent, however its slope is approximately 1/3 that of the $\Delta v = 1$ OH sample. The error bars reflect the estimation of the upper limit of the positional uncertainties for the lines.

Wavenumber

The first overtone OH lines span a very large range in wavenumber, from approximately 4600 to 6800 cm^{-1} . When the data are divided into three line strength bins, only the bin for the deepest lines shows a dependence upon wavenumber with a slope that differs from zero by $> 1 \sigma$ (see Figure 5.10).

Quantum Number

If the velocities of the line shifts are plotted as a function of quantum number (J), no dependence is seen. However, when the sample is divided into line depth bins, the strongest lines do show a dependence upon J (see Figure 5.11). The slope for this bin is non-zero by a margin $\geq 3 \sigma$, and for the middle strength bin, the slope is $\approx 1 \sigma$ away from zero. However, when the sample is binned by the individual bands, no dependence of velocity on J is found.

OH $\Delta v = 2$ R Branch

Only 38 lines of the R branch of the first overtone meet the selection criteria. When the distributions of line velocities with respect to line depth and wavenumber are examined, no definitive

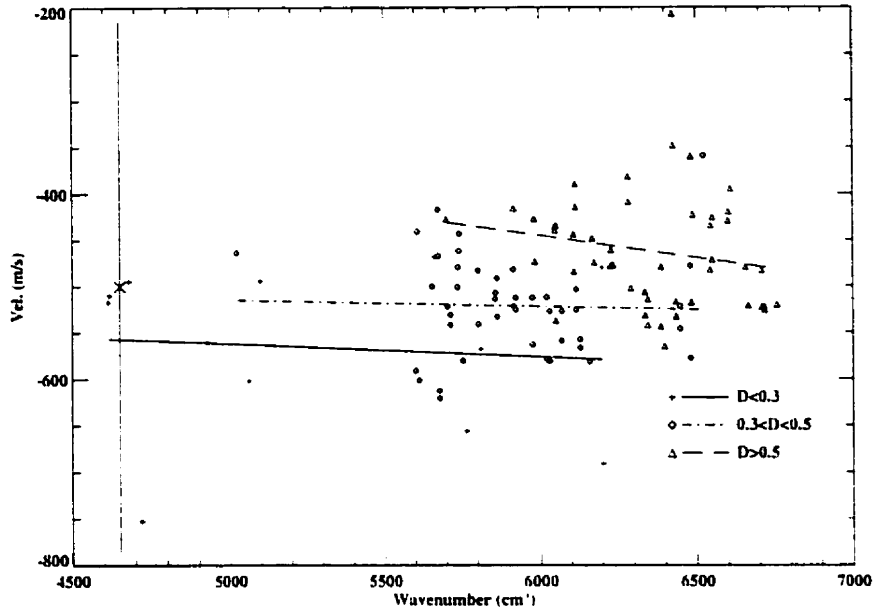


Figure 5.10: The $\Delta v = 2$ OH velocity shifts with respect to feature wavenumbers. Only the strongest lines show a clear ($> 1 \sigma$) sensitivity to wavenumber.

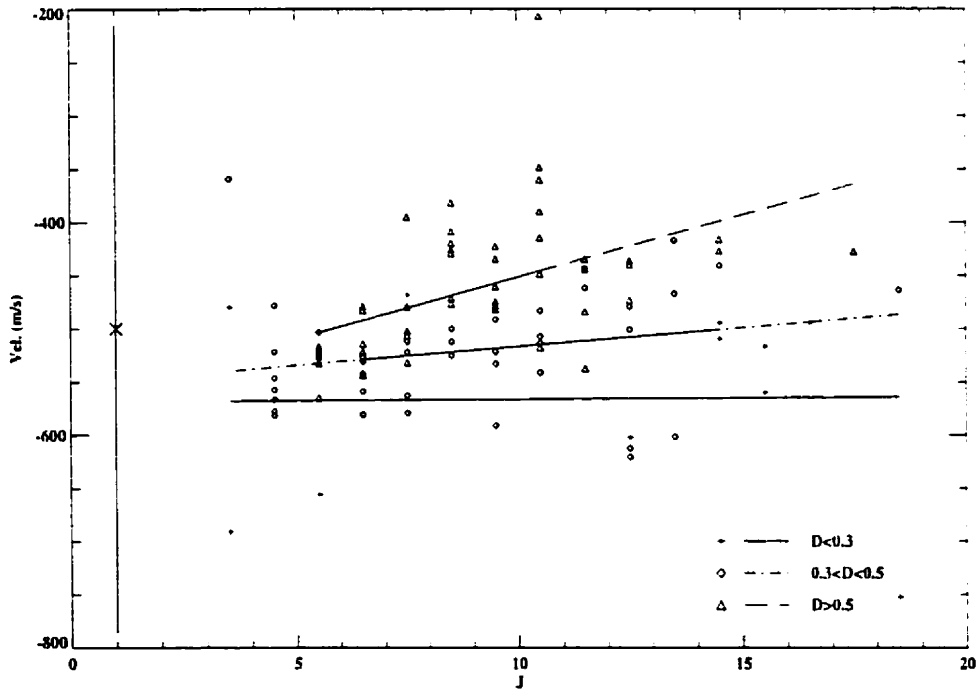


Figure 5.11: For the $\Delta v = 2$ OH line core shifts, only the strongest lines show any clear sensitivity to J . The other 2 strength bins displayed both have slopes within 1σ of zero.

dependencies are found. There may be a small dependence upon quantum number, however it has a slope that is less than 2σ away from zero. The wavenumber range is approximately 5800 to 6800 cm^{-1} , and each band is isolated from the others, unlike the P branch lines which have some overlap in wavenumber range. If we consider only the stronger lines, there appears to be a slight dependence (a slope within $\approx 2 \sigma$ of zero) on J – however, no other trends are apparent for this sample.

5.3.5 TiO

The Red/NIR sunspot spectrum is dominated by molecular TiO lines. The most prominent bands that contain relatively unblended features of sufficient strength are the γ ($\Delta v = -1, 0, +1$) bands. There are 78 lines that meet the selection criteria, and the majority of these lines are from the $\Delta v = 0$ band near $14,000 \text{ cm}^{-1}$. The distribution of line shifts show a small dependence upon line depth (with slopes within $\approx 1.9 \sigma$ from zero), however this dependence is in the opposite direction than was seen for all the other species in this study. For the TiO lines, the stronger lines are shifted more than the weaker lines (see Figure 5.12). The dependence itself is weak, approximately half that seen for the OH $\Delta v = 1$ R and P branch distributions and just under one quarter that of the CO $\Delta v = 2$ distribution.

Upon first inspection, there is an apparent dependence of line-shift on wavelength. However, when the lines are binned by line depth and the distribution of line-shifts over wavelength is examined, the slope of this dependence decreases to $\approx 1 \sigma$ away from zero. The distribution of line strengths with wavelength for TiO is non-uniform, with the weakest lines at longer wavelengths so the depth dependence accounts for the apparent wavelength dependence for the line-shifts. There is a small dependence upon quantum number J with a slope 2.4σ from zero (Figure 5.13). However, if the lines are binned by line depth, the slope of the line shifts as a function of J for each bin is within 1σ of zero. The exception to this is the bin for the strongest lines, which has a slope within 1.4σ of zero. Again, an apparent dependence for the line shifts is found to be due to a non-uniform distribution of line depths, with the weaker lines tending to have higher quantum numbers.

5.4 Discussion

The results of Chapter 4 demonstrated that the fundamental bands of CO can be used as a diagnostic for convective motions. In the solar umbral spectrum, the $4.6 \mu\text{m}$ region is heavily obscured by

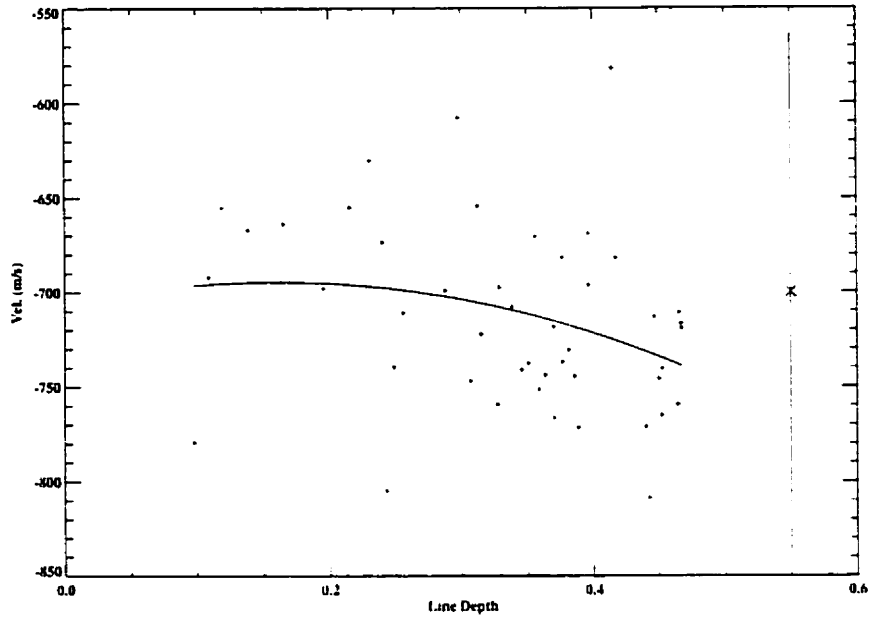


Figure 5.12: Line depth versus velocity shifts for the TiO γ bands. The TiO distribution displays behavior that is opposite to that of all the other species that have been studied: the stronger lines have an apparently larger line shift than the weaker lines. The error bar is the estimated upper limit for the positional uncertainty of an individual feature.

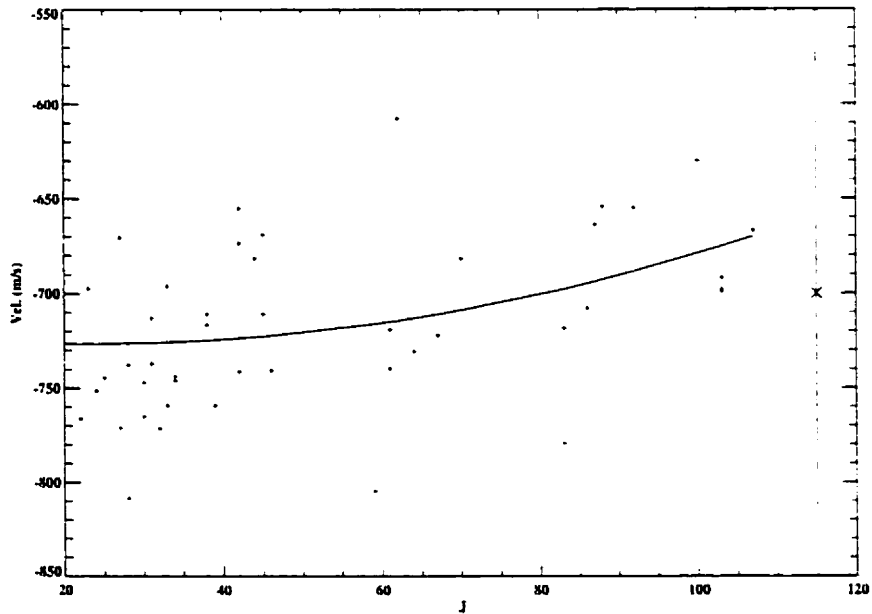


Figure 5.13: Quantum Number (J) versus line shift for the TiO sample. There is a slight dependence upon J , with the strongest lines showing the greatest sensitivity. However, the sensitivity is still small (the slope from the fit to the strongest lines is only 1.4σ away from 0.)

telluric lines and is difficult to observe, but the temperature in a sunspot is substantially cooler, so the $\Delta v = 2$ bands can be utilized in a similar manner to the way the CO fundamental bands were used in Chapter 4. The slope of the $\Delta v = 2$ CO distribution in Figure 5.2 is less than one quarter that of the $\Delta v = 1$ distribution in Figure 4.2. The velocity range between strong and weak $\Delta v = 2$ CO lines is only $\sim 200 \text{ ms}^{-1}$, indicating that the velocity differential is small, and in comparison with the photosphere, the motion is substantially suppressed. However, it is difficult to determine how much of this velocity is suppressed given that there are very few weak lines forming deep in the umbral photosphere. Previous studies indicate that there are no large scale vertical mass motions in umbrae (Beckers 1977), and the umbral dots exhibit velocities of only a few hundred meters per second, and contribute a relatively small minority of the umbral flux ($\sim 15\%$). This would lead to the expectation that the vertical velocities should be small, especially at the higher altitudes where strong lines are formed. One point to note when discussing the formation of lines over a sunspot is the Wilson Effect. Observations indicate that the umbral surface may be located ≈ 600 below the surface of the photosphere, and models attribute this depression in part to the lower local opacity and also possibly to the lower gas pressure for a given altitude (Foukal 1990). Thus, observations of umbral lines are sampling a greater physical depth than their counterparts in the photospheric spectrum; however the umbral temperature is $\approx 2000 \text{ K}$ cooler than the photospheric temperature.

However, the median bisectors and the line depth/line-shift distribution for the CO $\Delta v = 2$ lines have shapes and spans that are similar to those that have been associated with Strong Light Bridges and umbral dots (Sobotka et al. 1994; Lites et al. 1991). The convective velocity ($\sim 250 \text{ ms}^{-1}$) associated with these small scale features are comparable to the span in velocity seen in Figure 5.2 (or that of the median bisectors in Figure 5.6). Whether or not any of these small scale features were present when the FTS scans were obtained is unknown, however the instrument aperture spanned a diameter that would normally correspond to 5 to 7 photospheric granule cells.

This becomes further complicated with the realization that the actual physical depths sampled by the lines depend on the local opacity over the active regions. Stein and Nordlund (1998) point out that the physical location of a particular optical depth in the solar photosphere is actually spatially corrugated in altitude, and contours of constant opacity are not constant in physical depth over even a small region of the solar surface. While this result applies to the solar photosphere, it seems reasonable that a similar variation in altitude over a sunspot would also occur as the local opacity varies spatially. However, the amplitude of this corrugation may be different over an umbra. In the photosphere this variation is due to local changes in temperature and density, and the spatial

variations in temperature and density over this sunspot are not accurately known. While the Wilson Effect results from the lower local opacity over the umbra; and this implies the local gas pressure and density must also be lower; the umbral gas density and pressure are not easily measured (Foukal 1990). Sütterlin and Wiehr (1998) determined that the typical spatial temperature variations over an umbra were 700 K, due in large part to the 900-1300 K difference between the umbral dots and the diffuse umbral background. The actual physical area spanned by the aperture of the FTS is relatively small, corresponding to a diameter that would span approximately 5 to 7 granules in the photosphere. An integration over an area this small will probably be very sensitive to statistical variations. This situation is exacerbated by the potential spatial sensitivity to the opacity, and by the sensitivity of the line formation to temperature and to the length of its formation timescale – which determine at what altitude the individual lines actually form (see Chapter 4).

While there is little mass flux motion above an umbra, the neighboring penumbral regions have vigorous plasma motions associated with the Evershed flow (Schlichenmaier & Schmidt 1999), so in the overlying layers of the photosphere above the umbra there may be some material cross over, however it should not be substantial over the darkest portion of the umbra. Umbral oscillations are well established, but the periods for these oscillations are much shorter than the integration times (which were just under one hour each) used for the two spectra that were combined to give the infrared umbral atlas. While the umbral photosphere is radiative, it seems possible that some of the motions from the underlying convection (either oscillatory or the conventional overturning) should penetrate into the line formation region. If this is the case, then the relative upflow velocities for weaker lines should be greater than the velocities found for stronger lines – which is observed here for the OH and CO bands.

One of the primary purposes of this study is to examine diagnostics that may be applicable to cooler stars. The fundamental OH bands between 3.5 and 4.1 μm samples a region of the spectrum that is not covered by CO, and complements the $\Delta v = 2$ OH bands near 1.7 μm . The $\Delta v = 1$ OH lines are not prominent in the normal solar photosphere, but they have strong potential for application to cooler stars (such as K giants). The slope of the $\Delta v = 1$ distribution is approximately 3.5 times that of the $\Delta v = 2$ OH sample.

The $\Delta v = 2$ OH lines do show a small sensitivity to wavelength, with the strongest lines being the most sensitive – which is consistent with the results of earlier chapters. The wavelength region sampled by these lines is near 1.7 μm , the same wavelength region where the Fe I wavelength dependence noted in Chapter 3 was found to diminish substantially. The $\Delta v = 2$ band is not clearly

observed in the solar photospheric spectrum, but is apparent in the spectra of cooler stars. The strongest lines also show a sensitivity to quantum number, but unlike the CO lines, a “turnover” with J is not observed – although this may be a result of the paucity lines with higher values of J.

The TiO bands display some very unexpected behavior with line depth. The velocity/line depth distribution displays a trend opposite to what has been observed with all other species – the stronger the line the greater the blueshift. This implies that the light contributions to the stronger lines are dominated by upwelling material higher in the atmosphere, while the weaker lines coming from deeper in the atmosphere are moving at lower velocities – an inversion in the normal structure of the photosphere. However, the slope of this trend is very shallow, with a slope far less than that for the other species, and is within 2σ of a zero slope. This is further complicated by the small number of weak lines in the sample and the high number density of lines, which undermines the strength of the apparent trend. Clearly this result is inconclusive.

Chapter 6

Line Shifts in the Spectra of K Giants and Supergiants

6.1 Introduction

In the case of the Sun, the upper boundary of the solar convection zone lies just below the visible surface. Convective overshoot affects the line formation region and the granulation of the surface of the Sun is easily observed. For those stars cooler than the Sun, the atmospheric convection zone, driven by the ionization of hydrogen, lies deeper below the surface, and plays an important role in a number of different processes and phenomena: chemical mixing, abundance anomalies, hot bottom burning, generation of the magnetic dynamo, generation of acoustic and Alfvén waves, dredge-up and star spots are a few examples (Gray 1992). However, as the upper boundary of the convection zone recedes deeper into the star with decreasing temperature, the convection zone is less easily observed. The stellar granulation imprinted upon the surface is much less vigorous because the radiation produced by the granules has been absorbed and re-emitted as it passes through the lower portions of the line formation region (Dravins 1992). As a result, the convective signatures are less dramatic at cooler effective temperatures. However, Gray (1982) found that when average line bisectors are examined by spectral type, the spectral type G8V displayed the smallest line profile asymmetries, and the asymmetries increased slightly as later K stars were examined. This was attributed to a greater height penetration by the convective cells (Gray 1982). This becomes further complicated due to entanglement with composition. A lower metallicity decreases the opacity, and should allow for photons to escape from deeper within the atmosphere. Examinations of the line bisectors of two extremely metal-poor stars have been done by Allende Prieto et al. (1999), and have shown that the low metallicity stars have significantly larger bisector

velocity spans than comparable stars with solar abundance.

A change in $\log g$ should also alter the distribution of convective signatures. Lowering the gravity in the convection zone increases the local pressure scale heights, which results in an increase in the scale of a typical convection cell. Giant stars are expected to have a smaller number of cells upon their surface with larger relative surface areas, which should result in a higher scatter in measured velocities (Schwarzschild 1975; Dravins 1990). Recall that the net line-shift that is measured is a composite shift integrated over the whole surface of the star. If the number of cells is decreased the averaged velocity becomes more sensitive to the range of velocities, and this should be reflected in the scatter of the line-shift distributions (Dravins & Nordlund 1990).

This picture of granulation in solar-type stars is complicated by the existence of a “granulation boundary” on the Hertzsprung-Russell Diagram (Gray & Nagel 1989). This boundary extends from the early F dwarfs upwards to the early G supergiants. Those stars on the hot side of the boundary exhibit inverted ‘C’ bisectors, while those on the cool side of the boundary exhibit the typical ‘C’ bisectors. This characteristic of hotter stars is thought to be directly related to the physical extent of the superficial convection zone, however the shape and extent of the inverted bisectors imply that the “granules” on these stars are rising extremely rapidly, and comprise a relatively small amount of the star’s surface area (Gray 1992).

6.1.1 The G - K Giants and Supergiants

The G and K Giants and Supergiants provide an opportunity to study how the line-shift distributions behave with changes in T_{eff} and $\log g$. While it would be extremely interesting to use dwarf stars to probe the change in $\log g$ and T_{eff} , the giants are more useful because of their higher luminosity. Even moderate resolution observations of G and K dwarf stars can be quite time consuming – the more luminous giants are easier to observe.

An additional consideration, especially for cooler stars, is the extent of line blending. Giant stars have intrinsically narrower lines, and usually have low rotational velocities, and thus a smaller degree of blending. The line density in the visible portion of a cool giant star’s spectrum makes it extremely difficult to determine line-shifts – however the near infrared and infrared spectral regions have strong potential for examining line-shifts. Over this wavelength span the line density is lower than in the visible, the stars are highly luminous, and several different species are available for study. Many of these bands have already been studied in the solar photospheric and umbral spectra – which allows for direct comparisons to the Sun. In this chapter, we exploit the combination

of all these factors to examine the convective line shifts of a number of species in the spectrum of Arcturus, and the line-shift distributions of the $\Delta v = 2$ CO bands for several G and K Giants and Supergiants observed at the *Canada-France-Hawaii Telescope*.

While the line-shifts are determined with respect to absolute rest wavelengths, they are by no means absolute Doppler velocities. Each of these stars has a bulk radial velocity with respect to the observer and also a gravitational velocity shift, neither of which is established to the accuracy levels studied here. Rather, we are interested in the relative shapes of the distributions of line-shifts. Each individual line from a star will be affected by the same physical radial velocity and gravitational red-shift – which essentially amounts to a uniform shift in the entire velocity distribution, so the shape, slope and relative scatter of the distributions are unaffected.

6.2 Line-Shifts in Arcturus

Arcturus (α Boötes, HD 124897) is the brightest of the K giants (K1.5III) visible in the northern hemisphere. Arcturus has a long history as a spectroscopic standard, and has been studied extensively at high resolutions: most notably the *Photometric Atlas of the Spectrum of Arcturus* by Griffin (1968). The primary atlas for this study is that of Hinkle et al. (1995). *Infrared Atlas of the Arcturus Spectrum, 0.9 - 5.3 μ m*. This study has focused on the near- infrared and infrared wavelength regions of Arcturus because the high line density in the visible region produces a large number of blends and limits the potential candidate lines substantially. High resolution spectral atlases for Arcturus cover the wavelength range from the ultraviolet to the thermal infrared (for a list see Table 1 in Hinkle et al. 1995).

One of the advantages to using Arcturus as the fiducial cool star for this study, is the extent to which the observational characteristics of the star are known (see Table 2 in Hinkle et al. 1995). The radius of the star has been established via parallax and angular diameter observations. $R_{Arc} = 24.5 \pm 1.4 R_{\odot}$ (Di Benedetto & Foy 1986; Woolley et al. 1970): the effective temperature is estimated as $T_{eff} = 4290 \pm 30$ K and the surface gravity is $\log g = 1.94 \pm 0.05$ (Griffin & Lynas-Gray 1999), with a mass estimated between 0.5–1 M_{\odot} (Hinkle et al. 1995). The star has a lower metallicity than the Sun, $[Fe/H] = -0.68 \pm 0.02$ (Griffin & Lynas-Gray 1999). more consistent with that of globular cluster giants. Arcturus is known to be a radial velocity variable with multiple periods ranging from days to months, with an amplitude of ≈ 0.160 kms^{-1} (Hatzes & Cochran 1993), which is not unusual for an early K Giant (Hatzes & Cochran 1996).

The atlas of Hinkle et al. (1995) was obtained using an FTS at Kitt Peak on the 4 meter Mayall telescope. Details of the observational scans and the techniques used to optimize signal-to-noise and the reduction of the observations are given therein. The FWHM of the weak lines in Arcturus are $\sim 4 \text{ kms}^{-1}$ (Gray 1982), and the atlas has a resolving power of $\approx 100,000$, enough to resolve fully most of the spectral features. The signal-to-noise ratio at the peak in each filter for the scans was usually in excess of 100, however, for those regions of the scan heavily obscured by terrestrial telluric lines, the ratio was decreased substantially.

The atlas was a combination of scans taken through 9 different blocking filters, observed twice over two different seasons, midwinter and early summer, so as to take advantage of the maximum heliocentric velocity differential. Doing this allows the observation of stellar lines which are otherwise obscured by telluric lines. This also provided a redundancy check for errors in the spectra (Hinkle et al. 1995). The telluric lines were removed by a ratio of the Arcturus spectra with a terrestrial atmospheric spectrum. Those regions of the spectrum where the removal process was inadequate and reduced the signal-to-noise substantially were discarded. Since Arcturus is a radial-velocity variable, whose strongest mode has a period of just under 2 days and an amplitude of 160 ms^{-1} , the potential effects of this variability have to be considered. The individual scan observations from Hinkle et al. (1995) here are all of significantly shorter time spans than the 2 day period, and the *differential* shift in the line positions between the strongest and weakest lines should not be large. In addition to this, the redundancy of the two independent sets of observations observed at different times allow for a consistency check of the observed trends. As will be discussed in §6.2.2, the midwinter and early summer line-shift distributions are consistent with one another.

The atlas includes all the Doppler shifts used to adjust the scans to a common wavenumber scale in addition to the original and telluric spectra. Extensive line identifications, both molecular and atomic are also provided.

6.2.1 Line Selection

The species selected for study here were the same ones as used in Chapters 2 through 5: Fe I, CN, CO, and OH. The line positions and other characteristics for these species are discussed in these earlier chapters. The candidate line selection criteria and methodology are the same as those used for the solar observations, and the line positions were defined in the same manner.

While this instrument is not the same as those used for the observations in Chapters 2 through 5, it is a very similar design. Both of the KPNO instruments are continuous scan, double aperture

FTS's mounted on a stable platform, and the wavelengths are calibrated using laser metrology. The accuracy of the laser metrology restricts the accuracy in the measurement of the path differences. Hall et al. (1979) give the path difference *rms* accuracy as 0.002 waves at 6328 Å (the laser calibration wavelength), corresponding to 60 ms^{-1} at $1 \mu\text{m}$. All of the scans can be matched with one another using overlapping spectral lines, and the overall wavelength calibration is estimated to be accurate to 100 ms^{-1} .

6.2.2 Fe I

Wavenumber

One of the advantages that the Arcturus atlas provides is a means to examine the line-shift distributions during two different seasons. Because of the Earth's motion with respect to Arcturus, different sections of the spectrum are available at different times of the year. This permits a temporal analysis, to determine if there are any apparent differences in the distributions. When the distributions from the two sets of scans are compared, there are no clear or systematic differences found in the shapes or behavior of the line-shifts. In general, the winter spectrum provided a greater number of candidate lines for study, and for the rest of this chapter the Arcturus winter observations will be the principal source.

There are 176 Fe I lines in the winter spectrum that meet the selection criteria, with wavenumber coverage from $11,000$ to 4000 cm^{-1} (0.9 to $2.5 \mu\text{m}$). Figure 6.1 displays all 176 lines as a function of wavenumber. The lines have been binned by line strength and fit linearly. The bin for the strongest lines is the smallest (with only 8 members) and has the smallest range of wavenumber. The two medium strength bins both apparently exhibit a sensitivity to wavenumber. The weakest lines display a weak sensitivity that is very poorly constrained, and is very close to zero.

The summer spectrum of Arcturus contains 168 candidate Fe I lines over the same wavelength span. These lines display the same wavenumber dependence for the different bins, with the exception of the weakest lines. The weakest lines from the summer spectrum have a steep sensitivity to wavenumber, but the slope of the linear fit is still within one sigma of a zero slope – the scatter for these line-shifts is very high. Both the winter and summer spectra over the 4000 to $11,000 \text{ cm}^{-1}$ span are comprised of scans from three separate filters ($4000 - 6675$, $7400 - 8900$, $8900 - 10,950 \text{ cm}^{-1}$) obtained on different dates. These three bands all have relative Doppler velocities with one another, which were taken into account when the atlas was assembled (Hinkle et al. 1995).

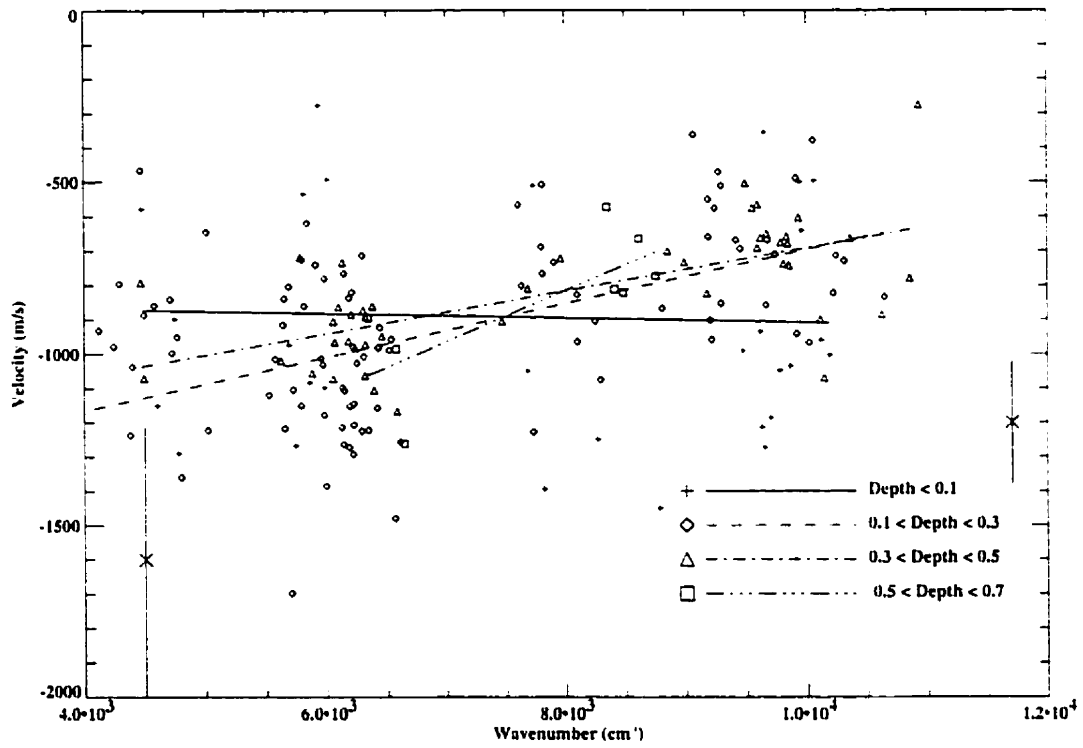


Figure 6.1: The 176 Fe I lines from the Arcturus Atlas, binned by line strength. An apparent dependence of line-shift on wavenumber is found for the three bins covering the strongest lines - although the bin for the strongest lines has a very small wavenumber range. The trend of line-shift with wavenumber is opposite of what was seen in the solar observations. The positional uncertainty at the wavenumber extremes are represented by the error bars.

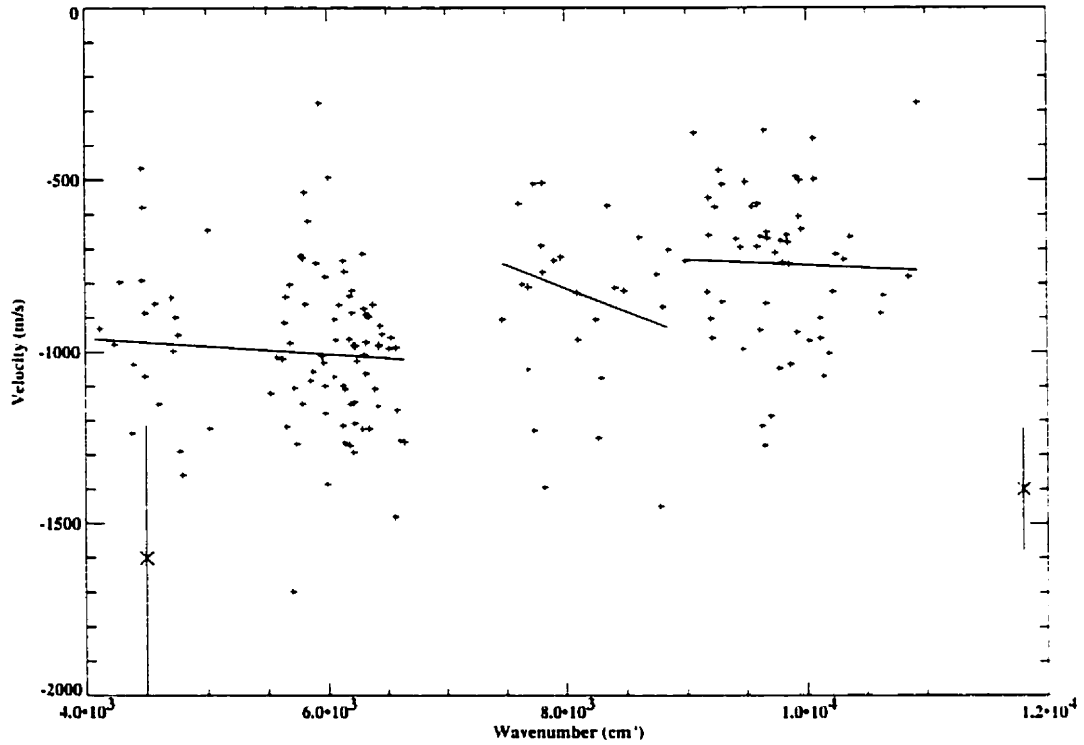


Figure 6.2: The line-shifts for the Fe I lines in the winter Arcturus spectrum over the three different bands. The trend with wavenumber noted in Figure 6.1 is not seen when the individual filter bands are examined. None of the different strength bins show any significant sensitivity to wavenumber for either the winter or the summer observations (all slopes are within one σ of zero). The wavenumber trend is probably a spurious result from a slight Doppler misalignment between the bands.

When the line-shifts in the individual scans are examined, the wavenumber sensitivity disappears. None of the various strength bins display a line-shift sensitivity to wavenumber that is not within one σ of zero. The largest span ($4000 - 6675 \text{ cm}^{-1}$) covers a very large range in wavenumber, and has a substantial number of candidate lines from the two medium strength bins (59 and 21 members), yet neither sample displays any clear sensitivity to wavenumber (see Figure 6.2). This observation holds for both the summer and the winter scans. When all the lines are considered across the scans, there is a general trend that the bluer lines exhibit smaller shifts. However, when the line-shifts in the individual filter bands are fit, the blue lines appear to have larger shifts, and the slopes for all three linear least squares fits are within one σ of zero.

The sensitivity seen for the Fe I lines across the scans in the infrared Arcturus atlas is the opposite of that seen in the visible solar flux (see Chapter 2) and the solar central intensity spectra (see Chapter 3). In the solar case, the bluer lines exhibited larger convective blue-shifts than comparable lines farther to the red. This wavelength dependence was seen to decrease at longer wavelengths, but was still apparent out to approximately $2 \mu\text{m}$. There is a strong possibility that the dependence of the line-shifts upon wavenumber seen in the Arcturus data is an artifact resulting from small differences in the Doppler corrections between the different scans. This is supported by the lack of any clear dependence upon wavenumber seen for any of the line depth bins within the six different filter bands (3 winter and 3 summer). However, the observation that both the composite winter and summer spectra exhibit very similar wavenumber sensitivities for the different bins implies that there may be a systematic error in the Doppler corrections applied to the bands. The consistency in the observed distributions for the two different seasons indicates that the effect of Arcturus' radial-velocity variability upon the observed line positions is relatively small. As was seen in Chapter 3, even solar spectra which are supposed to be calibrated to rest wavelengths, can show Doppler offsets of $\approx 200 \text{ ms}^{-1}$. In order to compensate for this potential problem, the different scans will be examined independently.

Line Depth

The Fe I line-shifts exhibit a very small dependence upon line depth, as shown in Figure 6.3(a)-(c). Both the linear and the parabolic fits are very shallow, and the quality of the fits (as judged by the χ^2 of the fits) are poor. This can largely be attributed to the significant scatter, especially for the weak lines. If a least-squares linear fit is done to all of the distributions with the weakest lines removed, the quality of the fit improves, while the slopes change only slightly (all three slopes are

approximately the same, and all have slopes close to one σ away from zero). The degree of the dependence of the line-shifts on depth does not change when wavenumber and χ_l are accounted for.

There is a significant amount of scatter for the weak and medium strength lines in Figure 6.3. The scatter in the Arcturus observations is far greater than the scatter seen in the solar observations, even when the solar observations are resampled and degraded to a comparable quality. In Figure 6.4, the solar NIR spectrum used in Chapter 3 (Wallace et al. 1993) was degraded and resampled to $\lambda/\Delta\lambda \approx 100,000$ and $S/N \approx 100$ (following the same method as used in §2.3 and 2.2.2). The 262 lines that met the selection criteria in §3.5 were then taken from this new solar spectrum and their line-shifts were determined. The scatter for the weakest lines in this degraded NIR solar spectrum has increased substantially, but is still substantially less than that seen for the Fe I lines from the Arcturus spectrum. This may be a reflection of the lower surface gravity of Arcturus, which is expected to result in a greater scatter of line-shift wavelengths. This can be attributed to the increase in the local scale height, and thus the size of the convection cells. If the granules are larger, their total number decreases, and this results in greater statistical variations.

The slope of the least squares fit to the NIR solar line-shifts with line depth (neglecting the weakest lines, with depths < 0.1) is slightly steeper than those found for the Arcturus line-shifts in Figure 6.3 (slopes of 403 versus ≈ 250 for Arcturus). A close inspection of Figure 6.4 also demonstrates that even at this resolving power, a parabolic fit is superior to a linear fit when the sample size is as large as the solar NIR sample is. The slope of the fit to the weak lines is clearly shallower than that for the stronger lines.

An additional factor to consider is that the NIR solar sample is a central intensity spectrum. In Chapter 3 it was shown that the limb darkening actually enhanced the contrast between the red and blue visible lines when the visible flux spectrum was compared to the visible central intensity spectrum. While this limb darkening effect should be smaller at longer wavelengths, it should still be present. This implies that the actual solar flux NIR distribution should be a little steeper than the central intensity observations used here, however this should be a minor difference. An additional important difference between the solar and Arcturus data sets (aside from their size), is the solar set contains a number of much stronger Fe I lines, and this alters the distribution somewhat.

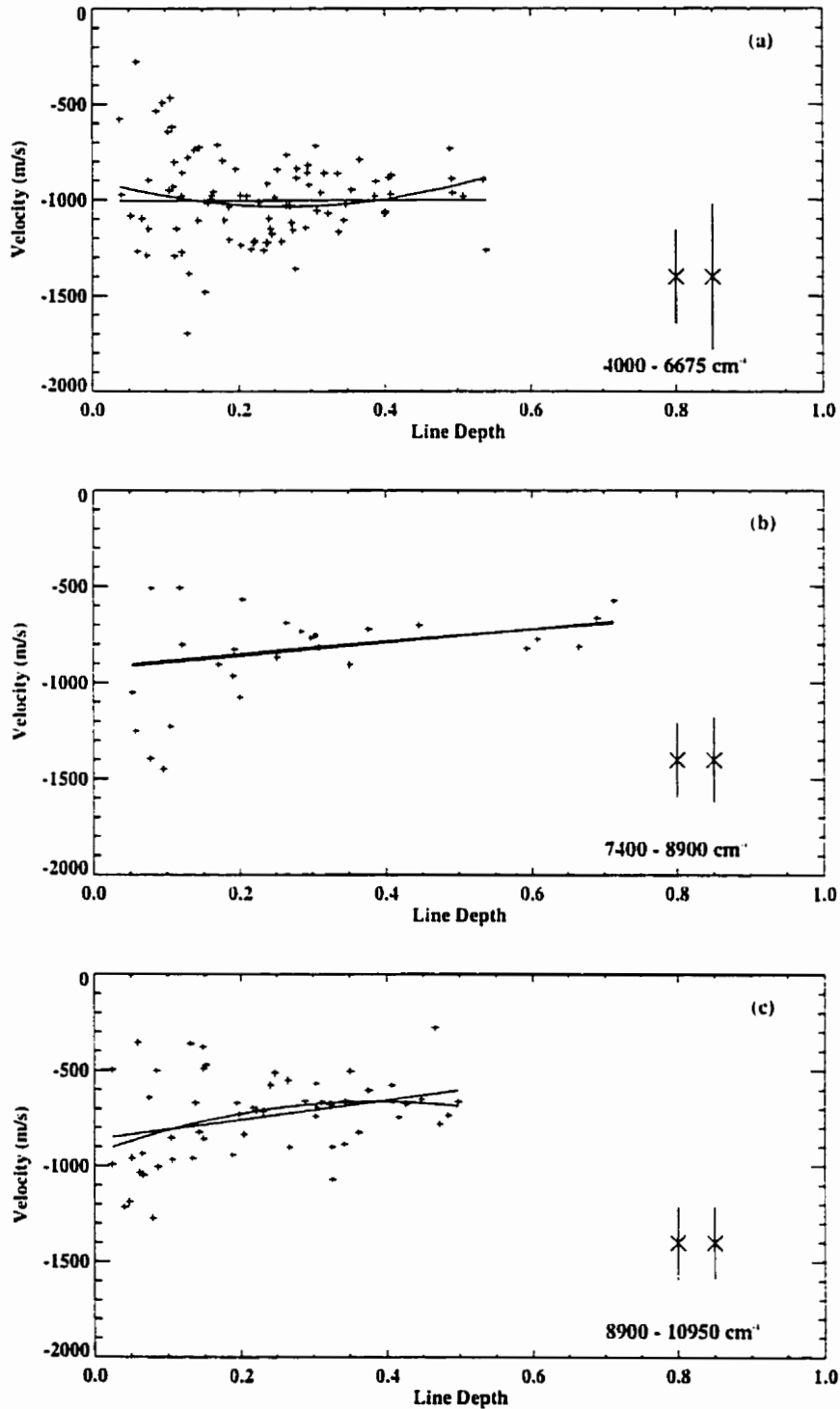


Figure 6.3: The Fe I line depth/line-shift distributions from each filter band in the Arcturus winter spectrum. The dependence of the line-shifts upon line depth is slight, and almost completely overwhelmed by scatter. Two fits are displayed, a linear fit and a parabolic least squares fit. The error bars reflect the range in positional uncertainty for each band.

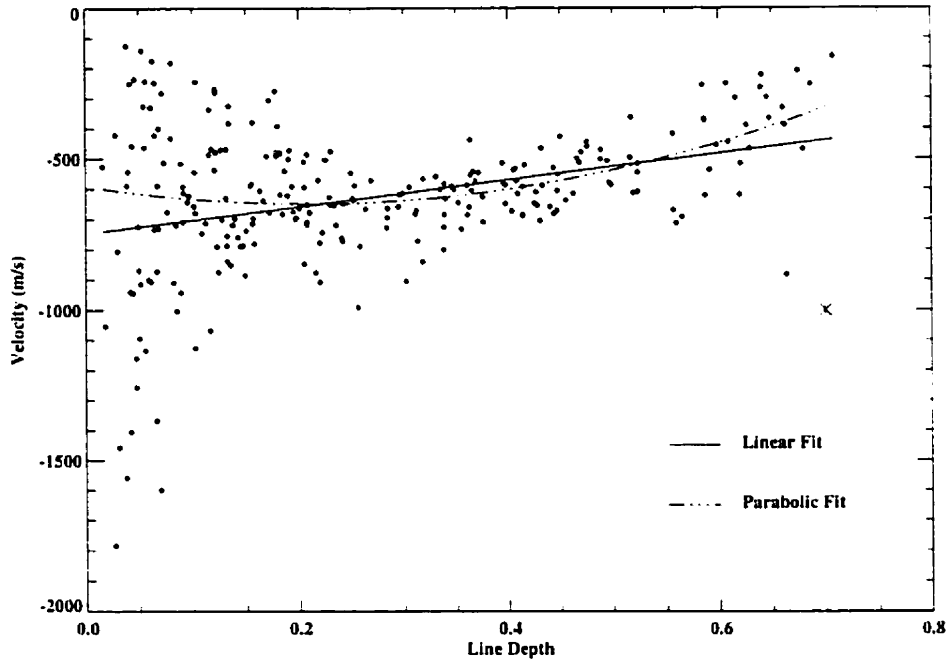


Figure 6.4: The Fe I line-shifts from the solar NIR samples (see Chapter 3), degraded and resampled to S/N of 100 and $\lambda/\Delta\lambda = 10^5$. The slope of this distribution is similar to that of the Arcturus sample, but with far less scatter.

Excitation Energy (χ_I)

Previous studies have found evidence that those lines with higher χ_I have larger blueshifts (Dravins et al. 1981; Dravins et al. 1986; Nadeau 1988; Nadeau & Maillard 1988). However, the results of Chapters 2 and 3 imply that this sensitivity is weak, and may be questionable in some cases. When the Fe I lines from the winter observations of Arcturus are examined, there appears to be a small dependence upon χ_I . Figure 6.5(a) shows all 176 lines, as a function of χ_I . This distribution of line-shifts resembles Figures 2.2 and 3.3, with most of the low energy lines having smaller shifts, and the higher energy lines having a wide dispersion of associated velocities.

To examine the possibility of a dependence upon χ_I for the Arcturus data, the lines from each filter band have been binned by line strength, to account for the effects of the other two parameters. The bin for the strongest lines has been ignored because of its small size (only 8 members spread between all three filter bands). There appears to be some sensitivity to χ_I over all three filter bands, however this sensitivity is highly questionable. All 9 fits in 6.5(b)-(d) are poorly constrained, and only two of the nine bins have a slope that is not within one σ of zero (the medium-weak lines in the $4000\text{-}6675\text{ cm}^{-1}$ filter, $m = -61 \pm 53$ and the medium-strong lines in the $8900\text{-}10950\text{ cm}^{-1}$ filter, $m = -63 \pm 37$). While there may be a sensitivity to χ_I , it is not clearly shown by this data.

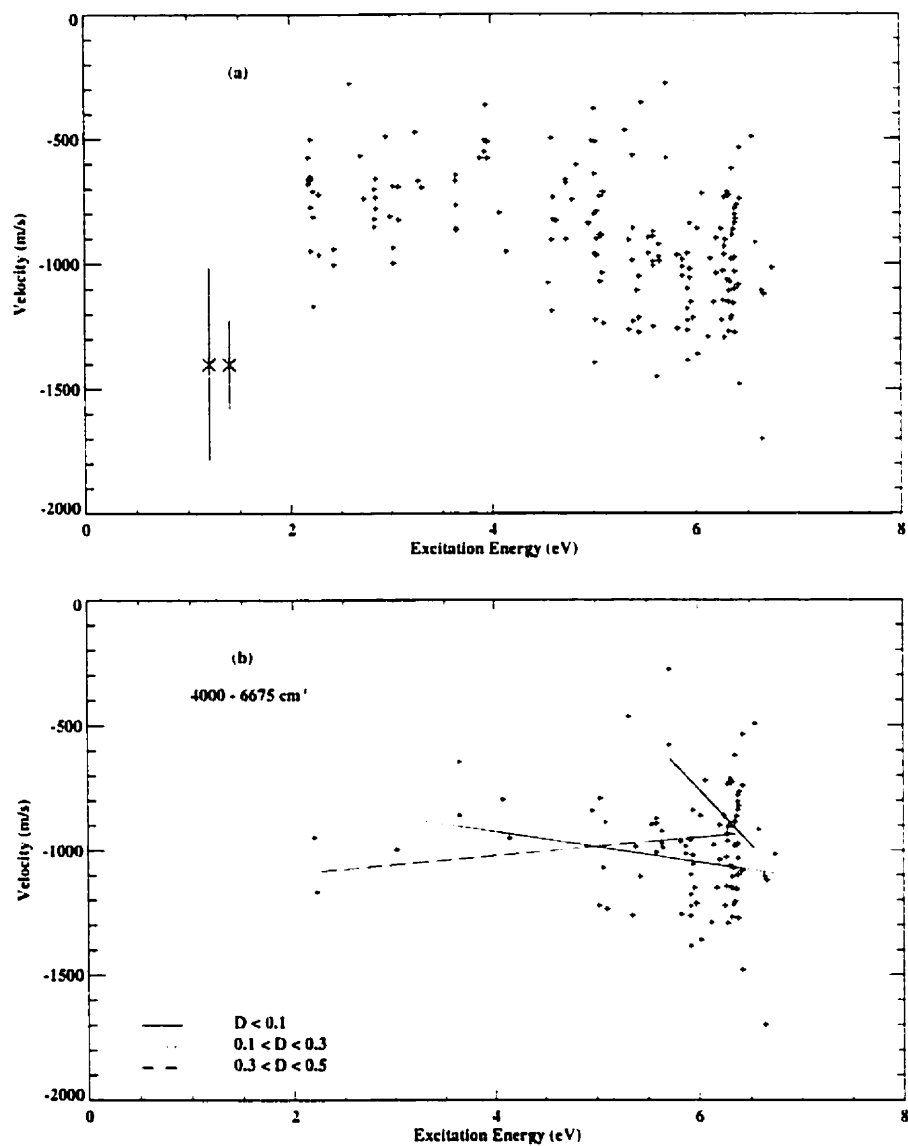
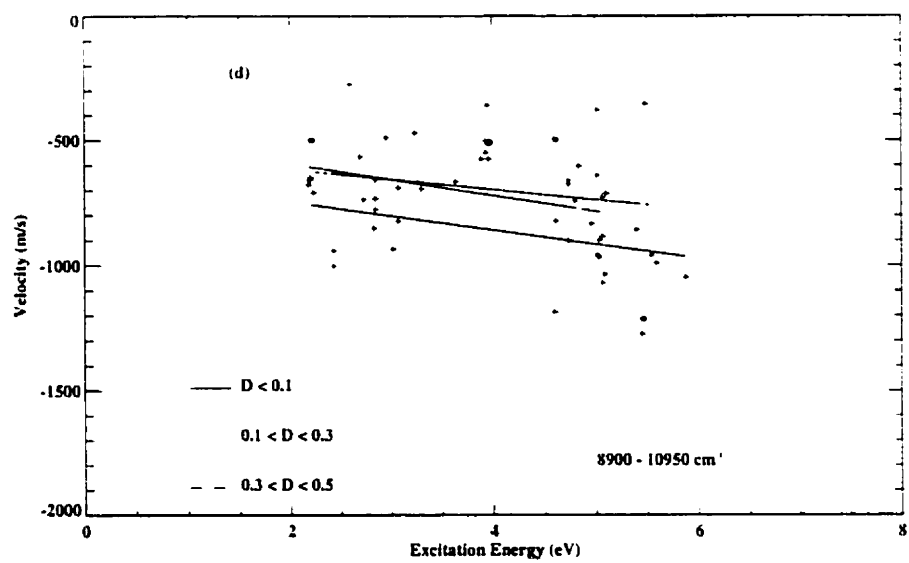
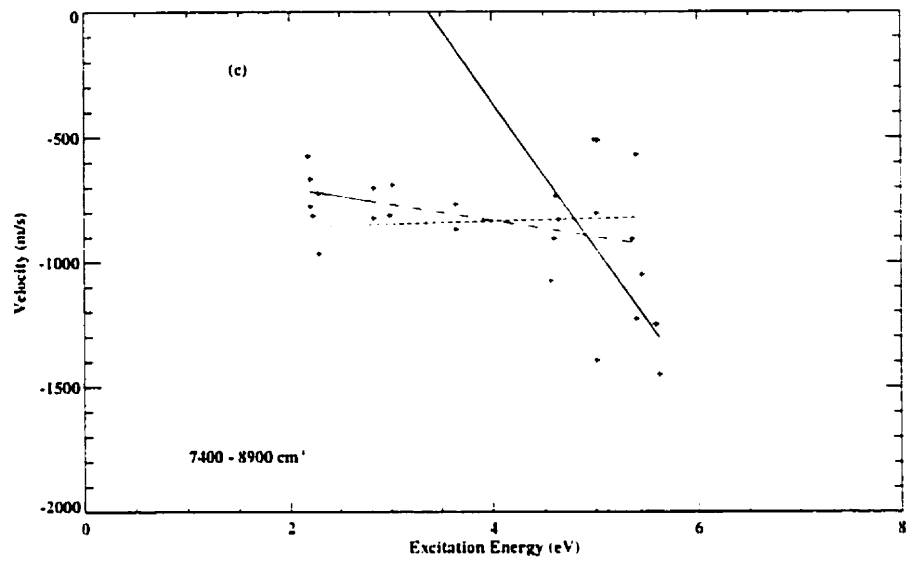


Figure 6.5: The Fe I lines display a small sensitivity to v_t . Part (a) displays the whole distribution, including the positional error estimations for the entire wavenumber range. In (b)-(d) the line-shifts for each filter band are binned by line depth. Any sensitivity is clearly questionable - only two bins have reasonable fits with slopes more than one σ from 0.



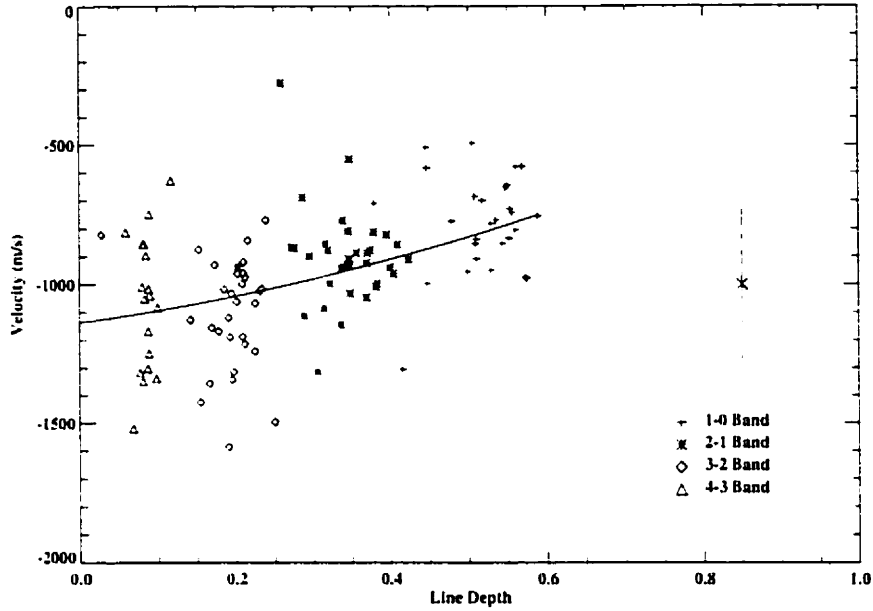


Figure 6.6: The depth dependence for the OH $\Delta v = 1$ bands. This distribution is a little steeper than those for the Fe I lines. Each band (1 – 0, 2 – 1, etc.) occupies a distinctive range in line depth. The plotted curve is a least-squares parabolic fit to the line-shifts, and 79% of the lines lie within 3σ of this curve.

6.2.3 OH

OH is not a prominent source of lines in the solar photospheric spectrum; however, it is in the infrared spectrum of Arcturus. The OH Meinel system has two major sets of bands in Arcturus: $\Delta v = 1$ and 2. There are 111 $\Delta v = 1$ lines that meet the selection criteria, between 2400 and 3400 cm^{-1} , and include the bands from 1 – 0 to 4 – 3. Figure 6.6 demonstrates that there is a clear line-shift dependence upon line depth for the OH lines. This distribution is actually a little steeper than those seen for the Fe I lines in Figure 6.2. The error estimation of $\sigma = 272 \text{ ms}^{-1}$ in the line positions is based upon the combination of the average $O - C$ in the laboratory rest positions (Abrams et al. 1994) (see §5.3.3) and the estimation of the wavelength calibration uncertainty. The curve is a least-squares parabolic fit to the line positions, and 71% of the line-shifts lie within 1σ of the fit, while 79% lie within 3σ of the parabolic fit.

Each OH band (such as 1 – 0) samples a distinct range in line depth, with the 1 – 0 lines the strongest. When the line-shifts are examined as a function of wavenumber, there is an apparent sensitivity – however this is merely a result of the uneven distribution of the different sequences over the wavenumber domain. The lower transition bands tend to have stronger lines, and are found at larger wavenumbers.

The $\Delta v = 2$ OH bands lie between 5400 and 6800 cm^{-1} . When the 48 lines that meet the selection criteria are examined there is no apparent sensitivity to line depth. However there does appear to be a very weak dependence upon wavenumber, with a very shallow slope $\approx 1 \sigma$ from zero. The lines to the blue tend to be shifted more than those in the red, with a very shallow slope, corresponding to a difference of 140 ms^{-1} across the wavenumber range. When the sample is broken up into the individual bands, the bands occupy distinct ranges of both line depth and wavenumber, with the strongest band (2-0, line depth $\approx 25 - 35\%$) tending to be the bluest. The non-uniform distribution of line strengths over wavenumber may account for the lack of a depth dependence in this sample.

6.2.4 CN

There are four sets of CN bands found in the near-infrared and infrared spectrum of Arcturus: $\Delta v = -2, -1, 0,$ and $+1$. For the $\Delta v = 1$ bands there are 75 lines split between the 2-1 and 1-0 bands in the near-infrared. In both bands, all three branches (P, Q and R) are present. The lines for both bands tend to be weak, with the 1-0 lines being slightly stronger (with an average line depth of 14% of continuum compared to 8% for the 2-1 transitions). There are no clear differences between the different $\Delta v = 1$ branches, which may very well simply reflect both the small sample sizes and the relative positional errors for the CN lines.

The $\Delta v = 0$ transitions (110 in all) are a little stronger (average depth of 17% of continuum) and have average shifts slightly less than the 2-1 and 1-0 sequences: $\langle v \rangle = -656 \text{ ms}^{-1}$ ($\sigma \approx 302$), versus -873 ms^{-1} ($\sigma \approx 296$) and -784 ms^{-1} ($\sigma \approx 384$) respectively. However, these differences are small, and well within the scatter for each sample. There are no apparent trends with line depth, wavenumber or quantum number.

The $\Delta v = -1$ and -2 sets of bands are both comprised of weak lines, for the most part with strengths less than 10% that of continuum, and are found between 6100 and 6400 cm^{-1} and 4400 and 5100 cm^{-1} respectively. There are 39 lines in the $\Delta v = -1$ sample and 57 in the $\Delta v = -2$ sample. There are no trends found with either wavenumber or strength with these samples, which is not surprising given the relative weaknesses of the lines. The average velocity shift for the $\Delta v = -1$ sample is -713 ms^{-1} ($\sigma \approx 234$), and the average velocity shift for the $\Delta v = -2$ sample is -761 ms^{-1} ($\sigma \approx 420$).

6.2.5 CO

There are three sets of bands of CO present in the Arcturus spectrum: $\Delta v = 1, 2$ and 3 . The $\Delta v = 1$ sample lies between 1800 and 2200 cm^{-1} , and 119 lines meet the selection criteria. The small size of the sample is due to telluric opacity blocking much of the $5 \mu\text{m}$ region, combined with a change in the relative populations of the different CO states due to Arcturus' lower temperature. These 119 lines sample bands from $1 - 0$ to $14 - 13$; the majority (65%) of these lines belong to the R branch. Unlike the situation in Chapter 4, the individual bands for each branch do not have high populations: the $5 - 4$ R band (with the largest number of lines) has only 9 members. This makes it extremely difficult to observe the fine detail that was apparent in the solar case. This is further complicated by the lower signal-to-noise of the Arcturus observations. This wavenumber region is heavily obscured by telluric lines, which results in greatly reduced signal-to-noise. However, while the amount of detail available in the solar observations cannot be matched, there are still some clear trends with these lines.

The $\Delta v = 1$ lines show a clear sensitivity to line depth (Figure 6.7). The distribution is not nearly as narrow as that seen in Figure 4.2, and none of the individual bands (e.g. $1 - 0$) sample the entire depth range. Instead, most of the members of a particular band that meet our criteria are found in approximately the same depth range.

The slope of the distribution is shallower than that seen in the solar CO lines. ($m_{\text{Arc}} = 1166 \pm 164$), although the resolution is approximately $1/2$ that of the ATMOS spectrum. If the ATMOS data is resampled and degraded to approximately match the Arcturus spectrum, the slope of the distribution of solar line-shifts becomes $m_{\odot} = 1451 \pm 24$. The solar $\Delta v = 1$ CO lines are taken from the ATMOS atlas, and while this atlas is a central intensity spectrum, the integration region spanned by the instrument aperture is very broad, corresponding to $0.27 R_{\odot}$. The ATMOS atlas is intermediary in nature between the other central intensity solar atlases and the flux observations. While the geometric surface of integration is large and contains some off axis contributions, it does not extend close to the solar limb (for $\lambda \leq 4.97 \mu\text{m}$). The line-shift distributions from the flux observations of Arcturus include contributions to the profile from the limb, and this will affect the slope of this distribution when compared to the solar case. In Chapter 3 the differences between the line-shifts from the visible flux and central-intensity observations indicated that the effects of limb darkening and limb contributions slightly enhanced the line-shift differences between the strong and weak lines. However, this was shown only for the visible, and the differences were found to

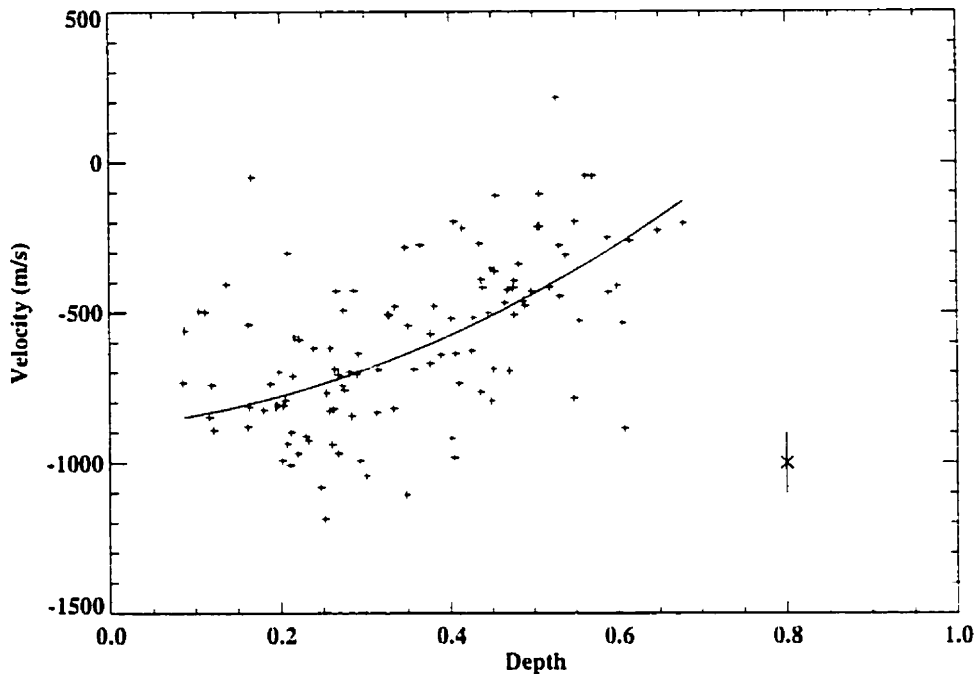


Figure 6.7: The 119 CO $\Delta v = 1$ lines show a clear dependence upon line depth, however the trends that were seen for the individual bands in the solar CO observations are not apparent here. The slope of the distribution is a little bit shallower than the solar case at the same resolving power.

decrease at longer wavelengths. The effects of contributions from the limb versus the disk center at infrared wavelengths have not been established, however the results of Chapter 3 imply that these differences will be secondary to the line depth sensitivity.

One important characteristic to note is that the scatter of the Arcturus CO line-shifts about their least squares fit is substantially larger than the scatter for the solar CO lines at the same approximate S/N and resolving power ($\sigma_{Arc} = 260$, $\sigma_{\odot} = 129$). The change in the signal-to-noise for the ATMOS atlas completely overwhelms the band structure in the line-shifts noted in §4.3.2. Clearly, the detailed “arching” structure seen in Figure 4.4 requires high signal-to-noise ratios.

The $\Delta v = 1$ lines do not show any sensitivity to wavenumber when line depth is accounted for. When the lower excitation energy is examined, it is found that there is a correspondence between those lines with low χ_l and the stronger lines, so the apparent trends in energy are reflecting the same dependence as the line depth. When binned by line depth, the line-shift sensitivity to χ_l disappears.

The CO $\Delta v = 2$ bands are very promising because this is a wavelength region where the amount of telluric obscuration is relatively low compared to the $\Delta v = 1$ region. There are 158 $\Delta v = 2$ lines

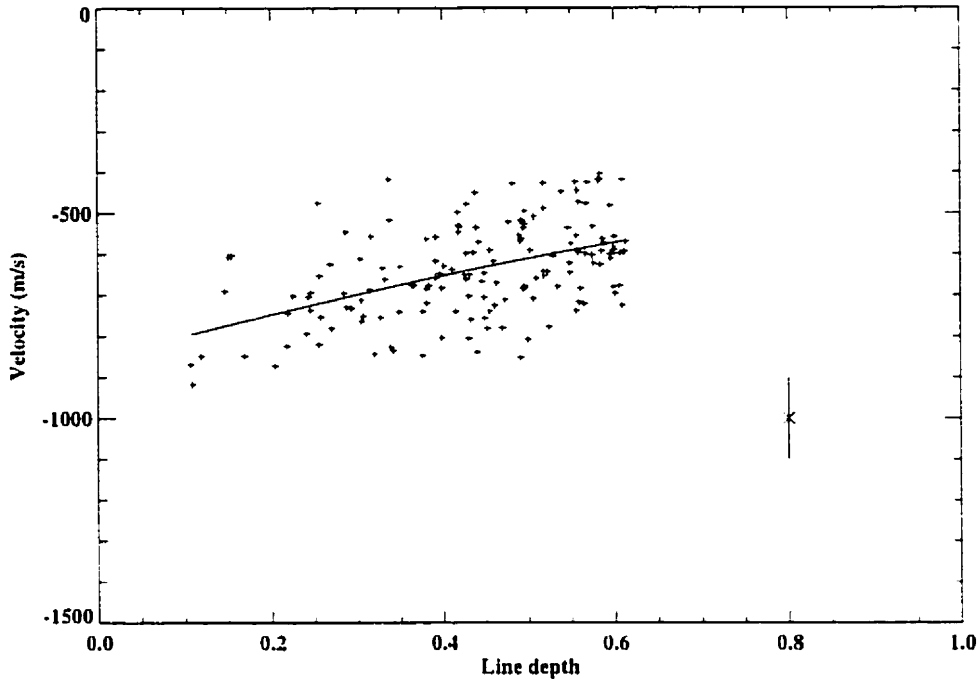


Figure 6.8: The $\Delta v = 2$ CO band as a function of line depth. There is a large scatter about the parabolic fit, but the trend with line depth is clear.

that meet the selection criteria, ranging from the 2–0 to the 7–5 bands. In the solar observations (see §4.3.3), the $\Delta v = 2$ sample was primarily composed of weak lines. For Arcturus, there is a much wider range of line strengths available. In Figure 6.8, there is a shallow but clear dependence of line-shift upon line depth. This band also exhibits a wide scatter, with a scatter of $\sigma \approx 100 \text{ ms}^{-1}$ about the least-squares parabolic fit in Figure 6.8.

The 2–0 and 3–1 R branch bands are the largest samples in the $\Delta v = 2$ sequence, with 28 and 34 lines respectively. Both span a wide range in line depth, χ_l and quantum number, and are the best samples to use for examining trends. The 2–0 band has the largest coverage in line strength, with both strong and weak lines. When a linear least-squares fit is applied to the line-shift/line depth distribution, the distribution has a slightly shallower slope than that found for the whole data set. Similarly, while having relatively few weak lines, the 3–1 band also has a slightly shallower slope than the whole distribution. However, in both cases the slopes lie within one sigma of the slope of the fit to the full data set. This is similar to the behavior noted in the solar CO $\Delta v = 1$ sample (§4.3.2) where the slopes of the fits to the line-shift/line depth distributions for the different bands steepen as the band numbers increased.

There are no sensitivities to wavenumber in this data set, and any sensitivity to χ_l and quantum

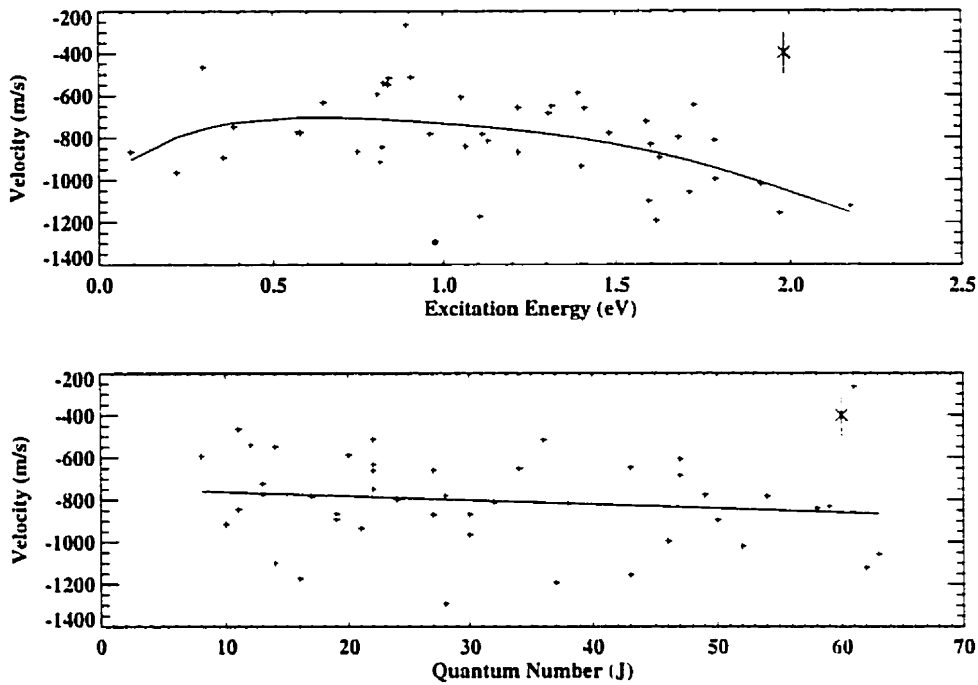


Figure 6.9: The $\Delta v = 3$ CO band as a function of lower excitation energy (in eV above the lowest level) (a). These are all weak lines, but there is a similarity between this distribution and what was seen in Figure 4.4. The lines with the higher energies tend to be both weaker and to also have larger blue-shifts. The $\Delta v=3$ CO band displays a weak trend with quantum number, analogous to what was seen in Chapter 4. Note that the higher energy transitions correspond to higher values in J , however the scatter is quite significant (b).

number that are found for the 2–0 and 3–1 bands are actually reflecting the line depth sensitivity. Lines with low quantum numbers tend to have low excitation energies and large line depths. If we remove the least squares fit to the line depth/line-shift distribution from the data, there are no clear sensitivities to either χ_l or quantum number.

There are 45 candidate lines from the $\Delta v = 3$ band that meet the selection criteria. All of these lines are weak, with only two having line depths greater than 15% that of continuum. The line-shifts display no sensitivity to wavenumber or line depth. However, there is a slight dependence upon χ_l for these lines. If the sample is broken down into individual bands and branches, the bin populations become quite small (< 10). However, if the whole sample is examined, there are apparent dependencies on both energy and quantum number. In Figure 6.9, the line-shifts display a shallow slope with χ_l that is 2.5σ away from a zero slope. There is some resemblance between the shape of this distribution and the “arching” seen in Chapters 4 and 5. There is a shallow dependence upon quantum number also (with a slope $\approx 1 \sigma$ from zero). These distributions with energy are consistent with what has been seen previously: low excitation energy transitions corresponding to

smaller blueshifts.

6.3 The CFHT Stars

One of the main challenges of observing in the infrared is the difficulty in obtaining moderate or high resolution observations over large bandpasses. The FTS is probably the best type of instrument for this type of observation, given the quality of its wavelength calibration and ability to work at a variety of resolving powers. However, the FTS is also a very slow instrument and long integration times are required to generate adequate signal-to-noise.

In October 1998 and January 1999, two short observing runs were undertaken using the FTS at the *Canada-France-Hawaii Telescope* (CFHT) on Mauna Kea. The purpose of these observations was to examine the line-shift distributions of a portion of the $\Delta v = 2$ CO bands over a range of effective temperatures and $\log g$. Unfortunately, both instrumentation and weather problems severely constrained the amount of observing time available. However, some data were still obtained that illustrates some of the behavior of convection in these stars.

The FTS at CFHT is a dual aperture/detector stepped-scan FTS optimized for observations between 0.9 and 5.5 μm , and is mounted at the $f/36$ infrared focus. These observations were done using the FTS in non-evacuated mode, although it can be used as an evacuated instrument. The FTS has a high throughput (approximately 25% of the incident flux), and the combination of the dual aperture/detector arrangement with rapid modulation of the path differences reduces the atmospheric scintillation and building vibration noise substantially. The use of a dual input also allows for continuous sky subtraction. The instrumental profile of the FTS is very clean, and there is no scattered light. The wavelength precision in a pass-band is 100 ms^{-1} , and is established using a thermally stabilized laser ($\Delta\lambda/\lambda \approx 10^{-9}$) (Bohlender 1994). The maximum path difference is 60 cm, and the two InSb photovoltaic detectors are in nitrogen cooled dewars. Further instrumentation details can be found in Maillard and Michel (1982) and in the CFHT FTS User's Manual (Bohlender 1994)¹.

Observations

Two observing sessions were carried out at CFHT: October 6th - 9th 1998 and January 23rd - 27th 1999. Both observing sessions were seriously compromised by both instrumentation and weather

¹www.cfht.hawaii.edu/Instruments/Spectroscopy/FTS

Table 6.1: Properties of Observed Stars

Star	HD	MK	K(mag.) ^a	T_{eff} (K)	$\log g$	[Fe/H]	RV (kms ⁻¹)	$v \sin i$ (kms ⁻¹)	Radii (R/R _☉)
α Cas	HD3712	K0IIIa	-0.25	4582 ⁿ	1.12 ^{b,i}	-0.026 ^f	-44 ^e	$\leq 18^d$	42 ^m
β Cnc	HD69267	K4III	-0.16	3900 ^j	1.61 ^{b,e}	-0.130 ^f	22 ^e	$\leq 8^d$	48 ^m
γ^1 And	HD12533	K3IIb	-0.31	4470 ^j	1.2 ⁱ	-0.153 ^f	-12 ^e	$\leq 8^d$	82 ^k
ϵ Gem	HD48329	G8Ib	0.22	4582 ^{b,h}	0.8 ^{b,h}	-0.05 ^{b,h}	10 ^e	$\leq 8^d$	140 ^m
ι Aur	HD31398	K3II	-0.63	4389 ^j	1.2 ⁱ	-0.045 ^f	18 ^e	$\leq 8^d$	106 ^k

^a Johnson et al. 1966, ^b Cayrel de Stobel et al. 1997, ^c Hoffleit & Jaschek 1982, ^d Bernacca & Perinotto 1970, ^e McWilliam 1990, ^f Taylor 1999, ^g Smith & Lambert 1987, ^h Gratton et al. 1982, ⁱ Dyck et al. 1998, ^k combination of Hipparcos catalogue data and Dyck et al. 1998, ^l Morossi et al. 1993, ^m Nordgren et al. 1999, ⁿ Alonso et al. 1999

problems, however a modest number of useful scans were obtained. The October 1998 observations were carried out using the K filter, which is centered at 2.339 μm and has a width of 0.568 μm . The January 1999 observations were limited to the CO $\Delta v = 2$ filter, which is a narrow band filter centered upon the $\Delta v = 2$ band (at 2.32 μm and a width of 0.097 μm). Observations of Sirius were undertaken during the January 1999 session to determine the telluric spectrum.

The January 1999 observing session resulted in moderately useful observations for four stars, while the October 1998 session resulted in moderately useful observations for only one star (α Cas). The general characteristics of each one of these stars are in Table 6.1. There seems to be a wide number of different estimations for T_{eff} , $\log g$ and [Fe/H] available in the literature, and some of these estimations are substantially divergent. The values given here are by no means definitive, and are used primarily to provide some information as to the characteristics of the observed stars. Values for the physical radii have been determined using optical interferometry obtained with the Naval Prototype Optical Interferometer and the Palomar Testbed Interferometer combined with distance determinations from Hipparcos (Dyck et al. 1998; Nordgren et al. 1999; ESA 1997).

The reduction procedure that was followed for these observations is fairly straightforward. When a scan was completed the interferogram was saved in FITS format. The FTS reduction program at CFHT was then used to convert the interferograms to unapodized spectra (Bohlender & Link 1995). It was done in the following manner: (1) the interferograms were converted from FITS format to the IRAF image format; (2) the scans were then converted into secondary interferograms; (3) the secondary interferograms were then transformed into spectra using a fast fourier transform algorithm. This reduction software provided estimations of signal-to-noise for each scan and spectrum, and also provided the wavenumber scale. The spectra were then normalized locally by fitting a polynomial or cubic spline to small sections of spectra ($\approx 20 \text{ cm}^{-1}$).

Before co-adding the spectra, three further corrections were required. Since the FTS was not

evacuated, the wavenumber scale has to be adjusted slightly to compensate for the difference in the index of refraction between the calibration wavenumber of the laser and the wavenumbers observed. This was done by adapting a FORTRAN program (Maillard 1999), which recalibrated the wavenumber scale using the refraction formula of Edlén (1966). This recalibration included temperature and pressure effects upon the index of refraction. Estimations of the temperature were based upon the average of the temperature readings recorded near the primary mirror during each observation and stored in the interferogram header files. Pressure estimations were based upon the records of the night assistant for each session. Tests were conducted to determine the sensitivity of the wavenumber calibration to variations in the temperature and pressure. These tests showed that the wavenumber calibration was insensitive (differences well below 100 ms^{-1}) to the typical variations in temperature and pressure recorded during the observing sessions.

The telluric spectrum was then removed from the observed spectra. This was done for the January 1999 data by co-adding the Sirius spectra and using that composite spectrum as a template for the telluric spectrum. Sirius is a relatively warm star with virtually no lines of its own in the $\Delta v = 2$ CO bandpass. Ideally, a telluric spectrum would be taken from a rapidly rotating star, however the observational constraints precluded this. Sirius has very few lines in this spectral region and is relatively bright, unlike any of the other possible telluric candidates. To remove the telluric lines in the stellar spectra, all the normalized spectra were ratioed with the normalized telluric template (the Sirius composite). This was done by taking the stellar data and re-sampling and interpolating it to the same wavenumber scale as the telluric template. The two spectra were then broken into small sections ($\approx 20 \text{ cm}^{-1}$ in size), the template and object were over-plotted, and the template spectrum was then logarithmically stretched or compressed until selected "clean" telluric lines matched between the two to adjust for the observations being done at slightly different airmasses. The sections of spectrum were then ratioed with the adjusted telluric template, and then the corrected sections were recombined to form the full spectrum. Both the original spectra, and the telluric spectra were retained for comparison. This method proved to be effective for telluric lines that were weaker than $\approx 50\%$ of continuum. None of the telluric observations from the October 1998 session were of the appropriate resolution or quality, so as a substitute, the telluric spectrum from the KPNO Arcturus Infrared Atlas (Hinkle et al. 1995) was used. This telluric template was resampled and interpolated to the appropriate resolution and used in the same manner as outlined above. The Arcturus telluric observations were used instead of the solar infrared observations because the Arcturus spectrum was closer in resolution to the CFHT observations of α Cas.

Table 6.2: CFHT Observations

Star	Band/Filter	Dispersion (cm^{-1})	$\lambda/\Delta\lambda(\lambda_c)$	Number of Scans	Final S/N (composite)
α Cas	K	0.0551	82,000	4	59
β Cnc	CO $\Delta v=2$	0.0501	86,000	12	105
γ^1 And	CO $\Delta v=2$	0.0501	86,000	6	90
ϵ Gem	CO $\Delta v=2$	0.0501	86,000	14	120
η Aur	CO $\Delta v=2$	0.0501	86,000	5	100
Sirius	CO $\Delta v=2$	0.0501	86,000	9	145

The last correction required was for the Earth's motion with respect to the star. These were determined using the **IRAF** *rvcorrect* package, and each individual spectrum was then shifted appropriately and co-added. All of the spectra were inspected for anomalies prior to addition, and the resulting spectrum was inspected before the addition of the next spectrum to the composite.

The properties of the final spectra are summarized in Table 6.2. Included in this table are the step separations in wavenumber, central wavelength resolving powers, number of scans used and the final, composite signal-to-noise ratios for the co-added, telluric removed spectra. The same information for Sirius is included at the bottom of Table 6.2. The S/N ratio includes the effects of dividing through the co-added spectra by the telluric spectrum, which unfortunately lowers the S/N considerably.

The line selection process was the same as in earlier chapters. The list of candidate lines was generated using both the line identifications for the Sun and Arcturus, and the line positions used were taken from the sources used in Chapters 2 through 5. As in earlier chapters, all of the candidate lines were inspected visually. In addition, both the telluric and the original spectra were over-plotted onto the composite to assist in evaluating the quality of the line profile. Those candidate lines that appeared to be blended, were close to strong telluric features or where the telluric removal process may have been inadequate, were discarded. After several iterations through this evaluation process, the line-shifts were determined using the process outlined in §2.2.2.

CO Results

All five of the stars observed at CFHT had spectral ranges that included the majority of the $\Delta v = 2$ CO band at resolving powers and signal-to-noise comparable to that used for the Arcturus study. Most of the $\Delta v = 2$ bands lie within the wavenumber range of these observations – however the specific lines, and the number available varies from star to star. This is primarily a consequence of the telluric absorption. Each of these stars has a different relative radial velocity with respect

Table 6.3: CO $\Delta v=2$ Distribution Properties

Star	Number of lines	Slope 1 ^a	Slope 2 ^b	Abs. Dev. ^c	<Obs.-Fit> ^a	$\sigma_{obs-fit}$
α Cas	47	1830 \pm 762	2354	324	325	235
β Cnc	86	418 \pm 91	438	84	85	69
γ^1 And	57	386 \pm 248	461	171	172	124
ϵ Gem	39	517 \pm 451	489	248	257	211
ι Aur	48	211 \pm 152	354	115	116	98
Arcturus ^d	158	437 \pm 63	432	80	80	59
Solar Umbral ^e	194	517 \pm 319	504	42	42	31
Solar Umbral II ^f	152	297 \pm 124	175	79	58	79

^a Linear least squares fit, ^b Linear least absolute deviation fit, ^c mean absolute deviation for points about the fit.

^d $R \approx 100,000$, ^e original data, $R \approx 210,000$, ^f Resampled and degraded, $R \approx 105,000$. $S/N \approx 100$

to the solar rest frame, so lines that may be unobscured in one star may be blended with strong telluric features in another.

There is no evidence of a wavenumber dependence for any of the line-shift distributions for these stars. However, this is not definitive, given the large scatter of velocities and the signal-to-noise of these observations. For all five stars the line-shift distributions are sensitive to line depth (Figure 6.10). The distributions of line-shift with line depth in Figure 6.10 are fit using both a linear least-squares method and a more robust linear absolute deviation technique. The characteristics of each of these fits are given in Table 6.3, including the scatter of the data around the fits and the estimated margins of error for the least-squares fits.

A few general attributes of these distributions are readily apparent. The lower the gravity, the greater the scatter in observed line-shifts. The star ϵ Gem is a G8Ib, and has the largest scatter of line-shifts. The star β Cancri has a spectral classification of K4III and is both the coolest of the stars observed at CFHT, and has the highest value of $\log g$. The line-shift distribution for β Cancri has the smallest scatter of all the stars observed at CFHT. The three coolest stars (β Cancri, HD12533 and HD31398) all have slopes that are comparable to each other and much shallower than those of the hotter stars. The actual order in T_{eff} for these three stars is somewhat uncertain, given the difficulty in determining accurate effective temperatures (see Table 6.1 and Section 6.4). Beta Cancri has the highest number of usable CO lines, and it is the same luminosity class as Arcturus, so it provides the best opportunity for comparison. For similar reasons α Cas would also have been useful for comparison to Arcturus. Unfortunately, the α Cas spectrum has the poorest resolution and signal-to-noise of any of the stars, and this severely hampered its utility.

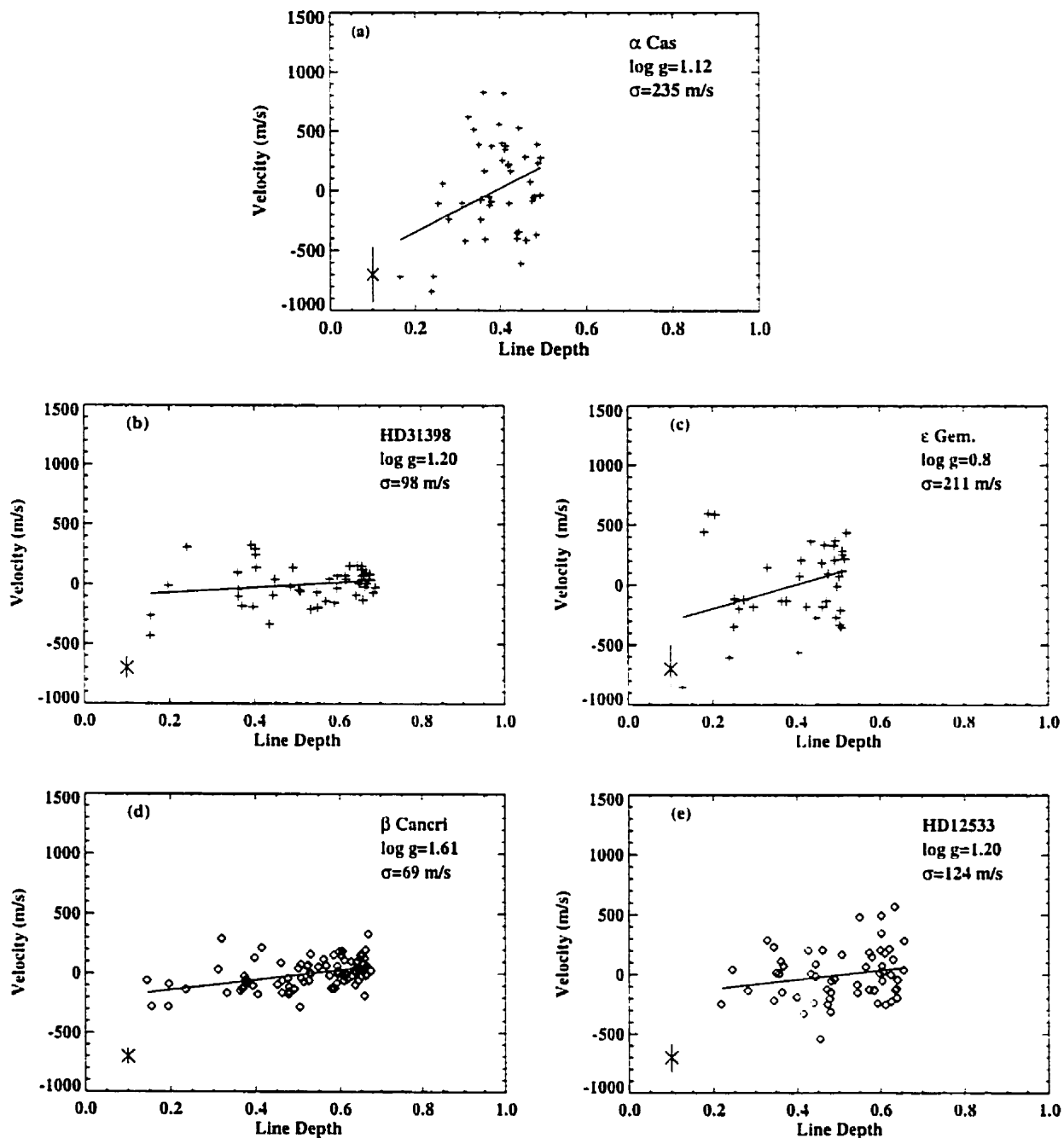


Figure 6.10: The CO $\Delta v = 2$ relative line-shifts as a function of line depth for the five stars observed at CFHT. All five stars have been set to a common relative velocity scale, with the average line-shift velocity set to 0. A least-squares linear fit to the velocities is shown for each star. The error bars display the scatter (σ) of the line-shift velocities about the linear fits. Note the increase in σ for the stars with lower $\log g$ in (b)-(d).

6.4 Discussion

The infrared and near-infrared wavelength regimes provide an opportunity for examining convection in stars cooler than the Sun. Studies over these wavelength regions enjoy the advantages of relatively low line density and the peak of the radiation distribution for stars cooler than the Sun, whereas the visible region is heavily blended and the relative quantity of radiation is substantially less. While there are Fe I lines present in the cooler stars, the molecular lines are more useful – especially the $\Delta v = 1$ and 2 CO bands.

The line-shift distributions found in the Arcturus spectrum reflect the presence of convection, however at a less vigorous level than is seen in the solar distributions. The Arcturus distributions also exhibit a greater scatter than is seen for these bands in the solar spectrum. Both of these observations are consistent with the picture of cool star convection (Dravins 1990; Gray & Toner 1985; Schwarzschild 1975). Previous studies of line asymmetries in Arcturus have illustrated one substantive difference when compared with the Sun: the shape of the bisectors (Dravins 1987b). Dravins (1987b) examined 7 visible Fe I lines at $R \approx 200,000$, and found that the line bisectors were no longer ‘C’-shaped, but rather ‘/’-shaped, with the weaker lines having slightly shallower slopes. Dravins (1987) found that the line bisectors for α Cen B (KIV) were closer to the traditional ‘C’ shape, and so attributed the differences between Arcturus and α Cen B to the difference in $\log g$. The Arcturus atlas used here has a much lower resolving power (less than half) and signal-to-noise than the Dravins data, however it comprises a much larger sample over different species and wavelengths. When the average and median bisectors are examined, they appear consistent with those from Dravins (1987b). Figure 6.9 shows the median bisectors for the Arcturus CO $\Delta v = 2$ lines binned by strength. The shapes and slopes of these bisectors are similar to those determined by Dravins (1987) and Gray (1980). Even though the signal to noise ratio and resolving power are substantially less than those used by Dravins (1987) and Gray (1980), the number of lines that form the sample from which the median bisectors were determined is several times greater. Careful inspection of Figure 6.9 shows that while the slopes of all of the median bisectors resemble a ‘/’ instead of the solar ‘C’, they all have different slopes and velocity spans.

The median bisector for the weakest lines has the shallowest slope and greatest velocity span, while the median bisector for the strongest lines has the steepest slope and smallest velocity span. All three median bisectors are offset in velocity from one another by approximately 150 ms^{-1} , so the line core positions of the weaker lines are blueshifted with respect to the stronger lines.

because of the shallower slope and the velocity offset. If an intensity point sufficiently below the continuum on the bisectors is selected (to avoid wing effects), the point for the weakest bisector will be $\approx 100\text{ms}^{-1}$ to the blue of the same intensity point on the medium bisector, which will also be $\approx 100\text{ms}^{-1}$ from the corresponding intensity point on the strongest median bisector. The bottoms of the bisectors are offset from each other in the same manner and scale as their corresponding differential line positions in Figure 6.3. Thus some of the information contained in the bisectors is also contained in the line shift distributions, but the shapes of the bisectors do not correspond with those of the bisectors.

In Table 6.3, the properties of the fits to each of the distributions for the CFHT stars are given as well as the same properties for the $\Delta v = 2$ CO bands in the Arcturus spectrum and in the umbral spectrum of the Sun (both at the original resolution and S/N and at a resolution of $R \approx 105,000$ and $S/N \approx 100$). With the exception of α Cas, the distributions shown in Figure 6.10 all have very similar slopes to that seen for the Arcturus $\Delta v = 2$ CO sample (see Figure 6.8). The supergiant ϵ Gem has the steepest slope, and the highest T_{eff} of all the stars in Table 6.3 (from now on the poorly observed α Cas will be ignored). However, the differences between the slopes of these distributions are minor, which is not surprising since the T_{eff} values for these stars are not that different ($\Delta T_{\text{eff}} \approx 600$ K), and are not all defined in a uniform manner. Thus the relative differences in the temperatures cannot be considered as firm.

The solar umbral case provides an interesting contrast when it has been degraded and resampled to mimic the quality of the CFHT observations. The slope of the distribution of line-shifts from the $R \approx 105,000$ umbral spectrum is fairly shallow compared to the other stars, and it has a scatter about its fit that is slightly smaller than that of either Arcturus or β Cancri. However, it should be noted that the solar umbral spectrum is an intensity measurement, whereas all of these other stars are flux measurements. In Chapter 3 it was shown that the differences between the solar flux and intensity line-shift distributions in the visible were minor; however the influence of the center-to-limb variation in the line profiles of the giant stars in the infrared is an unknown quantity. Any comparisons made between the solar intensity observations and the stellar flux observations have to be provisional.

Comparisons of these distributions can be made with the solar observations in Chapters 4 and 5, and all 6 distributions have slopes that are much shallower than the solar distributions for Fe I and the fundamental CO bands. A reduction in T_{eff} is expected to decrease the convection velocities at the surface through several means (Nordlund & Dravins 1990). A decrease in T_{eff} reduces the

amount of energy flux that is being transferred, and also decreases the local opacity for a given pressure. This results in an increase in the local density for a given optical depth, which means that the velocities required to transfer the energy flux are lower. The lower opacity allows radiative diffusion to play a more significant role in the transport of the energy just beneath the surface of the star (recall that H^- has a temperature sensitivity of 10^{10}), which reduces the amount of energy flux that convection transports (Nordlund & Dravins 1990).

These trends that are observed for these cooler stars are consistent with convection occurring deeper in the atmosphere, below the line formation region. The decrease in the line-shift/line depth distribution slopes indicates that the extent of convective penetration into the line formation region is dropping off. An increase in the scatter with $\log g$ would be consistent with the increased convective cell size that is predicted (Dravins & Nordlund 1990; Schwarzschild 1975). According to numerical simulations of α Cen A and β Hydri, a change in $\log g$ results in a proportional change in both the vertical and horizontal scales of convection. The vertical scale changes due to the change in the density scale height, and the horizontal scales change by the same factor so as to maintain conservation of mass (Nordlund & Dravins 1990).

If we examine the scatter of these distributions and the relative $\log g$ values for the stars, we see that the scatter does increase with decreasing gravity. Alpha Cas and ϵ Gem have the largest scatter in line-shifts (however α Cas also has significantly lower signal-to-noise ratio), followed by HD12533 (γ^1 And) and HD31398 (ι Aur), both of which have classifications of K3II, while Arcturus and β Cancri have the smallest scatter and are both giant stars. Red supergiants may have convection cells or supergranulation cells at scales comparable to the radius of the star, which could give rise to brightness variations in these stars (Schwarzschild 1975; Antia et al. 1984). It appears that the wide scatter in line-shifts recorded here, especially for ϵ Gem, are consistent with increased cell sizes and the corresponding decrease in the number of cells over the surface of the star. However, appearances can be misleading. Stars with lower values of $\log g$ also have different line widths. When a spectral line that is common to all the line-shift distributions is compared (Figure 6.11), it is clear that there is a substantial range in width for the line, and the width is sensitive to gravity. As discussed in §2.2.2, the bottom of the line profile is very sensitive to noise. The degree of sensitivity to noise depends upon the slope of the profile: a shallower slope is more sensitive to noise effects. The broader the line width, the shallower the slope will be in the bottom of the line core where the line position is measured. As Figure 6.11 clearly shows, the supergiant ϵ Gem has the broadest profile, the shallowest line profile slope and the lowest gravity, and is thus

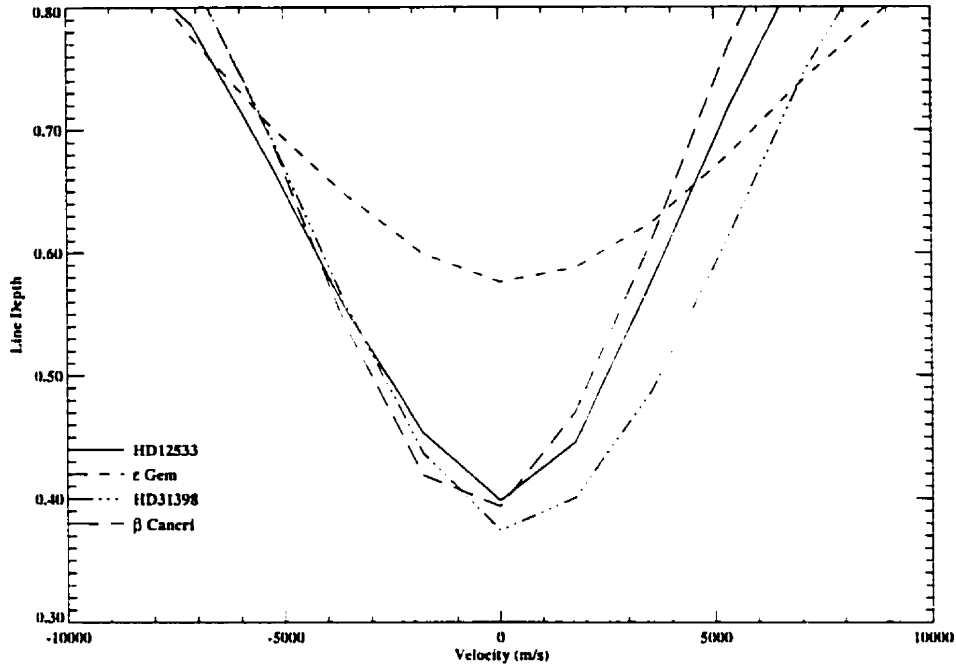


Figure 6.11: The bottom portions of the line profiles of the line at $\sigma=4222.9542 \text{ cm}^{-1}$ for HD 31398, HD 12533, β Can and ϵ Gem. All four profiles have been shifted so that their minima are at zero velocity; α Cas has not been included because of its poor quality. The change in the width and slope of the line profiles corresponds to the change in $\log g$, with the ϵ Gem profile having a width approximately twice that of the narrowest line (β Can).

the most sensitive to noise.

As was seen in Chapter §2.3.2, increasing the amount of noise (or decreasing the S/N ratio) results in increasing the scatter in the line-shift distributions. When this was examined in Chapter 2, it was done by increasing the amount of noise in the Solar Flux Atlas spectrum. Changing the slope of the bottom portion of the line profiles while maintaining the same S/N ratio for the continuum should have the effect of increasing the scatter in the determined line-shift positions. As a possible test of this, the line profiles from β Cancri were all broadened by multiplicative factors of 1.3, 1.6 and 1.9. Beta Cancri was selected as the test case because the observations were the best quality and the distribution had the narrowest lines of all of the CFHT stars and also had the largest sample of lines. The line-shift distributions were then found for each of these new broadened spectra. As would be expected from the results of §2.3.2, the scatter of these new distributions about the best linear fit increased substantially over the original scatter. The β Cancri spectrum which had profiles broadened by a factor of 1.9 had a scatter twice that of the original spectrum.

This result with the β Cancri observations indicates that the apparent trend of the scatter for the line-shift distributions can be attributed to the change in the slope of the bottom of line

profiles with $\log g$ rather than a change in the number of granules on the surface of the stars. This does not mean that the change in the number of granules does not have an effect on the scatter of line-shifts, but this effect is not observed in these observations. Perhaps observations at higher S/N or resolving power could provide insight. Recall that in Chapter 2, resolving powers of 200 000 revealed almost the same information as the resolving powers of 500 000. If observations such as these are repeated, the stars with broader profiles should be observed at substantially higher S/N, to compensate for their greater sensitivity to photometric error because of the shallower slopes at the bottom of their line cores.

A change in the scale of convection is not the only effect expected when $\log g$ is changed. For stars with the same temperature the net convective energy flux has to remain the same; however to transfer that flux through an atmosphere with a lower density, the velocity amplitudes or temperature contrast has to be greater (Nordlund & Dravins 1990). Evidence of these effects have been found in both simulations and observations (Nordlund & Dravins 1990; Dravins 1987b). Unfortunately, these secondary effects cannot be seen with our data since we do not have any stars with similar (and well established) T_{eff} but different $\log g$.

Previously, Nadeau and Maillard (1988a) examined the $\Delta v = 2$ CO lines, Ca I and Fe I lines in the K band of four M giants. These observations indicated that convection was observable for M giants, and when the high energy Fe I lines were combined with the lower energy CO lines, the M giants appeared to exhibit more vigorous convection as a function of χ_l than the Sun does. The scatter in line-shift velocity for the CO lines is very large, which may be consistent with the expected effects of lower $\log g$ values; and there are relatively few Fe I lines at higher energies. It was not possible for Nadeau and Maillard to disentangle the influences of χ_l and line depth on the line-shifts, and the line parameters used in the study were not as accurate as those used here. Nadeau and Maillard found that there may have been a velocity gradient in the CO line-shifts for one of their stars (HR 0045, M2III), but otherwise the detection of the line-shift gradients with χ_l required the combination of the Fe I and CO data - which introduces potential problems with sample size and the quality of the line positions.

In studies such as this, it is useful to observe more than one species, as we have done in the case of Arcturus. The OH bands seem to provide a strong complement to the CO bands, the OH lines appear to be somewhat intermediary in distribution of line strengths between the CO $\Delta v = 1$ and $\Delta v = 2$ bands, and occupy a spectral region that is not as fraught with telluric absorption lines as that for the CO $\Delta v = 1$ lines.

Unfortunately, the $\Delta v = 1$ OH bands are not observable in the normal solar spectrum. However, they are observed in the solar umbral spectrum (see Chapter 5). The $\Delta v = 1$ OH bands observed in Chapter 5 were observed at approximately the same resolving power as the Arcturus observations, and a direct comparison between the two distributions of line-shifts is interesting. The Arcturus OH lines are slightly stronger than the solar umbral lines, and the umbral line-shift/line depth distribution is actually steeper than the Arcturus distribution. The umbral distribution has a linear slope of 913 ms^{-1} versus a slope of 649 ms^{-1} for the Arcturus line-shift/line depth distribution. In addition to this, the umbral distribution has a larger scatter than the Arcturus distribution, 256 versus 161.

At first inspection, this difference between the umbral and Arcturus spectra appears contrary to expectations. The actual temperature of the sunspot is difficult to estimate, given the vagaries of the opacity – the classification for this particular spot was estimated based upon the strengths of the $2 - 0$ CO lines near $2.4 \mu\text{m}$. Any classification given is sensitive to the molecular band being used and the wavelength (Hinkle et al. 1995). The OH lines are sensitive temperature indicators, and a nominal temperature estimation of the sunspot based upon the $\Delta v = 1$ bands would indicate a umbral temperature slightly *warmer* than Arcturus. The difference between the umbral and Arcturus slopes are relatively small, and the solar sample is actually less than one half the size of the Arcturus sample, which may in part account for the higher scatter. The umbral sample is also much more sensitive to statistical effects, since the physical span of the aperture is very small, and equivalent in size to only a few convective elements.

One key issue that remains is the impact of metallicity upon the convection signatures. Ideally, a star with a lower metallicity (such as Arcturus) will have a lower opacity in the photosphere. This means that the line formation will be occurring at greater depths in the atmosphere, and thus the line-shifts should reflect the more vigorous convection of those depths. However, the change in the opacity will also change the relative contributions to energy transfer by radiation, and the structure of the convection zone should be sensitive to changes in opacity. Böhm-Vitense (1971) suggested that a decrease in opacity would increase the pressure, via the equation of hydrostatic equilibrium. By increasing the local pressure for a particular depth, the density would also increase. This increase in the density results in a decrease in the convective velocity in order to transfer the same amount of convective flux. This result was confirmed in a numerical study by Lester et al. (1982).

Allende Prieto et al. (1999) conducted a line profile study of two metal poor stars: Groombridge

1830 and HD 140283. They found that for the more metal poor star, the line bisectors exhibited substantially larger velocity spans than comparable stars with solar metallicity. This is interpreted as a lowering of the opacity in the visible. However, the less metal deficient star (Gmb 1830, $[\text{Fe}/\text{H}] \sim -1.3$) exhibited little or no difference in line profile, implying that the opacity effects only become significant for large scale metal discrepancies. This indicates that the line-shift distributions for Arcturus should not be greatly sensitive to its metallicity. This is somewhat contradictory with the results from Böhm-Vitense (1971) and Lester et al. (1982). However, what may be demonstrated here is a greater change in the convective velocity over the line formation region, as opposed to a greater absolute convective velocity. A more complete understanding of the role of metallicity and its effects upon the line-shifts could be examined by exploring the line-shift distributions for stars with similar T_{eff} and $\log g$, but different $[\text{Fe}/\text{H}]$ over a larger wavelength range. Unfortunately, the relative T_{eff} and $\log g$ scales of these stars are not sufficiently constrained enough to allow this. However, in the future, Arcturus would be an excellent star to use in such a study because of the quality of the observations and the low value of $[\text{Fe}/\text{H}]$.

Even in a star as cool as Arcturus, Fe I still persists as a useful diagnostic of convection. The Fe I line shift distributions still indicate a sensitivity to line depth and a small dependence upon χ_l . This allows for a direct comparison to the normal photospheric spectrum, from which we see that the convective velocities in Arcturus are suppressed and exhibit a greater scatter than in the solar case – which is most likely a result of Arcturus having broader line profiles, but the scatter may be consistent with the expectations of convection in a cool giant star. The high quality Arcturus atlas can be used as an anchor point against which other cool stars can be compared, whether the species is atomic or molecular.

Chapter 7

Summary and Future Work

The primary goal of this thesis was to determine the efficacy of using line-core displacements as a means of examining convection in solar-type stars. Traditionally stellar convection has been studied using line bisectors, which require extremely high resolving powers and signal-to-noise ratios. Previous line-shift studies have been done at comparable resolving powers to those using line bisectors. Unfortunately, spectrographs that have both the wavelength calibration stability and resolving power capability are relatively rare.

In this thesis an alternative method for determining line-shifts has been employed, and the line positions from several potential diagnostic species have been examined and tested using the solar spectrum as a fiducial source. The study of solar line positions has been extended into the Sun's infrared spectrum, and to a solar umbral spectrum. Molecular line-shifts have also been studied in the infrared spectra of several K giants and supergiants, including Arcturus.

7.1 Observing Convection in the Sun

In Chapter 1 the criteria for a diagnostic species were outlined, and Fe I meets almost all of the criteria. In previous studies (Dravins et al. 1981; Nadeau 1988; Allende Prieto & García López 1998), Fe I has been used to probe convection in the Sun, primarily in the visible portion of the spectrum. Chapter 2 outlines the technique used for determining the line-shifts using the most recent Fe I line positions available (Nave et al. 1994) and the visible solar flux spectrum (Kurucz et al. 1984).

The behavior of the Fe I line-shifts found using this technique was consistent with the results of Dravins et al. (1981), and the distributions of line-shifts were also consistent with the shape and extent of line bisectors. To test the technique, the original flux spectrum was degraded and

resampled to a variety of resolutions and signal-to-noise levels, and the results were then compared with the results of other techniques.

It was found that a decrease in resolution altered the shape of the line-shift distributions with wavelength and line depth; the differences between lines of different strengths and wavelengths became less pronounced at lower resolutions. However, there was still clear evidence of differences between lines of different strengths at resolving powers as low as 52,000 using the 2 point bisector technique, and at a much more pronounced level than was seen using the line-shift techniques utilized by others. Figure 2.12 shows that the change in the shape of the line depth/line-shift distribution behaves in a predictable fashion.

Using the bottom of a line profile to determine the line core position can be extremely sensitive to noise, as it is this portion of the line profile where the slope is shallowest and the signal is lowest. However, this affects all methods for determining the line core position using the line minimum. If the entire line profile is used to determine the line position, then the velocity shift is integrated over the whole line formation region and information is lost. As the resolving power decreases, the method used here determines the line core position from slightly steeper portions of the line profile where the profile is closer to the vertical and is less sensitive to noise. When noise was added to the flux spectrum, it was found that the shape of the line-shift distributions at a given resolution remained largely unchanged, with the weakest lines showing the greatest sensitivity to the noise.

7.1.1 Solar Flux: Fe I

The 298 Fe I lines found in the visible flux spectrum between 430 and 660 nm displayed clear dependence upon two parameters: line depth and wavelength. Previous studies have indicated a line depth dependence (Allende Prieto & García López 1998; Dravins et al. 1981), however they have differed on whether there was a sensitivity to wavelength. To properly determine the dependence upon a parameter, the effect of the other variable was minimized by binning the data into samples and then examining these smaller samples. When this was done, clear sensitivities to wavelength and line depth were found.

The shape of the line depth/velocity distributions for the Fe I lines strongly resembles the shape and extent of the median bisectors taken from the data, which confirms that similar information is being obtained by the two diagnostics. The stronger lines have little or no displacement from their rest wavelengths, while the weakest lines show the greatest shift, a difference of approximately 1000 ms^{-1} . It was found that a parabolic polynomial usually fit the line-shift/velocity distribution quite

well, with the slope steepest for the medium strength lines.

The wavelength dependence for these line-shifts can be masked by the uneven distribution of line strengths with wavelength. The strong lines tend to be found in the blue portion of the spectrum. When the lines were grouped by strength classes, it was found that there was a wavelength dependence that was steepest for the stronger lines, with lines at shorter wavelengths exhibiting larger line-shifts. It was also found that this wavelength dependence decreased at longer wavelengths. This behavior of the wavelength dependence is consistent with the change in brightness or temperature contrast between the lanes and granules. As described in Chapter 2, this contrast decreases at longer wavelengths, meaning that the contributions from the intergranular lanes becomes more significant.

7.1.2 Solar Central Intensity Observations

In Chapter 3 the effects of moderate rotation, limb darkening and the center-to-limb effect were examined by comparing the line-shifts for the Fe I lines in the solar visible flux and central intensity spectra. There were no dramatic differences between the two samples, however there were some subtle effects which for the flux observations actually enhanced the difference in line-shifts between the blue and red lines, while the dependence of the line-shifts on line depth was largely unaffected.

The central intensity observations also provided the opportunity to extend the study of the Fe I line-shifts to a much larger sample, spanning wavelengths from 400 nm to 5 μm , and extending the range of lower excitation energies to beyond 6 eV. The large wavelength coverage allows for an extensive study on the effects of both changing continuous opacity and the change in brightness contrast upon the distribution of line-shifts.

The dependence of the line-shifts on line depth in the NIR and IR was very similar in shape to that seen for the visible line-shifts. However, the wavelength dependence for the medium and strong lines declined, an effect that is largely attributable to the change in brightness contrast between the granules and lanes. There is also evidence that this change in the wavelength behavior is influenced by the change in the continuous opacity, with the change in the slopes of the line depth/velocity distributions on either side of the H^- opacity maximum. In general, for a given line depth, those lines at longer wavelengths had smaller blueshifts, which is consistent with both the change in contrast and opacity. With changes in continuous opacity, the levels of the atmosphere contributing to the line core formation change, as well as the relative areal contributions from the lanes and granules.

7.1.3 Molecular Line-shifts as Diagnostics

Fe I is the primary species used for examining line profile asymmetries in the solar spectrum. However, extending studies such as this to cooler stars or to other wavelength regions (specifically the infrared) necessitates using other species that meet most of the criteria outlined in §1.5. As was pointed out, the best candidates are the molecular bands of CO. Unfortunately, the precise mechanisms for CO line formation are poorly understood (see §4.4 and Uitenbroek 2000b for discussion). The spectra of CO are still potentially a powerful diagnostic, even if the exact conditions of formation are not well understood.

In Chapter 4 the line-shift distributions for the fundamental CO bands were examined using the shuttle-borne ATMOS FTS observations. The shapes of these distributions have proven to be quite interesting and unusual. The line depth/velocity distribution is similar to that of the visible Fe I line-shifts. The overall shape and velocity span is similar, however, the CO distribution is much steeper. If the ATMOS observations are calibrated to a common wavelength scale with the KPNO observations, the strongest CO lines exhibit a redshift. This is consistent with the observed contrast inversion predicted by numerical simulations (Stein & Nordlund 1998; Uitenbroek 2000). When one of the lower bands is examined, those strong lines with smaller ν_l and quantum numbers have line-shifts that are slightly smaller (or bluer) than their counterparts of similar strength. This could be a result of the domination of the higher energy lines by contributions from the descending lanes.

Further support for this scenario can be found when the medium and higher bands are examined. For the medium bands (e.g. the 5 – 4 band), there is no difference in behavior between lines of the same strength, but different energies/quantum numbers. For the higher bands (e.g. the 9 – 8 band) the lines with higher energies/quantum numbers have velocities to the blue of their lower energy counterparts. These weaker lines with high ν_l form deeper in the photosphere than the 1 – 0 lines and are dominated by contributions from the uprising granules. These contributions are further complicated by the relative changes in the areas occupied by the granules and the lanes, which changes with altitude.

A clear visualization of the conditions under which these lines are forming is required if the fine structure observed is to be understood. This necessitates three dimensional hydrodynamical models, which indicate that the CO line formation is very sensitive to the spatially corrugated local opacity and to the convection and line formation timescales (Uitenbroek 2000; Uitenbroek 2000b).

7.1.4 Umbral Line-shifts

The presence of strong magnetic flux tubes suppress convection near the surface of a sunspot. While some convective elements may penetrate the umbra (umbral dots and strong light bridges), the large scale granulation observed in the normal photosphere does not. In many ways, the solar umbral spectrum should be very similar to the spectrum of a cooler star, with a much smaller convective flux. Previous studies of convective motions in the umbral photosphere are consistent with no motion (Beckers 1976), or some small scale motion (Lites et al. 1991).

In Chapter 5 the positions for the first overtone bands of CO were examined. The line-shift distribution indicated that convective motions did penetrate into the umbral photosphere (on the scale of the aperture of the FTS used), but the degree of motion was substantially suppressed when compared to that seen in the normal solar photosphere. The shapes and slopes of the median line bisectors were consistent with the distributions of the line-shifts, and the span of velocities covered by the line depth/velocity distribution was approximately the same size as the velocity associated with umbral dots and light bridges.

The cooler temperatures of the umbra also permitted the use of the OH bands as a second diagnostic. The line-shift distributions for the OH bands resembled that of the CO first overtone - although they appeared to be slightly steeper, this may be reflecting the OH sampling slightly different levels of the atmosphere. To properly determine this would require accurate three dimensional magneto-hydrodynamic modeling of both CO and OH line formation. These observations increase the potential utility of the OH Meinel system as a diagnostic for cooler stars, making the OH bands a useful complement for the CO bands. The scatter in the line-shift velocities for the umbral distributions are greater than their counterparts in the normal solar spectrum, which reflects both the much smaller aperture size of the umbral spectrum (7 arc-seconds versus 40 arc-seconds, or larger) and the different nature of the convection between the two types of photosphere.

7.2 Observing Convection in Solar-Type Stars

In Chapter 6 a high resolution spectral atlas of Arcturus ($\Delta\lambda/\lambda \approx 10^5$) (Hinkle et al. 1995) was used to determine the line-shifts for Fe I, CO and OH over a large wavelength span in the near-infrared and infrared. The Fe I line-shifts display a very weak sensitivity to line depth, much less than that seen in the solar spectrum - which is consistent with the expected results of a decrease in the vigor of surface convection with lower effective temperature. When the Fe I line-shift

distributions are compared to the solar distributions at the same resolving power and signal-to-noise, the Arcturus line-shifts display a much larger scatter. Unlike the solar case, the shapes of the line-shift distributions do not mimic the bisector shapes. The median bisectors for Arcturus are shaped like ‘/’, with the slopes and relative positions of the bisectors depending upon line strength. However, the bottom position of these bisectors do match up to the line-shift distributions. The reason why Arcturus and other cool giants have these bisector shapes is unknown, although Dravins (1987) attributes the effect to a change in $\log g$, while Gray (1982) posits that it indicates a greater penetration of convection into the line formation region.

For cooler stars, the presence in the infrared of both CO and OH bands provides excellent opportunities to extend the diagnostics beyond the Fe I lines. The fundamental OH and CO bands both show a clear dependence of line-shift upon line depth. This sensitivity is much clearer than that seen for the Fe I distributions; the slopes of the distributions were steeper than those for the Fe I distributions, and the scatter for the molecular lines was smaller than the scatter for the Fe I samples. This difference in the slopes of the distributions is similar to what was seen when the CO and Fe I solar line-shifts were compared, and reflects both the differences in opacity between the different wavelength samples and also the different range of physical conditions under which the lines are formed. The decreased scatter is expected since the positional uncertainties for the molecular lines are much smaller than those for the Fe I lines. The line-shift distribution for the first overtone CO lines clearly indicated a sensitivity to line-depth, and as seen in the solar distributions, the $\Delta v = 1$ distribution had a shallower slope than the fundamental distribution. Unlike the solar observations, the ‘arch’ behavior of the line-shifts with quantum number and λ_l was not apparent. All energy and quantum number sensitivities largely disappeared when the sensitivity to line depth was removed.

The change in the behavior of the line-shift distributions was further examined using observations of five K giant and supergiant stars obtained at CFHT. These observations ($\Delta\lambda/\lambda \approx 85,000$, $S/N \approx 100$) were centered on the CO first overtone bands near $2.3 \mu\text{m}$. The CO line-shift distributions for these stars were then compared to those from Arcturus and the solar umbral spectrum (both the normal spectrum and one resampled and degraded to $\Delta\lambda/\lambda = 10^5$ and $S/N \approx 100$). The coolest stars have line-shift distributions with smaller sensitivities to line depth than the warmest stars, however finer differences between the distributions for the stars are hard to distinguish because of problems in establishing consistent temperature ordering from the available literature. There was a clear increase in the scatter of the line-shifts as $\log g$ decreased. However, this increase

in the scatter is probably caused by the difference in the slopes of the line profiles with $\log g$. Those stars with lower gravities are also broader, and the slopes of the portion of their line profiles used to define the line position are shallower, and are more sensitive to photometric noise. A simple test done on the star β Cancri indicated as the line profiles were broadened, the scatter of the line shift distribution increased. This probably accounts for most of the variation in the scatter of the line shift distributions; whether or not $\log g$ influences the scatter is an unanswered question. Perhaps with higher signal-to-noise ratios, or with higher resolving powers the question could be answered. By observing at higher resolutions, the points on the profile used to define the line position will come from much closer to the profile minimum and will have a smaller range in slope over the sample stars.

7.3 Future Projects

7.3.1 Exploring Convection in Stellar Parameter Space

The depth and extent of the photospheric convection zone is sensitive to $\log g$, T_{eff} and metallicity. Previous line bisector studies have demonstrated a ‘granulation boundary’ on the H-R diagram (Gray & Nagel 1989) and ‘naked granulation’ (Dravins 1990) is predicted for hotter stars, closer to this boundary. The temperature at which the ‘granulation boundary’ occurs is dependent upon $\log g$. A change in the metallicity should also affect the nature of the convection. While one of the stars in this study had a low $[\text{Fe}/\text{H}]$ value (Arcturus), a more comprehensive sample of stars with similar temperatures and $\log g$ but different $[\text{Fe}/\text{H}]$ would permit an empirical examination of how changes in opacity affect the scale of convection. Line-shift studies of stars near the granulation boundary of different metallicities will allow for an exploration of how convection behaves as these three parameters vary.

The present study can also be extended to hotter stars, permitting a more comprehensive examination of how T_{eff} affects the vigor of convection. The extra-solar planet and asteroseismology research efforts of the past few years have given rise to a large compendium of moderately high resolution ($\Delta\lambda/\lambda \approx 60,000$) and high signal-to-noise observations of solar type stars using spectrographs with well established wavelength calibrations; most notably the Applied Fiber-Optic Echelle spectrograph operated by the CfA and HAO (Brown et al. 1994). These spectra have been made available by Brown (private communication), and a study of Fe I line-shifts in the visible spectrum of Procyon has been started. Further visible spectra of comparable quality are also available,

spanning spectral classes from early K to early F for both dwarf and giant stars over a range of metallicities. Further observations of K giants and supergiants can also be pursued in the infrared using the FTS at CFHT (although the instrument is scheduled for decommissioning).

7.3.2 Fe I Line-shifts at High χ_l

The Fe I line-shifts in the visible and near-infrared solar spectrum showed some evidence of a sensitivity to χ_l ; however this sensitivity was very small when the line depth and wavelength dependencies were accounted for. The Fe I lines in the infrared displayed greater sensitivity to lower excitation energy, however in a rather strange fashion. The lines with higher excitation energies appear to have the largest blue shifts by a substantial margin (which is somewhat consistent with results from Dravins et al. (1981; 1986)), however this behavior appears to reverse itself at the highest energies ($\chi_l > 6.8$ eV), with a number of lines at high χ_l having velocities that differed by over $+1500$ ms^{-1} from lines of comparable strength and wavelength. This change in the sensitivity to energy occurs at the longest wavelengths in this study (beyond 4 μm), which are those lines with the least accurately defined line positions. The behavior of these line-shifts at these extreme conditions may be spurious. Transitions this close to the ionization energies may be subject to pressure effects (Nave, private communication); however high excitation energy transitions are very useful for probing deeper into the atmosphere. A further investigation of these transitions and their parameters may determine if the line-shift behavior seen here is real. Similarly, extending the study to higher energy transitions (such as Fe II) may also provide some insight into the correlation between χ_l and line-shifts.

7.3.3 CO Formation Altitudes

The details of CO line formation in the Sun are not currently well understood (see Chapter 4 and Uitenbroek (2000; 2000b) for discussions). The fundamental bands of CO have line-shift distributions that exhibit some unusual behavior, where lines of comparable strength, but different excitation energies (and quantum numbers) have different velocities - implying that the lines formed at different altitudes or their flux profile was dominated by different contributions between the lanes and the granules. This scenario is consistent with the contrast inversion observed in the cores of CO lines (Uitenbroek 2000) and predicted by numerical simulations (Stein & Nordlund 1998). Uitenbroek (2000; 2000b) has attempted to model some of the CO lines that display this contrast inversion using three dimensional hydrodynamics, and has suggested that the CO line formation

timescales may be comparable to the convective timescales. If this is the case, slightly different formation timescales for different excitation energies could give rise to the behavior seen here. Further study of these lines using the techniques of Uitenbroek (spectro-heliograms combined with multi-dimensional models) may allow for a confirmation of this scenario.

Extending observations of the CO fundamental bands to other solar type stars will also permit more complete comparisons with the solar atmosphere. The possibility of observing the fine detail seen in the observations of the CO solar lines in the spectra of other stars is unlikely given resolution and signal-to-noise constraints combined with the integration of the profiles over the disk and problems with observing at the $5\ \mu\text{m}$ wavelength region, however, statistical differences for groups of line-shifts may be observable, and these may provide insight into how the solar atmosphere compares to those of other stars.

Bibliography

Abrams, M. C. 1999 private communication

Abrams, M. C., Davis, S. P., Rao, M. L. P., Engelman Jr., R., Brault, J. W. 1994, *ApJSS*, 93, 351

Abrams, M. C., Goldman, A., Gunson, M. R., Rinsland, C. P., Zander, R. 1996, *Applied Optics*, 35:16, 2747

Adam, M. G., Ibbetson, P. A., Petford, A. D. 1976, *MNRAS*, 177, 687

Allende Prieto, C., García López, R. J. 1998, *A&ApSS*, 129, 41

Allende Prieto, C., García López, R. J., Lambert, D. L., Gustafsson, B. 1999, *ApJ*, 526, 991

Alonso, A., Salaris, M., Arribas, S., Martinez-Roger, C. Asensio, R. A. 1999, *A&A*, 355, 1060

Antia, H. M., Chitre, S. M., Narasimha, D. 1984, *ApJ*, 282, 574

Ayres, T. R. 1981, *ApJ*, 244, 1064

Ayres, T. R., Testerman, L., Brault, J. W. 1986, *ApJ*, 304, 542

Ayres, T. R., Brault, J. W. 1990, *ApJ*, 363, 705

Ayres, T. R., Rabin D. 1996, *ApJ*, 460,1042

Balthasar, H. 1984, *Solar Physics*, 93, 219

Balthasar, H. 1985, *Solar Physics*, 99, 31

Basu, S., Antia, H. M. 1994, *J. Astropys. Astr.*, 15,143

Beckers, J. 1976, *ApJ*, 203, 739

Beckers, K. 1977, *ApJ*, 213, 900

- Bernacca, P. L., Perinotto, M. 1970, *Contr. Oss. Astrof. Padova in Asiago*, 239
- Blanchflower, S. M., Rucklidge, A. M., Weiss, N. O. 1998, *MNRAS*, 301, 593
- Böhm-Vitense, E. 1971, *A&A*, 14, 390
- Böhm-Vitense, E. 1958, *Zs. F. Ap.*, 46, 108
- Bohlender, D. A. 1994, *User's Manual for the CFHT Fourier Transform Spectrometer*, www.cfht.hawaii.edu/Instruments/Spectroscopy/FTS/, Mauna Kea, Hawaii
- Bohlender, D., Link B. 1995, *The CFHT Fourier Transform Spectrometer Data Reduction Program User's Guide*, www.cfht.hawaii.edu/Instruments/Spectroscopy/FTS/, Mauna Kea, Hawaii
- Bray, R. J., Loughhead, R. E., Durrant, C. J. 1984, *The Solar Granulation, Second Edition*, Cambridge University Press, Cambridge UK
- Brown, T. M. 1999, private communication
- Brown, T. M., Noyes, R. W., Nineson, P., Korzennik, S. G., Horner, S. 1994, *PASP*, 106, 1285
- Butler, R. P., Marcy, G. W., Williams, E., McCarthy, C., Dosanjuh, P., Vogt, S. S. 1996, *PASP*, 108, 500
- Canuto, V. M. 1992, *ApJ*, 392, 218
- Canuto, V. M. 1993, *ApJ*, 416, 331
- Canuto, V. M. 1997, *ApJ*, 482, 827
- Canuto, V. M. 2000, *ApJ*, 541, L79
- Canuto, V. M., Dubovikov, M. 1998, *ApJ*, 493, 834
- Canuto, V. M., Goldman, I., Mazzitelli, I. 1996, *ApJ*, 473, 550
- Canuto, V., Mazzitelli, I. 1991, *ApJ*, 370, 295
- Canuto, V., Mazzitelli, I. 1992, *ApJ*, 389, 724
- Cayrel de Strobel, G., Soubiran, C., Friel, E. D., Ralite, N., Francois, P. 1997, *A&ASS*, 124, 299

- Cox, J.P., Giuli, R. T. 1968, *Principles of Stellar Structure. Volume 1: Physical Principles*, New York, Gordon and Breach
- Crosswhite, H. M. 1975, *J. Research N.B.S.*, 79A, 17
- D'Antona, F., Mazzitelli, I., Gratton, R. G. 1992 *A&A*, 257, 539
- D'Antona, F., Mazzitelli, I. 1994, *ApJSS*, 90, 467
- Davis, S. P. 1997 private communication
- Di Benedetto, G. P., Foy, R. 1986. *A&A*, 166, 204
- Dravins, D. 1982. *ARA&A*, 20, 61
- Dravins, D. 1987a, *A&A*, 172, 200
- Dravins, D. 1987b, *A&A*, 172, 211
- Dravins, D. 1990. *A&A*, 228, 218
- Dravins, D. 1992, *ESO Workshop on High Resolution Spectroscopy with the VLT*, ed. Ulrich, M.-H., European Southern Observatory, Garching bei Munchen, Germany, p.55
- Dravins, D., Larsson, B., Nordlund, Å. 1986, *A&A*, 158, 83
- Dravins, D., Lindegren, L., Nordlund, Å. 1981, *A&A*, 96, 345
- Dravins, D., Nordlund, Å. 1990. *A&A*, 228, 203
- Dyck, H. M., van Belle, G. T., Thompson, R. R. 1998, *AJ*, 116, 981
- Edlén B. 1966. *Metrologia*, 2, 71
- ESA, *The Hipparcos and Tycho Catalogues*, ESA SP-1200, 1997
- Fernandez-Villacanas, J. L., Rego, M., Cornide, M. 1990. *AJ*, 99, 1961
- Forsberg, P. 1991, *Physica Scripta*, 44, 446
- Foukal, P. 1990, *Solar Astrophysics*, John Wiley & Sons, Inc., New York
- Freytag, B., Ludwig, H.-G., Steffen, M. 1996, *A&A*, 313, 497

- Freytag, B., Holweger, H., Steffen, M., Ludwig, H.-G. 1997, *Science with the VLT Interferometer*. ed. Paresce, F., Springer-Verlag, Berlin, p.316
- Gardiner, R. B., Kupka, F., Smalley, B. 1999, *A&Ap*, 347, 876
- Gough, D. O. 1969, *Journal of the Atmospheric Sciences*, 26, 448
- Gratton, L., Gaudenzi, S., Rossi, C., Gratton, R. G. 1982, *MNRAS*, 201, 807
- Gray, D. 1980, *ApJ*, 235, 508
- Gray, D. F. 1982, *ApJ*, 255,200
- Gray, D. 1992, *Seventh Cambridge Workshop on Cool Star. Stellar Systems and the Sun. ASP Conf. Ser. Vol. 26*, eds. Giampapa, M. S., Bookbinder, J. A.. San Francisco, CA, p.127
- Gray, D. F., Nagel, T. 1989, *ApJ*, 341, 421
- Gray, D. F., Toner, C. G. 1985, *PASP*, 97, 543
- Griffin, R. E. M., Lynas-Gray, A. E. 1999, *AJ*, 117, 2998
- Griffin, R. F. 1968, *A Photometric Atlas of the Spectrum of Arcturus $\lambda\lambda$ 3600-8825 Å*. Cambridge Philosophical Society, Cambridge, England
- Grossman, S. A. 1996, *MNRAS*, 279, 305
- Hall, D. N. B., Ridgway, S. T., Bell, E. A., Yarborough, J. M. 1979. *Proc. SPIE*, 172, 121
- Hatzes. A. P., Cochran, W. D. 1993. *ApJ*, 413, 339
- Hatzes. A. P., Cochran, W. D. 1996. *Cool Stars. Stellar Systems. and the Sun: 9.ASP Conf. Ser. Vol. 109*, eds. Pallavicini, R., Dupree, A. K.. Astronomical Society of the Pacific, San Francisco CA, p. 527
- Hinkle, K., Wallace, L., Livingston, W. 1995, *Infrared Atlas of the Arcturus Spectrum, 0.9-5.3 μ m*. Astronomical Society of the Pacific, San Francisco, CA
- Hoffleit, D., Jaschek, C. 1982. *The Bright Star Catalogue, 4th revised edition*. Yale University Observatory, New Haven CT
- Irwin, A. 1998, private communication

- Johnson, H. L., Iriarte, B., Mitchell, R. I., Wisniewskj, W. Z. 1966. *Comm. Lunar Planetary Lab.*, 4, 99
- Kleinmann, S. G., Hall, D. N. B. 1986, *ApJSS*, 62, 501
- Kneer, F. 1973, *Sol. Phys.*, 28, 361
- Knobloch, E., Weiss N. O. 1984, *MNRAS*, 207, 203
- Kupka, F. 1996, *Stellar Surface Structure*, eds. Strassmeir, K. G., Linsky, J. L., IAU Coll., p. 557
- Kupka, F. 1999a, *ApJ*, 526, L45
- Kupka, F. 1999, *Theory and Tests of Convection in Stellar Structure: First Granada Workshop*, eds. Giménez, Á., Guinan, E. F., Montesinos, B. A.S.P. Conf. Ser. Vol 173, p.157
- Kurucz, R., Avrett, E. H. 1982. SAO Special Report 391
- Kurucz, R., Furenlid, I., Brault, J., Testerman, L. 1984. *Solar Flux Atlas from 296 to 1300 nm*, N.S.O. Technical Report #91-001, NOAO:Tucson AZ
- Lang, K. R. 1980. *Astrophysical Formaulae. 2nd edition*, Springer-Verlag, Berlin
- Leighton, R. B. 1957. *PASP*, 69, 497
- Lester, J. B., Lane, M. C., Kurucz, R. L. 1982. *ApJ*, 260, 272
- Lindgren, L. Dravins, D., Madesn, S. 1999, *Precise Stellar Velocities. IAU Colloquium 170*, eds. Hearnshaw, J. B, Scarfe, C. D. A.S.P. Conf. Ser. Vol 185, p.73
- Lites, B. W., Bida, T. A., Johannesson, A., Scharmer, G. B. 1991, *ApJ*, 373, 683
- Livingston, W., Wallace, L. 1991, *An Atlas of the Solar Spectrum in the Infrared from 1850 to 9000 cm^{-1} (1.1 to 5.4 μm)*, N.S.O Technical Report #91-001, NOAO:Tucson AZ
- Maillard, J.-P. 1999, private communication
- Maillard, J.-P., Michel, G. 1982. *Instrumentation for Astronomy with Large Optical Telescopes*, ed. Humphries, C. M., D. Reidel Publishing Co., Dordrecht Holland, p.213
- Mazzitelli, I. 1999, *Theory and Tests of Convection in Stellar Structure: First Granada Workshop*, eds. Giménez, Á, Guinan, E. F., Montesinos, B. A.S.P. Conf. Ser. Vol 173, p.77

- Mazzitelli, I., D'Antona, F., Caloi V. 1995, A&A, 302, 382
- McWilliam, A. 1990, ApJSS, 74. 1075
- Mihalas, D. 1978, *Stellar Atmospheres, Second Edition*. W. H. Freeman and Company, New York, USA
- Moore, C. E., Minnaert, M. G. J., Houtgast, J. 1966, *The Solar Spectrum 2935 Å to 8770 Å* NBS Monograph 61, Washington D.C.
- Moore, R. L. 1981. Space Sci. Rev., 28. 387
- Nadeau, D. 1988. ApJ, 325. 480
- Nadeau, D., Maillard, J.-P. 1988. ApJ. 327. 321
- Nave, G. 1999. private communication
- Nave, G., Johansson, S., Learner, R. C. M., Thorne, A. P., Brault, J. W. 1994, ApJSS, 94, 221
- Neckel, H., Labs, D. 1990. Solar Physics. 126, 207
- Nordgren, T. E. , Germain, M. E., Benson, J. A., Mozurkewich, D., Sudol, J. J., Elias II, N. M., Hajian, A. R., White, N. M., Hutter, D. J., Johnston, K. J., Gauss, F. S., Armstrong, J. T., Pauls, T. A., Rickard, L. J. 1999, AJ, 118. 3032
- Nordlund, Å. 1982. A&A, 107. 1
- Nordlund, Å. 1985. Solar Physics. 100. 209
- Nordlund, Å., Dravins, D. 1990, A&A. 228. 155
- Nordlund, Å., Stein, R. F. 1996. *Stellar Evolution: What Should Be Done. Proceedings of the 32nd Liège Int. Astroph. Coll.*, eds. Noels et al., Univ. Liège, Inst. d'Astrophys., 75
- Nordlund, Å., Spruit, H. C., Ludwig, H.-G., Trampedach, R. 1997, A&A. 328. 229
- Noyes, R., W., Hall, D. N. B. 1972, ApJ, 176. L89
- Paternò, L., Ventura, R., Canuto, V. M., Mazzitelli, I. 1993. A&A, 402. 733
- Pierce, K. 1991. Solar Physics. 133. 215

- Pierce, K., Breckinridge, J. B. 1973, *The Kitt Peak Table of Photographic SWolar Spectrum Wavelengths*, Tucson:KPNO
- Ram, R. S., Bernath, P. F., Wallace, L. 1996, *ApJSS*, 107, 443
- Ram, R. S., Bernath, P. F., Dulick, M., Wallace, L. 1999 *ApJSS*, 122, 331
- Rast, M. P. 1995, *ApJ*, 443, 863
- Rosenthal, C. S., Christensen-Dalsgaard, J., Nordlund, Å., Stein, R. F., Trampedach, R. 1999. *A&A*, 351, 689
- Rutten, R. J., van der Zalm, E. B. J. 1984. *A&ApSS*. 55. 143
- Schlichenmaier, R., Schmidt, W. 1999, *A&A*, 349, L37
- Schwarzschild, M. 1975, *ApJ*, 195, 137
- Shine, R. A., Title, A. M., Tarbell, T. D., Smith, K., Frank, Z. A., Scharmer, G. 1993. *Solar Surface Magnetism*, eds. Rutten, R. J., Schrijver, C. J., Kluwer Academic Publishers. Netherlands. 197
- Smalley, B., Kupka, F. 1997 *A&A*. 328. 349
- Smith, V. V., Lambert, D. L. 1987. *MNRAS*, 226. 563
- Sobotka, M. 1997, *First Advances in Solar Physics Euroconference: Advances in the Physics of Sunspots*, ASP Conf. Ser. 118, eds.Schmieder, B.,del Tolo Iniesta, J. C., Vázquez, M., ASP. San Francisco, USA. p. 155
- Sobotka, M., Bonet, J. M., Vázquez, M. 1994. *ApJ*. 426. 404
- Solanki, S., Livingston, W., Muglach, K., Wallace, L. 1996. *A&A*. 315. 303
- Spruit, H. C. 1996, *BASI*, 24, 211
- Spruit, H. C. 1997, *MmSAIt.*, 68, 397
- Steffen, M. 2000. to appear in *Pacific Rim Conference on Stellar Astrophysics*, Kluwer Academic Publishers
- Stein, R. F., Nordlund, Å. 1998. *ApJ*. 499. 914

- Stein, R. F., Nordlund, Å. 1989. ApJ, 342, L95
- Stothers, R. B., Chin, C.-W. 1995, ApJ, 297, 440
- Sütterlin, P., Wiehr, E. 1998, A&A, 336, 367
- Swensson, J. W., Benedict, W. S., Delbouille, L., Roland, G. 1970, *The Solar Spectrum From λ 7498 to λ 12016*, Mémoires de la Société Royale des Sciences de Liège, Special Volume No. 5
- Taylor, B. J. 1999, A&ASS, 1334. 523
- Uitenbroek, H. 2000, ApJ, 531, 571
- Uitenbroek, H. 2000b, ApJ, 536. 481
- Wallace, L., Huang, Y. R., Livingston, W. 1988. ApJ, 327, 399
- Wallace, L., Livingston, W. 1992. *An Atlas of a Dark Sunspot Umbral Spectrum from 1970 to 8640 cm^{-1} (1.16 to $5.1\ \mu\text{m}$)*. N.S.O. Technical Report #92-001. NOAO:Tucson AZ
- Wallace, L., Hinkle, K., Livingston, W. 1998. *An Atlas of the Spectrum of the Solar Photosphere from $13,500$ to $28,000\text{ cm}^{-1}$ (3570 to $7405\ \text{Å}$)*. N.S.O. Technical Report #98-001. NOAO:Tucson AZ
- Wallace, L., Hinkle, K., Livingston, W. 1993, *An Atlas of the Photospheric Spectrum from 8900 to 13600 cm^{-1} (7350 to $11230\ \text{Å}$)*, N.S.O. Technical Report #93-001. NOAO:Tucson AZ
- Wallace, L., Livingston W. C., Bernath, P. F., Ram, R. S. 1998. *An Atlas of the Sunspot Umbral Spectrum in the Red and Infrared from 8900 to $15,050\text{ cm}^{-1}$ (6642 to $11,230\ \text{Å}$)*. N.S.O. Technical Report #98-002, NOAO:Tucson AZ
- Weiss, N. O., Brownjohn, D. P., Hurlburt, N. E., Proctor, M. R. E. 1990, MNRAS, 245. 434
- Woolley, R., Epps, E. A., Penston, M. J., Pcock, S. B. 1970, Roy. Obs. Ann. #5
- Xiong, D. R., Cheng, Q. L., Deng, L. 1997, ApJSS, 108. 529
- Zahn, J.-P. 1999. *Theory and Tests of Convection in Stellar Structure: First Granada Workshop*. eds. Giménez, Á., Guinan, E. F., Montesinos, B. A.S.P. Conf. Ser. Vol 173. p. 121